

## INFORMATION TO USERS

This manuscript has been reproduced from the microfilm master. UMI films the text directly from the original or copy submitted. Thus, some thesis and dissertation copies are in typewriter face, while others may be from any type of computer printer.

**The quality of this reproduction is dependent upon the quality of the copy submitted.** Broken or indistinct print, colored or poor quality illustrations and photographs, print bleedthrough, substandard margins, and improper alignment can adversely affect reproduction.

In the unlikely event that the author did not send UMI a complete manuscript and there are missing pages, these will be noted. Also, if unauthorized copyright material had to be removed, a note will indicate the deletion.

Oversize materials (e.g., maps, drawings, charts) are reproduced by sectioning the original, beginning at the upper left-hand corner and continuing from left to right in equal sections with small overlaps. Each original is also photographed in one exposure and is included in reduced form at the back of the book.

Photographs included in the original manuscript have been reproduced xerographically in this copy. Higher quality 6" x 9" black and white photographic prints are available for any photographs or illustrations appearing in this copy for an additional charge. Contact UMI directly to order.

# UMI

A Bell & Howell Information Company  
300 North Zeeb Road, Ann Arbor MI 48106-1346 USA  
313/761-4700 800/521-0600



**THE MAGNETIC PENETRATION DEPTH AND THE VORTEX CORE  
RADIUS IN TYPE-II SUPERCONDUCTORS**

By

Jeffrey E. Sonier

Honors B.Sc. University of Western Ontario, 1991

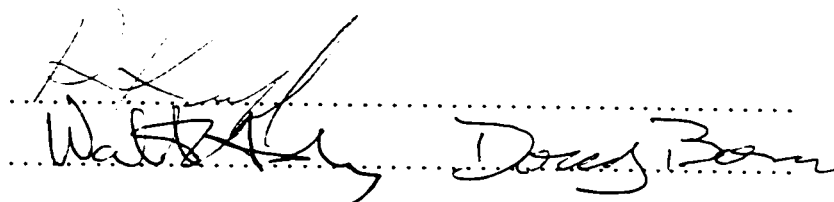
M.Sc. University of British Columbia, 1994

A THESIS SUBMITTED IN PARTIAL FULFILLMENT OF  
THE REQUIREMENTS FOR THE DEGREE OF  
DOCTOR OF PHILOSOPHY

in

THE FACULTY OF GRADUATE STUDIES  
DEPARTMENT OF PHYSICS AND ASTRONOMY

We accept this thesis as conforming  
to the required standard



THE UNIVERSITY OF BRITISH COLUMBIA

© Jeffrey E. Sonier, 1998



National Library  
of Canada

Acquisitions and  
Bibliographic Services

395 Wellington Street  
Ottawa ON K1A 0N4  
Canada

Bibliothèque nationale  
du Canada

Acquisitions et  
services bibliographiques

395, rue Wellington  
Ottawa ON K1A 0N4  
Canada

*Your file* *Votre référence*

*Our file* *Notre référence*

The author has granted a non-exclusive licence allowing the National Library of Canada to reproduce, loan, distribute or sell copies of this thesis in microform, paper or electronic formats.

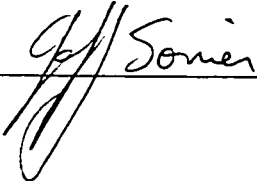
The author retains ownership of the copyright in this thesis. Neither the thesis nor substantial extracts from it may be printed or otherwise reproduced without the author's permission.

L'auteur a accordé une licence non exclusive permettant à la Bibliothèque nationale du Canada de reproduire, prêter, distribuer ou vendre des copies de cette thèse sous la forme de microfiche/film, de reproduction sur papier ou sur format électronique.

L'auteur conserve la propriété du droit d'auteur qui protège cette thèse. Ni la thèse ni des extraits substantiels de celle-ci ne doivent être imprimés ou autrement reproduits sans son autorisation.

0-612-27252-4

In presenting this thesis in partial fulfilment of the requirements for an advanced degree at the University of British Columbia. I agree that the Library shall make it freely available for reference and study. I further agree that permission for extensive copying of this thesis for scholarly purposes may be granted by the head of my department or by his or her representatives. It is understood that copying or publication of this thesis for financial gain shall not be allowed without my written permission.

  
\_\_\_\_\_

Department of Physics and Astronomy  
The University of British Columbia  
6224 Agricultural Road  
Vancouver, Canada  
V6T 1W5

Date:

April 6, 1998

## Abstract

In this thesis, muon spin rotation ( $\mu$ SR) measurements of the internal magnetic field distribution in the vortex state of the high- $T_c$  superconductor  $\text{YBa}_2\text{Cu}_3\text{O}_{7-\delta}$  and the conventional type-II superconductor  $\text{NbSe}_2$  are presented. From the measured field distributions, the “characteristic length scales of superconductivity” are extracted. It is found that both the  $\hat{a}$ - $\hat{b}$  plane magnetic penetration depth  $\lambda_{ab}$  and the vortex-core radius  $r_0$  (which is closely related to the coherence length  $\xi_{ab}$ ) vary as functions of temperature and magnetic field in both materials.

The behaviour of  $\lambda_{ab}(H, T)$  and  $r_0(H, T)$  at low temperatures is found to be substantially different in  $\text{YBa}_2\text{Cu}_3\text{O}_{7-\delta}$  from what is observed in  $\text{NbSe}_2$ . This reflects the unconventional nature of the pairing mechanism in this compound. The temperature dependence of  $\lambda_{ab}$  in the vortex state of  $\text{YBa}_2\text{Cu}_3\text{O}_{7-\delta}$  agrees well with microwave cavity measurements in the Meissner state. The magnetic field dependence of  $\lambda_{ab}$  in  $\text{YBa}_2\text{Cu}_3\text{O}_{7-\delta}$  is found to be considerably stronger than in  $\text{NbSe}_2$ . This is likely due to both the nonlinear and the nonlocal effects associated with nodes in the superconducting energy gap. However, in  $\text{NbSe}_2$  (where nonlocal effects are negligible), it is not clear whether the field dependence of  $\lambda_{ab}$  can be explained solely in terms of the nonlinear effects associated with an isotropic  $s$ -wave energy gap.

The vortex-core radius  $r_0$  is found to decrease with increasing magnetic field in both superconductors. The reduction in the vortex-core size appears to be due to the increased strength of the vortex-vortex interactions. An important consequence of this variation with field is that  $\xi_{ab}$  in the vortex state, which is generally regarded to be extremely small in the high- $T_c$  compounds, is comparatively large at low magnetic

fields.

The vortex-core radius is also found to increase with increasing temperature. The strength of this variation is considerably weaker in  $\text{YBa}_2\text{Cu}_3\text{O}_{7-\delta}$  than in  $\text{NbSe}_2$ . One possible interpretation is that the quantum limit is realized at much higher temperatures in the high- $T_c$  compound. The measured temperature dependence of  $r_0$  in both superconductors is weaker than current theoretical predictions for an isolated vortex.

Finally, the effects of vortex pinning and thermal fluctuations of the vortex lines are considered. It is found that the vortex lattice is strongly pinned in  $\text{YBa}_2\text{Cu}_3\text{O}_{7-\delta}$ . The vortex lattice in the underdoped compound  $\text{YBa}_2\text{Cu}_3\text{O}_{6.60}$  is found to exhibit quasi-2D behaviour. In particular, a field-induced transition of the 3D-vortex lattice to a 2D-vortex lattice is observed—which appears to be due to the small  $\hat{c}$ -axis coherence length and vortex pinning in the  $\text{CuO}_2$  layers of this material. Also, the 3D-solid vortex lattice in  $\text{YBa}_2\text{Cu}_3\text{O}_{6.60}$  at low temperatures is found to melt and/or undergo a transition to a 2D-vortex lattice as the temperature is increased.

## Table of Contents

|  |             |
|--|-------------|
| <b>Abstract</b>  | <b>ii</b>   |
| <b>Table of Contents</b>   | <b>iv</b>   |
| <b>List of Tables</b>  | <b>vii</b>  |
| <b>List of Figures</b>   | <b>viii</b> |
| <b>Acknowledgements</b>  | <b>xii</b>  |
| <b>1 Introduction</b>  | <b>1</b>    |
| <b>2 The Characteristic Length Scales of Superconductivity</b>             | <b>6</b>    |
| 2.1 The Magnetic Penetration Depth . . . . .                               | 6           |
| 2.1.1 The London Penetration Depth . . . . .                               | 7           |
| 2.1.2 The BCS Penetration Depth . . . . .                                  | 11          |
| 2.1.3 Penetration Depth for a $d_{x^2-y^2}$ -Wave Superconductor . . . . . | 15          |
| 2.2 The Superconducting Coherence Length . . . . .                         | 16          |
| 2.3 The Magnetic Field Dependence of the Penetration Depth at Low $T$ . .  | 18          |
| 2.3.1 Nonlinear Effects in an $s$ -Wave Superconductor . . . . .           | 18          |
| 2.3.2 Nonlinear Effects in a $d_{x^2-y^2}$ -Wave Superconductor . . . . .  | 22          |
| 2.3.3 Nonlinear and Nonlocal Effects in the Vortex State . . . . .         | 25          |
| 2.4 The GL Penetration Depth and Coherence Length . . . . .                | 26          |
| 2.5 Measuring the Characteristic Length Scales . . . . .                   | 31          |



|          |  |            |
|----------|--|------------|
| <b>3</b> | <b>The <math>\mu</math>SR Technique</b>                                    | <b>33</b>  |
| 3.1      | $\mu$ SR vs. NMR . . . . .   | 33         |
| 3.2      | Measuring the Internal Field Distribution with $\mu$ SR . . . . .          | 36         |
| 3.2.1    | The Raw Asymmetry for a Pair of Counters . . . . .                         | 38         |
| 3.2.2    | The Corrected Asymmetry . . . . .  | 39         |
| 3.2.3    | The Relaxation Function . . . . .  | 40         |
| 3.2.4    | Four-Counter Geometry and the Complex Polarization . . . . .               | 41         |
| 3.2.5    | The Fourier Transform . . . . .  | 43         |
| 3.3      | The Rotating Reference Frame . . . . .                                     | 43         |
| <b>4</b> | <b>Modelling the Internal Field Distribution</b>                           | <b>45</b>  |
| 4.1      | The Field Distribution of the Vortex Lattice . . . . .                     | 45         |
| 4.2      | Pinning, Thermal Fluctuations, Dimensional Crossover and Melting . . . . . | 49         |
| 4.3      | Gaussian Field Distribution Analysis . . . . .                             | 58         |
| 4.4      | Field Distribution of the Vortex Lattice . . . . .                         | 63         |
| 4.4.1    | Vortex Lattice in a <i>s</i> -Wave Superconductor . . . . .                | 65         |
| 4.4.2    | Vortex Lattice in a <i>d</i> -Wave Superconductor . . . . .                | 70         |
| <b>5</b> | <b>Experimental Details</b>  | <b>80</b>  |
| 5.1      | The Apparatus . . . . .  | 80         |
| 5.2      | The Samples . . . . .  | 83         |
| 5.3      | General Comments on the Fitting Procedure . . . . .                        | 87         |
| <b>6</b> | <b>Experiment: NbSe<sub>2</sub></b>  | <b>90</b>  |
| <b>7</b> | <b>Experiment: YBa<sub>2</sub>Cu<sub>3</sub>O<sub>6.95</sub></b>           | <b>118</b> |
| <b>8</b> | <b>Experiment: YBa<sub>2</sub>Cu<sub>3</sub>O<sub>6.60</sub></b>           | <b>146</b> |

|                      |            |
|----------------------|------------|
| <b>9 Conclusions</b> | <b>170</b> |
| <b>Bibliography</b>  | <b>174</b> |

## List of Tables

|     |   |     |
|-----|---|-----|
| 5.1 | Sample Characteristics . . . . .  | 87  |
| 6.2 | Comparison of Models for the Vortex Lattice . . . . .   | 94  |
| 6.3 | Magnetic Field Dependence in NbSe <sub>2</sub> . . . . .  | 99  |
| 7.4 | Magnetic Penetration Depth in YBa <sub>2</sub> Cu <sub>3</sub> O <sub>6.95</sub> . . . . .                  | 130 |
| 7.5 | Magnetic Field Dependence of $\lambda_{ab}$ in YBa <sub>2</sub> Cu <sub>3</sub> O <sub>6.95</sub> . . . . . | 132 |
| 8.6 | Magnetic Penetration Depth in YBa <sub>2</sub> Cu <sub>3</sub> O <sub>6.60</sub> . . . . .                  | 151 |

## List of Figures

|     |   |    |
|-----|---|----|
| 2.1 | Plane vacuum-superconductor interface . . . . .   | 10 |
| 2.2 | Energy gap function for a $s$ -wave and a $d_{x^2-y^2}$ -wave superconductor . . .                  | 13 |
| 2.3 | Nonlinear effects for a $s$ -wave superconductor . . . . .  | 20 |
| 2.4 | Nonlinear effects for a $d_{x^2-y^2}$ -wave superconductor . . . . .                                | 23 |
|     |   |    |
| 3.1 | Basic positron counter arrangement . . . . .  | 37 |
|     |   |    |
| 4.1 | The muon spin precession signal in $\text{YBa}_2\text{Cu}_3\text{O}_{6.95}$ . . . . .               | 47 |
| 4.2 | The $\mu\text{SR}$ line shape in $\text{YBa}_2\text{Cu}_3\text{O}_{6.95}$ . . . . .                 | 48 |
| 4.3 | Theoretical magnetic field distribution for a triangular vortex lattice . . .                       | 49 |
| 4.4 | Magnetic phase diagram . . . . .  | 55 |
| 4.5 | Fitting the muon precession signal with a Gaussian relaxation function . . .                        | 61 |
| 4.6 | The muon depolarization rate in $\text{YBa}_2\text{Cu}_3\text{O}_{6.95}$ . . . . .                  | 62 |
|     |   |    |
| 5.1 | The low background $\mu\text{SR}$ apparatus . . . . .   | 82 |
| 5.2 | The crystal structure of $\text{NbSe}_2$ . . . . .  | 84 |
| 5.3 | The crystal structure of $\text{YBa}_2\text{Cu}_3\text{O}_7$ . . . . .                              | 85 |
|     |   |    |
| 6.1 | The temperature dependence of the $\mu\text{SR}$ line shape in $\text{NbSe}_2$ . . . . .            | 91 |
| 6.2 | The magnetic field dependence of the $\mu\text{SR}$ line shape in $\text{NbSe}_2$ . . . . .         | 92 |
| 6.3 | The magnetic field dependence of $\lambda_{ab}$ in $\text{NbSe}_2$ for three different models . . . | 93 |
| 6.4 | The quality of the fits in $\text{NbSe}_2$ for three different models . . . . .                     | 95 |
| 6.5 | Comparison of fits for different theoretical models . . . . .                                       | 97 |
| 6.6 | The magnetic field dependence of $\lambda_{ab}$ in the vortex state of $\text{NbSe}_2$ . . . . .    | 98 |

|      |  |     |
|------|--|-----|
| 6.7  | The average supercurrent density in the Meissner and vortex states . . .   | 100 |
| 6.8  | The behaviour of the additional broadening parameter $\sigma_{\text{dis}}$ and the quality of the fits in NbSe <sub>2</sub> . . . . .          | 103 |
| 6.9  | The random disorder in the vortex lattice in NbSe <sub>2</sub> . . . . .   | 104 |
| 6.10 | The supercurrent density profile for an isolated vortex . . . . .  | 105 |
| 6.11 | The magnetic field dependence of the vortex-core radius in NbSe <sub>2</sub> for three different models . . . . .                              | 106 |
| 6.12 | $\mu$ SR and STM measurements of the magnetic field dependence of the vortex-core radius in NbSe <sub>2</sub> . . . . .                        | 107 |
| 6.13 | The magnetic field dependence of $\xi_{ab}$ in NbSe <sub>2</sub> . . . . .   | 110 |
| 6.14 | The magnetic field dependence of the GL parameter $\kappa$ in NbSe <sub>2</sub> . . . . .  | 111 |
| 6.15 | Fits to the muon precession signal in NbSe <sub>2</sub> . . . . .  | 113 |
| 6.16 | Difference between data and theory for fixed values of $\xi_{ab}$ in NbSe <sub>2</sub> . . .   | 114 |
| 6.17 | The quality of fits for fixed values of $\xi_{ab}$ in NbSe <sub>2</sub> . . . . .  | 115 |
| 6.18 | The temperature dependence of $\lambda_{ab}$ and $r_0$ in NbSe <sub>2</sub> . . . . .  | 116 |
| 7.1  | The temperature dependence of the $\mu$ SR line shape in YBa <sub>2</sub> Cu <sub>3</sub> O <sub>6.95</sub> . . .                              | 120 |
| 7.2  | The magnetic field dependence of the $\mu$ SR line shape in YBa <sub>2</sub> Cu <sub>3</sub> O <sub>6.95</sub> . .                             | 121 |
| 7.3  | Vortex-lattice pinning in YBa <sub>2</sub> Cu <sub>3</sub> O <sub>6.95</sub> . . . . .   | 123 |
| 7.4  | Thermal depinning of the vortex-lattice in YBa <sub>2</sub> Cu <sub>3</sub> O <sub>6.95</sub> . . . . .  | 124 |
| 7.5  | The temperature dependence of $\lambda_{ab}^{-2}$ in YBa <sub>2</sub> Cu <sub>3</sub> O <sub>6.95</sub> . . . . .                              | 127 |
| 7.6  | The temperature dependence of $\lambda_{ab}^{-2}$ in YBa <sub>2</sub> Cu <sub>3</sub> O <sub>6.95</sub> at different magnetic fields . . . . . | 129 |
| 7.7  | The magnetic field dependence of $\lambda_{ab}$ in YBa <sub>2</sub> Cu <sub>3</sub> O <sub>6.95</sub> . . . . .                                | 131 |
| 7.8  | The magnetic field dependence of $\lambda_{ab}$ in YBa <sub>2</sub> Cu <sub>3</sub> O <sub>6.95</sub> and NbSe <sub>2</sub> . . .              | 133 |

|      |   |     |
|------|---|-----|
| 7.9  | The temperature dependence of the coefficient of the term linear in $H$ for $\lambda_{ab}(H)$ in $\text{YBa}_2\text{Cu}_3\text{O}_{6.95}$ . . . . . | 134 |
| 7.10 | The behaviour of the additional broadening parameter $\sigma_f$ and the quality of the fits in $\text{YBa}_2\text{Cu}_3\text{O}_{6.95}$ . . . . .   | 135 |
| 7.11 | The random disorder in the vortex lattice in $\text{YBa}_2\text{Cu}_3\text{O}_{6.95}$ . . . . .   | 137 |
| 7.12 | The temperature dependence of the GL parameter in $\text{YBa}_2\text{Cu}_3\text{O}_{6.95}$ . . . . .  | 138 |
| 7.13 | The magnetic field dependence of the GL parameter in $\text{YBa}_2\text{Cu}_3\text{O}_{6.95}$ . . . . .   | 139 |
| 7.14 | Fits to the muon precession signal in $\text{YBa}_2\text{Cu}_3\text{O}_{6.95}$ . . . . .  | 140 |
| 7.15 | Difference between data and theory for fixed values of $\xi_{ab}$ in $\text{YBa}_2\text{Cu}_3\text{O}_{6.95}$ . . . . .                             | 141 |
| 7.16 | The quality of fits for fixed values of $\xi_{ab}$ in $\text{YBa}_2\text{Cu}_3\text{O}_{6.95}$ . . . . .  | 142 |
| 7.17 | The temperature dependence of $\xi_{ab}$ in $\text{YBa}_2\text{Cu}_3\text{O}_{6.95}$ . . . . .  | 144 |
| 7.18 | The magnetic field dependence of $\xi_{ab}$ in $\text{YBa}_2\text{Cu}_3\text{O}_{6.95}$ . . . . .   | 145 |
| 8.1  | The $\mu\text{SR}$ line shape in $\text{YBa}_2\text{Cu}_3\text{O}_{6.60}$ and $\text{YBa}_2\text{Cu}_3\text{O}_{6.95}$ . . . . .                    | 148 |
| 8.2  | The $\mu\text{SR}$ line shape in $\text{YBa}_2\text{Cu}_3\text{O}_{6.60}$ and $\text{YBa}_2\text{Cu}_3\text{O}_{6.95}$ . . . . .                    | 149 |
| 8.3  | The temperature dependence of $\lambda_{ab}^{-2}$ in $\text{YBa}_2\text{Cu}_3\text{O}_{6.60}$ . . . . .   | 150 |
| 8.4  | The temperature dependence of $\lambda_{ab}^{-2}$ in $\text{YBa}_2\text{Cu}_3\text{O}_{6.60}$ at different magnetic fields . . . . .                | 152 |
| 8.5  | The magnetic field dependence of $\lambda_{ab}$ in $\text{YBa}_2\text{Cu}_3\text{O}_{6.60}$ . . . . .   | 154 |
| 8.6  | The relationship between the additional broadening parameter $\sigma_f$ and $\lambda_{ab}$ . . . . .  | 155 |
| 8.7  | The behaviour of the additional broadening parameter $\sigma_f$ and the quality of the fits in $\text{YBa}_2\text{Cu}_3\text{O}_{6.60}$ . . . . .   | 156 |
| 8.8  | The random disorder in the vortex lattice in $\text{YBa}_2\text{Cu}_3\text{O}_{6.60}$ . . . . .   | 157 |
| 8.9  | The temperature dependence of the GL parameter in $\text{YBa}_2\text{Cu}_3\text{O}_{6.60}$ . . . . .  | 158 |
| 8.10 | The magnetic field dependence of the GL parameter in $\text{YBa}_2\text{Cu}_3\text{O}_{6.60}$ . . . . .   | 159 |
| 8.11 | The temperature dependence of $\xi_{ab}$ and $r_0$ in $\text{YBa}_2\text{Cu}_3\text{O}_{6.60}$ . . . . .  | 160 |

|      |  |     |
|------|--|-----|
| S.12 | The magnetic field dependence of $\xi_{ab}$ and $r_0$ in $\text{YBa}_2\text{Cu}_3\text{O}_{6.60}$ . . . . .                          | 161 |
| S.13 | The magnetic field dependence of $\xi_{ab}$ in $\text{YBa}_2\text{Cu}_3\text{O}_{6.60}$ and $\text{YBa}_2\text{Cu}_3\text{O}_{6.95}$ | 162 |
| S.14 | Dimensional vortex-lattice transition in $\text{YBa}_2\text{Cu}_3\text{O}_{6.60}$ . . . . .  | 165 |
| S.15 | Changing the applied field with a quasi-2D vortex-lattice in $\text{YBa}_2\text{Cu}_3\text{O}_{6.60}$                                | 167 |
| S.16 | The magnetic field dependence of the $\mu\text{SR}$ line shape in detwinned<br>$\text{YBa}_2\text{Cu}_3\text{O}_{6.60}$ . . . . .    | 169 |

## Acknowledgements

First and foremost I thank my thesis supervisor Rob Kiefl for his contribution to the physics in this thesis, his support and encouragement, and the decisions made in the best interest of my career. Equal thanks to Jess Brewer who has been like a second supervisor and a fine promoter of the work that I've done.

Special thanks to Walter Hardy and Doug Bonn for many inspiring discussions and for being a continuous source of leading edge information. I thank the crystal growers Ruixing Liang and Joseph Brill whose samples made the experiments possible.

I am grateful to the following individuals for their helpful theoretical input during the years this work was conducted: Ian Affleck, Mohammed Amin, John Berlinsky, Marcel Franz, Alexander Golubov, Uwe Hartmann, Catherine Kallin, Alan MacDonald, Kazushige Machida, Philip Stamp and Alain Yaouanc. I also thank the Canadian Institute of Advanced Research for providing me with the opportunity to meet and collaborate with top level researchers in the field of superconductivity.

I thank the following for their assistance in performing the experiments which are presented in this thesis: Jacques Chakhalian, Kim Chow, Sarah Dunsiger, Tim Duty, Graeme Luke, Andrew MacFarlane, Roger Miller, Phillippe Mendels, Gerald Morris, David Noakes, Tanya Riseman, Carey Stronach and Morris White Jr. Special thanks to the TRIUMF technical staff for the many overtime hours devoted to building and assembling the experimental apparatus: Donald Arseneau, Curtis Ballard, Mel Good, Bassam Hitti, Keith Hoyle and Syd Kreitzman.

Finally, I thank Pauline who doesn't understand anything in this thesis, but has provided the loving support we all need in our lives.



## Chapter 1

### Introduction

When a small magnetic field  $H < H_{c1}$  is applied to a type-II superconductor, the field is expelled from the interior of the sample—while in an applied magnetic field  $H_{c1} < H < H_{c2}$  it becomes energetically favourable for the field to penetrate the sample in the form of quantized flux lines, called vortices. In the first case (the “Meissner state”) the supercurrents which shield the inside of the superconductor from the magnetic field flow around the perimeter of the sample, whereas in the latter case (the “vortex state”) shielding currents circulate around the individual vortices.

In the Meissner state, there is some penetration of magnetic field into the surface of the superconductor where the shielding currents circulate. In particular, the magnetic field decays from the surface into the superconductor over a characteristic length scale  $\lambda$ , called the “magnetic penetration depth”.

In the vortex state, the superconducting carriers which make up the shielding currents circulate faster near the vortex axis. Beyond a critical velocity, superconductivity is destroyed. The region of normal state material near the vortex axis defines the “core”. The local magnetic field has a maximum in the center of the vortex core and decays outside the core over the length scale  $\lambda$ . If the vortices are spaced at a distance much greater than  $\lambda$  apart, the field decays to zero—otherwise the field is finite everywhere in the superconductor. The density of the superconducting carriers [or order parameter  $\psi(\mathbf{r})$ ] is zero at the vortex center and rises to its maximum value over a

distance of the order of  $\xi$ , which is called the "coherence length".

Together,  $\lambda$  and  $\xi$  represent the characteristic length scales of superconductivity. In particular,  $\lambda^{-2}$  is proportional to the density of superconducting carriers. Measurements of this quantity provide a means of investigating the spectrum of low-lying excitations in the superconducting state. On the other hand,  $\xi$  is the shortest distance over which the density of superconducting carriers can vary appreciably. Put another way,  $\xi$  is the characteristic length scale of the superconducting order parameter  $\psi(\mathbf{r})$ . A complete understanding of the behaviour of these parameters (*i.e.* as a function of temperature, impurities and magnetic field) is an essential ingredient of any theory which attempts to explain the mechanism responsible for superconductivity in the high- $T_c$  materials.

The behaviour of  $\lambda$  and  $\xi$  is generally considered to be the same in both the Meissner and vortex phases. However, when measuring these length scales, several complications arise from the presence of vortices. At low magnetic fields in the vortex state, the vortex cores are essentially isolated. In this case, one might expect that measurements of  $\lambda$  in the vortex state should show the same variation with temperature  $T$  and magnetic field  $H$  as measurements of  $\lambda$  in the Meissner state. However, at higher magnetic fields the vortices interact appreciably with one another, changing the distribution of magnetic field between them. Measurements of  $\lambda$  as a function of temperature or magnetic field are sensitive to the way in which the field distribution between the vortices changes. In particular, the function  $\lambda(H, T)$  which is obtained from experiment depends on the way in which these changes are modelled. Thus in general,  $\lambda(H, T)$  obtained from measurements in the vortex state cannot be directly compared to  $\lambda(H, T)$  obtained from measurements in the Meissner state.

A second important complication is that the interior of a vortex has an electronic structure which changes with temperature and magnetic field. This electronic structure

is a unique property of the vortex and need not be like the quasiparticle states in the normal phase. The precise nature of this electronic structure is still a matter of debate, especially in the high- $T_c$  materials. In these materials the normal state exhibits many anomalous properties, so there is good reason to expect that the electronic structure of the vortex cores is different than that in conventional superconductors.

In the vortex state, the order parameter  $\psi(\mathbf{r})$  is diminished appreciably (from its bulk value) in the region of a vortex core. Since  $\xi$  is the characteristic length for variations in  $\psi(\mathbf{r})$ , then  $\xi$  is related to the size of the vortex cores. In a conventional superconductor, the radius of a vortex core  $r_0$  is about the size of  $\xi$  [1]. Because of the close relationship between  $r_0$  and  $\xi$  in the vortex state, the terms “vortex-core radius” and “coherence length” will be used interchangeably throughout this thesis. However,  $\xi$  should not be confused with the coherence length in the Meissner state. For instance, the size of a vortex core changes as its electronic structure changes. As a result, the variation of  $\xi$  with temperature and magnetic field in the vortex state is directly linked to the vortex cores. Thus, there is no reason to expect that measurements of  $\xi(H, T)$  in the vortex state will exhibit the same behaviour as  $\xi(H, T)$  in the Meissner phase.

The behaviour of  $\lambda$  and  $\xi$  is expected to be sensitive to the symmetry of the pairing state. Their behaviour as a function of temperature and magnetic field can be used to resolve the structure of the energy gap in a superconductor. For instance, it is now widely believed that the pairing state in the high- $T_c$  superconductors is one possessing  $d_{x^2-y^2}$  symmetry, which has four nodal lines on the Fermi surface. The presence of these nodes means that the superconducting state is more sensitive to perturbations than a conventional superconductor, which has an energy gap everywhere on the Fermi surface. In particular, this sensitivity will appear as anomalous changes in the temperature and field dependence of  $\lambda$ , which is related to the fraction of the superfluid component.

Measurements of  $\lambda$  and  $\xi$  (*i.e.*  $r_0$ ) in the vortex state using muon spin rotation

( $\mu$ SR) spectroscopy is the primary focus of this thesis. What is really measured is the magnetic field distribution in the bulk of the superconductor, which is predominantly due to the vortex lattice. Extracting  $\lambda$  and  $\xi$  requires some modelling of this distribution. Generally speaking, the current theoretical models are inadequate to fully describe this field distribution. Nevertheless, the data can be fit very well with the field distributions predicted from basic models in which the characteristic length scales are defined. Deviations in the measured behaviour of these length scales, from that predicted by the theory used to model the data, can be attributed to a problem with the definition of  $\lambda$  and  $\xi$  in the theory itself. In this sense, what is really reported in this thesis is an “effective” penetration depth and an “effective” coherence length.

I will begin with a basic introduction to the characteristic length scales as they pertain to conventional and unconventional superconductors. I shall proceed to discuss how the  $\mu$ SR technique can be used to obtain both  $\lambda$  and  $r_0$  (which is closely related to the coherence length  $\xi$ ), from the measured internal field distribution. Currently, this technique is the only way to study  $\xi$  in the “bulk” of the high- $T_c$  cuprates, deep in the superconducting state.

I shall then explain how one can model the measured internal field distribution. The effects of pinning and thermal fluctuations will be discussed as they pertain to both a 3D and a 2D vortex lattice. This will be followed by an outline of the current theoretical description of the vortex structure in both conventional  $s$ -wave and unconventional  $d$ -wave superconductors.

Next, I shall present measurements of  $\lambda_{ab}$  and  $r_0$  in the conventional superconductor NbSe<sub>2</sub>, and in the optimally doped and underdoped high- $T_c$  superconductors YBa<sub>2</sub>Cu<sub>3</sub>O<sub>6.95</sub> and YBa<sub>2</sub>Cu<sub>3</sub>O<sub>6.60</sub>, respectively. The results are taken from our most recent work which appears in a series of short papers [2,3,4,5]. We shall find that  $\lambda_{ab}$  exhibits unconventional behaviour as a function of both temperature and magnetic field

in  $\text{YBa}_2\text{Cu}_3\text{O}_{7-\delta}$ . I also show that  $r_0$  changes dramatically as a function of temperature and field, and that the strength of these variations differs markedly in  $\text{YBa}_2\text{Cu}_3\text{O}_{7-\delta}$  from what is observed in  $\text{NbSe}_2$ . I shall show that the qualitative behaviour of the extracted values of  $\lambda_{ab}$  and  $r_0$  is fairly robust with respect to the way in which the  $\mu\text{SR}$  data is modelled. I conclude by summarizing and discussing the novel features associated with the measurements in  $\text{YBa}_2\text{Cu}_3\text{O}_{7-\delta}$  relative to those of  $\text{NbSe}_2$ .

## Chapter 2

### The Characteristic Length Scales of Superconductivity

In this chapter the definitions of the characteristic superconducting length scales ( $\lambda$  and  $\xi$ ) in the London, BCS and GL theories are introduced. Both the linear and the nonlinear response of a superconductor to a static external magnetic field are discussed. The effect of nonlocal electrodynamics on the behaviour of the length scales is also considered in connection with a  $d_{x^2-y^2}$ -wave superconductor. The chapter concludes with a brief summary of how one can measure  $\lambda$  and  $\xi$ .

#### 2.1 The Magnetic Penetration Depth

For a static magnetic field  $B(0)$  applied parallel to a planar vacuum-to-superconducting interface, the magnetic penetration depth can be defined as [1]

$$\lambda = \frac{1}{B(0)} \int_0^\infty B(r) dr . \quad (2.1)$$

where  $r$  is the distance into the superconductor measured from the surface and  $B(r)$  is a function describing the decay of the magnetic field into the superconducting region. The response of the superconductor to the magnetic field is usually defined in terms of the expectation value of the induced supercurrent density, which can be determined quantum mechanically [6]. The momentum-space relation between the induced current and a static magnetic field for an isotropic superconductor is

$$\mathbf{J}(\mathbf{k}) = -\frac{c}{4\pi} Q(\mathbf{k}) \mathbf{A}(\mathbf{k}) . \quad (2.2)$$

where  $Q(\mathbf{k})$  is a circularly symmetric electromagnetic response kernel and  $\mathbf{A}(\mathbf{k})$  is the classical vector potential. In general, the electromagnetic response kernel is a tensor. In an AC field,  $\mathbf{J}$ ,  $Q$  and  $\mathbf{A}$  are also functions of the frequency  $\omega$ —however, in this thesis only DC magnetic fields are used. In real space the relation between the induced supercurrent density and the vector potential can be written as

$$\mathbf{J}(\mathbf{r}) = -\frac{c}{4\pi} \int Q(\mathbf{r} - \mathbf{r}') \mathbf{A}(\mathbf{r}') d^3 \mathbf{r}' . \quad (2.3)$$

where  $Q(\mathbf{r})$  is the Fourier transform of  $Q(\mathbf{k})$ . In this case,  $\mathbf{J}$ ,  $Q$  and  $\mathbf{A}$  are also functions of time in an AC field. The relation between  $Q(k)$  and an applied field  $B(0)$  is [1]

$$B(r) = \frac{2B(0)}{\pi} \int_0^\infty \frac{k \sin(kr)}{Q(k) + k^2} dk . \quad (2.4)$$

Equation (2.1) and Eq. (2.4) can be combined to give a general relation for  $\lambda$  in terms of  $Q(k)$

$$\lambda = \frac{2}{\pi} \int_0^\infty \int_0^\infty \frac{r \sin(kr)}{Q(k) + k^2} dr dk . \quad (2.5)$$

Equation (2.5) is generally valid and can be used with the kernel  $Q(k)$  corresponding to any theory.

### 2.1.1 The London Penetration Depth

Let us first consider the magnetic penetration depth in the context of the conventional London theory [7] at  $T=0$ . If a magnetic field is applied to a superconductor which is initially in zero field, the magnetic field is a function of time. According to the Maxwell equation  $\nabla \times \mathbf{E} = -\frac{1}{c} \partial \mathbf{B} / \partial t$ , the time-varying magnetic field gives rise to an electric field. In a normal metal this will induce eddy currents, but in a superconductor the  $\mathbf{E}$ -field will give rise to persistent currents (*i.e.* supercurrents). The induced supercurrents will in turn generate a magnetic field of their own which opposes the applied magnetic field. If the applied magnetic field is weak, the flux is totally screened from the bulk of

the superconductor. This phenomenon is often described as “perfect diamagnetism”. From Newton’s law, the equation of motion for a superconducting carrier with mass  $m$  and charge  $-\epsilon$  in the presence of an electric field  $\mathbf{E}$  is

$$\mathbf{F} = m \frac{d\mathbf{v}_s}{dt} = -\epsilon \mathbf{E}. \quad (2.6)$$

where  $\mathbf{v}_s$  is the velocity of the superconducting carrier. The field-induced supercurrent density is given by

$$\mathbf{J}_s = -\epsilon n_s \mathbf{v}_s. \quad (2.7)$$

where  $n_s$  is the local density of superconducting carriers. Substituting Eq. (2.7) into Eq. (2.6) gives

$$\frac{d\mathbf{J}_s}{dt} = \frac{n_s \epsilon^2}{m} \mathbf{E}. \quad (2.8)$$

which is known as the “first London equation”. Taking the *curl* of both sides of Eq. (2.8) gives

$$\frac{m}{n_s \epsilon^2} \left( \nabla \times \frac{d\mathbf{J}_s}{dt} \right) = \nabla \times \mathbf{E}. \quad (2.9)$$

which can be rewritten using the Maxwell equation  $\nabla \times \mathbf{E} = -\frac{1}{c} d\mathbf{B}/dt$  to give

$$\frac{mc}{n_s \epsilon^2} \left( \nabla \times \frac{d\mathbf{J}_s}{dt} \right) + \frac{d\mathbf{B}}{dt} = 0. \quad (2.10)$$

In order to obtain the Meissner effect (*i.e.*  $\mathbf{B} = 0$  in the bulk of the superconductor) the London brothers removed the time derivative in Eq. (2.10) and postulated the new equation

$$\frac{mc}{n_s \epsilon^2} (\nabla \times \mathbf{J}_s) + \mathbf{B} = 0. \quad (2.11)$$

Equation (2.11) is commonly referred to as the “second London equation”. Since the supercurrent density is related to the field  $\mathbf{B}$  by another Maxwell equation

$$\mathbf{J}_s = \frac{c}{4\pi} (\nabla \times \mathbf{B}). \quad (2.12)$$



substitution of Eq. (2.12) into Eq. (2.11) gives

$$\lambda_L^2(\nabla \times \nabla \times \mathbf{B}) + \mathbf{B} = 0, \quad (2.13)$$

where

$$\frac{1}{\lambda_L^2} = \frac{4\pi n_s e^2}{mc^2}. \quad (2.14)$$

The variable  $\lambda_L$  is called the London penetration depth. Note that  $\lambda_L^{-2}$  is proportional to the superfluid density  $n_s$ .

The relationship between  $\lambda_L$  and  $\mathbf{B}$  is best realized by a simple example. Consider the vacuum-superconductor interface illustrated in Fig. 2.1. If a field  $\mathbf{B}(0)$  is applied parallel to the surface of the superconductor, the solution of Eq. (2.13) is

$$\mathbf{B}(x) = \mathbf{B}(0) \exp(-x/\lambda_L). \quad (2.15)$$

Thus, both the magnetic field  $B(x)$  and the supercurrent density  $J_s(x)$  decay exponentially with distance inside the superconductor over the length scale  $\lambda_L$ .

Equation (2.14) was derived for  $T=0$ . At nonzero temperature the behaviour of  $\lambda_L$  can be approximated by incorporating the two-fluid model of Gorter and Casimir [8]. In this model the electron system is assumed to contain a superconducting component with electron density  $n_s$ , and a normal component with an electron density  $n_n$ . The total electron density  $n = n_s + n_n$  becomes  $n = n_s$  at  $T=0$ , and  $n = n_n$  for  $T > T_c$ , where  $T_c$  is the superconducting transition temperature. For arbitrary temperature, Gorter and Casimir found that good agreement with early experiments could be obtained if one assumes that  $n_s(T) = n[1 - (T/T_c)^4]$ . When this expression is combined with Eq. (2.14) the penetration depth is given by

$$\lambda_L(T) = \frac{\lambda_L(0)}{[1 - (T/T_c)^4]^{1/2}}. \quad (2.16)$$

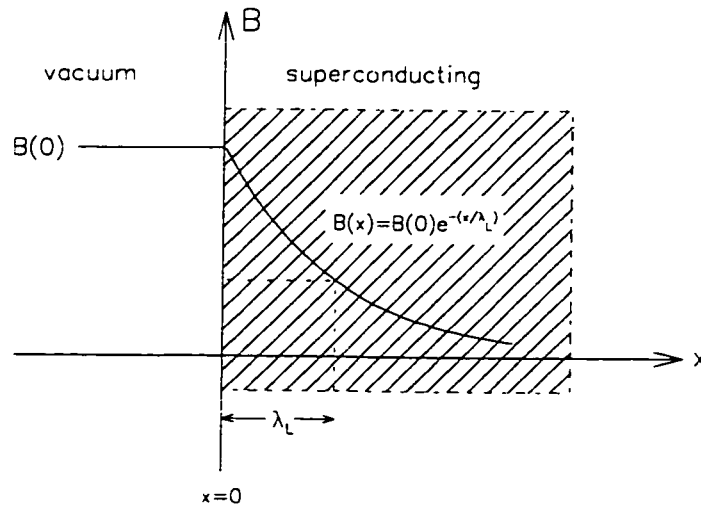


Figure 2.1: A magnetic field of magnitude  $B(0)$  applied parallel to a plane vacuum-superconductor interface. The field decays to  $B(0)/e$  at a distance  $x = \lambda_L$  in the superconducting region.

As the temperature  $T$  increases,  $n_s$  is reduced and the magnetic penetration depth increases with  $T$ , such that  $\lambda_L \rightarrow \infty$  as  $T \rightarrow T_c$ . Although this relation gives a good first-order description of many of the experimental results for conventional superconductors, the temperature dependence is not a prediction from the two-fluid model. Better agreement is obtained with the behaviour predicted from the microscopic theory developed by Bardeen, Cooper and Schrieffer (BCS) [9].

Before considering the BCS theory, let us work backwards to determine the kernel  $Q(\mathbf{k})$  in Eq. (2.2) for the London theory. The second London equation [*i.e.* Eq. (2.13)] can be rewritten using the Maxwell relation in Eq. (2.12) and the relation  $\mathbf{B} = \nabla \times \mathbf{A}$  to give

$$\frac{4\pi\lambda_L^2}{c}(\nabla \times \mathbf{J}_s) + \nabla \times \mathbf{A} = 0. \quad (2.17)$$

which is easily solved for  $\mathbf{J}_s$  to give

$$\mathbf{J}_s(\mathbf{r}) = -\frac{c}{4\pi\lambda_L^2}\mathbf{A}(\mathbf{r}). \quad (2.18)$$

The  $\mathbf{k}$ th Fourier component of  $\mathbf{J}_s$  is thus

$$\mathbf{J}_s(\mathbf{k}) = -\frac{c}{4\pi\lambda_L^2}\mathbf{A}(\mathbf{k}). \quad (2.19)$$

Comparing Eq. (2.19) with Eq. (2.2) gives the following simple result for the London kernel

$$Q_L(\mathbf{k}) = \frac{1}{\lambda_L^2}. \quad (2.20)$$

Clearly,  $Q_L$  is independent of  $\mathbf{k}$ . This implies that the London theory is a local theory, where the value of  $\mathbf{J}_s$  at a point  $\mathbf{r}$  only depends on the value of  $\mathbf{A}$  at that same point  $\mathbf{r}$ . Generally, the value of  $\mathbf{A}$  in the vicinity of the point where  $\mathbf{J}_s$  is being measured is also important. In a more general nonlocal theory,  $Q(\mathbf{k})$  depends on  $\mathbf{k}$ .

The current density due to the normal electrons is

$$\mathbf{J}_n = \sigma_n \mathbf{E} = -en_n \mathbf{v}_n. \quad (2.21)$$

where  $\sigma_n$  is the finite conductivity of the normal fluid. Thus, the total current density at arbitrary temperature below  $T_c$  is simply

$$\begin{aligned} \mathbf{J} &= \mathbf{J}_s + \mathbf{J}_n \\ &= -e(n_s \mathbf{v}_s + n_n \mathbf{v}_n). \end{aligned} \quad (2.22)$$

### 2.1.2 The BCS Penetration Depth

Consider the BCS ground state for a conventional superconductor with a cylindrical Fermi surface, such that the axis of the Fermi cylinder is parallel to the  $\hat{k}_z$ -axis. A cross-section of the Fermi cylinder in the  $\hat{k}_x$ - $\hat{k}_y$  plane is shown in Fig 2.2. In the

superconducting ground state, the electrons near the Fermi surface are paired through a virtual phonon-induced attractive interaction (*i.e.* Cooper pairs). The BCS ground state differs from the normal state in that some of the states just above the normal Fermi surface are occupied, while some just below are unoccupied. The attractive interaction between paired electrons lowers the total energy relative to the normal ground state of unpaired electrons. The energy reduction is maximized if the two electrons making up a pair (i) have equal and opposite momenta  $\hbar\mathbf{k}$  and  $-\hbar\mathbf{k}$ , so that the total center-of-mass momentum of a Cooper pair is zero and (ii) if they have opposite spins (*i.e.* in a spin-singlet state  $S=0$ ). The two electrons which make up a Cooper pair are continuously scattered between states of equal and opposite momentum by virtual phonons. However, the scattering pairs interfere with each other so that the superconducting state is a highly correlated many-body state. The BCS theory calculates the superconducting ground state using an explicit  $N$ -particle wavefunction with all of these correlations built in. The wavefunctions corresponding to the Cooper pairs in the original BCS theory were assumed to have orbital angular momentum  $l=0$ . Thus, in a conventional superconductor the pairing is considered to be *s*-wave, spin singlet. At a given instant of time, a Cooper pair is in a state  $(\mathbf{k}_i \uparrow, -\mathbf{k}_i \downarrow)$ , where the wavefunction describing the pair consists of all states “ $i$ ” occupied by the pair during its lifetime. It should be noted that the original BCS theory can be extended to explain other systems. For instance, the BCS theory can be generalized to describe the superfluid state of  $^3\text{He}$ . The  $^3\text{He}$  atoms form *p*-wave ( $l=1$ ) spin-triplet ( $S=1$ ) pairs. In this case, the  $^3\text{He}$  atoms are held together by magnetic interactions, rather than phonons.

One of the important features emerging from the BCS theory, is the existence of a temperature-dependent energy gap function  $\Delta_{\mathbf{k}}$  at the Fermi surface. For an energy

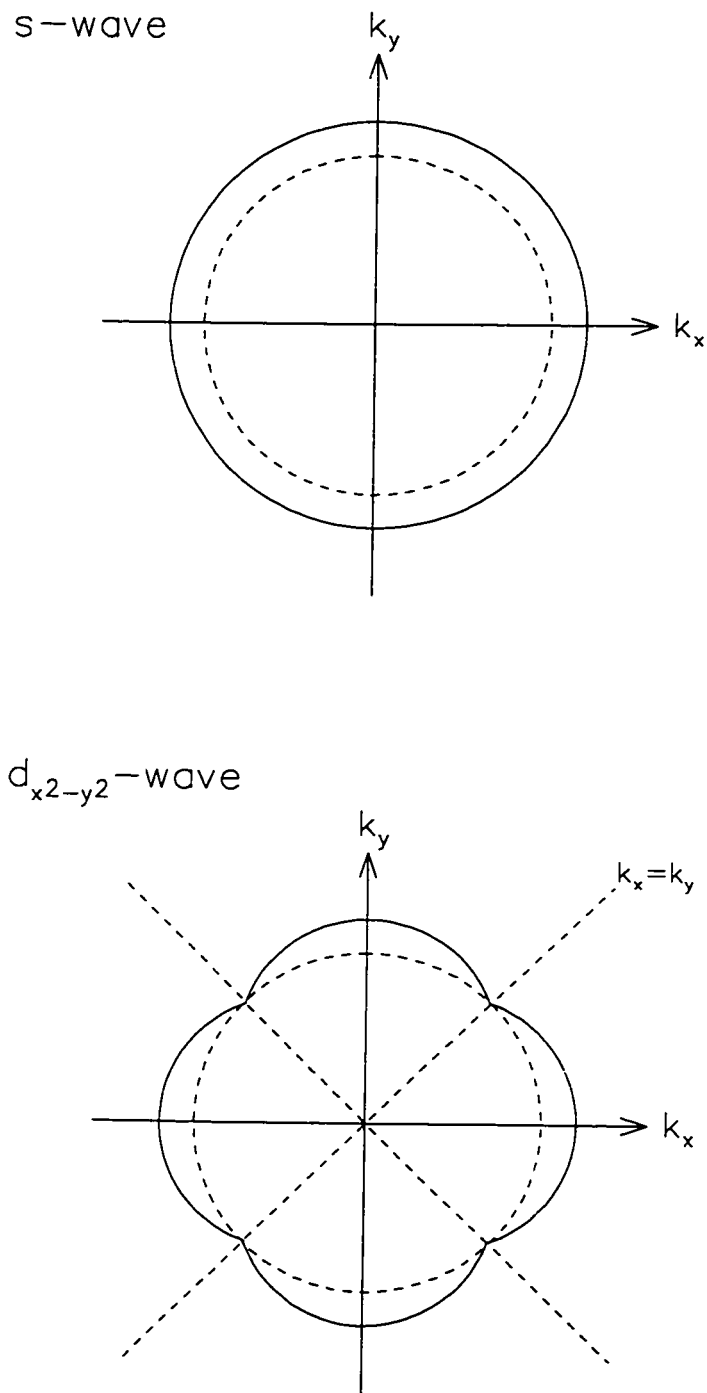


Figure 2.2: The energy gap function in 2D for a  $s$ -wave (top) and  $d_{x^2-y^2}$ -wave (bottom) superconductor. In each case the 2D Fermi surface is represented by a dashed circle, whereas the solid circle or solid curves denote the first excited quasiparticle states. Note that the distances between the solid and dashed lines represent energy differences, not distance in  $\mathbf{k}$ -space.

gap with *s*-wave symmetry.  $\Delta$  is independent of  $\mathbf{k}$ . The energy gap  $\Delta$  is the minimum energy required to create a single electron (hole) excitation from the superconducting ground state, so that the binding energy of a Cooper pair is  $2\Delta$ . Many conventional superconductors are in the weak-coupling limit in which  $\Delta \ll \hbar\omega_D$ , where  $\hbar\omega_D$  is the Debye energy for phonons in the lattice. In the weak-coupling limit at  $T = 0$ , the uniform energy gap is simply proportional to  $T_c$

$$\Delta(0) = 1.76k_B T_c. \quad (2.23)$$

At arbitrary temperature the energy gap is given by

$$\Delta(T) = \Delta(0) \exp [f(\Delta(T)/k_B T)], \quad (2.24)$$

where  $f$  is a universal function of the ratio  $\Delta(T)/k_B T$ . Near  $T_c$  this yields

$$\Delta(T) = 1.74\Delta(0) \left(1 - \frac{T}{T_c}\right)^{1/2}. \quad (2.25)$$

As the temperature is raised above  $T = 0$ , an increasing number of electrons are thermally excited across the energy gap into single quasiparticle states. The minimum energy to create an excitation is  $2\Delta$ , which is the binding energy of a Cooper pair. A single quasiparticle excitation of momentum  $\hbar\mathbf{k}$  has energy

$$E_{\mathbf{k}} = \sqrt{\varepsilon_{\mathbf{k}}^2 + \Delta_{\mathbf{k}}^2}. \quad (2.26)$$

where  $\varepsilon_{\mathbf{k}} = (\hbar^2 k^2 / 2m) - E_F$  is the quasiparticle energy in the absence of a gap measured relative to the Fermi surface.

The penetration depth in BCS theory is determined by first calculating  $Q(\mathbf{k})$  and then substituting the result into Eq. (2.5). The expression for the BCS kernel is nonlocal, and therefore more general than the London kernel. Since the expression for  $Q(\mathbf{k})$  and hence  $\lambda$  turns out to be nontrivial, only the BCS result in the low-temperature

limit is presented here. In particular, for a clean superconductor in which  $T \ll T_c$ , the number of quasiparticles excited to energy states above the gap is exponentially activated such that [10]

$$\frac{\lambda(T) - \lambda(0)}{\lambda(0)} \simeq \sqrt{\pi\Delta(0)/2k_B T} \exp(-\Delta(0)/k_B T). \quad (2.27)$$

### 2.1.3 Penetration Depth for a $d_{x^2-y^2}$ -Wave Superconductor

If there are line or point nodes in the energy gap function  $\Delta_{\mathbf{k}}$ , a power law dependence is expected, where  $\lambda(T) - \lambda(0) \propto T^n$  ( $n = 1, 2, 3$  or  $4$ ) [11,12]. The presence of the nodes on the Fermi surface allows quasiparticle excitations to occur for an infinitesimal amount of thermal energy. In particular, for the high- $T_c$  superconductors there is strong evidence that the energy gap has  $d_{x^2-y^2}$  symmetry. In this case the energy gap function is given by

$$\Delta_{\hat{\mathbf{k}}} = \Delta_0(\hat{k}_x^2 - \hat{k}_y^2) = \Delta_0 \cos(2\theta) \quad (2.28)$$

where  $\Delta_0$  is the maximum value of the energy gap. For this symmetry there are line nodes on the Fermi surface. At low temperatures an approximate analytical expression can be obtained for the magnetic penetration depth [13]

$$\lambda(T) - \lambda(0) \simeq \lambda(0)C \frac{T}{\Delta(0)}. \quad (2.29)$$

where  $C = \ln(2)$  for a circular Fermi surface. There are now many published measurements of the penetration depth in high- $T_c$  compounds, which support this linear- $T$  behaviour. Recent measurements in the Meissner state of high quality single crystals of  $\text{YBa}_2\text{Cu}_3\text{O}_{7-\delta}$  [14,15,16],  $\text{Bi}_2\text{Sr}_2\text{CaCu}_2\text{O}_{8+\delta}$  [17,18,19,20] and magnetically aligned powders of crystalline  $\text{HgBa}_2\text{Ca}_2\text{Cu}_3\text{O}_{8+\delta}$  [21] show a strong linear- $T$  dependence for  $\lambda(T) - \lambda(0)$  at low  $T$ . Muon spin rotation ( $\mu\text{SR}$ ) measurements have determined that  $\lambda(T)$  also changes linearly as a function of  $T$  in the vortex state of  $\text{YBa}_2\text{Cu}_3\text{O}_{7-\delta}$

[2.3.5] and  $\text{La}_{1.85}\text{Sr}_{0.15}\text{CuO}_4$  [22]. Experiments on the high- $T_c$  materials which show  $T$  dependences other than linear are often explained in terms of extrinsic effects. For instance, in a  $d_{x^2-y^2}$ -wave superconductor, impurity scattering can change the low-temperature behaviour of  $\lambda(T)$  from a  $T$  to  $T^2$  dependence [13.23]. This has been verified experimentally by substituting small quantities of the non-magnetic impurity  $\text{Zn}^{2+}$  for  $\text{Cu}^{2+}$  in  $\text{YBa}_2\text{Cu}_3\text{O}_{7-\delta}$  [24.25]. An exception in the high- $T_c$  family appears to be the electron-doped superconductors. For instance, measurements of  $\lambda_{ab}(T)$  in  $\text{Nd}_{1.85}\text{Ce}_{0.15}\text{CuO}_4$  single crystals are consistent with  $s$ -wave BCS theory and show no evidence of a linear- $T$  term [26.27]. However, the large rare earth moments which are present in the electron-doped high- $T_c$  cuprates may have a large effect on the measured  $\lambda_{ab}(T)$ . This extrinsic effect may mask the intrinsic nature of the superfluid which is common to the hole-doped high- $T_c$  materials.

## 2.2 The Superconducting Coherence Length

To explain numerous experimental results which deviated from the predictions of the London theory, Pippard [28] proposed the following general nonlocal relation for the supercurrent response

$$\mathbf{J}_s(\mathbf{r}) = -\frac{3}{\xi_0} \left( \frac{c}{4\pi\lambda_L} \right)^2 \int \frac{\mathbf{R}[\mathbf{R} \cdot \mathbf{A}(\mathbf{r}')] \exp(-R/\xi) d^3r'}{R^4} \quad (2.30)$$

where  $\mathbf{R} = \mathbf{r} - \mathbf{r}'$ ,  $\xi_0$  is the coherence length and  $\xi$  is an effective coherence length related to the electron mean-free path  $l$  through the equation

$$\frac{1}{\xi} = \frac{1}{\xi_0} + \frac{1}{\alpha l} \quad (2.31)$$

where  $\alpha$  is a constant on the order of unity. For a pure superconductor,  $\xi = \xi_0$ . The response of the superconductor to the applied magnetic field is nonlocal, in the sense that the value of  $\mathbf{J}_s$  measured at a point  $\mathbf{r}$  depends on the value of  $\mathbf{A}$  throughout a



volume of radius  $\xi$  surrounding the point  $\mathbf{r}$ . The Pippard kernel relating the  $k$ th Fourier component of  $\mathbf{J}_s$  to the vector potential  $\mathbf{A}(k)$  can be determined from Eq. (2.30), and is given by

$$Q_P(k) = \frac{\xi}{\xi_0 \lambda_L^2} \left\{ \frac{3}{2(k\xi)^3} [(1 + k^2 \xi^2) \tan^{-1}(k\xi) - k\xi] \right\}. \quad (2.32)$$

$Q_P(k)$  is always smaller than the London kernel  $Q_L(k)$ . As a result, substituting the expression for  $Q_P(k)$  into Eq. (2.5) will always yield a value for  $\lambda$  which is larger than  $\lambda_L$ . In particular, for  $\xi \ll \lambda$

$$\lambda = \lambda_L \left( \frac{\xi_0}{\xi} \right)^{1/2}. \quad (2.33)$$

and for  $\xi \gg \lambda$

$$\lambda = \left( \frac{\sqrt{3}}{2\pi} \xi_0 \lambda_L^2 \right)^{1/3}. \quad (2.34)$$

Note that in the first limiting case,  $\lambda$  agrees with the London prediction in a pure superconductor. On the other hand, the second limiting case is completely independent of the electron mean-free path. A superconductor described by the first equation, is called a "type-II superconductor", whereas one that is described by the second equation is a "type-I superconductor".

Using an argument based on the uncertainty principle, Pippard estimated that the coherence length in a pure metallic superconductor is

$$\xi_0 = a \frac{\hbar v_f}{k_B T_c}, \quad (2.35)$$

where  $v_f$  is the Fermi velocity and  $a = 0.15$ . In BCS theory, the response kernel  $Q(\mathbf{k})$  is similar to that in Pippard theory. The BCS coherence length  $\xi_0$ , is the range of the Fourier transform of  $Q(\mathbf{k})$  and is defined as

$$\xi_0 = \frac{\hbar v_f}{\pi \Delta_0}, \quad (2.36)$$

where  $\Delta_0$  is the uniform energy gap at  $T = 0$ . Since  $\Delta_0 \sim k_B T_c$ , the Pippard estimate is close to the BCS coherence length. In a conventional superconductor,  $v_f$  and hence  $\xi_0$

is large. The bound electron pairs which make up the superfluid have a spatial extent on the order of  $\xi_0$ .

The high- $T_c$  materials differ markedly from conventional superconductors in that they have much smaller coherence lengths. Consequently, these materials are in the extreme type-II limit. The small value of the coherence length also means that the high- $T_c$  compounds are generally in the clean limit, where  $\xi \ll l$ . Furthermore, both fluctuation and boundary effects are much stronger in these short  $\xi$  superconductors. In a  $d_{x^2-y^2}$ -wave superconductor where the energy gap is anisotropic, one must define an angle dependent coherence length

$$\xi_0(\hat{\mathbf{k}}) = \frac{\hbar v_f}{\pi \Delta_{\hat{\mathbf{k}}}} \quad (2.37)$$

where  $\Delta_{\hat{\mathbf{k}}} = \Delta_0(\hat{k}_x^2 - \hat{k}_y^2)$  and  $\Delta_0$  is the maximum value of the energy gap. The divergence of Eq. (2.37) along the node directions  $|\hat{k}_x| = |\hat{k}_y|$  means that the extreme nonlocal limit is obtained near the nodes (*i.e.*  $\xi_0 \rightarrow \infty$ ). Recently, Kosztin and Legget [29] determined that nonlocal electrodynamics leads to a crossover from a  $T$  to a  $T^2$  dependence for the penetration depth in the Meissner state at extremely low temperatures. To observe this experimentally, one must distinguish this effect from the  $T^2$  dependence expected from sample impurities. Both the temperature and magnetic field dependence of  $\xi$  will be discussed later in the thesis.

## 2.3 The Magnetic Field Dependence of the Penetration Depth at Low $T$

### 2.3.1 Nonlinear Effects in an $s$ -Wave Superconductor

Since the high- $T_c$  compounds are extreme type-II superconductors, they should be well described by the London theory. The underlying assumption in the linear relation between the supercurrent density  $\mathbf{J}_s$  and the vector potential  $\mathbf{A}$  that appears in the

London model is that the applied field is both weak and slowly varying over a distance  $\xi$ . This in turn implies that the wave functions of the superconducting carriers are independent of magnetic field  $H$  and that  $\mathbf{J}_s$  scales exactly with the velocity of the superfluid  $\mathbf{v}_s$  [see Eq. (2.7)].

Let us first consider an  $s$ -wave superconductor in the Meissner state for the case where  $T=0$ , so that there is no contribution to  $\mathbf{J}$  from thermally excited quasiparticles [*i.e.* the second term in Eq. (2.22) is zero]. If a static magnetic field is then applied to the BCS ground state, each electron with initial momentum  $\hbar\mathbf{k}$  will have a new momentum given by

$$\hbar\mathbf{k} \longrightarrow \hbar\mathbf{k} - \frac{\epsilon}{c}\mathbf{A}. \quad (2.38)$$

The other electron in a pair has momentum  $-\hbar\mathbf{k}$ , so that the new momentum of these electrons is simply

$$-\hbar\mathbf{k} \longrightarrow -\hbar\mathbf{k} - \frac{\epsilon}{c}\mathbf{A}. \quad (2.39)$$

The net effect is to shift the entire Fermi circle in  $\mathbf{k}$ -space as shown in Fig. 2.3.

The change in kinetic energy of an electron pair is

$$2\frac{\hbar^2 k^2}{2m} \longrightarrow \frac{1}{2m} \left( \hbar\mathbf{k} - \frac{\epsilon}{c}\mathbf{A} \right)^2 + \frac{1}{2m} \left( -\hbar\mathbf{k} - \frac{\epsilon}{c}\mathbf{A} \right)^2 = 2\frac{\hbar^2 k^2}{2m} + \frac{\epsilon^2}{mc^2}\mathbf{A}^2. \quad (2.40)$$

Using Eq. (2.7) and Eq. (2.18) and summing up the contribution from all Cooper pairs gives the total increase in kinetic energy due to the applied magnetic field as

$$\Delta KE = \frac{n_s}{2} \frac{\epsilon^2}{mc^2} \mathbf{A}^2 = \frac{1}{2} n_s m \mathbf{v}_s^2. \quad (2.41)$$

This is just the classical equation for  $n_s$  electrons per unit volume moving with a velocity  $\mathbf{v}_s = (-\epsilon/mc)\mathbf{A}$ . Thus, the supercurrents are determined solely by the applied field, and only exist in its presence. Provided the displacement of the Fermi circle does not exceed the width of the energy gap [as in Fig. 2.3(a)], the supercurrent response

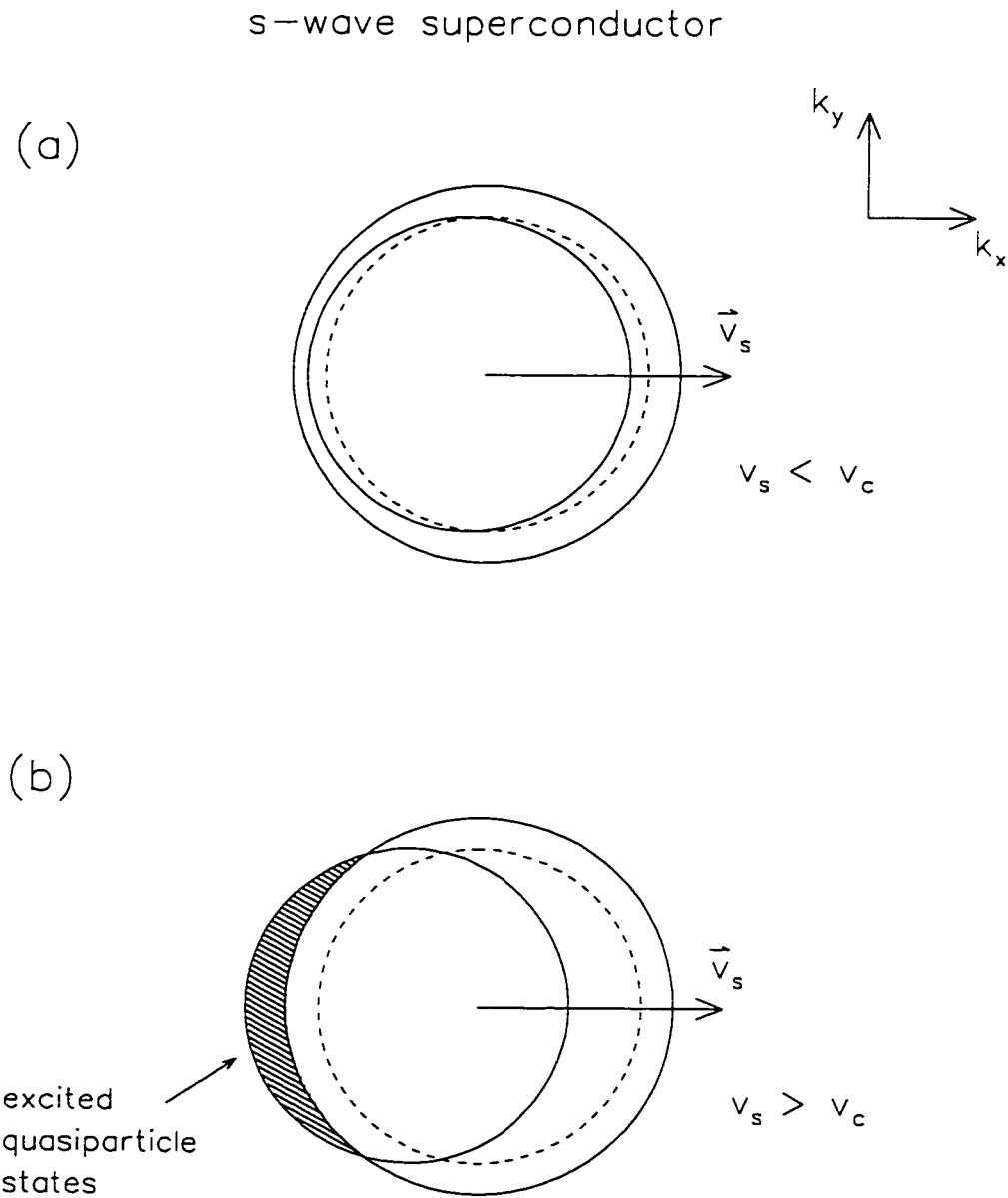


Figure 2.3: The shift in the Fermi circle for a *s*-wave superconductor due to a field-induced superflow, where (a)  $v_s < v_c$  and (b)  $v_s > v_c$ . The zero-field Fermi surface is shown as a dashed circle. Note that the distances between the solid and dashed lines represent energy differences, not distance in  $\mathbf{k}$ -space. The shaded region in (b) represents the region occupied by the excited quasiparticle states.

will remain linear. However, if the applied field is large enough, the shift will exceed this limit and quasiparticle excitations will occur. This latter case is illustrated in Fig. 2.3(b). Naturally, this will lead to a reduction in  $n_s$  and a corresponding increase in  $\lambda$ . Near the Fermi surface, a quasiparticle has kinetic energy  $(1/2)m\mathbf{v}_F^2$ . The change in kinetic energy of the quasiparticle due to the superflow velocity  $\mathbf{v}_s$  is

$$\frac{1}{2}m(\mathbf{v}_F + \mathbf{v}_s)^2 - \frac{1}{2}m\mathbf{v}_F^2 \approx m\mathbf{v}_F \cdot \mathbf{v}_s. \quad (2.42)$$

so that there is a shift in the quasiparticle excitation spectrum such that

$$E_{\mathbf{k}} = \sqrt{\varepsilon_{\mathbf{k}}^2 + \Delta_{\mathbf{k}}^2} + m\mathbf{v}_F \cdot \mathbf{v}_s. \quad (2.43)$$

The shift in quasiparticle energy relative to the energy gap  $\Delta$ , can be used to define a critical velocity for  $v_c$ , below which the supercurrent response is linear in the Meissner state of an  $s$ -wave superconductor

$$v_c = \frac{\Delta}{mv_F}. \quad (2.44)$$

Thus, if  $v_s < v_c$  then  $\mathbf{J}_s = -\epsilon n_s \mathbf{v}_s$ . For velocities greater than  $v_c$ , there is a quasiparticle contribution  $\mathbf{J}_{qp}$  such that the supercurrent density is

$$\mathbf{J}_s = -\epsilon n'_s \mathbf{v}_s + \mathbf{J}_{qp}. \quad (2.45)$$

where  $n'_s$  is the reduced value of the superfluid density (relative to its maximum value  $n_s$  in the linear regime). Thus  $\mathbf{J}_s$  drop rapidly when  $v_s > v_c$  so that the supercurrent response becomes nonlinear. If the energy shift is larger than the condensation energy (which will be derived later), the sample will become normal.

For  $T > 0$ , the size of the energy gap is reduced, so that the value of  $v_c$  decreases. The precise form of the supercurrent-velocity relation of Eq. (2.45) is [30]

$$\mathbf{J}_s = -\epsilon n'_s(T) \mathbf{v}_s \left[ 1 - \beta_1(T) \left( \frac{v_s}{v_c} \right)^2 \right]. \quad (2.46)$$

where the prefactor  $\beta_1(T)$  is a  $T$ -dependent coefficient that decreases rapidly with  $T$ , with  $\beta_1(T) \rightarrow 0$  as  $T \rightarrow 0$ . At low temperatures,  $\beta_1(T) \sim \exp(-\Delta/k_B T)$ . Using Eq. (2.46), the nonlinear London equations can be constructed to determine the field dependence of  $\lambda$ . It is found that for a conventional  $s$ -wave superconductor at low  $T$ ,  $\lambda$  changes quadratically with  $H$ <sup>1</sup>

$$\frac{\lambda(H, T)}{\lambda(0, T)} = 1 + \beta_1(T) \left[ \frac{H}{H_0(T)} \right]^2, \quad (2.47)$$

where  $H_0(T) = \epsilon \lambda(T) / c v_c(T)$  is a characteristic field on the order of the thermodynamic critical field  $H_c(T)$ , which is of course related to  $v_c$ . Above  $H_0(T)$  the nonlinear effects become important. The  $H^2$  behaviour in Eq. (2.47) has been confirmed experimentally in the type-I superconductors Sn and In [31.32.33] and the type-II superconductor  $V_3Si$  [34]. The coefficient  $\beta_1(T)$  in Eq. (2.47) is typically small in conventional superconductors.

### 2.3.2 Nonlinear Effects in a $d_{x^2-y^2}$ -Wave Superconductor

For a  $d_{x^2-y^2}$ -wave superconductor, the presence of nodes on the Fermi surface means that the supercurrent response to a weak applied magnetic field will be nonlinear even at  $T=0$ . This is clearly seen in Fig. 2.4, where, due to the nodes, quasiparticle excitations will result from even a small displacement of the Fermi cylinder. For a given shift, the precise number of quasiparticle excitations will depend on the slope of the energy gap function  $\Delta_{\mathbf{k}}$  at the nodes and the direction of  $\mathbf{v}_s$ . The excited quasiparticles located in a narrow wedge at the nodes produce a current density which flows in a direction opposite to that of the superfluid.

---

<sup>1</sup>In this equation,  $\lambda$  is defined from the initial decay rate of the field, where the supercurrents are largest [35]. However, measurements of  $\lambda$  involve a distribution of supercurrent densities over one or more spatial dimensions. Thus Eq. (2.1) is a more appropriate definition for  $\lambda$ .

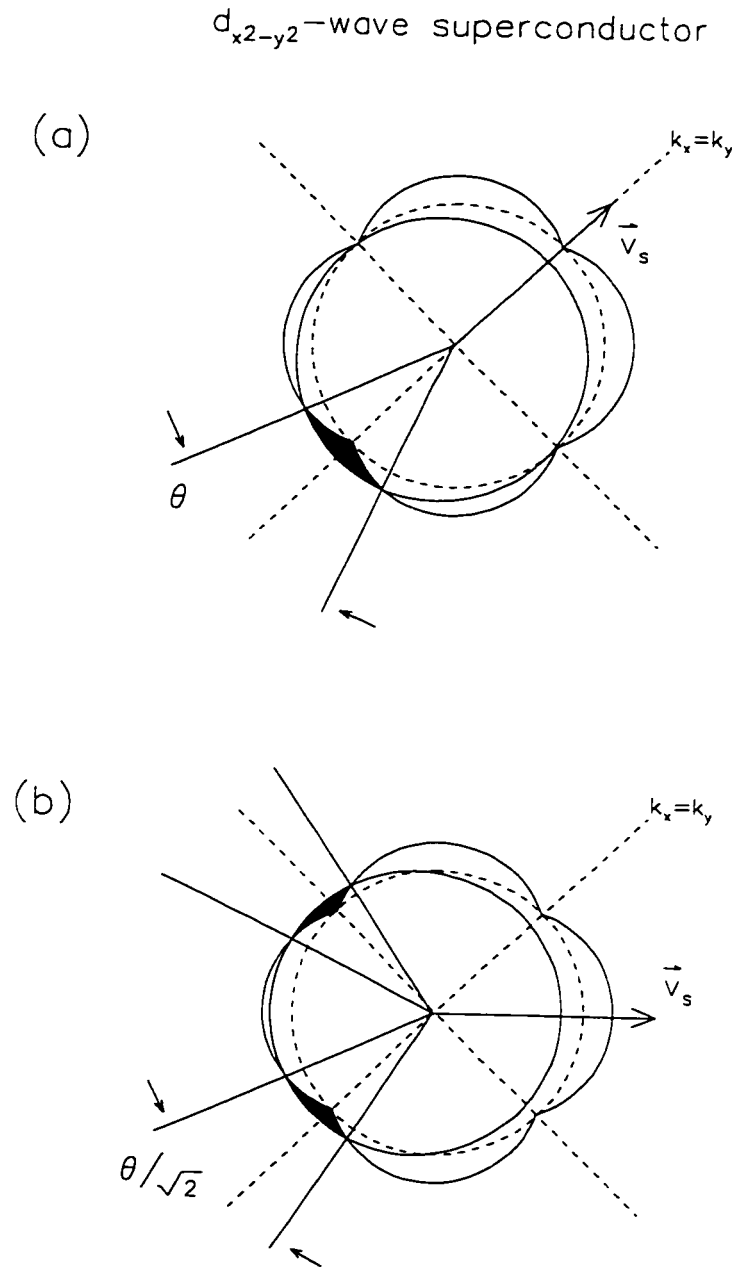


Figure 2.4: The shift in the Fermi circle for a  $d_{x^2-y^2}$ -wave superconductor due to a field-induced superflow, where (a)  $v_s$  is parallel to a node and where (b)  $v_s$  is parallel to an antinode. The unshifted Fermi surface is shown as a dashed circle. Note that the distances between the solid and dashed lines represent energy differences, not distance in  $k$ -space. The shaded area represents the region occupied by the excited quasiparticle states. The angle  $\theta$  defines the wedge of occupied states.

For the case in which  $\mathbf{v}_s$  is directed along a node, as shown in Fig. 2.4(a), the supercurrent-velocity relation is

$$\mathbf{J}_s = -\epsilon n'_s v_s \left( 1 - \frac{|\mathbf{v}_s|}{v_0} \right). \quad (2.48)$$

where  $v_0 = (d|\Delta(\theta)|/d\theta)/v_F^*$ , such that  $(d|\Delta(\theta)|/d\theta)$ , is the angular slope of the energy gap at the node, and  $v_F^*$  is the Fermi velocity at the node. For the case in which  $\mathbf{v}_s$  is directed along an antinode, as shown in Fig. 2.4(b), the supercurrent density is

$$\mathbf{J}_s = -\epsilon n'_s v_s \left( 1 - \frac{1}{\sqrt{2}} \frac{|\mathbf{v}_s|}{v_0} \right). \quad (2.49)$$

The additional factor of  $1/\sqrt{2}$  is easy to understand by comparing the angular size of the wedges at the nodes in Fig. 2.4(b) to the angular size of the wedge in Fig. 2.4(a). Due to the anisotropy of the nonlinear response, Yip and Sauls [30] proposed that the field dependence of the penetration depth in the Meissner state could be used to resolve the structure of the energy gap in a superconductor. The magnetic penetration depth can be derived using the expressions for  $\mathbf{J}_s$ . The result is that  $\lambda$  changes linearly with  $H$  at low  $T$  [30,35,36]

$$\frac{\lambda(H, T)}{\lambda(0, T)} = 1 + \beta_2(T) \left[ \frac{H}{H_0(T)} \right], \quad (2.50)$$

where  $H_0 = 3cv_0/2\epsilon\lambda$  and  $\beta_2(T)$  is a temperature dependent coefficient which remains finite at  $T = 0$  due to the nodes in the gap. The actual value of  $\beta_2(T)$  will of course depend on the direction of  $\mathbf{v}_s$ . The definition of  $\lambda$  in Eq. (2.50) is the same as that in Eq. (2.47) (*i.e.* it is related to the initial decay rate of the field).

As the temperature is increased, there is eventually a crossover to a situation in which thermal excitation of quasiparticles also occurs away from the nodes. Below this crossover temperature  $T^*(H)$ ,  $\lambda(H, T)$  is linear in  $H$  but quadratic in  $T$ , whereas above  $T^*(H)$ ,  $\lambda(H, T)$  is quadratic in  $H$  and linear in  $T$  [36]. The first evidence for a linear  $H$ -dependence accompanied with a  $T^2$ -dependence in a high- $T_c$  material, was obtained



by Maeda *et al.* [37] for measurements of the in-plane magnetic penetration depth  $\lambda_{ab}$  in  $\text{Bi}_2\text{Sr}_2\text{CaCu}_2\text{O}_y$ . Similar results have since been reported in  $\text{YBa}_2\text{Cu}_3\text{O}_{7-x}$  and  $\text{Tl}_2\text{Ba}_2\text{CaCu}_2\text{O}_y$  [38]. However, the results of these experiments are suspect because of the large demagnetization effect (associated with the shape of the sample) which arises from applying a magnetic field perpendicular to the flat  $\hat{a}\text{-}\hat{b}$  plane. Early measurements of  $\lambda(H, T)$  in a single crystal of  $\text{YBa}_2\text{Cu}_3\text{O}_{6.95}$  found a large  $H^2$  term [39], but the sample had a reduced  $T_c$  indicating there may have been extrinsic effects due to impurities.

### 2.3.3 Nonlinear and Nonlocal Effects in the Vortex State

Predicting the behaviour of  $\lambda$  in the vortex state is far more complicated. This is because, compared to the Meissner state, the problem must be solved in two dimensions, rather than one. A second complication is that the magnitude of the order parameter is spatially inhomogeneous due to the presence of vortices. Very recently, some progress has been made in understanding the nature of the field dependence of  $\lambda$  in the vortex state of a  $d_{x^2-y^2}$ -wave superconductor [40]. The nonlinear effects which were discussed in the previous section also affect the supercurrent response in the vortex state. The mechanism for these nonlinear effects is identical to that in the Meissner phase. In a  $d_{x^2-y^2}$ -wave superconductor, the supercurrent response is also nonlocal due to the nodes on the Fermi surface. Near the nodes  $\xi \gg \lambda$ , which was discussed earlier in connection with Eq. (2.37). There it was noted that these nonlocal effects will affect the temperature dependence of  $\lambda$  at very low  $T$ .

Nonlocal effects will not affect the measured field dependence of  $\lambda$  in the Meissner state. This can be realized, for instance, by incorporating a  $\mathbf{k}$ -dependence into the London kernel  $Q_L(\mathbf{k})$ . The terms in  $Q_L(k)$  which contain  $k$  will affect the precise way the field decays into the superconductor. However, since  $k$  itself does not depend on the magnetic field, this will not create a field-dependence for  $\lambda$ .

The situation is quite different in the vortex state. Since the theory is nontrivial and the predicted behaviour of  $\lambda(H)$  in Ref. [40] is given as a numerical result, the discussion here will be qualitative only. The authors of Ref. [40] introduce an appropriate  $\mathbf{k}$ -dependent kernel into the London model to account for the nonlocal effects arising at the nodes. The higher-order  $k$  terms are more important for large values of  $k$ . Since large  $k$  values correspond to small values of  $r$  in real space, the nonlocal effects are most important near the vortex cores. At fields just above  $H_{c1}$  where the vortex cores are isolated from each other, the measured penetration depth is virtually unaffected. However, with increasing applied field, the vortex cores move closer together and the nonlocal regions overlap. This in turn leads to significant changes in the distribution of magnetic field between the vortices and a field dependence for the corresponding effective penetration depth. In particular, the effective  $\lambda$  is found to increase with increasing magnetic field. At fields in which the vortices begin to interact, this field dependence is very strong. The strength of the field dependence weakens somewhat at higher magnetic fields. In the same study, the nonlinear corrections are found to have a small effect on the field dependence of  $\lambda$ . However, it should be noted that the calculations in Ref. [40] were performed assuming that the size of the vortex cores are small, which is not always the case.

## 2.4 The GL Penetration Depth and Coherence Length

The temperature and magnetic field dependence of both the penetration depth and coherence length appear quite naturally in Ginzburg-Landau (GL) theory [41]. Like the London model, the GL model is independent of the underlying mechanism for superconductivity. However, it must be emphasized that GL theory is strictly valid only near the normal-to-superconducting phase boundary, and is thus not generally applicable at

low temperatures. In the theory, a complex order parameter  $\psi$  is introduced, where  $\psi$  is a function of temperature, magnetic field and the spatial coordinates. Ginzburg and Landau assumed that near  $T_c$  where  $\psi$  is small, the free-energy difference per unit volume between the normal and superconducting state at zero magnetic field may be expanded as a function of  $\psi$

$$F_s(0) = F_n(0) + a|\psi|^2 + b|\psi|^4, \quad (2.51)$$

where  $a$  and  $b$  are temperature-dependent coefficients such that near  $T_c$

$$a(T) \approx -a_0 \left(1 - \frac{T}{T_c}\right) \quad \text{and} \quad (2.52)$$

$$b(T) \approx b_0. \quad (2.53)$$

where  $a_0$  and  $b_0$  are positive coefficients, so that  $a < 0$  below  $T_c$ . Minimizing the free energy with respect to  $|\psi|^2$  gives the zero-field value of the order parameter

$$|\psi_0|^2 = -\frac{a}{b} = \frac{|a|}{b}. \quad (2.54)$$

In the presence of a magnetic field, the free energy in the superconducting state is increased. In particular, the work done on the sample by the magnetic field  $\mathbf{H}$  is

$$- \int_0^V dV \int_0^H \mathbf{M} \cdot d\mathbf{H} \quad (2.55)$$

where  $V$  is the volume of the sample and  $\mathbf{M}$  is the sample magnetization. In the Meissner phase,  $\mathbf{B} = 0$  so that  $\mathbf{M} = -\mathbf{H}/4\pi$ , whereas in the normal state  $\mathbf{M}$  is essentially zero. This means that the Gibbs free energy per unit volume in the superconducting state increases in the presence of a magnetic field to

$$G_s(\mathbf{H}) = G_s(0) + \frac{H^2}{8\pi}, \quad (2.56)$$

whereas in the normal state

$$G_n(\mathbf{H}) = G_n(0). \quad (2.57)$$

At the phase change,  $G_s(H_c) = G_n(H_c)$  where  $H_c$  is the critical field. Thus, using Eq. (2.56) and Eq. (2.57), one has

$$G_n(0) - G_s(0) = \frac{H_c^2}{8\pi}. \quad (2.58)$$

Using the Legendre transformation  $F(\mathbf{H}) = G(\mathbf{H}) + \frac{1}{4\pi} \mathbf{B} \cdot \mathbf{H}$ , Eq. (2.58) may be written in terms of the Helmholtz free energy per unit volume

$$F_n(0) - F_s(0) = \frac{H_c^2}{8\pi}. \quad (2.59)$$

This implies that an energy  $H_c^2/8\pi$ , called the "condensation energy", is given up by the formation of the superconducting state.

Assuming that the order parameter  $\psi$  is not completely rigid in the presence of a magnetic field, there is an additional energy term associated with variations in  $\psi$ . This term was assumed by Ginzburg and Landau to take the form

$$\frac{1}{2m^*} \left| \left( -i\hbar\nabla + \frac{e^*}{c} \mathbf{A} \right) \psi \right|^2, \quad (2.60)$$

where later it was found that  $m^* = 2m$  and  $e^* = -2e$ . Thus, the total free energy per unit volume of the superconducting state in the presence of a magnetic field is

$$\begin{aligned} F_s(H) &= F_s(0) + \frac{1}{2m^*} \left| \left( -i\hbar\nabla + \frac{e^*}{c} \mathbf{A} \right) \psi \right|^2 + \frac{H^2}{8\pi} \\ &= F_n(0) + a|\psi|^2 + b|\psi|^4 + \frac{1}{2m^*} \left| \left( -i\hbar\nabla + \frac{e^*}{c} \mathbf{A} \right) \psi \right|^2 + \frac{H^2}{8\pi}. \end{aligned} \quad (2.61)$$

Minimizing this expression with respect to  $\psi$  leads to the "first GL equation"

$$\frac{1}{2m^*} \left( -i\hbar\nabla - \frac{e^*}{c} \mathbf{A} \right)^2 \psi + a\psi + b|\psi|^2\psi = 0, \quad (2.62)$$

and with respect to  $\mathbf{A}$ , the "second GL equation"

$$\mathbf{J}_s = -\frac{i\hbar e^*}{2m^*} (\psi^* \nabla \psi - \psi \nabla \psi^*) - \frac{e^{*2}}{m^* c} \psi^* \psi \mathbf{A}, \quad (2.63)$$

which is the standard expression for the quantum-mechanical current. This equation has the same form as the London equation, except that  $\psi$  is spatially varying. The GL equations can be solved analytically for simple cases only.

Consider a superconductor in a weak magnetic field with the sample dimensions much greater than the magnetic penetration depth. To first order in  $\mathbf{B}$ ,  $|\psi|^2$  in Eq. (2.63) can be replaced by its equilibrium zero-field value  $|\psi_0|^2$  from Eq. (2.54)

$$\mathbf{J}_s = -\frac{\epsilon^* c^2}{m^* c} |\psi_0|^2 \mathbf{A}. \quad (2.64)$$

Taking the *curl* of both sides of this equation gives

$$\nabla \times \mathbf{J}_s = -\frac{\epsilon^* c^2}{m^* c} |\psi_0|^2 \nabla \times \mathbf{A} = -\frac{\epsilon^* c^2}{m^* c} \frac{|a|}{b} \mathbf{B}. \quad (2.65)$$

Using Eq. (2.12), this can be rewritten as

$$\frac{m^* c^2}{4\pi \epsilon^*} \frac{b}{|a|} (\nabla \times \nabla \times \mathbf{B}) + \mathbf{B} = 0, \quad (2.66)$$

which, upon comparing to the expression in Eq. (2.13), gives

$$\lambda(T) = \left( \frac{m^* c^2 b(T)}{4\pi \epsilon^* |a(T)|} \right)^{1/2}. \quad (2.67)$$

which is the same as the London penetration depth if  $|\psi_0|^2 = |a|/b = n_s^* = n_s/2$ .

Consider a second example where  $\psi$  varies only in the  $\hat{z}$ -direction, but the applied magnetic field is zero. In this case the first GL equation becomes

$$-\frac{\hbar^2}{2m^*} \frac{d^2 \psi}{dz^2} + a\psi + b|\psi|^2 \psi = 0. \quad (2.68)$$

Assuming  $\psi$  is real, we can introduce a dimensionless order parameter

$$f(z) = \frac{\psi(z)}{|\psi_0|}. \quad (2.69)$$

where  $|\psi_0|$  is given by Eq. (2.54). Thus, Eq. (2.68) becomes

$$-\frac{\hbar^2}{2m^* |a|} \frac{d^2 f}{dz^2} - f + f^3 = 0. \quad (2.70)$$

A natural length scale for spatial variations of the order parameter is thus

$$\xi(T) = \left( \frac{\hbar^2}{2m^*|a(T)|} \right)^{1/2}. \quad (2.71)$$

which is known as the GL coherence length. Note that both the GL coherence length and the GL penetration depth are temperature dependent quantities. From Eq. (2.53) it is clear that both  $\lambda(T)$  and  $\xi(T)$  vary as  $(1 - T/T_c)^{-1/2}$  with temperature, so that their ratio is independent of temperature

$$\kappa(T) = \frac{\lambda(T)}{\xi(T)}. \quad (2.72)$$

$\kappa$  is known as the “GL parameter”. A precise calculation from the microscopic theory gives a weak temperature dependence for  $\kappa$ , with  $\kappa$  increasing as  $T$  decreases [42]. In GL theory, a superconductor is called “type-I” if  $\kappa < 1/\sqrt{2}$  and “type-II” if  $\kappa > 1/\sqrt{2}$ . When the order parameter throughout the sample is essentially a constant, the GL model reduces to the London model. This occurs when  $\kappa \gg 1$ , which is the case for the high- $T_c$  superconductors.

GL theory is particularly useful in modelling the small variation of  $\lambda$  with magnetic field found near  $T_c$ . Pippard [31] first used a simple thermodynamic argument, which distributes the entropy difference due to changes in  $H$  over a layer of thickness  $\xi$ , to explain the field dependence of  $\lambda$  he observed in the type-I superconductor Sn. Historically, this marks the introduction of  $\xi$  as a fundamental length scale in superconductivity theory. Although the field dependence is built into the GL theory, for arbitrary  $H$ ,  $\psi$  has a non-negligible dependence on field. Thus, in general, the field dependence of both  $\lambda$  and  $\xi$  must be obtained by numerically solving the complete nonlinear GL equations. Analytical results can be obtained in special cases, such as for thin films.

## 2.5 Measuring the Characteristic Length Scales

In the Meissner state,  $\lambda$  can be measured by excluded volume techniques (such as microwave cavity perturbation), inductive methods and far infrared reflectivity. The latter is a surface measurement which can determine the absolute value of  $\lambda$ . In the vortex state,  $\mu$ SR, nuclear magnetic resonance (NMR) or small angle neutron scattering can be used to measure the magnetic field inhomogeneity due to the vortex lattice in the bulk of the sample, from which an absolute value of  $\lambda$  can be obtained.

In contrast, there are few direct measurements of  $\xi$ . Estimates of its magnitude can be obtained from the contribution of fluctuations to measured quantities such as the specific heat, susceptibility or conductivity. Scanning tunneling microscopy (STM) can be used to measure the vortex-core radius  $r_0$  at the sample surface, which provides an estimate of  $\xi$ <sup>2</sup>. However, the coherence length is most often determined indirectly from measurements of the upper critical field,  $H_{c2}$ . At this field the vortices begin to overlap and the superconductor undergoes a first order phase transition into the normal state. Since the radius of a normal vortex core is about the size of the coherence length, then at  $H_{c2}$  there is a direct relationship with  $\xi$ . In particular, from GL theory

$$\xi(T) = \sqrt{\frac{\Phi_0}{2\pi H_{c2}(T)}}. \quad (2.73)$$

In the high- $T_c$  materials,  $H_{c2}$  is extremely large (*e.g.* on the order of  $10^2$  T in  $\text{YBa}_2\text{Cu}_3\text{O}_7$  at  $T=0$ ) and is therefore difficult to measure accurately. Measurements are generally limited to temperatures near  $T_c$  where  $H_{c2}$  is considerably smaller ( $H_{c2} \rightarrow 0$  as  $T \rightarrow T_c$ ). However, near  $T_c$  thermal fluctuations of the vortex lines can depin or melt the solid 3D vortex-lattice into a vortex liquid phase. Rather than  $H_{c2}$ , what is often measured is the transition of the ordered 3D vortex solid into a vortex fluid phase, in which many

---

<sup>2</sup>The relationship between  $r_0$  and  $\xi$  will be discussed more fully, later in this thesis.

of the vortices are free to move independently of each other. The phenomenon is analogous to the way in which thermal vibrations of water molecules cause ice to melt into water. The problem of thermal fluctuations is most serious in short coherence length superconductors with high transition temperatures. This is because fluctuation effects become important when the thermal energy  $k_B T$  exceeds the condensation energy  $\xi_a \xi_b \xi_c H_c^2 / 8\pi \propto (T - T_c)^{1/2}$  [43]. Here,  $\xi_a(T) \xi_b(T) \xi_c(T)$  is the minimum volume occupied by the fluctuation and  $H_c$  is the thermodynamic critical field. In the high- $T_c$  materials, thermal fluctuations are mainly responsible for the large variation in reported values of  $\xi$  determined from  $H_{c2}$  measurements. A more appropriate way to determine  $\xi$  is to perform measurements deep in the superconducting state, well away from the strong fluctuation regime. This can be achieved with  $\mu$ SR, a bulk technique which is described next.



## Chapter 3

### The $\mu$ SR Technique

This chapter describes how one can measure the field distribution associated with the vortex lattice in the bulk of a superconductor using muon spin rotation ( $\mu$ SR) spectroscopy. A comparison is made with the nuclear magnetic resonance (NMR) technique which can also be used to measure the field distribution.

#### 3.1 $\mu$ SR vs. NMR

In a transverse field  $\mu$ SR experiment, one measures the internal magnetic field distribution of a superconductor in the vortex state. Prior to the development of this technique, the internal field distribution could be studied with NMR, which in principle provides the same information as  $\mu$ SR.

The basic principles of the NMR technique are as follows: The interaction of the magnetic moment of a nucleus  $\mu_N = -\gamma_N \hbar \mathbf{I}$  (where  $\mathbf{I}$  is a nonzero nuclear spin and  $\gamma_N$  is the gyromagnetic ratio characteristic of the nucleus) with the local magnetic field  $\mathbf{B}$  at its site is described by the Hamiltonian

$$H = -\gamma_N \hbar \mathbf{I} \cdot \mathbf{B}, \quad (3.1)$$

which splits the nuclear energy levels into  $2I + 1$  lines with energies

$$E_m = -\gamma_N \hbar B m, \quad (3.2)$$

where  $m$  is an integer or a half-integer in the range  $-I < m < I$ , depending on whether  $I$  is an integer or a half-integer. The energy separation between adjacent nuclear energy levels is then

$$\Delta E_{m,m+1} = E_m - E_{m+1} = \gamma_N \hbar B \equiv \Delta E. \quad (3.3)$$

Nuclear magnetic dipole transitions may be excited among these levels by applying a RF field of an appropriate frequency. In particular, when the frequency  $\omega$  of the RF field is such that the energy  $\hbar\omega$  is equal to the energy separation  $\Delta E$  between the quantum states of the nuclear spin, there is an absorption of energy. The resulting resonance can be detected and the local field identified as  $B = \omega/\gamma_N$ . Since the distances between similar nuclei in a superconductor are small relative to the separation of the vortices, the magnetic field distribution associated with the vortex lattice is sampled by measuring the fields at the sites of the nuclei. As long as the nuclei are uniformly distributed, the sampling is volume-weighted.

An NMR technique which is a close parallel to  $\mu$ SR is “pulsed NMR”, in which one observes time-dependent transverse nuclear polarization or so-called “free induction decay” of the nuclear polarization. In this form of NMR, an RF pulse is applied to rotate the nuclear spins  $90^\circ$  from the direction of the local magnetic field  $\mathbf{B}$ . When the RF field is switched off, the nuclear spins perform a free precession around the local field  $\mathbf{B}$  and relax back to their initial direction along  $\mathbf{B}$ . The precession is detected by a pickup coil. The frequency of the nuclear spin precession is a measure of the local field (*i.e.*  $B = \omega/\gamma_N$ ). In this pulsed NMR technique, the different precession frequencies are observed simultaneously without variation of the RF or DC magnetic fields [44]. However, there are several limitations and added difficulties associated with the NMR technique which are overcome in a  $\mu$ SR experiment.

The first problem is that because the skin depth of the RF field probe is small,

NMR only probes the surface of the sample. For most high- $T_c$  samples, the surface has many imperfections, which results in strong vortex-line pinning and a highly disordered vortex lattice—a topic which will be discussed in the next section. To measure the field distribution in the bulk, magnetically aligned powders are often used (see for example Ref. [51]). However, the vortex-lattice structure in the bulk of a small crystallite is also likely to be affected by the strong pinning of the vortices at the crystallite surface. Furthermore, it is difficult to align all of the crystallites with the applied field. Due to mass anisotropy, the field distribution will not be the same in crystallites with different orientations. To account for the misaligned fraction, one must measure the NMR spectrum before and after alignment, and then subtract out the random powder contribution by using a predetermined percentage of alignment. The penetration depth of the RF field also limits the range over which the vortex lattice can be sampled.

On the other hand,  $\mu$ SR is a bulk probe that is easily performed on single crystals, so that one can measure the “true” magnetic field distribution in the bulk. The importance of having this capability will become clear when the structure of the vortex-lattice is discussed in some detail later in this thesis.

Other problems with NMR are the additional sources of line broadening in the measured internal field distribution (*i.e.* line broadening sources which are negligible in  $\mu$ SR). For instance, in the high- $T_c$  materials the linewidths originating from the copper and oxygen nuclei are very broad due to quadrupole interactions and chemical shifts (or metallic Knight shifts). A field distribution which corresponds more closely to that of the vortex lattice is obtained with the  $\mu$ SR technique. Since the muon is a spin 1/2 particle, it has no quadrupole interaction. Also,  $\mu$ SR is sensitive over relaxation times as small as 10 ns compared to 10  $\mu$ s for NMR. The signal relaxation in  $\mu$ SR due to the inhomogeneous field distribution of the vortex lattice typically occurs over the first few  $\mu$ s.

### 3.2 Measuring the Internal Field Distribution with $\mu$ SR

In a  $\mu$ SR experiment, positively charged muons are implanted one at a time into the bulk of the superconductor. The muon is a lepton which has spin 1/2, a rest mass that is 206.729 times that of an electron, and a magnetic moment of  $4.84 \times 10^{-3} \mu_B$ . In the cuprates the muon comes to rest at a definite position in the crystallographic unit cell—becoming hydrogen bonded to an oxygen atom [45]. Fortunately, in magnetic fields appropriate for a  $\mu$ SR experiment, the intervortex spacing is much larger than the dimensions of the crystallographic unit cell (typically  $10^2 - 10^3$  times larger) so that a muon stops randomly on the length scale of the vortex lattice. The implanted muon precesses about the local magnetic field  $B$  with a Larmor frequency

$$\omega_\mu = 2\pi\nu_\mu = \gamma_\mu B. \quad (3.4)$$

where  $\gamma_\mu/2\pi = 135.5342$  MHz/T is the muon gyromagnetic ratio. After a mean lifetime  $\tau_\mu = 2.2 \mu\text{s}$ , the positive muon decays into a positron and two neutrinos (*i.e.*  $\mu^+ \rightarrow e^+ + \nu_e + \bar{\nu}_\mu$ ). The distribution of decay positrons is asymmetric with respect to the spin polarization vector  $\mathbf{P}(t)$  of the muon, where the highest probability of emission is along the direction of the muon spin. Consequently, the time evolution of the muon spin polarization  $\mathbf{P}(t)$  can be monitored, since the muon partially reveals its spin direction at the time of decay.

Scintillation detectors placed around the sample can be used to detect the positrons emerging from the muon decay. Figure 3.1 shows a simple four-counter arrangement. The number of decay positrons recorded per time bin  $\Delta t$  in the  $i$ th counter is given by

$$N_i(t) = N_i^\circ e^{-t/\tau_\mu} [1 + A_i^\circ P_i(t)] + B_i^\circ, \quad (3.5)$$

where  $N_i^\circ$  is a normalization constant,  $A_i^\circ$  is the maximum precession amplitude,  $B_i^\circ$  is a time-independent random background and  $P_i(t)$  is the time evolution of the muon

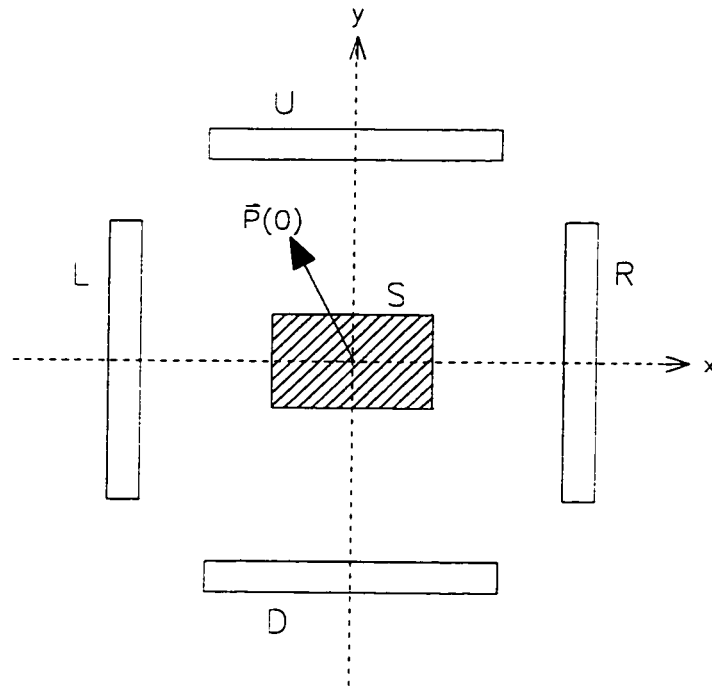


Figure 3.1: Typical arrangement of four positron detectors  $L$ ,  $R$ ,  $U$  and  $D$  around a sample  $S$ . The initial muon-spin polarization is denoted as  $\bar{\mathbf{P}}(0)$  and the applied field is assumed to be out of the page.

spin polarization component in the  $i$ th direction, which is given by

$$P_i(t) = \cos(\omega_\mu t + \theta_i). \quad (3.6)$$

where  $\theta_i$  is the initial phase of the muon spin polarization vector relative to the  $i$ th direction. Generally  $\theta_i$  is nonzero, since the muons will precess during their flight through the magnetic field to the sample. There is no significant loss of polarization during the short time over which the muons thermalize. This is because the primary interactions by which the muons rapidly lose their initial kinetic energy are electrostatic in nature and hence do not affect the muon spin [46].

### 3.2.1 The Raw Asymmetry for a Pair of Counters

Consider a pair of opposing counters—*e.g.*  $L$  and  $R$  in Fig. 3.1 with a magnetic field applied parallel to the  $\hat{z}$  axis. The “raw asymmetry” of the histograms  $N_L(t)$  and  $N_R(t)$  is defined as

$$A_{\text{raw}}(t) \equiv A_{LR}(t) = \frac{[N_L(t) - B_L^0] - [N_R(t) - B_R^0]}{[N_L(t) - B_L^0] + [N_R(t) - B_R^0]} \quad (3.7)$$

where

$$N_L(t) = N_L^0 e^{-t/\tau_\mu} [1 + A_L^0 P_L(t)] + B_L^0 \quad \text{and} \quad (3.8)$$

$$N_R(t) = N_R^0 e^{-t/\tau_\mu} [1 + A_R^0 P_R(t)] + B_R^0 \quad (3.9)$$

so that

$$A_{\text{raw}}(t) = \frac{N_L^0 [1 + A_L^0 P_L(t)] - N_R^0 [1 + A_R^0 P_R(t)]}{N_L^0 [1 + A_L^0 P_L(t)] + N_R^0 [1 + A_R^0 P_R(t)]} \quad (3.10)$$

The reason for introducing  $A_{\text{raw}}(t)$  is to eliminate the muon lifetime (which is a well known quantity) and the random backgrounds  $B_L^0$  and  $B_R^0$ . Ideally, the two counters in question are identical to one another, so that the histograms recorded by the two counters differ only by a phase. In this idealistic situation the difference in phase between the histograms is due solely to the geometry of the positron counters with respect to the sample. The polarization of the muon spin which is seen by each counter is

$$P_L(t) = \cos(\omega_\mu t + \psi) \quad (3.11)$$

$$P_R(t) = \cos(\omega_\mu t + \phi) \quad (3.12)$$

where  $\psi$  and  $\phi$  are the initial phases of the muon spin polarization vector in counters  $L$  and  $R$ , respectively. If the counters are aligned precisely opposite one another, the

difference between these phases is  $|\psi - \phi| = 180^\circ$ , so that

$$P_L(t) = \cos[\omega_\mu + (\phi + \pi)] = -\cos(\omega_\mu + \phi) = -P_R(t). \quad (3.13)$$

The counters  $L$  and  $R$  measure the projection of the muon polarization on the  $\hat{x}$  axis so that

$$P_L(t) \equiv P_x(t) \quad \text{and} \quad P_R(t) = -P_L(t) \equiv -P_x(t). \quad (3.14)$$

Thus Eq. (3.7) becomes

$$A_{\text{raw}}(t) = \frac{(\mathcal{N}_L^\circ - \mathcal{N}_R^\circ) + (\mathcal{N}_L^\circ A_L^\circ + \mathcal{N}_R^\circ A_R^\circ) P_x(t)}{(\mathcal{N}_L^\circ + \mathcal{N}_R^\circ) + (\mathcal{N}_L^\circ A_L^\circ - \mathcal{N}_R^\circ A_R^\circ) P_x(t)}. \quad (3.15)$$

If  $\mathcal{N}_i^\circ = \mathcal{N}_j^\circ$  and  $A_i^\circ = A_j^\circ \equiv A^\circ$  then Eq. (3.15) reduces to

$$A_{\text{raw}}(t) = A^\circ P_x(t) \quad (3.16)$$

If  $B_i^\circ = B_j^\circ$ , then using Eqs. (3.7), (3.8), (3.9) and (3.16) the  $x$ -component of the polarization can be written as

$$P_x(t) = \frac{N_i(t) - N_j(t)}{N_i^\circ + N_j^\circ} e^{t/\tau_\mu}. \quad (3.17)$$

### 3.2.2 The Corrected Asymmetry

In practice, there are differences in the efficiency of the counters and also geometrical misalignment of the counters. If the sensitivity of the individual positron counters is not the same, the normalization constant  $\mathcal{N}^\circ$ , the maximum decay asymmetry  $A^\circ$  and the random background levels  $B^\circ$  will not be the same in all of the counters. The number of recorded events in each counter also depends on the solid angle they subtend at the sample. If the coverage of the solid angle is not maximized because of counter misalignments, there will be a decrease in the number of decay positrons detected. The raw asymmetry thus depends on the variables

$$\alpha = \frac{\mathcal{N}_R^\circ}{\mathcal{N}_L^\circ} \quad \text{and} \quad \beta = \frac{|A_R^\circ|}{|A_L^\circ|}. \quad (3.18)$$

In a superconductor, these variables are best determined by fitting the muon spin precession signal in the normal state where the magnetic field in the sample is more or less homogeneous. The “corrected asymmetry”  $A_{\text{corrected}}(t)$  is obtained by substituting Eq. (3.18) into Eq. (3.10) so that

$$A_{\text{corrected}}(t) = \frac{(1 - \alpha) + A^{\circ} P_x(t)(1 + \alpha\beta)}{(1 + \alpha) + A^{\circ} P_x(t)(1 - \alpha\beta)} = \frac{(1 - \alpha) + A_{\text{raw}}(t)(1 + \alpha\beta)}{(1 + \alpha) + A_{\text{raw}}(t)(\alpha\beta - 1)}. \quad (3.19)$$

where  $A_L^{\circ} \equiv A^{\circ}$  and  $P_L(t) = -P_R \equiv P_x(t)$ .

### 3.2.3 The Relaxation Function

In the vortex state the muons experience a spatially varying magnetic field due to the periodic arrangement of the vortices. In this case the  $x$ -component of the time evolution of the total muon polarization is

$$P_x(t) = \frac{1}{N} \sum_{i=1}^N \cos[\gamma_{\mu} B(\mathbf{r}_i)t + \theta]. \quad (3.20)$$

where the sum extends over all muon sites and  $B(\mathbf{r}_i)$  is the local field at the site  $i$ . Ideally, the sum is replaced by an integral so that

$$P_x(t) = \int_0^{\infty} n(B) \cos(\gamma_{\mu} Bt + \theta) dB. \quad (3.21)$$

where  $n(B)$  is the probability that the muon will precess at the frequency  $\omega_{\mu} = 2\pi\nu_{\mu} = \gamma_{\mu} B$ . The muon spin polarization  $P_x(t)$  decays with increasing time because of the inhomogeneous field distribution. Models of the field profile  $B(\mathbf{r})$  for a perfectly ordered vortex lattice will be discussed in the next chapter.

In a real superconductor there are other independent contributions to the variation in the local field. These additional sources of field inhomogeneity can be accounted for by multiplying the muon polarization function by a “relaxation function”  $G(t)$  so that

$$P_x(t) = G(t) \int_0^{\infty} n(B) \cos(\gamma_{\mu} Bt + \theta) dB. \quad (3.22)$$



The relaxation function  $G(t)$  describes the damping of the muon precession signal which results from the additional sources of field inhomogeneity. One such source is the nuclear dipolar fields in the sample. A Gaussian relaxation function approximately describes the corresponding damping of the muon precession signal [47]

$$G(t) = e^{-\sigma_{\text{dip}}^2 t^2 / 2}. \quad (3.23)$$

where  $\sigma_{\text{dip}}$  is the muon spin "depolarization rate" due to the nuclear dipolar fields.

Signal damping also results from disorder in the vortex lattice. According to Brandt [122] random disorder can be approximated with a Gaussian relaxation function. The relaxation function which contains the effects of the nuclear dipolar moments and the disorder in the vortex lattice is

$$G(t) = e^{-(\sigma_{\text{dip}}^2 + \sigma_{\text{dis}}^2) t^2 / 2} = e^{-\sigma_f^2 t^2 / 2}. \quad (3.24)$$

where  $\sigma_{\text{dis}}$  is the muon spin depolarization rate due to the lattice disorder and  $\sigma_f$  is the effective depolarization rate such that  $\sigma_f^2 = \sigma_{\text{dip}}^2 + \sigma_{\text{dis}}^2$ .

### 3.2.4 Four-Counter Geometry and the Complex Polarization

Now consider the complete set of four positron counters in Fig. 3.1. Ignoring geometric misalignments and differences in counter efficiency, the  $x$ -component of the muon polarization  $P_x(t)$  [monitored by the  $L$  and  $R$  counters] differs from the  $y$ -component of the muon polarization  $P_y(t)$  [monitored by the  $U$  and  $D$  counters] by a phase of  $90^\circ$ . The two components of the muon polarization can be combined to form a "complex" polarization function

$$\tilde{P}(t) = P_x(t) + i P_y(t). \quad (3.25)$$

where

$$P_x(t) = G(t) \int_0^\infty n(B) \cos(\gamma_\mu B t + \theta) dB. \quad (3.26)$$

and

$$\begin{aligned} P_y(t) &= G(t) \int_0^\infty n(B) \cos(\gamma_\mu Bt + \theta - \pi/2) dB \\ &= G(t) \int_0^\infty n(B) \sin(\gamma_\mu Bt + \theta) dB. \end{aligned} \quad (3.27)$$

The complex asymmetry for the four-counter setup is defined as

$$\begin{aligned} \tilde{A}(t) &= A^\circ \tilde{P}(t) \\ &= A^\circ P_x(t) + i A^\circ P_y(t) \\ &= A_x(t) + i A_y(t). \end{aligned} \quad (3.28)$$

where  $A_x(t)$  and  $A_y(t)$  are the real and imaginary parts of the complex asymmetry, respectively. The number of counts per second in the  $i^{\text{th}}$  counter ( $i = L, R, U$  or  $D$ ) is

$$N_i(t) = N_i^\circ e^{-t/\tau_\mu} [1 + A_i(t)] + B_i, \quad (3.29)$$

where  $A_i(t) = A^\circ P_i(t)$  is the asymmetry function for the  $i^{\text{th}}$  raw histogram. Rearranging Eq. (3.29) gives

$$A_i(t) = e^{t/\tau_\mu} \left[ \frac{N_i(t) - B_i}{N_i^\circ} \right] - 1. \quad (3.30)$$

In terms of the individual counters, the real asymmetry  $A_x(t)$  and the imaginary asymmetry  $A_y(t)$  are

$$A_x(t) = \frac{1}{2} [A_R(t) - A_L(t)] \quad \text{and} \quad (3.31)$$

$$A_y(t) = \frac{1}{2} [A_U(t) - A_D(t)]. \quad (3.32)$$

In this thesis the real and imaginary parts of the asymmetry were fit simultaneously, assuming a phase difference of  $90^\circ$  between them.

### 3.2.5 The Fourier Transform

The Fourier transform of the complex muon polarization  $\tilde{P}(t)$  gives a good approximation of the actual internal field distribution. The Fourier transform is

$$n(B) = \int_0^{\infty} \tilde{P}(t) e^{-i(\gamma_{\mu} B t + \theta)} dt. \quad (3.33)$$

Due to the finite counting rates, the Fourier transform contains statistical noise. The noisy or distorted portions of the asymmetry spectrum can be eliminated from the Fourier transform through “apodization”. Apodization is achieved by multiplying the asymmetry spectrum by a weighting function which varies between one and zero [48]. For example, the Fourier transform can be apodized with a Gaussian function so that

$$n_A(B) = \int_0^{\infty} \tilde{P}(t) e^{-i(\gamma_{\mu} B t + \theta)} e^{-\sigma_A^2 t^2 / 2} dt. \quad (3.34)$$

Unfortunately, this apodization procedure also broadens the Fourier transform. The apodization parameter  $\sigma_A$  is chosen to provide a compromise between the statistical noise in the spectrum and the additional broadening of the spectrum which such a procedure introduces. The Fourier transform will also appear broader than the actual field distribution in the sample because the muon spin precession signal is measured over a finite time interval. Because of the finite number of recorded events, the integral in Eq. (3.34) is replaced with a sum. Examples of the Fourier transform of the muon precession signal in the vortex state will be presented in the next chapter. Since  $\omega_{\mu} = 2\pi\nu_{\mu} = \gamma_{\mu} B$ , the Fourier transform can be presented as a function of either magnetic field  $B$  or the muon precession frequency  $\nu_{\mu}$ .

### 3.3 The Rotating Reference Frame

It is often convenient to fit the measured asymmetry spectrum in a “rotating reference frame” (RRF). To do this, one multiplies the complex muon polarization  $\tilde{P}(t)$  by a

function  $e^{i\omega_{RRF}t}$ . The RRF frequency  $\omega_{RRF}$  is chosen to be slightly lower than the average Larmor-precession frequency  $\bar{\omega}_\mu$  of the muon in the sample. There are two important benefits from this procedure. The first is that the quality of the fit can be visually inspected. The precession signal viewed in this rotating reference frame has only low frequency components on the order of  $\bar{\omega}_\mu - \omega_{RRF}$ , where  $\bar{\omega}_\mu$  is the average precession frequency in the lab frame. Second and most important, it allows the data to be packed into much fewer bins, greatly enhancing the speed of fitting.

Further details of the  $\mu$ SR technique may be found elsewhere (*e.g.* see Refs. [47,46,49,50]). The essential point is that the muon accurately probes the local distribution of magnetic fields in the bulk of the superconductor. The resulting  $\mu$ SR line shape contains considerable information. Of particular interest, are the magnetic penetration depth  $\lambda$ , the coherence length  $\xi$  and the vortex-lattice structure. Unfortunately, the  $\mu$ SR line shape also contains information not generally wanted—such as the effects of flux lattice disorder and additional fields such as those due to nuclear dipolar moments. Furthermore, extracting quantities such as  $\lambda$  and  $\xi$  from the data requires some modelling of the internal field distribution. This is the major difficulty in employing the  $\mu$ SR technique.

## Chapter 4

### Modelling the Internal Field Distribution

This chapter reviews the current theoretical and experimental picture of the vortex-lattice structure in conventional and high- $T_c$  superconductors. The volume of published work on this topic is large. The purpose of this chapter is not to provide an exhaustive compilation of these studies, but rather to highlight the most significant developments through a discussion of selected references. The initial part of this chapter discusses the general structure of the vortex lattice and the corresponding field distribution, and how this structure is affected by pinning, thermal fluctuations and anisotropy. Next, the problems associated with modelling the field distribution with a simple Gaussian function are discussed. The second half of the chapter concerns itself with a more accurate way of modelling the field distribution associated with the vortex lattice. In particular, the vortex-lattice structure in both an  $s$ -wave and a  $d_{x^2-y^2}$ -wave superconductor are discussed in some detail. In addition, vortex-lattice imaging experiments in both conventional and high- $T_c$  superconductors are reviewed.

#### 4.1 The Field Distribution of the Vortex Lattice

Figure 4.1 shows a typical muon-spin precession signal in the normal and vortex states of  $\text{YBa}_2\text{Cu}_3\text{O}_{6.95}$  obtained by applying a magnetic field parallel to the  $\hat{c}$ -axis. For convenience these signals are displayed in a reference frame rotating at about 3 MHz below the average muon Larmor precession frequency in the vortex lattice. A damped

signal results from the inhomogeneous distribution of magnetic field in the sample. The undamped signals arising from individual muons precessing in different local static fields combine to give a signal which decays over time. Above  $T_c$  where flux penetrates the sample uniformly, there is only a slight damping of the signal which is attributed mainly to the random local fields of nuclear dipolar moments. On the other hand, below  $T_c$  the strongly damped signal is primarily due to the inhomogeneous field distribution of the vortex lattice.

Figure 4.2 shows the finite Fourier transforms of the time spectra in Fig. 4.1. The real amplitude of the Fourier transform represents a good approximation to the internal field distribution. Above  $T_c$  the  $\mu$ SR line shape is symmetric with some broadening due to the nuclear dipolar moments (see top panel of Fig. 4.2). Below  $T_c$  the observed line shape is primarily due to the vortex lattice. The sharp peak at 67.3 MHz is attributed to the residual background signal from muons which miss the sample.

Figure 4.3 shows a general theoretical field distribution corresponding to a triangular vortex lattice. The sharp cutoff at low fields is due to the minimum in the field distribution which occurs at the center of the triangle formed from three adjacent vortices. The peak is due to the saddle point midway between two adjacent vortices. The long tail is due to the region around the vortex core, and the high-field cutoff is due to the maximum field at the center of the core. As shown in the bottom panel of Fig. 4.2, the sharp features expected from the vortex lattice are smeared in the Fourier transform of the measured muon precession signal. This is primarily due to the broadening effects associated with the Fourier transform (which were discussed in the previous chapter). The measured line shape also contains broadening effects due to the nuclear dipolar moments, fluctuations in the temperature and magnetic field, demagnetization effects associated with the sample geometry and disorder in the vortex lattice caused

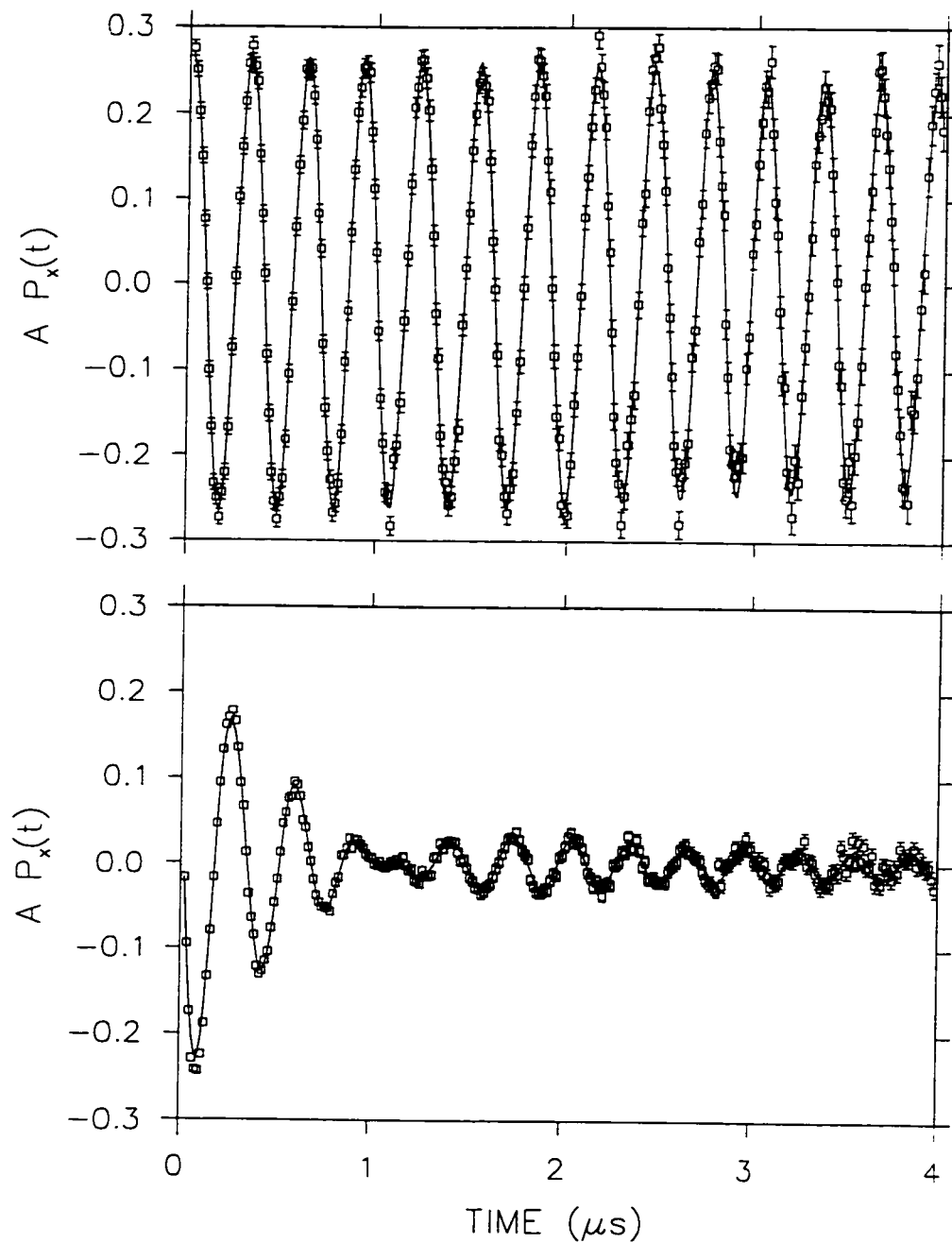


Figure 4.1: The muon spin precession signal in  $YBa_2Cu_3O_{6.95}$  in the normal state at  $T=120$  K (top panel) and the vortex state at  $T=2.4$  K (bottom panel).

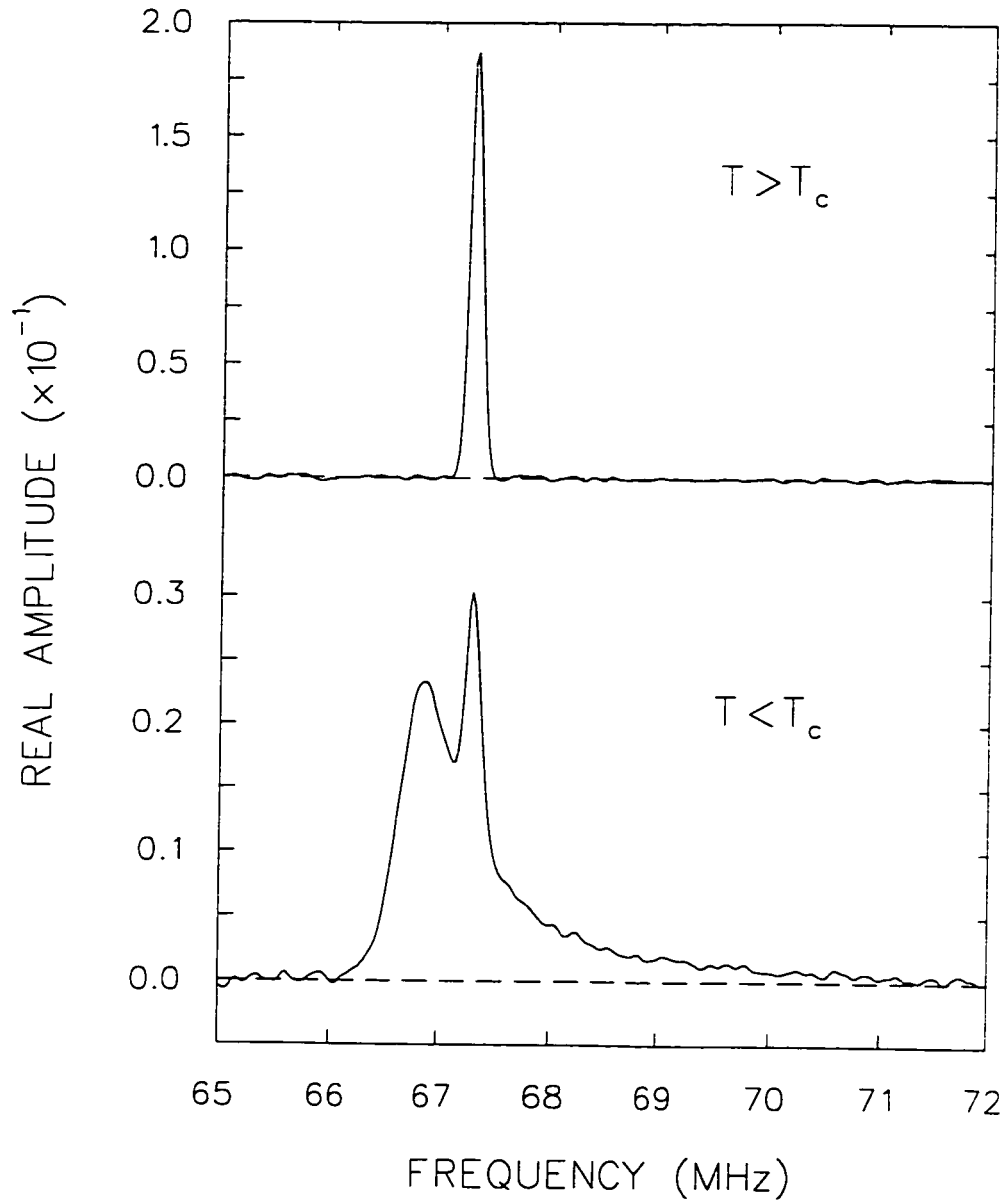


Figure 4.2: The Fourier transform of the signals in Fig. 4.1 using a Gaussian apodization with  $\sigma_A = 3 \mu\text{s}^{-1}$ .



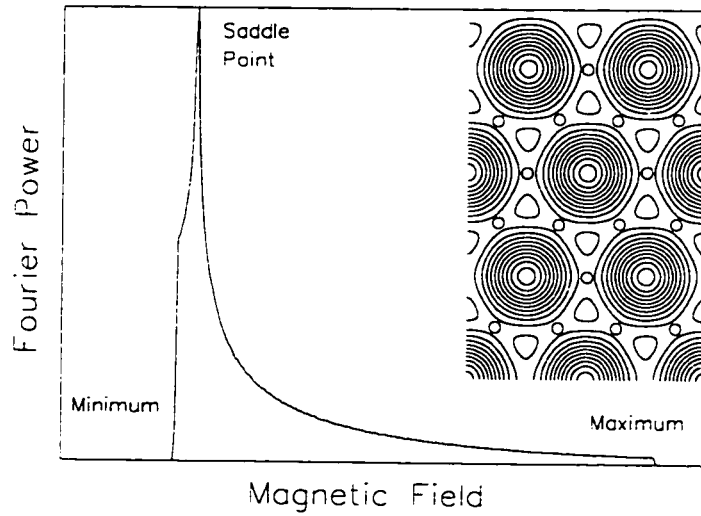


Figure 4.3: Theoretical magnetic field distribution for a triangular vortex lattice. The inset shows a contour plot of the local fields.

by pinning.

## 4.2 Pinning, Thermal Fluctuations, Dimensional Crossover and Melting

When the magnetic field applied to a type-II superconductor exceeds  $H_{c1}$ , the total free energy of the system is lowered by allowing partial flux penetration in the form of vortices. Since the core of a vortex line is essentially normal, there is a gain in energy equivalent to the condensation energy per unit length  $(H_c^2/8\pi)\pi\xi^2$  for each vortex formed—assuming that  $r_0 \sim \xi$ . However, this energy gain is more than compensated for by the decrease in magnetic energy per unit length  $(H_c^2/8\pi)\pi\lambda^2$  due to the region around the vortex which is no longer diamagnetic. The vortex line can lower its own energy by interacting with a nearby nonsuperconducting inhomogeneity, so as to become “pinned”. Spatial inhomogeneities in the superconducting order parameter

arising from impurities or other structural defects, chemical vacancies, grain boundaries, twin boundaries, etc., exert an attractive force on the vortex. The effective range  $r_p$  of the pinning force must be at least of the order of the coherence length (vortex core radius), since this is the smallest length scale resolveable by the vortex core [52]. Pinning from inhomogeneities smaller than this is much less effective. For weakly interacting vortices, the energy saved by the vortex line passing through a point defect of range  $r_p = \xi$  and length  $d$  along the vortex axis is  $U_p = (H_c^2/8\pi)\pi\xi^2 d \sim H_c^2\xi^2 d$  (Ref. [53]). The elementary pinning force  $f_p$  acting on the vortex core is given by  $f_p = dU_p/dx$ . To depin, the vortex line must move over the distance  $\xi$ , so that  $f_p = U_p/\xi \sim H^2\xi d$ . Modelling extended defects, such as grain boundaries, is generally more complicated since one must integrate over the entire inhomogeneity. To obtain the bulk pinning force per unit volume of the superconductor, one must sum over all the contributions from the various pinning inhomogeneities. In general this summation is non-trivial.

In magnetic fields where the repulsive interaction between vortex lines becomes significant, the pinning of vortices to fixed positions in the superconductor can deform the vortex lattice from its ideal configuration. The deformation of the vortex lattice in response to the force exerted by a pinning center is determined by its elastic properties, namely the shear and tilt moduli  $c_{66}$  and  $c_{44}$  [54,55,56,57,58]. Deformations will increase the elastic energy of the vortex lattice. According to the "collective pinning" theory of Larkin and Ovchinnikov [59], the equilibrium configuration is achieved by minimizing the sum of the vortex line energy and the elastic energy of the vortex lattice. At low magnetic fields the interaction energy between vortex lines is weak, so that random pinning centers will cause only a small increase in the elastic energy of the vortex lattice. This implies that random pinning of the vortex lines will be most prominent at low magnetic fields. At high magnetic fields, weak pinning centers cannot compete with the increased strength of the vortex-vortex interactions. In this case, only strong

pinning sites will hold individual vortex lines in place independently of the repulsive interaction with neighboring vortices.

In the high- $T_c$  cuprates, the vortex lines are particularly susceptible to pinning because the vortex lattice is “soft”. In particular, they have a small line tension due to the weak coupling between the  $\text{CuO}_2$  planes which gives way to highly flexible vortices [52]. Due to this flexibility, the vortices can become twisted, distorted or entangled [60]. Pinning effects will be stronger in these short coherence length superconductors. According to Brandt [61], randomly positioned stiff vortex lines will always broaden the  $\mu\text{SR}$  line shape, whereas the pinning of segments of highly flexible vortex lines will sharpen the measured magnetic-field distribution. In  $\text{YBa}_2\text{Cu}_3\text{O}_{7-\delta}$ ,<sup>1</sup> rough surfaces, oxygen vacancies and twin boundaries are the dominant sources of pinning. In powdered samples or thin films, pinning by rough surfaces can dominate the vortex-lattice configuration in the bulk. Oxygen vacancies appear to be the dominant “point-like” defect in single crystals [53]. Twin planes occur naturally in  $\text{YBa}_2\text{Cu}_3\text{O}_{7-\delta}$  along the (110) and (1 $\bar{1}$ 0) directions, because of the orthorhombic crystal structure. The depression of the order parameter at a twin boundary attracts vortices, and can result in the creation of multivortex chains oriented along the boundary. If the twin plane spacing is not commensurate, this can produce distortions in the vortex-lattice geometry. In  $\text{YBa}_2\text{Cu}_3\text{O}_{7-\delta}$ , changes in the vortex-lattice geometry can stem from a combination of twin-boundary pinning and in-plane mass anisotropy. This will be discussed more fully below.

At low temperatures the vortices are essentially frozen into their distorted configuration. As the temperature is raised, however, thermal fluctuation of the vortex-line positions become important. Thermal fluctuations in the high- $T_c$  materials are considerably stronger than in conventional superconductors. This is partly due to: (1)

---

<sup>1</sup>See section 5.2 for a description of the crystal structure for this compound.

the small value of the in-plane coherence length  $\xi_{ab}$ , (2) the high  $T_c$  which allows for high thermal energies to be reached in the superconducting state, and (3) the layered nature of these compounds. Strong thermal fluctuations greatly reduce the pinning strength. According to Feigel'man *et al.* [62], because of thermal motion of the vortex lines, the vortex core will experience a defect potential averaged over the increased effective range  $r_p \approx \sqrt{\xi^2 + u^2}$ , where  $\langle u^2 \rangle^{1/2}$  is the root-mean-square (RMS) average of the vortex-line thermal displacements from their equilibrium positions [62]. The pinning strength is reduced by this smoothing of the effective pinning potential accompanied by a reduction in the collective pinning force. Thermal depinning will occur at a temperature  $T_p(H)$  at which  $\langle u^2 \rangle^{1/2} \approx \xi$ . The depinning of vortices results in a region of reversibility in the phase diagram. Below the so-called "irreversibility line", the vortices are pinned by defects, whereas above this line the vortices are free to move in response to an external force. As noted earlier, the presence of the reversible region complicates measurements of  $H_{c2}(T)$ . In particular, the resistive transition between the superconducting and normal states is no longer sharp due to the motion of vortices (which experience a Lorentz force from the applied current). The energy which keeps the vortices moving is removed from the current—so that the resistance of the material is not zero above the irreversibility line. Thus, it is the irreversibility line which is usually measured, since  $H_{c2}(T)$  no longer exists as a phase boundary.

If the vortex fluctuations are sufficiently large, the vortex lattice will undergo a melting transition at a temperature  $T_m(H)$  ( $< T_c$ ) into a vortex-liquid phase. In the liquid phase, the vortex lines are not pinned and the interaction force between vortices is weak. As a result, there is generally no long range order in the lattice. It is currently a matter of debate whether or not the melting temperature  $T_m$  coincides with the thermal depinning temperature  $T_p$ . Since pinning is sample dependent, so is the irreversibility line. Thus, only some experiments suggest that  $T_m = T_p$ .

Vortex-lattice melting has been observed at high temperatures and/or magnetic fields in nearly-optimally doped, untwinned and high-quality twinned  $\text{YBa}_2\text{Cu}_3\text{O}_{7-\delta}$  single crystals. from magnetization measurements using a mechanical torsional oscillator [63.64], from sharp drops in resistivity measured at high magnetic fields [65.66.67.68.69.70.71.72] from discontinuous jumps in magnetization measured using a SQUID magnetometer [73.74.75.76], from jumps in ac susceptibility measured using a Hall probe [77] and from measured steps in specific heat [78.79.80.81]. Many of these experiments also support a first-order melting transition of the 3D vortex lattice in  $\text{YBa}_2\text{Cu}_3\text{O}_{7-\delta}$ .

It should be noted that the melting of the vortex lattice is a phenomenon which is not unique to the high- $T_c$  materials. Melting behaviour has been observed at high magnetic fields in Nb-Ti and  $\text{Nb}_3\text{Sn}$  wires [82], polycrystalline Nb foils and  $\text{NbSe}_2$  single crystals [83] and Nb thin films [84] and Nb single crystals [85]. It should be noted that there are other more likely interpretations [86] of the measurements in Ref. [85] and other experiments [87] show no evidence for melting in Nb over the field range claimed. Recently, Ghosh *et al.* [88] performed AC susceptibility measurements on single crystals of  $\text{NbSe}_2$  at low magnetic fields in the vortex state. They observed a re-entrant “peak effect” at low fields, which may be a signature of vortex-lattice melting. The peak effect refers to an abrupt and nonmonotonic increase in the critical current density, which shows up as a negative peak in the AC susceptibility. A narrow melted-vortex region between the solid vortex state and the Meissner state was originally proposed by Nelson [89]. Figure 4.4 shows a simplified magnetic phase diagram, which roughly illustrates the vortex-solid and vortex-liquid regions.

Theoretical predictions for the shape of the melting line in the  $H$ - $T$  phase diagram [62.90.91.92] are usually based on the Lindemann criterion [93]. In this picture the vortex lattice is expected to melt when  $\langle u^2 \rangle^{1/2}$  exceeds some small fraction  $c_L$  of the intervortex spacing  $L$ . Typically the Lindemann number  $c_L$  is of the order 0.1, although

experimentally, some variation in this number is expected since the Lindemann criterion does not account for the effects of pinning. Pinning is expected to modify the first order melting transition, to perhaps a “vortex-glass” transition [94], where the lattice freezes into a state in which the vortices form an irregular disordered pattern or into a highly disordered state in which the vortex lines are “entangled” [95,96]. The melting transition in the  $H$ - $T$  phase diagram is reasonably described by the power-law relation  $H_m(T) \sim (T_c - T_m)^n$  in moderate magnetic fields  $H_{c1} \ll H \ll H_{c2}$ . Brandt [91] and Houghton *et al.* [92] considered a nonlocal elastic theory for the vortex lattice to arrive at a power-law exponent  $n = 2$ . Blatter and Ivlev [97,98] later argued that this result is really only valid in  $\text{YBa}_2\text{Cu}_3\text{O}_{7-\delta}$  close to  $T_c$ . They performed a more rigorous calculation which takes into account the suppression of the order parameter near  $H_{c2}(T)$ , as well as quantum fluctuations, to yield a melting line which is better described with a smaller value of  $n$ . This prediction is supported by several experiments on  $\text{YBa}_2\text{Cu}_3\text{O}_{7-\delta}$  which report exponents of  $n < 1.45$  [65,68,70,73,75,76,77,99]. Some of these experiments [75,76,77] report power-law dependences for the melting line in which  $n = 4/3$ , the critical exponent expected within the 3D XY critical regime [100].

Although  $\text{YBa}_2\text{Cu}_3\text{O}_{7-\delta}$  is a layered material, near optimal doping the vortex lattice behaves in an essentially three-dimensional manner over most of the  $H$ - $T$  phase diagram. This is not the case for the highly anisotropic compound  $\text{Bi}_2\text{Sr}_2\text{CaCu}_2\text{O}_{8+\delta}$ , where the coupling between planes is very weak even well below  $T_c$ . For this material it is useful to consider the 3D vortex line as being composed of a stack of aligned 2D vortex “pancakes”, where the pancakes exist within the superconducting layers (*i.e.*  $\text{CuO}_2$  planes) [101]. The Lawrence-Doniach (LD) model [102] is a reasonable starting point for a theoretical treatment of this problem. In this model adjacent superconducting layers are separated by an insulating layer of thickness  $s$ . The vortex pancakes in

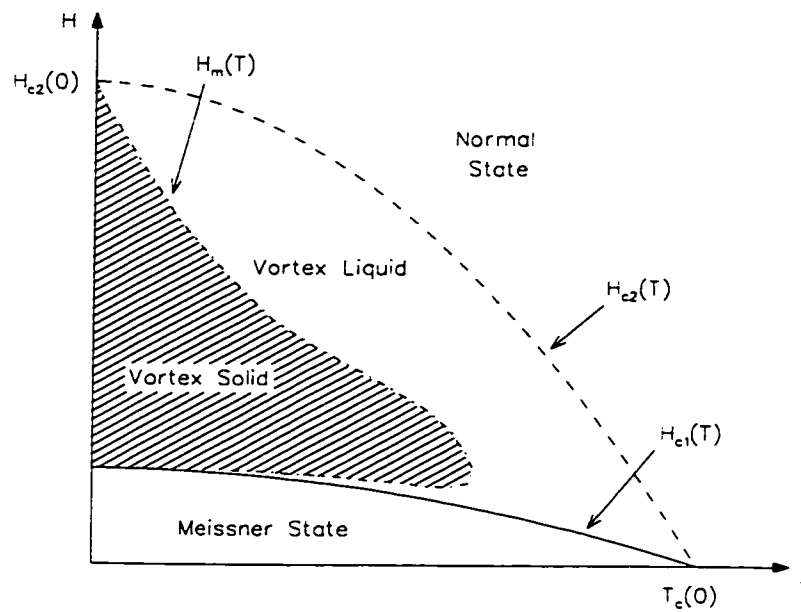


Figure 4.4: Magnetic phase diagram showing the normal state, the Meissner state, the vortex-solid and vortex-liquid states.

neighboring layers are connected by Josephson vortices which exist within the Josephson junctions between the superconducting layers. The vortex pancakes in adjacent  $\text{CuO}_2$  planes thus couple through both magnetic interactions and Josephson tunneling. A third coupling mechanism, namely the indirect effect of the Coulomb interaction, has been suggested by Duan [103]. The relevant parameter in the LD model is the ratio of the  $\hat{c}$ -axis coherence length  $\xi_c$  to  $s$ . When  $\xi_c/s > \sqrt{2}$  there is no phase difference in the order parameter between neighboring layers, so that in the absence of pinning the vortex lattice exhibits 3D behaviour—equivalent to the anisotropic London and GL models. On the other hand, when  $\xi_c/s < \sqrt{2}$  there may be a phase difference and the LD theory describes a quasi-2D vortex structure. The LD model will not be completely satisfactory in a superconductor in which the material between the superconducting layers is not completely insulating. In this case the proximity effect may become important.

At low temperatures vortex pancakes between neighboring layers are aligned. However, in a superconductor with random inhomogeneities, pinning will displace some of the pancakes and cause a suppression of the phase coherence between layers [104]. The effects of random pinning-induced misalignment of the vortex pancakes on the measured  $\mu\text{SR}$  field distribution has been the focus of several studies [61,104,105,106,107,108,109]. The effects include a reduction in both the line shape width and the line shape asymmetry. When the magnetic field is increased, the interaction between pancake vortices within a layer will eventually exceed the coupling strength between the pancake vortices in neighboring layers. In this case random pinning in the layers will lead to a misalignment of the pancake vortices between layers. Thus, in a highly anisotropic system with inhomogeneities, a dimensional crossover from a 3D to a 2D vortex structure can be induced by magnetic field. Harshman *et al.* [106] observed a narrowing and a loss of asymmetry in the  $\mu\text{SR}$  line shape for  $\text{Bi}_2\text{Sr}_2\text{CaCu}_2\text{O}_{8+\delta}$  at low temperatures



and high magnetic fields, which they attributed to pinning-induced misalignment of the pancake vortices. In the same study, the  $\mu$ SR line shape for  $\text{YBa}_2\text{Cu}_3\text{O}_{7-\delta}$  under similar conditions was found to be in agreement with a 3D vortex lattice. Other  $\mu$ SR studies on  $\text{Bi}_2\text{Sr}_2\text{CaCu}_2\text{O}_{8+\delta}$  [107,108] provide additional support for a field-induced dimensional crossover.

Clem [101] has shown that the thermal energy required to misalign 2D pancake vortices is extremely small. The effect of thermal fluctuations on the vortex lattice is very different between the regions of weak and strong magnetic fields [110]. In low magnetic fields the displacement amplitude of the pancake vortices due to thermal fluctuations is much larger than the relative displacement of the vortices between layers. On the other hand, as just noted, in strong magnetic fields the vortex-vortex interactions within a layer are stronger than those between layers. In this case thermal fluctuations act in a quasi-2D manner.

The effects of thermal fluctuations on the measured internal field distribution have been previously studied by  $\mu$ SR in  $\text{Bi}_2\text{Sr}_2\text{CaCu}_2\text{O}_{8+\delta}$  [107,111]. Rapid fluctuation of a vortex about its average position can increase the apparent core radius and smear the magnetic field out over an effective radius of  $\langle u^2 \rangle^{1/2}$  [61]. The smearing effect reduces the average of the field distribution in the vortex-core region. The muon detects the field averaged over the fluctuations, since the typical time scale for thermal fluctuations of the vortices ( $\sim 10^{-10}$  s [51]) is much shorter than  $2\pi/\gamma_\mu\Delta B$ , where  $\gamma_\mu$  is the muon gyromagnetic ratio and  $\Delta B$  is the range of the field fluctuation at the muon site. The result is a premature truncation of the high-field tail in the measured  $\mu$ SR line shape. A proper analysis of the corresponding muon precession signal would lead to an overestimate of the vortex-core radius  $r_0$ . The effect of thermal fluctuations on the high-field tail was nicely demonstrated in Ref. [111]. The melting transition in  $\text{Bi}_2\text{Sr}_2\text{CaCu}_2\text{O}_{8+\delta}$  was determined by Lee *et al.* [107,111] by observing additional changes in the  $\mu$ SR line

shape—namely, a reduction in the line width and in the asymmetry of the line shape as a function of temperature and magnetic field. Numerical simulations of the magnetic field distribution were later provided by Schneider *et al.* [112], for both a vortex liquid phase and a disorder-induced 2D phase. Good agreement was reported between these theoretical line shapes and those measured in the experiments by Lee *et al.*

Although the coupling strength between  $\text{CuO}_2$  planes in fully oxygenated  $\text{YBa}_2\text{Cu}_3\text{O}_{7-\delta}$  is sufficient to yield a vortex structure which exhibits 3D behaviour over the majority of the  $H$ - $T$  phase diagram, such is not the case in the underdoped material. Magnetization measurements performed on  $\text{YBa}_2\text{Cu}_3\text{O}_{6.60}$  are consistent with quasi-2D fluctuation behaviour [113]. As I will show later, due to this reduced dimensionality,  $\mu\text{SR}$  measurements of the internal magnetic field distribution in  $\text{YBa}_2\text{Cu}_3\text{O}_{6.60}$  yield a rich phase diagram which is comparable to that for  $\text{Bi}_2\text{Sr}_2\text{CaCu}_2\text{O}_{8+\delta}$ .

### 4.3 Gaussian Field Distribution Analysis

Traditionally, the behaviour of the magnetic penetration depth in the vortex state of a superconductor has been determined from the variation of the second moment (*i.e.* the square of the width) of the  $\mu\text{SR}$  line shape. The second moment of the local magnetic field distribution  $n(B)$  is

$$\langle \Delta B^2 \rangle = \int_{-\infty}^{+\infty} n(B) (\langle B \rangle - B)^2 dB. \quad (4.1)$$

where  $\langle B \rangle$  is the first moment of  $n(B)$  (*i.e.* the average local magnetic field). At moderate magnetic fields, the second moment of the field distribution for a vortex lattice (which is considered in the next section) has been shown in the London picture to be [123]

$$\langle \Delta B^2 \rangle = 0.00371 \Phi_0^2 \lambda^{-4}. \quad (4.2)$$

A simple way to model the second moment is to assume that  $n(B)$  is a Gaussian distribution of static internal magnetic fields. The corresponding muon polarization function is [47]

$$P(t) = P(0) \exp(-\sigma^2 t^2 / 2) \cos(\gamma_\mu \langle B \rangle t). \quad (4.3)$$

where  $\sigma$  is the muon depolarization rate. For a Gaussian field distribution, the second moment is given by [114]

$$\langle \Delta B^2 \rangle = \frac{2\sigma^2}{\gamma_\mu}. \quad (4.4)$$

so that

$$\sigma \propto 1/\lambda^2 \propto n_s. \quad (4.5)$$

However, this method is extremely crude since the field distribution corresponding to a vortex lattice is generally asymmetric. It is mentioned here only because many of the earlier  $\mu$ SR experiments arrived at conclusions regarding the pairing-state symmetry in the high- $T_c$  compounds based on this type of analysis [114,115,116,117,118]. Figure 4.5(a) shows an example of fitting the early time part of the muon-spin precession signal in NbSe<sub>2</sub> with a Gaussian relaxation function. The spectrum was obtained by field cooling the sample to  $T = 2.4$  K in a magnetic field  $H = 0.35$  T applied parallel to the  $\hat{c}$ -axis. The quality of the fit ( $\chi^2$ ) is 4076 for 412 degrees of freedom. The real Fourier transform of both the data and the Gaussian fit are shown in Fig. 4.5(b). The small peak near 47.5 MHz is due to muons which miss the sample and avoid the background suppression system. Typically this constitutes 5 to 15% of the total signal amplitude for our apparatus.

Figure 4.6(a) shows the temperature dependence of  $\sigma$  for a mosaic of three high quality YBa<sub>2</sub>Cu<sub>3</sub>O<sub>6.95</sub> single crystals. Despite the poor quality of the fits, the Gaussian function appears to effectively model the change in the second moment of the  $\mu$ SR line shape. As the temperature is increased,  $\chi^2$  decreases dramatically due to the

natural progression towards a symmetric internal field distribution as the penetration depth grows. A serious drawback with this method is its inability to resolve the several phenomena which separately contribute to the width of the  $\mu$ SR line shape. For example, one cannot assume that the linear  $T$  dependence of  $\sigma(T)$  at low temperatures necessarily implies that  $\lambda^{-2}(T)$  has the same linear dependence. For instance, some of the change in the line width may arise from thermal fluctuations of the vortex lines which result in a narrowing of the  $\mu$ SR line shape at higher temperatures. Thus, the magnitude of the linear term in  $\lambda^{-2}(T)$  could be different than that of  $\sigma(T)$ , or worse,  $\sigma(T)$  could have a different leading term.

Consider Fig. 4.6(b), which shows the temperature dependence of the muon depolarization rate  $\sigma(T)$  in single crystal  $\text{YBa}_2\text{Cu}_3\text{O}_{6.95}$  for two different applied magnetic fields. There is a distinct drop in  $\sigma$  at low  $T$  when the applied magnetic field is changed from 0.5 to 1.5 T. Moreover, the term linear in  $T$  decreases at the higher field. However, there is no way to determine whether the field dependence of the muon depolarization rate is due to intrinsic or extrinsic effects. We now believe that the field dependence of  $\sigma(T)$  observed in some of the earlier  $\mu$ SR experiments was misinterpreted as being due to an increase in flux-lattice disorder at low magnetic fields. The precise cause of this field dependence will be addressed later on in this report.

There are many other serious limitations or problems associated with using a simple Gaussian analysis. For instance, the shape of the internal field distribution will change when there are variations in the vortex-lattice geometry and at a crossover at low fields where the intervortex spacing  $L$  equals  $\lambda$ . Fitting to a Gaussian function will misidentify these changes in the  $\mu$ SR line shape as changes in  $\lambda$ . This simple analysis is also insensitive to the high-field tail of the measured internal field distribution --so that no information regarding the structure of the vortex cores or the behaviour of  $\xi$

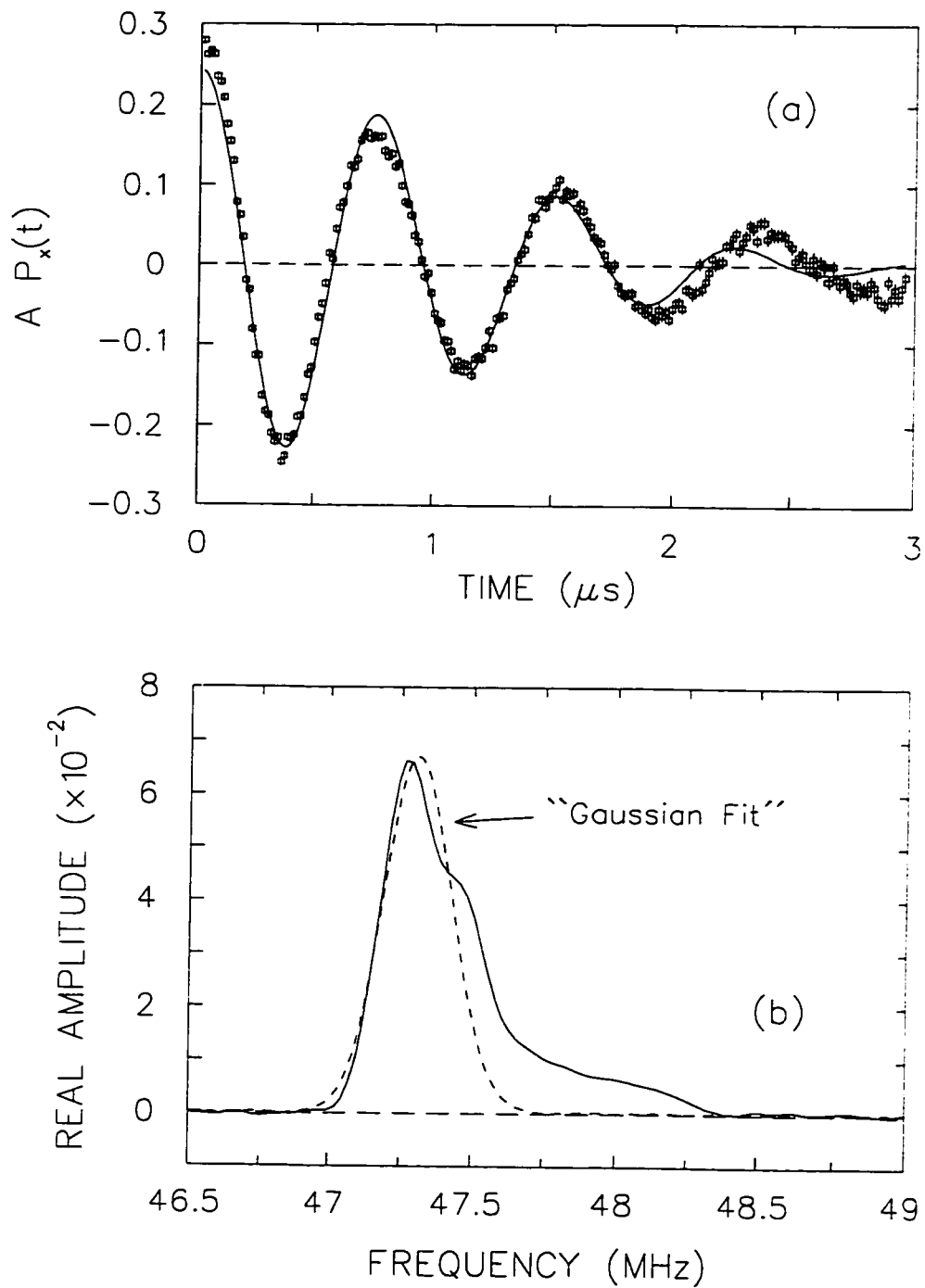


Figure 4.5: (a) The muon spin precession signal in  $NbSe_2$  after field cooling to  $T = 2.4$  K in a magnetic field  $H = 0.35$  T. The solid line is a fit to a Gaussian relaxation function  $\exp(-\sigma^2 t^2 / 2)$ . (b) Fourier transformation of data (solid line) and fit (dashed line) from (a).

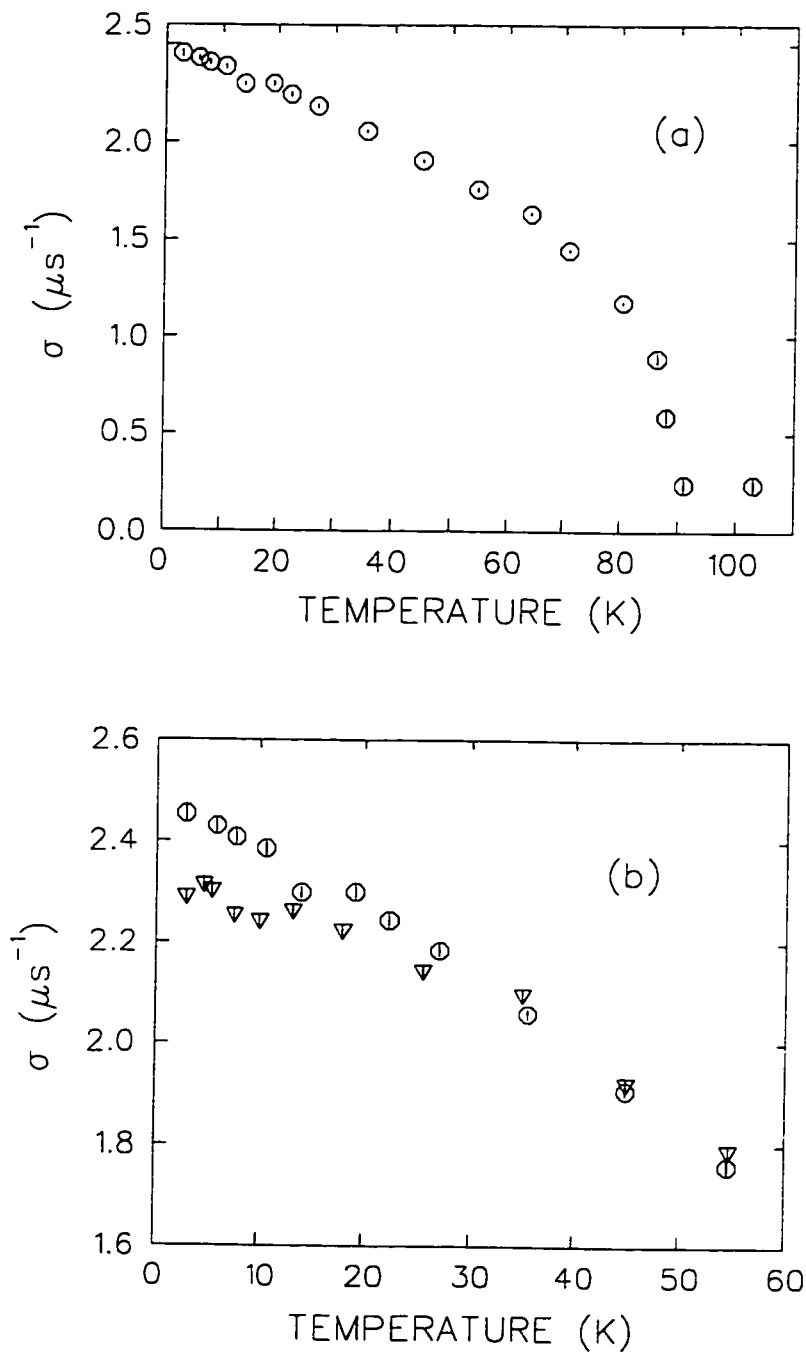


Figure 4.6: The temperature dependence of the muon depolarization rate  $\sigma$  in the vortex state of  $\text{YBa}_2\text{Cu}_3\text{O}_{6.95}$  at (a)  $H = 0.50$  T and (b)  $H = 0.50$  T (open circles) and  $H = 1.49$  T (open triangles).

can be obtained.

#### 4.4 Field Distribution of the Vortex Lattice

A more appropriate way of analyzing the measured field distribution is to model the contributions to the line shape separately. The London theory provides the simplest approach to modelling the internal field distribution  $n(B)$  corresponding to the vortex lattice. The London model applies exclusively to extreme type II superconductors in which  $\lambda \gg \xi$ , and is independent of the detailed mechanism responsible for superconductivity. Furthermore, the London picture is valid at all temperatures below  $T_c$  and for applied magnetic fields  $H \ll H_{c2}$ . Both of these conditions are usually satisfied in a  $\mu$ SR experiment.

For a magnetic field applied in the  $\hat{z}$ -direction parallel to the crystallographic  $\hat{c}$ -axis, the London equation [*i.e.* Eq. (2.13)] for the field profile  $\mathbf{B}(\mathbf{r})$  resulting from vortices positioned at the sites  $\mathbf{r}_n$  is

$$\mathbf{B}(\mathbf{r}) + \lambda_{ab}^2 [\nabla \times \nabla \times \mathbf{B}(\mathbf{r})] = \Phi_0 \sum_n \delta(\mathbf{r} - \mathbf{r}_n) \hat{\mathbf{z}}. \quad (4.6)$$

where  $\lambda_{ab} = (\lambda_a \lambda_b)^{1/2}$ ,  $\delta(\mathbf{r})$  is a two-dimensional delta function and  $\Phi_0 = 2.068 \times 10^{-15}$  T·m<sup>2</sup> is the flux associated with each vortex. We restrict the discussion throughout this report to the above mentioned orientation between the applied magnetic field and the crystal lattice—hence avoiding generalizing equations to include the  $\hat{c}$ -axis penetration depth. The points  $\mathbf{r}_n$  form a two-dimensional periodic lattice in the  $\hat{a}$ - $\hat{b}$  plane, so that  $\mathbf{B}(\mathbf{r})$  may be expanded in a Fourier series. The Fourier transform  $\mathbf{B}_{\mathbf{K}}$  is

$$\mathbf{B}_{\mathbf{K}} = n_f \int_{cell} \mathbf{B}(\mathbf{r}) e^{-i\mathbf{K} \cdot \mathbf{r}} d^2\mathbf{r}. \quad (4.7)$$

Here  $n_f$  is the number of vortices per unit area and  $\mathbf{K}$  are the reciprocal lattice vectors.

From Eq. (4.6) the Fourier components are

$$\mathbf{B}_{\mathbf{K}} = \frac{B_0}{1 + K^2 \lambda_{ab}^2} \hat{\mathbf{z}}. \quad (4.8)$$

where  $B_0 = n_f \Phi_0$  is the average internal field. Thus the total field at the point  $\mathbf{r}$  is given by

$$\mathbf{B}(\mathbf{r}) = \sum_{\mathbf{K}} \mathbf{B}_{\mathbf{K}} e^{-i\mathbf{K}\cdot\mathbf{r}} = B_0 \sum_{\mathbf{K}} \frac{e^{-i\mathbf{K}\cdot\mathbf{r}}}{1 + K^2 \lambda_{ab}^2} \hat{\mathbf{z}}. \quad (4.9)$$

Eq. (4.9) does not account for the finite size of the vortex cores, which are assumed to be infinitely small—*i.e.* a delta function is used as the source term in Eq. (4.6). The spatial dependence of the order parameter which goes to zero at the center of the vortex cores is not built into the London theory. As a result Eq. (4.9) has the unphysical property that  $\mathbf{B}(\mathbf{r})$  diverges on the axis of the vortex line at  $\mathbf{r}_n$ . To correct for the finite size of the vortex cores, one can modify Eq. (4.9) by multiplying each term by a cutoff factor which suppresses the higher Fourier components and produces a smooth variation of field to a finite maximum value at the center of the vortex core. A sharp cutoff such as at  $K = 2\pi/\xi_{ab}$  is generally inappropriate because it introduces an oscillatory cutoff in real space [119]. A smooth cutoff may be obtained by solving the GL equations. At reduced fields  $b = B_0/B_{c2} < 0.25$ , Brandt [120] derived the cutoff factor  $\exp(-K^2 \xi^2/2)$  from the isotropic GL theory for  $\kappa \gg 1$ . At low fields  $b \ll 1$ , the cutoff factor is better approximated by  $\exp(-\sqrt{2}K\xi)$  [121]. To account for the field dependence of the order parameter in GL theory, Brandt also replaces  $\lambda$  and  $\xi$  with  $\lambda/\sqrt{1-b}$  and  $\xi/\sqrt{1-b}$ , respectively. With the external magnetic field applied parallel to the crystallographic  $\hat{c}$ -axis, the local field at any point in the  $\hat{a}$ - $\hat{b}$  plane is then given by Brandt's modified London model [54.122.123]

$$B(\mathbf{r}) = B_0 \sum_{\mathbf{K}} \frac{e^{-i\mathbf{K}\cdot\mathbf{r}} e^{-K^2 \xi_{ab}^2/2(1-b)}}{1 + K^2 \lambda_{ab}^2/(1-b)}. \quad (4.10)$$



where  $\mathbf{B}(\mathbf{r}) = B(\mathbf{r})\hat{\mathbf{z}}$  and the cutoff factor should be replaced with  $\exp(-\sqrt{2}K\xi_{ab}/\sqrt{1-b})$  when  $b \ll 1$ . In Chapter 6, we shall show that Eq. (4.10) is a reasonable model for the internal field distribution due to the vortex lattice in a real superconductor.

#### 4.4.1 Vortex Lattice in a *s*-Wave Superconductor

The vortex core in a clean *s*-wave superconductor was first studied by Caroli, de Gennes and Matricon [124]. Using a Bogoliubov formalism these authors calculated the low-energy spectrum of quasiparticle bound states in an isolated vortex core in which  $E < \Delta_0$ , where  $\Delta_0$  is the bulk energy gap in zero magnetic field. They determined that the vortex core radius  $r_0$  (*i.e.* where the order parameter changes appreciably) was on the order of the coherence length  $\xi$ . The model is conceptually the same as the quantum mechanical picture of a particle in a cylindrical potential well of radius  $\xi \simeq \hbar v_F / \pi \Delta_0$  and depth  $\Delta_0$ . The eigenvalues of the low-lying quasiparticle states may be written as  $E_\mu \simeq \mu \Delta_0^2 / E_F \sim \mu \Delta_0 / k_F \xi$ , where  $\mu = 1/2, 3/2, 5/2, \dots$  are the angular momentum quantum numbers and  $E_F$  is the Fermi energy.<sup>2</sup> Bardeen *et al.* [126] later extended the calculations of Caroli *et al.* to determine the higher energy scattering states with  $E > \Delta_0$  and the effects of the magnetic field on the energy of the bound states in the vortex core. Neumann and Tewordt [127] determined the vortex structure near  $T_c$  by numerically solving the GL equations while various other authors obtained vortex-lattice solutions of the Gor'kov microscopic equations [128,129] near  $H_{c2}$  using a variety of approximations [130,131,132,133,134].

To determine the vortex structure for arbitrary temperature, magnetic field and impurity concentrations, numerous efforts were made to numerically solve Eilenberger's equations [135], which are a reformulation of the microscopic Gor'kov theory. In the

---

<sup>2</sup>The quantity  $\mu$  must be an odd half-integer to ensure that the wave functions  $u$  and  $v$  in the Bogoliubov equations describing the excited states in the vortex core are single-valued, as discussed in Ref. [125].

dirty limit the transport-like Eilenberger equations reduce to the simpler diffusion-like Usadel equations [136,137]. Using a circular-cell approximation, Kramer *et al.* [138] determined the vortex structure in the dirty limit by numerically solving the Usadel equations near  $H_{c1}$ . They found that the size of the vortex core shrinks with decreasing  $T$  at low temperatures, but that the effect is much weaker than expected in the clean limit. Numerical solutions of the Eilenberger equations for nearly isolated vortices in the clean limit were later obtained [139,140], again using a circular-cell approximation. In the clean limit the size of the vortex core region was found to shrink more drastically and the field at the center of the core increased with decreasing temperature. In particular, for  $T \ll T_c$  the order parameter  $\psi(\mathbf{r})$  and the supercurrent density  $J_s(\mathbf{r})$  are predicted to increase from the center of an isolated vortex core over a length scale  $\xi_1$  which has a temperature dependence given by [140]

$$\xi_1 = \xi_0 \frac{T}{T_c}. \quad (4.11)$$

where  $\xi_0$  is the coherence length defined in BCS theory. This prediction is commonly referred to as the “Kramer-Pesch effect”. The predicted temperature dependence of the vortex core size is related to thermally activated quasiparticle excitations which populate the higher energy bound states. At high temperatures the bound states with energies  $E_\mu$  are densely packed within the low-energy region of the vortex core (*i.e.*  $E_\mu \ll \Delta_0$ ). Upon reducing the temperature, the bound state energies  $E_\mu$  increase so that there are fewer bound states in the vortex core region. The minimum size of the vortex core is obtained when only the lowest bound state is populated [141]. The case of arbitrary impurity concentration was treated in the context of the Eilenberger equations using a circular-cell approximation by Rammer *et al.* [142] and by Klein [143], who rigorously solved the Eilenberger equations numerically for a hexagonal vortex lattice without making any approximations. Impurities reduce the maximum field in

the vortex core. Near  $T_c$  the effects of impurities on the magnetic field distribution are negligible.

More recently, Hayashi *et al.* [148] have investigated the quantum regime of a single vortex in a clean  $s$ -wave superconductor, by self-consistently solving the Bogoliubov-de-Gennes (BdG) equations. The temperature dependence of the vortex-core radius is found to essentially agree with the Kramer-Pesch effect except at temperatures below the so-called “quantum limit”. In this limit the temperature is low enough that there is no thermal smearing of the discrete bound quasiparticle states in the vortex cores (*i.e.*  $k_b T < E_\mu$ ). According to Hayashi *et al.*, the quantum limit is reached below  $T < 50$  mK in NbSe<sub>2</sub>. In this temperature region the shrinkage of the vortex cores must saturate. Unfortunately, experiments thus far have not probed this low-temperature regime.

Scanning tunneling microscopy (STM) experiments on the layered hexagonal conventional type-II superconductor NbSe<sub>2</sub> by Hess *et al.* [144] confirmed the existence of localized states in the cores. In the vicinity of a single vortex they measured the differential conductance  $dI/dV$ , which is proportional to the local density of states (LDOS). Well away from the vortex center, the  $dI/dV$  vs.  $V$  scan resembled the standard BCS density of states for zero magnetic field. In the vortex core region, however, instead of the constant LDOS expected for the normal state, they observed a pronounced peak in the differential conductance centered at zero bias voltage. The peak has been interpreted as being due to the bound states localized inside the vortex core. Theoretical efforts [145,146,147,149,150] shortly followed which focused on calculating the LDOS observed in this now famous experiment and subsequent experiments on NbSe<sub>2</sub> by Hess *et al.* [151,152,153]. In a conventional  $s$ -wave superconductor with an isotropic energy gap, the LDOS has circular symmetry around an isolated vortex core. Hess *et al.* observed that the LDOS has a sixfold star shape around a vortex in NbSe<sub>2</sub> [151]. Furthermore, the orientation of the star was found to depend on the quasiparticle energy

and at intermediate bias voltages the rays split [152]. The origin of the sixfold symmetry in the LDOS has been explained in terms of vortex-vortex interactions [154], gap anisotropy [155], the anisotropic Fermi surface [156], and combinations of these effects [155]. The magnetic field distribution  $B(\mathbf{r})$  in the vortex core region will depend on which of these interpretations is correct. For instance, if vortex-vortex interactions are the major source then the field distribution  $B(\mathbf{r})$  will be nearly circularly symmetric in the vortex core region and will progress to a definite sixfold symmetry farther away from the vortex center (as shown in Ref. [154]). The circular symmetry will extend further out from the vortex center as the magnetic field is weakened. On the other hand, if the sixfold symmetry observed in the STM experiments is due to an anisotropic  $s$ -wave energy gap, the sixfold symmetry in  $B(\mathbf{r})$  will be more prominent in the vortex core region. Even in this latter case, however, the field distribution in the vortex core region can be reasonably approximated by circular symmetry.

The GL theory has the spatial dependence of the order parameter built in and thus provides a natural description of the magnetic field in the vortex-core region. Abrikosov [157] predicted the vortex state from his famous periodic solution of the GL equations near  $H_{c2}$ . He also provided an approximate analytical solution of the GL equations for an isolated vortex near  $H_{c1}$ . For intermediate fields, the GL equations must be solved numerically. The magnetic field distribution obtained from the exact numerical solutions of the GL equations coincides with that from the modified London model at low fields and arbitrary  $\kappa$  [158]. J.R. Clem [159] proposed a variational model to solve the GL equations based upon a trial function for the order parameter:  $f = r/(r^2 + \xi_v^2)^{1/2}$ , where  $\xi_v$  is a variational core radius parameter. This model solves the GL equations approximately at low magnetic fields (*i.e.* isolated vortices) yielding an analytical

expression for the magnetic field distribution

$$B(\mathbf{r}) = B_0 \sum_{\mathbf{K}} \frac{K_1(\xi_v \sqrt{K^2 + \lambda_{ab}^{-2}}) e^{-i\mathbf{K}\cdot\mathbf{r}}}{K_1(\xi_v/\lambda_{ab}) \lambda_{ab} K}. \quad (4.12)$$

where  $K_1(x)$  is a modified Bessel function. For extreme type-II superconductors ( $\kappa \gg 1$ ),  $\xi_v \approx \sqrt{2}\xi$ , where  $\xi$  is the GL coherence length.

Hao *et al.* [160] extended the Clem model to larger magnetic fields through the linear superposition of the field profiles of the individual vortices. This included multiplying the trial function for the order parameter by a second variational parameter  $f_\infty$  to take into account the depression of the order parameter due to the overlapping of vortices. In particular,  $f_\infty \rightarrow 1$  as  $B \rightarrow 0$  (*i.e.* the Clem limit) and  $f_\infty \rightarrow 0$  as  $B$  approaches the upper critical field. Yaouanc *et al.* [121] recently simplified Hao's analytical model exclusively to the case of  $\lambda^2 K_{min}^2 \gg 1$ , where  $K_{min}$  is the smallest non-zero reciprocal lattice vector of the vortex lattice. This condition is satisfied even at low fields for large  $\kappa$  superconductors like the high- $T_c$  compounds. The result is that the local field at any point in the  $\hat{a}$ - $\hat{b}$  plane due to an applied field along the  $\hat{c}$ -axis is [121]

$$B(\mathbf{r}) = B_0(1 - b^4) \sum_{\mathbf{K}} \frac{e^{-i\mathbf{K}\cdot\mathbf{r}} u K_1(u)}{\lambda_{ab}^2 K^2}. \quad (4.13)$$

where  $K_1(u)$  is a modified Bessel function and

$$u^2 = 2\xi_{ab}^2 K^2 (1 + b^4) [1 - 2b(1 - b)^2]. \quad (4.14)$$

The Bessel function has the asymptotic limits  $K_1(u) = 1/u - (u/2) \ln(1.7139/u)$  for ( $u \ll 1$ ) and  $K_1(u) = (\pi/2u)^{1/2} \exp(-u)$  for ( $u \gg 1$ ). Yaouanc *et al.* [121] argued that there is no general theory for the field distribution valid at arbitrary temperature and that the  $B(\mathbf{r})$  derived from GL theory should be applicable down to  $B = 0$ . This seems unlikely since the symmetry of the LDOS around a vortex core depends on the energy  $E$  of the quasiparticle bound states relative to the temperature dependent energy

gap  $\Delta(T)$ . Nevertheless, Brandt [161] has recently developed an iteration method for solving the GL equations, to compute the field profile  $B(\mathbf{r})$  for a vortex lattice of arbitrary symmetry at any value of magnetic field. Equation (4.13) is found to agree extremely well with these exact numerical solutions of the GL equations at low reduced fields  $b$  [121].

To employ Eq. (4.10) or Eq. (4.13) one must assume an appropriate geometry for the vortex lattice. Theoretically, the equilibrium structure of the vortex lattice can be found by minimizing the Gibbs free energy

$$G_L = F_L - \frac{BH}{4\pi}. \quad (4.15)$$

where the London free energy per unit volume associated with the vortices is [162]

$$F_L = \int [\mathbf{h}^2 + \lambda^2(\nabla \times \mathbf{h})^2] d^2\mathbf{r} / 8\pi A, \quad (4.16)$$

where  $A$  is the area of the sample. The vortex-lattice geometry which minimizes the free energy for a conventional  $s$ -wave superconductor is a triangular lattice [162,163,164].

Ideally, the vortex structure is determined by experiment. This is possible in superconductors which contain few foreign contaminants or structural defects. For instance, STM [144,153] and small angle neutron scattering (SANS) [165] measurements on the anisotropic conventional type-II superconductor  $\text{NbSe}_2$  show a perfect triangular lattice with long-range order, when the magnetic field is applied parallel to the  $\hat{c}$ -axis.

#### 4.4.2 Vortex Lattice in a $d$ -Wave Superconductor

The problem of an isolated vortex line in a  $d_{x^2-y^2}$ -wave superconductor was first seriously considered by Soininen *et al.* [166], using a simple microscopic model for electrons on a lattice in the BdG formalism. In calculating the spatial distribution of the order parameter for a single vortex, they found that an  $s$ -wave component is induced

near the vortex core with opposite winding of phase relative to the  $d$ -wave component. Several authors [167.168.169.170.171] have studied the effect of this induced  $s$ -wave order parameter on both an isolated vortex and the vortex-lattice structure, in terms of two-component GL equations containing both  $s$ -wave and  $d$ -wave order parameters. In these equations the  $s$ -wave component couples to the  $d$ -wave component through mixed gradient terms. Because of this coupling, the  $s$ -wave component is induced by spatial variations in the  $d$ -wave order parameter which occur in the vicinity of a vortex line. In a tetragonal superconductor the induced  $s$ -wave order parameter has fourfold symmetry and the  $d$ -wave order parameter has circular symmetry. Thus, in the core region of an isolated vortex, the magnetic field distribution is fourfold symmetric, whereas away from the core region, where the  $s$ -wave component vanishes, the field distribution has circular symmetry. At low temperatures near  $H_{c2}$ , the vortex lattice is oblique—reflecting the fourfold symmetry of the  $s$ -wave order parameter. However, near  $T_c$  the  $s$ -wave component becomes negligible and the vortex lattice is triangular. This latter prediction is crucial to the study of  $\text{YBa}_2\text{Cu}_3\text{O}_{7-\delta}$  in this thesis. Later it will be shown that when  $\text{YBa}_2\text{Cu}_3\text{O}_{6.95}$  is cooled through  $T_c$  in the presence of a magnetic field, the vortex lattice becomes strongly pinned at  $T \approx 0.75 T_c$  and remains so for further reductions in temperature. Thus the vortex lattice geometry at low temperatures is governed by the geometry at the pinning temperature—which is nearly triangular in the two-component GL model.

It is well known that the orthorhombic crystal structure of  $\text{YBa}_2\text{Cu}_3\text{O}_{7-\delta}$  results in a significant mass anisotropy in the  $\hat{a}$ - $\hat{b}$  plane—although the actual value of  $\gamma = (m_a/m_b)^{1/2}$  is clearly a doping-dependent quantity. For instance, according to infrared reflectance measurements at zero field:  $\gamma = \lambda_a/\lambda_b = 1.55$  and  $\lambda_{ab}(T = 0) = (\lambda_a \lambda_b)^{1/2} = [(1600)(1030)]^{1/2} = 1284 \text{ \AA}$  in  $\text{YBa}_2\text{Cu}_3\text{O}_{6.95}$  [172], while  $\gamma = 1.31$  and  $\lambda_{ab} = (\lambda_a \lambda_b)^{1/2} = [(2100)(1600)]^{1/2} = 1833 \text{ \AA}$  in  $\text{YBa}_2\text{Cu}_3\text{O}_{6.60}$  single crystals [173] similar to those used

in the present study. Xu *et al.* [170] have extended the two-component GL theory to include the effects of mass anisotropy. When the magnetic field is applied parallel to the crystallographic  $\hat{c}$ -axis, both the  $s$ -wave and  $d$ -wave order parameters show a two-fold symmetry, where the  $d$ -wave order parameter has essentially elliptical symmetry. Within the GL formalism, Heeb *et al.* [174] find a similar reduction from fourfold to twofold symmetry in the presence of orthorhombic distortions. More recently, Ichioka *et al.* [175] reconstructed the two-component GL theory to investigate the vortex lattice in a pure  $d_{x^2-y^2}$ -wave superconductor at low temperatures near  $H_{c2}$ . These authors argue that correction terms derived from the Gor'kov equations which are absent in conventional GL theory must be included at low  $T$ . They find that the unit-cell shape of the vortex lattice transforms from hexagonal to square at low temperatures, with the fourfold symmetry of the cores becoming clearer, even when there is no induced  $s$ -wave component included in the theory.

It is important to realize that the results using the two-component GL theory are strictly valid only along the superconducting-to-normal phase boundary near  $H_{c2}$ , and therefore do not necessarily provide an understanding of the vortex-lattice structure deep in the superconducting state where  $\mu$ SR experiments are performed. Near  $H_{c2}$ , where the vortices are close together, the fourfold symmetry of the induced  $s$ -wave component in the cores leads to a fourfold symmetry in the vortex-lattice configuration. However, there is no reason to expect this to be the case at low fields where the density of vortices in the superconductor (and hence the influence of the cores on the flux-lattice geometry) is diminished. For instance, in the borocarbide superconductors  $R\text{Ni}_2\text{Bi}_2\text{C}$  ( $R = \text{Er, Lu}$ ) the vortex lattice has been shown to transform from square to triangular at low fields [176,177]. Although the origin of the fourfold symmetry at high fields is as yet unresolved in this family of compounds, it is clear that the geometry of the vortex lattice can change with reduced vortex-vortex interactions. Of course all of this



is irrelevant if the vortex lattice “freezes” in at high temperatures, as mentioned earlier.

Another serious problem with the two-component GL theory, is that it contains too many phenomenological parameters to be useful in fitting the measured internal field distributions. Recently, Affleck *et al.* [178] attempted to resolve these issues by generalizing the London model to include four-fold anisotropies in a tetragonal material. Starting from a GL free energy density with  $s$  and  $d$ -wave order parameters, they derived the corresponding London equation. For a magnetic field applied along the  $\hat{c}$ -axis, the field profile which is obtained may be written as [178]

$$B(\mathbf{r}) = B_0 \sum_{\mathbf{K}} \frac{\epsilon^{-i\mathbf{K}\cdot\mathbf{r}} \epsilon^{-K^2 \xi_{ab}^2/2}}{1 + K^2 \lambda_{ab}^2 + 4\epsilon \lambda_{ab}^2 \xi_{ab}^2 (K_x K_y)^2}, \quad (4.17)$$

where  $\epsilon$  is a dimensionless parameter which controls the strength of the coupling between the  $s$  and  $d$ -wave components. For  $\epsilon=0$ , Eq. (4.17) reduces to Eq. (4.10). Unfortunately, the vortex-lattice structure obtained by minimizing the Gibbs free energy of Eq. (4.15) depends on the choice of  $\epsilon$ , which cannot be determined independently.

Franz *et al.* [179] have recently developed a generalized London model derived from a simple microscopic model, which takes into account the nonlocal behaviour which occurs in the vicinity of the nodes in a  $d_{x^2-y^2}$ -wave superconductor. This modified London model predicts novel changes in the vortex-lattice geometry, including two first order phase transitions at low  $T$ . More recently, this work has been extended to account for both nonlinear and nonlocal effects as discussed earlier [40]. It is found that the nonlocal corrections are the dominant effect in determining the vortex-lattice geometry. In particular, the numerical calculations in Ref. [40] yield a nearly triangular vortex lattice. It should be noted, however, that the source term the authors used in the London equation was derived from the GL equations near  $H_{c2}$  [120], and is not theoretically valid for lower magnetic fields.

Shiraishi *et al.* [180] have studied the vortex lattice using the extended GL theory.

which includes the fourth-order derivative term and accounts for the finite size of the vortex cores. The fourfold symmetry of the vortex cores leads to a first order transition in the vortex-lattice geometry with increasing magnetic field. In particular, in weak fields the vortex lines form a triangular lattice which slowly transforms with increasing magnetic field, and then suddenly changes to a square lattice. Near  $T_c$  they predict a crossover field given by  $H_{cr} = 0.524H_{c2}(T/T_c)/(\sqrt{-\ln(T/T_c)}\kappa)$ .

The structure of a single isolated vortex in a pure  $d_{x^2-y^2}$ -wave superconductor has been calculated using the quasiclassical Eilenberger theory [181,182], which is valid at arbitrary temperature. A fourfold symmetry appears in the LDOS, the pair potential, the supercurrent and the magnetic field distribution around a vortex. The fourfold symmetry about the vortex center is strongest in the core region and gradually fades to circular symmetry toward the outer region. On the other hand, using an approximate version of the BdG equations Morita *et al.* [183] found that the LDOS around a single  $d_{x^2-y^2}$ -wave vortex has circular symmetry, and exhibits fourfold symmetry only when an  $s$ -wave component is mixed in. Franz and Ichioka [184] have since argued that the circular symmetry obtained by these authors is an unphysical artifact of the approximations used for the BdG equations. The BdG equations have been solved numerically for a vortex lattice of a  $d$ -wave superconductor [166,185]. Unfortunately, there are currently no calculations (in any formalism) of the vortex-lattice structure in a  $d_{x^2-y^2}$ -wave superconductor, which are valid at both low  $T$  and low  $H$  where experiments are generally performed.

Several authors [182,185,186] have suggested that the low-lying quasiparticle excitations cannot be bound in a  $d$ -wave vortex core because of the presence of the nodes. Rather than states which are localized in the core as in a  $s$ -wave superconductor, the states are peaked in the core region but extend along the node directions. According

to Ichioka *et al.* [182], in the vortex state of a  $d_{x^2-y^2}$ -wave superconductor the quasi-particles do not flow along conventional closed circular trajectories, but rather flow along open trajectories which connect with those of nearest-neighbor vortices. This theoretical model requires that the nodes lie along the line connecting nearest-neighbor vortices. In the absence of anisotropy, this implies that the nearest-neighbor direction must be  $45^\circ$ .

So far, experiments have not entirely resolved the issue of the vortex-lattice structure in the high- $T_c$  materials either. The major problem has been in determining how much of the observed vortex structure is directly attributable to the  $d_{x^2-y^2}$ -wave pairing state and how much is due to deformations of the lattice caused by extrinsic effects. Generally speaking, Bitter decoration experiments which image the vortex lattice at the sample surface indicate that the vortices arrange themselves to form a triangular lattice. For instance, Gammel *et al.* [187] observed a triangular lattice with long-range order in  $\text{YBa}_2\text{Cu}_3\text{O}_7$ . Decoration experiments by Dolan *et al.* [188] show a triangular lattice in  $\text{YBa}_2\text{Cu}_3\text{O}_7$ , with a slight distortion probably caused by the  $\hat{a}$ - $\hat{b}$  plane anisotropy. A triangular vortex lattice with long-range order was also observed by Vinnikov *et al.* [189] in  $\text{Tl}_2\text{Ba}_2\text{CaCu}_2\text{O}_x$  at  $T=0.04T_c$  and in  $\text{Bi}_2\text{Sr}_2\text{CaCu}_2\text{O}_{8+\delta}$  by Kim *et al.* [190] at high temperatures. Since the Bitter decoration technique is resolution limited to low magnetic fields, the results obtained may not be representative of the lattice structure at higher magnetic fields, particularly in a sample dominated by extrinsic effects.

The structure of the vortex lattice in the bulk of a superconductor can be investigated using small-angle neutron scattering (SANS). The pattern generated by neutrons scattering from the vortex lattice is the reciprocal lattice of the real-space vortex lattice. Large single crystals are generally required so that the diffracted neutron intensity is strong enough to clearly resolve the peaks resulting from Bragg reflection. The scattered intensity is proportional to the square of the spatial variation in the local magnetic

field, which is of the order  $\lambda^{-4}$  [191]. In principle, one can measure the temperature dependence of  $\lambda$  using SANS. The signal-to-noise ratio is reduced in samples which contain defects which scatter the neutrons in the same small angle as those scattered from the vortex lattice. In clean conventional superconductors like Nb and NbSe<sub>2</sub>, a perfect triangular lattice with long-range order is observed using SANS [165,192]. A triangular lattice has also been observed in the high- $T_c$  superconductor Bi<sub>2</sub>Sr<sub>2</sub>CaCu<sub>2</sub>O<sub>8+ $\delta$</sub>  at low temperatures [193]. On the other hand, resolving the vortex-lattice geometry in YBa<sub>2</sub>Cu<sub>3</sub>O<sub>7- $\delta$</sub>  has been more difficult. Forgan *et al.* [191] investigated the vortex lattice in small single crystals of YBa<sub>2</sub>Cu<sub>3</sub>O<sub>7</sub> up to fields of 0.6 T. Only diffraction spots corresponding to vortices parallel to the twin boundaries were strong. Relatively weak diffraction spots were observed in the other directions—which implies that the vortex lattice was non-uniform. A diffraction pattern with square symmetry was observed by Yethiraj *et al.* [194] in a SANS study of the vortex lattice in YBa<sub>2</sub>Cu<sub>3</sub>O<sub>7</sub>. The authors attribute the observed geometry to twin planes, since the intensity peaks are aligned along the (110) direction. More recently, Keimer *et al.* [195] studied the vortex lattice in a larger single crystal of YBa<sub>2</sub>Cu<sub>3</sub>O<sub>7</sub> for magnetic fields of 0.5 to 1.5 T applied along the crystallographic  $\hat{c}$ -axis, at  $T = 4.2$  K. These authors reported that the vortices form an oblique (fourfold symmetric) lattice with an angle of 73° between two nearly equal primitive vectors, and that one of the primitive vectors is oriented at an angle of 45° with respect to either the  $\hat{a}$  or  $\hat{b}$  axis. The alignment of one primitive vector of the oblique lattice with the (110) or (1 $\bar{1}$ 0) direction of the underlying crystal lattice was observed in four different orientational domains of the crystal. Walker and Timusk [196] noted that the vortex-lattice geometry observed in this SANS experiment is easily explained as a combination of strong pinning effects due to twin planes and the  $\hat{a}$ - $\hat{b}$  plane anisotropy in YBa<sub>2</sub>Cu<sub>3</sub>O<sub>7</sub>. In particular, an equilateral-triangular vortex lattice with one side aligned along a twin boundary, which is then stretched (due to

the  $\hat{a}$ - $\hat{b}$  plane anisotropy) along a line which makes a  $45^\circ$  angle with the twin boundary, yields the observed vortex-lattice geometry.

An oblique lattice was also found in STM measurements performed by Maggio-Aprile *et al.* [197] on the (001) surface of twinned  $\text{YBa}_2\text{Cu}_3\text{O}_{7-\delta}$ , at  $H = 6$  T and  $T = 4.2$  K. Consistent with the SANS results, they report an angle of  $77^\circ$  between nearly equal primitive vectors—although they could not determine the orientation of the vortex lattice with respect to the crystal lattice. The oblique lattice imaged in this experiment was only observed locally, with no apparent long-range order. These authors also report that the vortex cores are ellipsoidal in shape with the ratio of the principle axes being about 1.5. The elongation of the cores is consistent with the  $\hat{a}$ - $\hat{b}$  plane anisotropy in  $\text{YBa}_2\text{Cu}_3\text{O}_{7-\delta}$ —*i.e.* other than this anisotropy the vortex cores appear to be approximately circular. As is the case for the SANS experiments, the geometry of the observed vortex lattice can also be explained as a combination of the  $\hat{a}$ - $\hat{b}$  plane anisotropy and an alignment of vortex lines with twin boundaries. Thus in a detwinned or sparsely twinned sample of  $\text{YBa}_2\text{Cu}_3\text{O}_{7-\delta}$ , it is likely that the vortex lattice is triangular at moderate magnetic fields.

There are several serious discrepancies between the current experiments on high- $T_c$  superconductors in the vortex state and the theoretical models for the vortex lattice of a  $d_{x^2-y^2}$ -wave superconductor:

1. None of the current theoretical models can explain, in terms of an intrinsic mechanism, both the vortex-lattice geometry (observed in the SANS and STM experiments on  $\text{YBa}_2\text{Cu}_3\text{O}_{7-\delta}$ ) and the orientation of the vortex lattice with respect to the crystallographic axis (observed in SANS experiments in  $\text{YBa}_2\text{Cu}_3\text{O}_{7-\delta}$ ). To fully understand the influence that the symmetry of the pairing state has on the vortex-lattice geometry, it will be necessary to perform imaging experiments on

untwinned crystals and/or tetragonal superconductors.

2. The STM image of the vortex core on  $\text{YBa}_2\text{Cu}_3\text{O}_{7-\delta}$  by Maggio-Aprile *et al.* [197] does not show the fourfold anisotropy predicted for the LDOS near a  $d_{x^2-y^2}$ -wave vortex.
3. Experiments performed on both  $\text{YBa}_2\text{Cu}_3\text{O}_{7-\delta}$  [197,198] and  $\text{Nd}_{1.85}\text{Ce}_{0.15}\text{CuO}_{4-\delta}$  [199] are more consistent with a picture in which a few bound quasiparticle states exist in the vortex core—which contradicts the idea that the low-lying quasiparticle excitations cannot be bound in a  $d_{x^2-y^2}$ -wave vortex core because of the nodes. For instance, in the STM experiment on  $\text{YBa}_2\text{Cu}_3\text{O}_{7-\delta}$  [197] two peaks separated by about 11 meV were observed in the differential conductance  $dI/dV$  (*i.e.* the LDOS) measured at the center of a vortex core. A natural interpretation of this result is that these peaks correspond to the lowest bound quasiparticle energy levels.

Franz and Tešanović [186] have recently attempted to address some of these issues by proposing a mixed  $d_{x^2-y^2} + id_{xy}$  pairing state. For this symmetry there is a finite energy gap everywhere at the Fermi surface so that bound quasiparticle states can exist. Within a BdG formalism these authors predict near spatially-isotropic bound quasiparticle states—however, the size of the  $d_{xy}$  component required to reproduce the gap observed in the tunneling conductance at the center of the vortex core in Ref. [197] may be difficult to reconcile with other experiments. For instance, the linear- $T$  dependence of  $\lambda_{ab}$  found in our own  $\mu\text{SR}$  studies of  $\text{YBa}_2\text{Cu}_3\text{O}_{7-\delta}$  in the vortex state [2.3.5] imply that any finite gap which opens along the node directions cannot be too large.

Given the anomalous normal state properties in the high- $T_c$  compounds, it is quite reasonable to expect deviations from the conventional picture of a vortex core in these

materials. One such novel description is the prediction from  $SO(5)$  theory for the existence of a superconducting vortex with an antiferromagnetic core in underdoped high- $T_c$  compounds [200,201]. Recently, we have investigated this possibility in a  $\mu$ SR study of  $\text{YBa}_2\text{Cu}_3\text{O}_{6.57}$  (Ref. [202]). However, neither this study or any other has produced clear evidence for the existence of antiferromagnetism in the vortex core.

With experiment and theory in apparent disagreement, it seems reasonable to model the vortex lattice in the simplest possible manner. Furthermore, it does not matter whether theory predicts a fourfold symmetric vortex lattice for  $\text{YBa}_2\text{Cu}_3\text{O}_{7-x}$ , if pinning “freezes in” the threefold (triangular) lattice just below  $T_c$ . In this thesis, the contribution of the vortex lattice to the measured  $\mu$ SR line shape will be modelled with both Brandt’s modified London model [see Eq. (4.10)] and Yaouanc’s version of Hao’s analytic solution to the GL equations [see Eq. (4.13)]. The primary advantage of using these phenomenological models is that they contain a manageable number of parameters for fitting the  $\mu$ SR spectra. In addition, both models are conveniently valid at low reduced fields  $b$  where  $\mu$ SR experiments are generally performed. I will show in this study that fitting to these models yields a good description of the  $T$  and  $H$ -dependences of the fundamental length scales  $\lambda$  and  $\xi$  (*i.e.*  $r_0$ ) in both conventional and unconventional superconductors.

## Chapter 5

### Experimental Details

This chapter begins by describing the novel  $\mu$ SR apparatus used for the experiments contained in this thesis. This is followed by a discussion of the characteristics of the compounds studied.

#### 5.1 The Apparatus

A novel low background apparatus [204] was employed to greatly suppress the signal originating from muons which miss the sample. Previous  $\mu$ SR studies have been plagued by a large background signal which contributes significant spectral weight to the measured line shape. This has been a problem particularly for the high- $T_c$  compounds because of the small size of good quality samples. For instance, the ratio of the cross-sectional area of the sample to the beam spot area is typically 1/3. Since the average magnetic field of the background signal is close to the average field in the sample, the background signal always appears near the middle of the measured internal field distribution of the sample.

The experimental arrangement is shown in Fig. 5.1. The crystals were mounted on a thin piece of aluminized Mylar stretched over a hollow cylindrical aluminum sample holder. A small amount of Apiezon N grease was used to attach the crystals to the Mylar. The crystals were mounted so that their  $\hat{c}$ -axes were parallel to the magnetic field



and muon beam directions. The muons were injected with their initial spin polarization  $\mathbf{P}(t=0)$  perpendicular to the magnetic field direction. A thin scintillation counter ( $M$ ) was used to detect the incoming muons. The signal from the  $M$  counter started a clock provided that no muon had entered the sample in the previous time interval ( $\sim 11 \mu s$ ). The clock stopped when a decay positron was detected. A cup-shaped veto counter ( $V$ ) placed behind the sample was used to suppress the unwanted background signal from muons which missed the sample. The decay positrons from muons stopping in the sample were detected by overlapping cylindrical forward ( $F$ ) and backward ( $B$ ) counters. As shown in the lower illustration of Fig. 5.1, the  $F$  and  $B$  counters consisted of four individual counters  $F_1, F_2, F_3, F_4$  and  $B_1, B_2, B_3, B_4$ , respectively. A valid muon stop was defined as  $M \cdot \bar{V}$  and a valid positron event was defined as  $F_i \cdot B_i \cdot \bar{V}$  where  $i = 1, 2, 3$  or  $4$ . The dashed lines in the top illustration of Fig. 5.1 show the solid angle subtended by the overlapping  $F$  and  $B$  counters. Note that the arrangement of the  $F, B$  and  $V$  counters is such that decay positrons originating from muons which miss the sample and stop in the back of the  $V$  counter are rejected. Since these “bad” muons register neither a valid muon stop nor a valid decay positron, they are logically excluded from the experiment.

The sample and veto counter were contained within a horizontal  $^4\text{He}$  gas-flow cryostat. The  $\mu\text{SR}$  time spectra in this study were recorded under conditions of field cooling (*i.e.* cooled below  $T_c$  in an applied magnetic field). Typically each spectrum consisted of  $2 \times 10^7$  “good” muon decay events. The measurements were performed on either the M15 or the M20 beam line at TRIUMF, each of which produces a beam of spin-polarized positive muons of mean momentum 28 MeV/c.

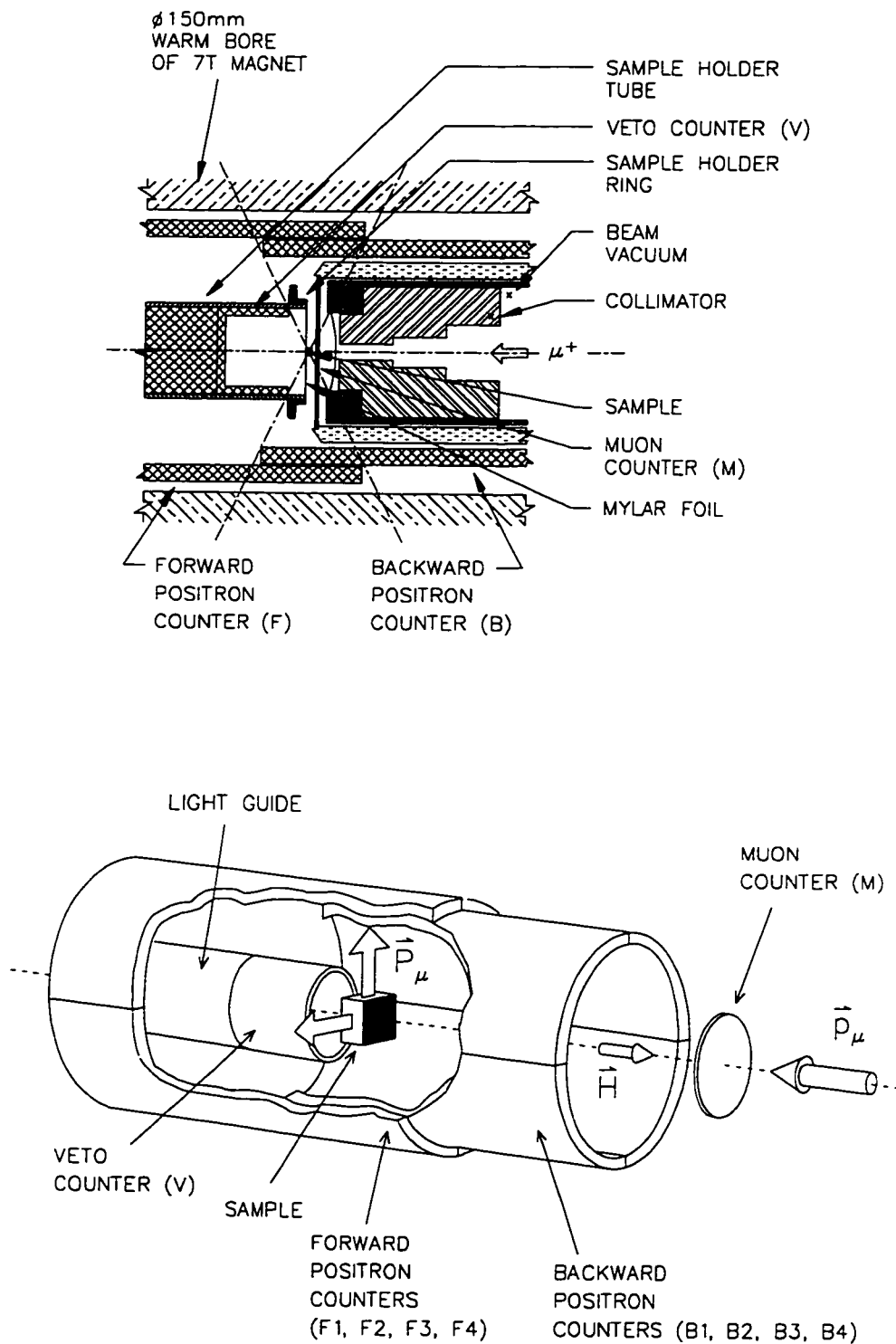


Figure 5.1: The low background  $\mu$ SR apparatus. The sample and veto counter (V) are contained within a cryostat which is not shown for clarity. The lower figure shows the arrangement of the positron and muon counters in 3 dimensions.

## 5.2 The Samples

The structure of the NbSe<sub>2</sub> single crystal used in this thesis is shown in Fig. 5.2. The precise chemical formula is 2H-NbSe<sub>2</sub>. The numeral 2 indicates the number of layers in a unit cell, while the capital letter H indicates the type of crystal symmetry (*i.e.* H stands for hexagonal). Each layer is a “sandwich” of two layers of Se atoms with a layer of metallic Nb atoms between them. The Nb and Se atoms within a sandwich are covalently bonded, and these atoms form a 2D-hexagonal lattice. The NbSe<sub>2</sub> layers are weakly coupled by van der Waals forces. As a result, the mechanical and electrical properties of 2H-NbSe<sub>2</sub> are extremely anisotropic. For instance, this material is very easy to cleave along a plane parallel to the layers. This feature makes NbSe<sub>2</sub> ideal for studies of the vortex lattice using surface techniques (such as STM) since clean, fresh, smooth surfaces are easily obtained. The 2D nature of the electronic properties in NbSe<sub>2</sub> is similar to that in YBa<sub>2</sub>Cu<sub>3</sub>O<sub>7- $\delta$</sub> . Electrons can move freely within the layers, however the overlap of the electron wave functions between the layers is small. Consequently, the conductivity perpendicular to the layers is several orders of magnitude smaller than that within the layers.

The NbSe<sub>2</sub> single crystal was grown by a standard vapour transport technique as discussed in Ref. [83]. The characteristics of this sample are listed in Table 5.1. The near zero-field  $T_c$  was 7.0 K with a transition width less than 0.1 K, determined from magnetization measurements. The upper critical field was also measured with magnetization and is roughly described by the relation  $H_{c2}(T) = H_{c2}(0)[1 - t^p]$ , where  $t = T/T_c$ ,  $H_{c2}(0) = 3.5$  T and  $p = 1.55$ .

Figure 5.3 shows the unit cell of the fully oxygenated compound YBa<sub>2</sub>Cu<sub>3</sub>O<sub>7</sub>. The unit cell is orthorhombic with dimensions  $a = 3.83$  Å,  $b = 3.88$  Å and  $c = 11.68$  Å. The layers containing the Cu(2) and O(3) sites are often referred to as the “CuO<sub>2</sub> planes”.

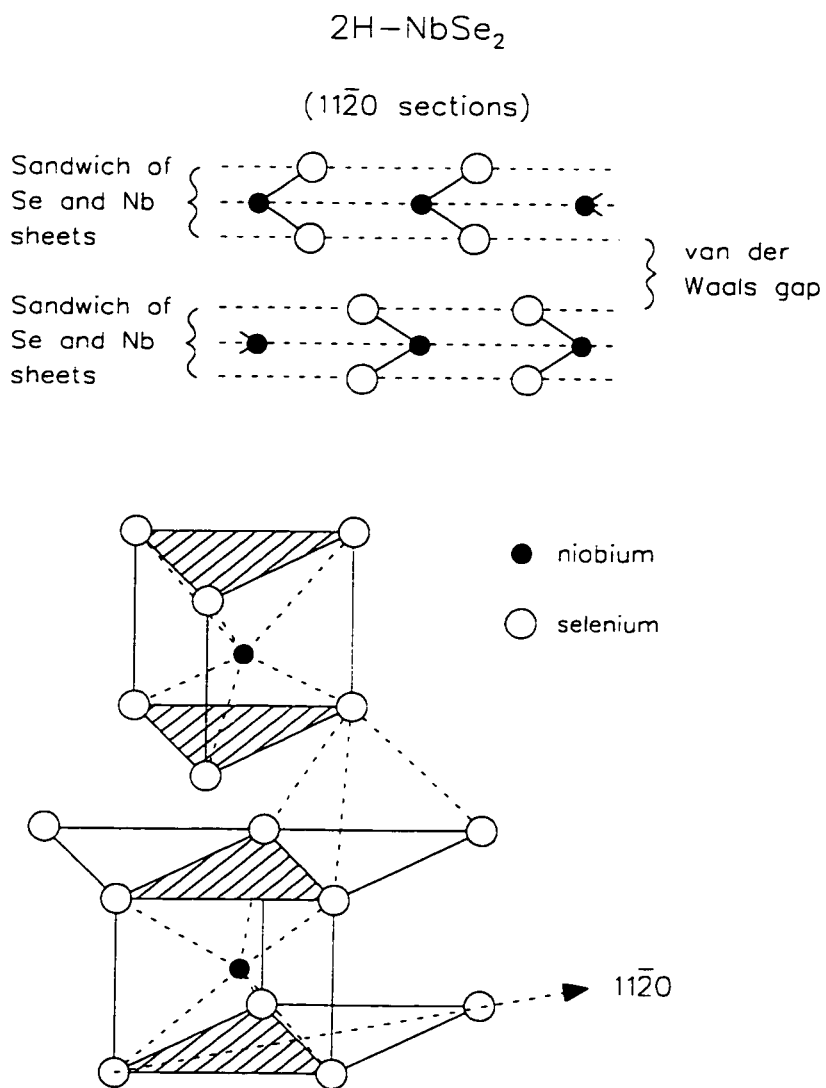
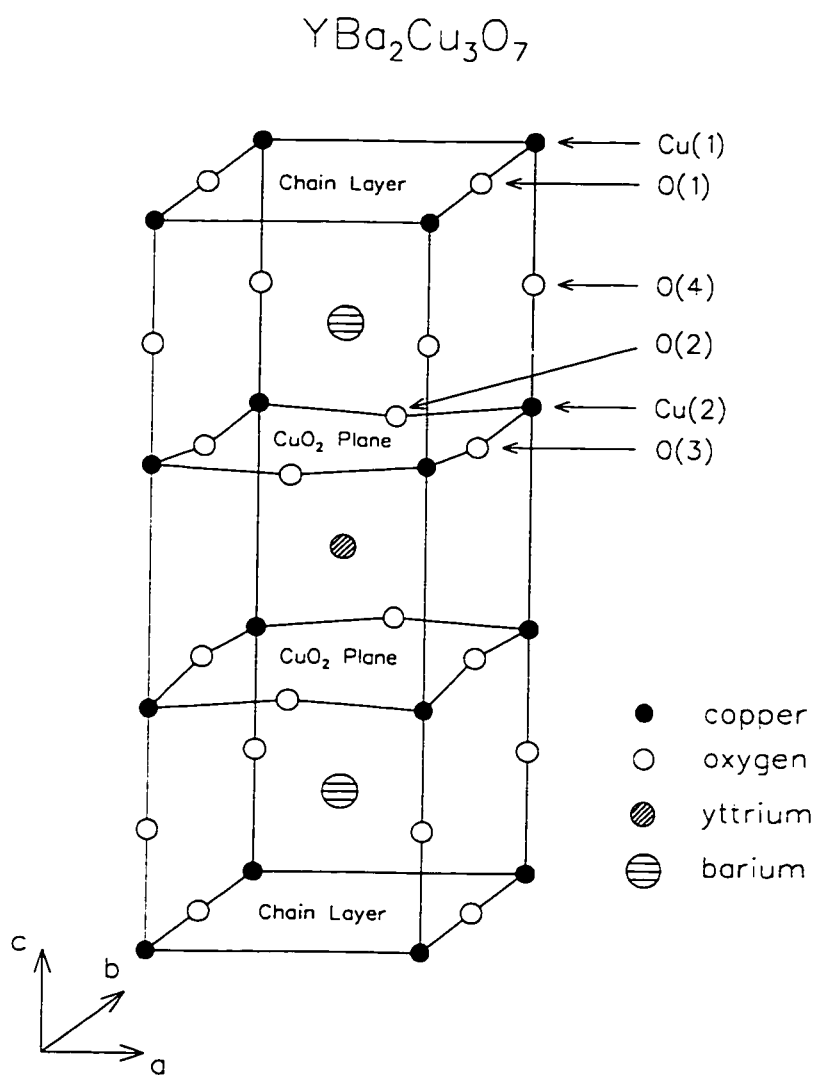


Figure 5.2: Top: Structure of the layers in  $2H-NbSe_2$  (shown in the  $11\bar{2}0$  plane). bottom: Structure of  $2H-NbSe_2$  in three dimensions.

Figure 5.3: The unit cell of  $\text{YBa}_2\text{Cu}_3\text{O}_7$ .

whereas the layers containing the Cu(1) and O(1) sites along the  $\hat{b}$ -axis are commonly referred to as the “chain layers”. The O(2) and O(3) sites in the  $\text{CuO}_2$  planes are almost always occupied. Deoxygenation involves the removal of oxygen primarily from the O(1) sites.

The most significant improvement in experimental studies of  $\text{YBa}_2\text{Cu}_3\text{O}_{7-\delta}$  in recent years is the availability of high-quality single crystals. The single crystals used in the present study were grown at the University of British Columbia (UBC) by a flux method in yttria-stabilized-zirconia (YSZ) crucibles [203]. The purity of the UBC crystals has been determined to be greater than 99.5%. The impurities which are present in the crystals originate from corrosion of the crucibles. The characteristics of the  $\text{YBa}_2\text{Cu}_3\text{O}_{7-\delta}$  samples used in the present study are summarized in Table 5.1. The transition temperatures were determined by low-field magnetization measurements. All samples were on the order of 0.1 mm thick. The high quality of these crystals has been verified by other characterization methods, namely resistivity, microwave surface resistance and heat capacity measurements (see Ref. [203]).

Hole doping in  $\text{YBa}_2\text{Cu}_3\text{O}_{7-\delta}$  is primarily controlled by adding or removing oxygen in the O(1) sites in the CuO chain layers. The local oxygen configuration is highly sensitive to the temperature and oxygen partial pressure in the annealing process. Impurities tend to impede the mobility of some of the oxygen. Thus, the most uniform oxygen configuration can be achieved in the purest crystals. The highest value of  $T_c$  is obtained with  $\delta \approx 0.05$ , so that  $\text{YBa}_2\text{Cu}_3\text{O}_{6.95}$  will frequently be referred to in this thesis as the “optimally doped” compound. Note that there are still some oxygen vacancies at this doping level which may act as pinning sites for vortex lines. At  $\delta = 0.4$ , every other CuO chain in a chain layer is essentially empty. The compound  $\text{YBa}_2\text{Cu}_3\text{O}_{6.60}$  will often be referred to as the “underdoped” compound.

| Sample Name | Chemical Formula                                   | Number of Crystals | $T_c$<br>[K] | Total Mass<br>[mg] | Surface Area<br>[mm <sup>2</sup> ] | Detwinned | Ref.  |
|-------------|--|--------------------|--------------|--------------------|------------------------------------|-----------|-------|
| O1          | YBa <sub>2</sub> Cu <sub>3</sub> O <sub>6.95</sub> | 3                  | 93.2(0.25)   | 53                 | 36                                 | no        | [2,3] |
| O2          | YBa <sub>2</sub> Cu <sub>3</sub> O <sub>6.95</sub> | 1                  | 93.2(0.25)   |                    | 25                                 | no        | [3]   |
| O3          | YBa <sub>2</sub> Cu <sub>3</sub> O <sub>6.95</sub> | 1                  | 93.2(0.25)   |                    | 25                                 | yes       |       |
| U1          | YBa <sub>2</sub> Cu <sub>3</sub> O <sub>6.60</sub> | 3                  | 59.0(< 0.1)  | 53                 | 36                                 | no        | [5]   |
| U2          | YBa <sub>2</sub> Cu <sub>3</sub> O <sub>6.60</sub> | 2                  | 59.0(< 0.1)  |                    | 30                                 | yes       | [5]   |
| NB          | NbSe <sub>2</sub>                                  | 1                  | 7.0(< 0.1)   | 43                 | 30                                 | no twins  | [4]   |

Table 5.1: Sample characteristics.

To remove the twin planes, some of the samples were mechanically detwinned and subsequently reannealed to set the oxygen doping level. Sample O3 was completely free of twins after this process. However, some of the twin planes reformed in sample U2 when reannealed. The separation between the twin boundaries in U2 was on the order of  $10^4$  Å, which is substantially larger than the spacing between vortex lines for the field range considered in this study.

### 5.3 General Comments on the Fitting Procedure

All of the  $\mu$ SR spectra were fit in the time domain. In particular, the real and imaginary parts of the corrected asymmetry were simultaneously fit in a rotating reference frame as explained in Chapter 3. The spectra were fit with the following nine variable parameters:

1.  $A_s^\circ$ : the maximum precession amplitude of the corrected asymmetry for the signal originating from within the sample.

2.  $\nu_\mu$ : the average precession frequency of the muon spin in the sample [*i.e.*  $\nu_\mu = (\gamma_\mu/2\pi)B_0$ , where  $B_0$  is the average internal field in Eq. (4.13)].
3.  $\theta$ : the initial phase of the muon spin polarization vector.
4.  $\sigma_f$ : the effective depolarization rate due to random disorder in the vortex lattice and nuclear dipolar moments in the sample [see Eq. (3.24)].
5.  $A_{\text{bkgd}}^\circ$ : the maximum precession amplitude of the corrected asymmetry for the residual background signal (as will be explained in Chapter 6, the residual background signal was fit assuming a Gaussian broadened distribution of magnetic fields).
6.  $\sigma_{\text{bkgd}}$ : the depolarization rate corresponding to the residual background signal.
7.  $\nu_{\text{bkgd}}$ : the average precession frequency of the muon spin due to the average field  $B_{\text{bkgd}}$  of the background signal.
8.  $\lambda_{ab}$ : see Eq. (4.13).
9.  $\xi_{ab}$ : see Eq. (4.13).

The sum over reciprocal lattice vectors in Eq. (4.13) was carried out by sampling 2814 evenly spaced points in the triangle formed by three adjacent vortices. Significant changes in the fitted parameters was found for sums less than 1626 points, whereas an increase in the sum to 4902 reciprocal lattice points changed the fitted value of  $\lambda_{ab}$  by less than 1 %.

In all cases the first 6  $\mu\text{s}$  of the time spectrum were fit. There was essentially no change in the fitted parameters corresponding to the sample signal when the time range was increased to 10  $\mu\text{s}$ . The raw data was binned so that there were approximately



1200 data points (*i.e.* 600 in the imaginary part and 600 in the real part of the corrected asymmetry spectrum). Doubling the bin size (to reduce the total number of data points to about 600) did not change the fitted value of  $\lambda_{ab}$  and changed the fitted value of  $\xi_{ab}$  by no more than 3 % in  $\text{YBa}_2\text{Cu}_3\text{O}_{6.95}$ .

## Chapter 6

### Experiment: NbSe<sub>2</sub>

In this chapter, recent  $\mu$ SR measurements of the  $\hat{a}$ - $\hat{b}$  plane magnetic penetration depth  $\lambda_{ab}$  and the vortex core radius  $r_0$  in the conventional type-II superconductor NbSe<sub>2</sub> are presented.

Figures 6.1 and 6.2 show the Fourier transforms of the muon precession signal in NbSe<sub>2</sub> as functions of temperature and applied magnetic field, respectively. The horizontal axes are in terms of the internal magnetic field  $B$  relative to the average field of the background signal  $B_{\text{bkgd}}$ , which by definition is centered at 0 G. As the temperature or magnetic field is lowered, the line shape broadens and the high-field tail becomes longer due mainly to a decrease in  $\lambda_{ab}$ . The high-field cutoff is clearly visible in all of the measured line shapes for NbSe<sub>2</sub>. This implies that the vortex cores occupy a significant volume of the sample. This fractional volume depends on both the size of the vortex cores and the areal density of vortices.

In order to test the effects of the analysis procedure on the determined behaviour of  $\lambda_{ab}$  and  $\xi_{ab}$ , three different models for the theoretical internal field distribution corresponding to the vortex lattice were considered:

1. the modified London (ML) model given in Eq. (4.10) with a Gaussian cutoff factor  $\exp(-K^2\xi_{ab}^2/2(1-b))$ .
2. the ML model with a Lorentzian cutoff factor  $\exp(-\sqrt{2}K\xi_{ab}/\sqrt{1-b})$ .

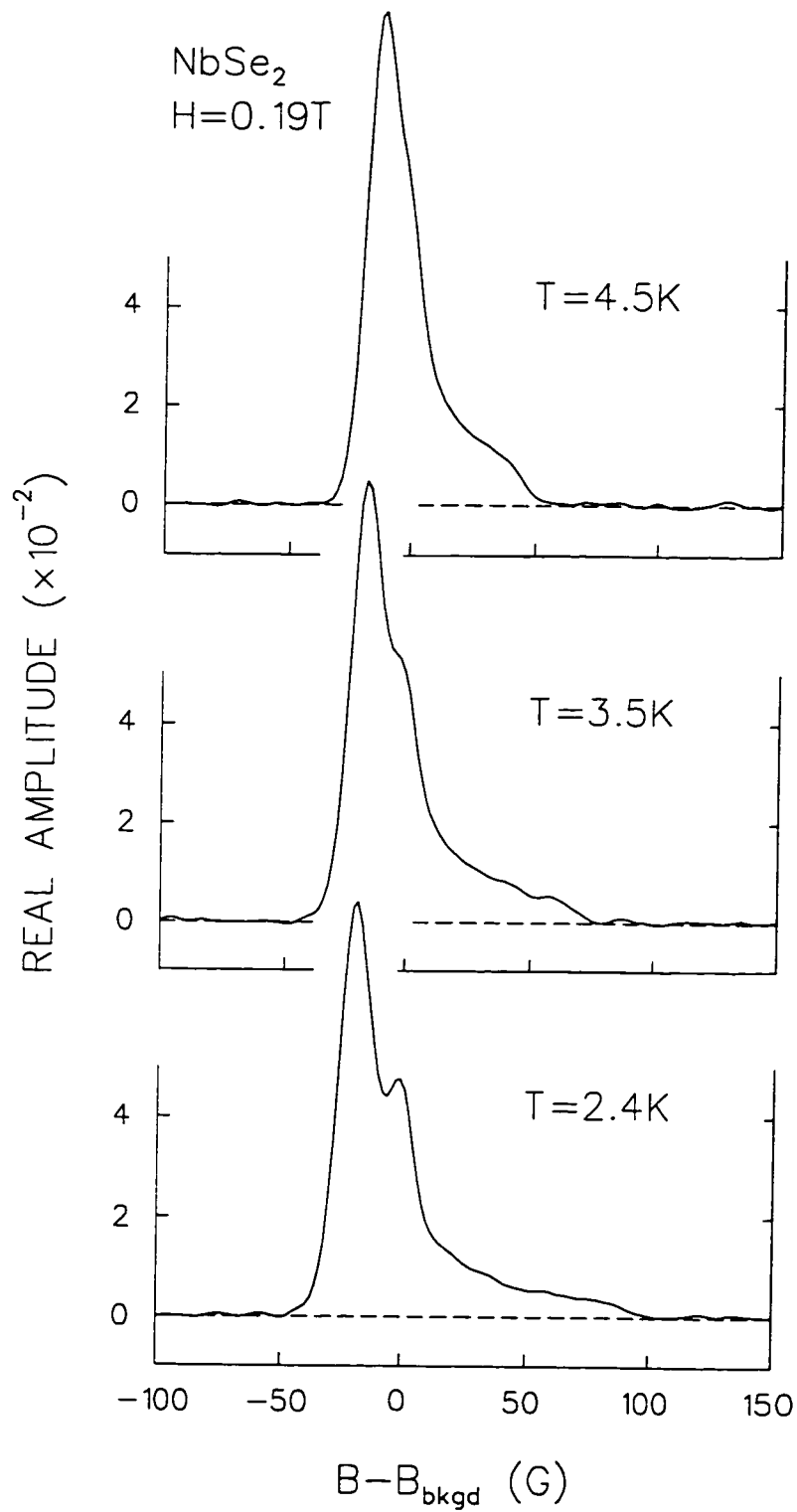


Figure 6.1: Fourier transforms of the muon spin precession signals in  $\text{NbSe}_2$  after field cooling to  $T = 4.5$ ,  $3.5$  and  $2.4$  K in a magnetic field  $H = 0.19$  T. The average magnetic field of the residual background signal is centered at  $B - B_{\text{bkgd}} = 0$  G.

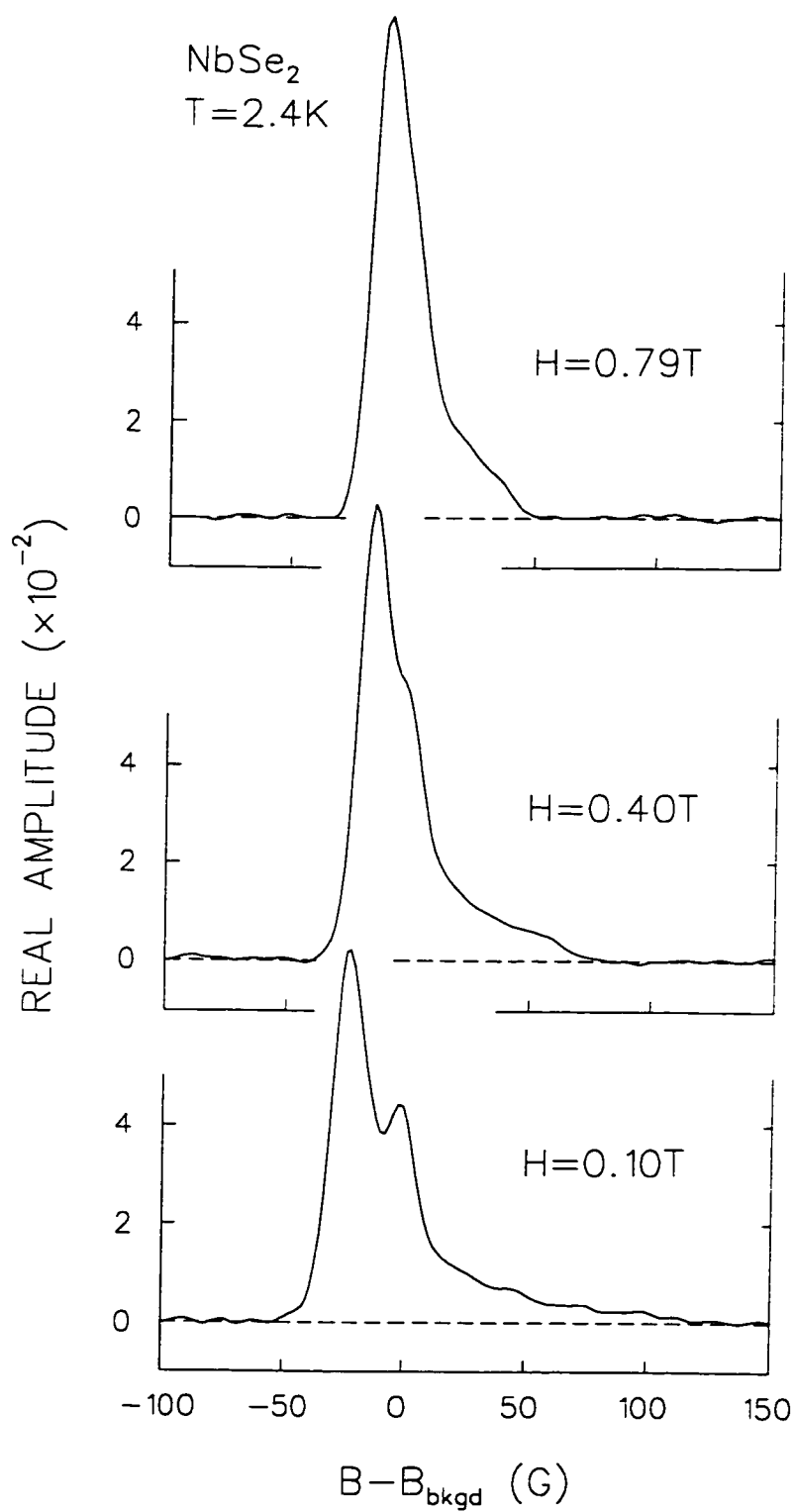


Figure 6.2: Fourier transforms of the muon spin precession signals in  $\text{NbSe}_2$  after field cooling to  $T = 2.4\text{K}$  in magnetic fields of  $H = 0.79, 0.40$  and  $0.10\text{T}$ .

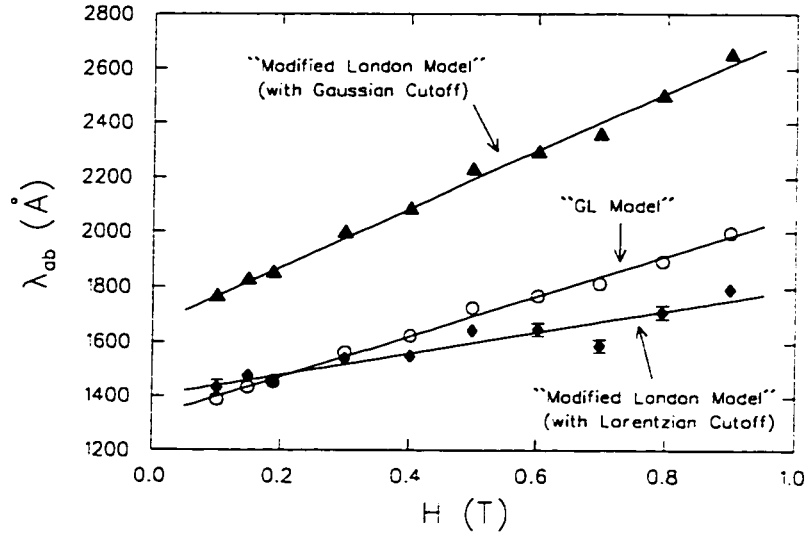


Figure 6.3: The magnetic field dependence of  $\lambda_{ab}(H)$  at  $T = 0.33 T_c$  in NbSe<sub>2</sub>, determined from fits to three different models for the field profile  $B(\mathbf{r})$  of the vortex lattice. The solid line fits are described in the text.

3. the analytical GL model given in Eq. (4.13).

In all three cases, a triangular vortex lattice was assumed. The cutoff factors assume circular symmetry, so that within these models a sixfold symmetry around a vortex line is generated solely from vortex-vortex interactions. The theoretical muon polarization function  $\tilde{P}(t)$  is generated by assuming a field profile given by one of these three models, and then multiplying by a Gaussian relaxation function  $G(t) = \exp(-\sigma_f^2 t^2 / 2)$  to account for random disorder in the vortex lattice and the contribution of the nuclear dipolar moments. In addition, a Gaussian broadened distribution of fields with width  $\sigma_{\text{bkgd}}$  and average field  $B_{\text{bkgd}}$  was used to fit the residual background signal independently.

Figure 6.3 shows the magnetic field dependence of  $\lambda_{ab}$  at  $T = 0.33 T_c$  (*i.e.*  $T = 2.3$  K) obtained by fitting the  $\mu$ SR time spectra with a polarization function which assumes one of the three models for the field distribution due to the vortex lattice. From

| Model for $B(\mathbf{r})$    | $\lambda_{ab}(0)$ [Å] | $\beta$ |
|------------------------------|-----------------------|---------|
| <i>ML: Gaussian Cutoff</i>   | 1659(1)               | 1.85(4) |
| <i>ML: Lorentzian Cutoff</i> | 1398(2)               | 0.81(3) |
| <i>Analytical GL Model</i>   | 1323(2)               | 1.62(3) |

Table 6.2: Parameters from fits of  $\lambda_{ab}(H, T = 0.33T_c)$  to Eq. (6.1) for NbSe<sub>2</sub>.

magnetization measurements.  $H_{c2}(0.33 T_c) = 2.9$  T, so that the results extend over the field range  $0.03 < h < 0.31$ , where  $h = H/H_{c2}$ . A clear linear  $H$ -dependence for  $\lambda_{ab}(H)$  is obtained for all three types of analysis, although there is some difference in the absolute value of  $\lambda_{ab}(H)$  and the strength of the linear term. The solid lines in Fig. 6.3 are fits to the linear relation

$$\lambda_{ab}(H) = \lambda_{ab}(0)[1 + \beta h]. \quad (6.1)$$

The results of these fits are given in Table 6.2. At low magnetic fields there is good agreement between the ML model with a Lorentzian cutoff factor and the analytic GL model. This is reasonable since the Lorentzian cutoff is strictly valid only at low reduced fields  $b = B/B_{c2}$ . On the other hand, the ML model with a Gaussian cutoff gives a significantly higher value for  $\lambda_{ab}$ . The Gaussian cutoff is derived from the solution of the GL equations near  $B_{c2}$  and is thus not valid at low reduced fields. Unfortunately, a Gaussian cutoff was used in some of our earlier work [2.3.50] and in various theoretical studies by others.

Figure 6.4 shows the magnetic field dependence of the quality of the fits at  $T = 0.33 T_c$ , obtained for the three different models. The ratio of  $\chi^2$  to the number of

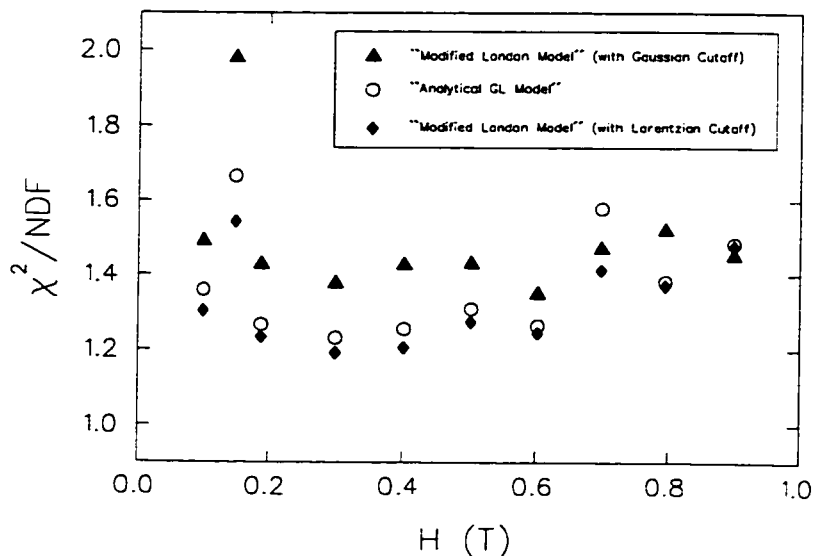


Figure 6.4: The ratio of  $\chi^2$  to the number of degrees of freedom (NDF) at  $T = 0.33 T_c$  in NbSe<sub>2</sub>, determined from fits to three different models for the field profile  $B(\mathbf{r})$  of the vortex lattice.

degrees of freedom (NDF) is significantly greater than 1.0 in most cases due to the high statistics of the measured magnetic field distribution. For a non-perfect fit, higher statistics magnify the value of  $\chi^2$ . Fits to the ML model with a Gaussian cutoff generally yield the worst  $\chi^2$  value. On the other hand, fits assuming a Lorentzian cutoff are only slightly better than fits to the analytical GL model.

Figure 6.5 shows, in the frequency domain, how the quality of the fits obtained (in the time domain) from the ML model using a Gaussian cutoff factor and from the analytical GL model are virtually indistinguishable. One would expect the results from these two models to converge at higher magnetic fields. However, as shown in Fig. 6.3,  $\lambda_{ab}(H)$  determined for the two different models appear to diverge slowly at high  $H$ . The reason is that the analytical GL model deviates significantly from the exact numerical GL solutions at high reduced fields [121], and also, according to Brandt [123], the ML

model is really only applicable when  $b < 0.25$ .

Despite the quantitative differences between the three phenomenological models, which is related to their validity in different field ranges, the finding of a linear- $H$  dependence for  $\lambda_{ab}(H)$  is common to all. Since the analytical GL model properly accounts for the finite size of the vortex cores and our measurements are taken essentially at low reduced fields (especially in the case of YBa<sub>2</sub>Cu<sub>3</sub>O<sub>7- $\delta$</sub>  which we consider later) the results obtained using this model should most faithfully reflect the behaviour of the fundamental length scales. Unless otherwise stated, results presented in the remainder of this thesis were obtained assuming this model.

Figure 6.6 shows a comparison between  $\lambda_{ab}(H)$  in NbSe<sub>2</sub> at two different temperatures. A linear- $H$  dependence is observed between  $T = 0.33 T_c$  and  $0.6 T_c$ . The field dependence at lower  $T$  was not investigated because the <sup>4</sup>He gas flow cryostat limited us to temperatures above  $T = 2.3$  K. In the Meissner state of a conventional  $s$ -wave superconductor,  $\lambda_{ab}$  is expected to increase quadratically as a function of magnetic field, due to nonlinear effects. The nonlinear corrections to the supercurrent response are the same in both the Meissner and vortex states. However, the average supercurrent density  $\langle J_s \rangle = (c/4\pi) \langle |\nabla \times \mathbf{B}(\mathbf{r})| \rangle$  scales quite differently in the Meissner and vortex states, as shown in Fig. 6.7. The curve in the top panel of Fig. 6.7 (*i.e.* the Meissner state) was generated assuming that the magnetic field decays exponentially [see Eq. (2.15)] and that  $\lambda$  is field independent. Thus in the Meissner state,  $\langle J_s \rangle \propto H$ . It follows that if  $\lambda_{ab} \propto H^2$ , then  $\langle J_s \rangle \propto \sqrt{\lambda_{ab}}$ .

The solid curve in the bottom panel of Fig. 6.7 (*i.e.* the vortex state) was generated with the field profile  $B(\mathbf{r})$  from the analytical GL model. The dashed curve in this figure shows that the average supercurrent density in the vortex state is approximately proportional to  $H^{0.44} \approx \sqrt{H}$ . Thus, if  $\langle J_s \rangle \propto \sqrt{H}$  and  $\lambda_{ab} \propto H$  (as measured here), then



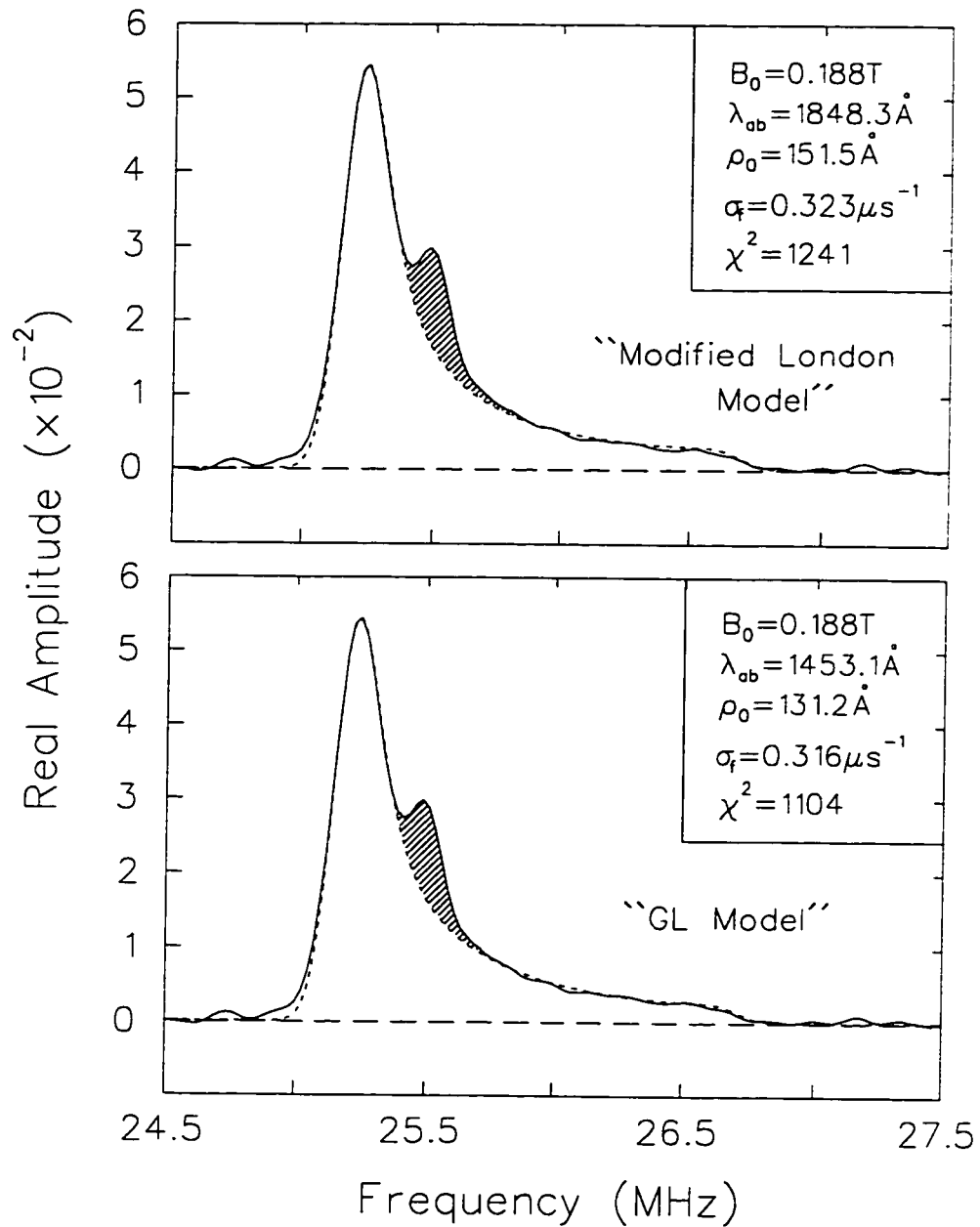


Figure 6.5: Fourier transforms of the muon spin precession signal in NbSe<sub>2</sub> after field cooling in a magnetic field  $H = 0.188$  T down to  $T = 0.33 T_c$ . The dashed curve is the Fourier transform of the simulated muon polarization function which best fits the data assuming the ML model with a Gaussian cutoff factor (top panel) and the analytical GL model (lower panel). The shaded region is the residual background signal.

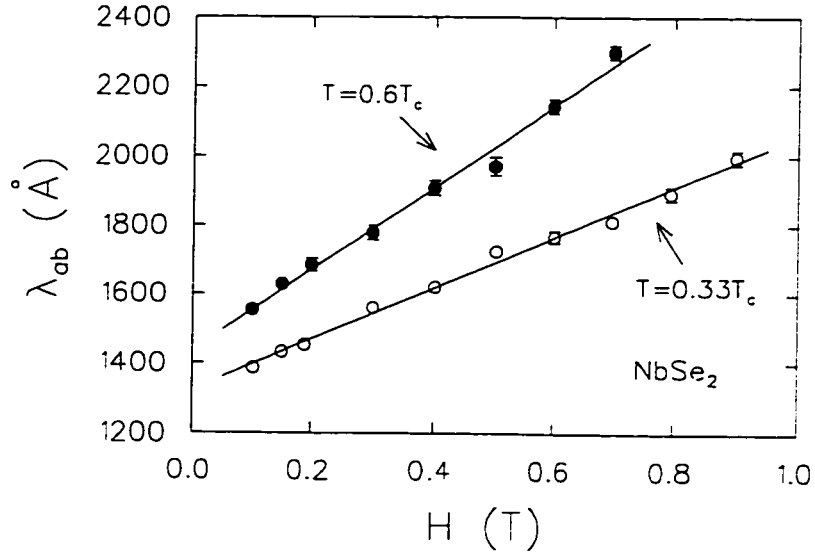


Figure 6.6: The magnetic field dependence of  $\lambda_{ab}(H)$  in the vortex state of  $\text{NbSe}_2$  at  $T = 0.33 T_c$  (open circles) and  $T = 0.6 T_c$  (solid circles). The solid line fits are described in Table 6.3.

as in the Meissner state  $\langle J_s \rangle \propto \sqrt{\lambda_{ab}}$ . This suggests that the field dependence of  $\lambda_{ab}$  in the vortex state of  $\text{NbSe}_2$  is due to nonlinear effects. However,  $\lambda_{ab}$  measured in our  $\mu\text{SR}$  experiment is by definition not the same as the penetration depth which appears in the nonlinear theory or which is measured in the Meissner state. Relating  $\lambda$  from the nonlinear theory to the effective  $\lambda_{ab}$  measured by  $\mu\text{SR}$  is nontrivial and requires a proper account of the vortex source term.

In the vortex state, the strength of the term which is linear in  $H$  is almost the same at both temperatures considered, when normalized with respect to the value of  $H_{c2}(T)$  (see parameter  $\mathcal{J}$  in Table 6.3). As the temperature is increased, the energy gap in the quasiparticle excitation spectrum shrinks, leading to the thermal excitation of quasiparticles. The reduction in the size of the energy gap also means that quasiparticles can be excited by relatively smaller magnetic fields. For this reason, in the Meissner state,

| Equation   | $T = 0.33T_c$            |          | $T = 0.6T_c$             |          |
|--|--------------------------|----------|--------------------------|----------|
|  | $\lambda_{ab}(0)$<br>[Å] | $\beta$  | $\lambda_{ab}(0)$<br>[Å] | $\beta$  |
| $\lambda_{ab}(H) = \lambda_{ab}(0)[1 + \beta h]$ | 1323(2)                  | 1.62(3)  | 1436(3)                  | 1.56(2)  |
| $\kappa(H) = \kappa(0)[1 + \eta h]$              | $\kappa(0)$              | $\eta$   | $\kappa(0)$              | $\eta$   |
|  | 8.4 (2)                  | 7.4 (2)  | 5.7(2)                   | 8.2(3)   |
| $\kappa'(H) = \kappa'(0)[1 + \gamma h]$          | $\kappa'(0)$             | $\gamma$ | $\kappa'(0)$             | $\gamma$ |
|  | 6.9(2)                   | 9.5(3)   | 5.1(2)                   | 10.2(4)  |

Table 6.3: Magnetic field dependence of parameters from fits to the NbSe<sub>2</sub> data using the analytical GL model.

the strength of the term quadratic in  $H$  is found to increase with increasing  $T$ . Since the strength of the coefficient  $\beta$  for the term linear in  $H$  in Eq. (6.1) does not appear to change over a large range of temperature in the vortex state, it seems unlikely that the mechanism responsible for the nonlinear Meissner effect can be solely responsible for the observed  $H$ -dependence of  $\lambda_{ab}(H, T)$  in the vortex state. Furthermore, according to the calculations of Amin *et al.* [40], it seems unlikely that nonlinear corrections to the supercurrent response in the vortex state can result in a field dependence for the effective penetration depth measured by  $\mu$ SR which is as strong as that found here. However, as just mentioned, the calculation of the effective  $\lambda$  is rather sensitive to the vortex source term, so that the size of the vortex cores should be included in such calculations.

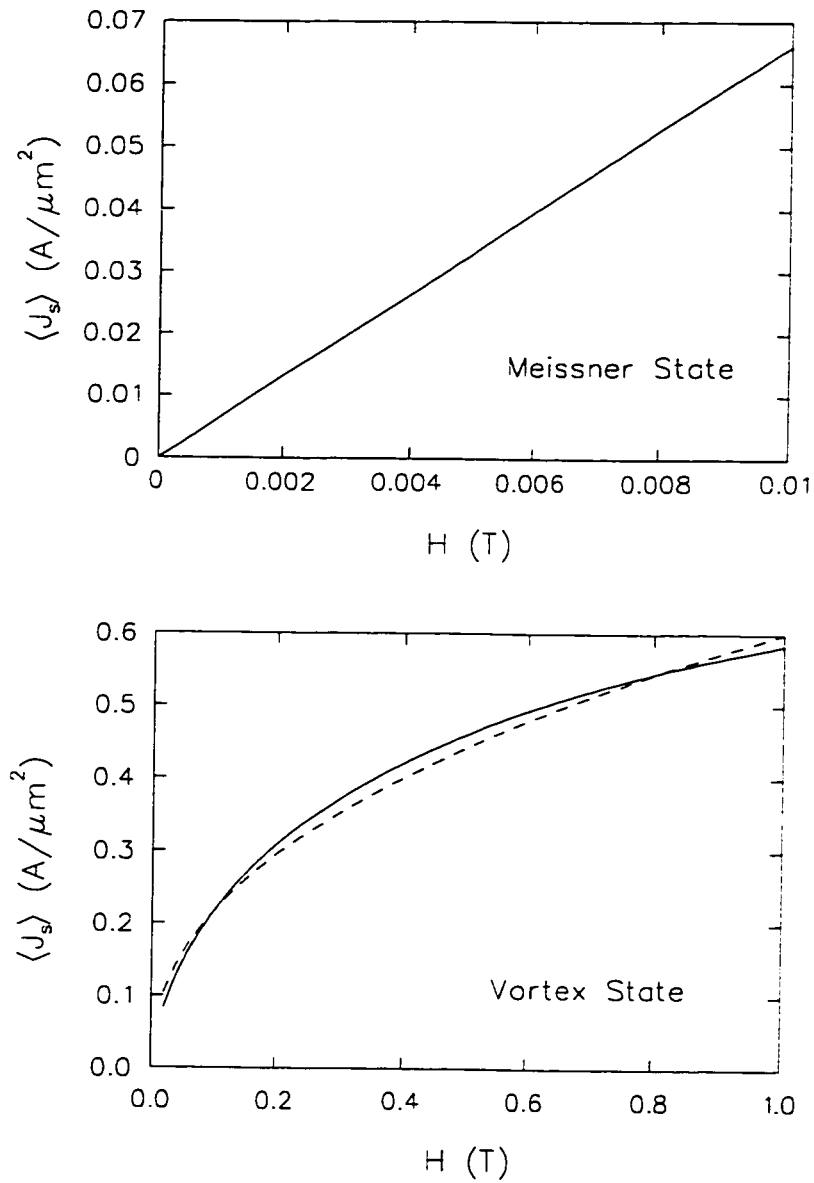


Figure 6.7: The magnetic field dependence of the average supercurrent density in the Meissner (top) and the vortex (bottom) states for  $\lambda = 1400 \text{ \AA}$  and  $\kappa = 10$ . In the bottom panel the solid curve was generated from the analytical GL model and the dashed curve is the relation  $\langle J_s \rangle = 0.6H^{0.44}$ .

Since  $\lambda_{ab}$  is not the only parameter which contributes to the fitted  $\mu$ SR line width, it is necessary to monitor the behaviour of the additional broadening parameter  $\sigma_f$ . Besides disorder in the vortex lattice, the large  $^{93}\text{Nb}$  nuclear moments ( $3.34 \times 10^{-3} \mu_B$ ) in NbSe<sub>2</sub> also slightly broaden the  $\mu$ SR line shape. For instance, in the normal state the muon depolarization rate  $\sigma_N$  at  $T = 10$  K is found to increase linearly from  $\sigma_N = 0.19 \mu\text{s}^{-1}$  at  $H = 0.19$  T to  $\sigma_N = 0.22 \mu\text{s}^{-1}$  at  $H = 0.90$  T. To determine the degree of disorder in the vortex lattice, the contribution of the  $^{93}\text{Nb}$  nuclear moments  $\sigma_{\text{dip}}$  to the muon depolarization rate can be subtracted in quadrature from the fitted value of  $\sigma_f$

$$\sigma_{\text{dis}}^2 = \sigma_f^2 - \sigma_{\text{dip}}^2. \quad (6.2)$$

Assuming  $\sigma_{\text{dip}}$  is temperature independent, the normal state value  $\sigma_N$  is approximately the value of  $\sigma_{\text{dip}}$  in the vortex state. The parameter  $\sigma_{\text{dis}}$  due to disorder in the vortex lattice [plotted in Fig. 6.8(a)] is relatively small and is weakly dependent on magnetic field and temperature. This indicates that the determined behaviour of  $\lambda_{ab}(H, T)$  does not arise from a systematic interplay between  $\lambda_{ab}$  and  $\sigma_f$  in the fitting procedure. Figure 6.8(b) shows the quality of the fits ( $\chi^2$ ) normalized by the number of degrees of freedom (NDF), as a function of  $H$  for  $T = 0.33 T_c$  and  $0.6 T_c$ . The quality of the fits is essentially independent of  $H$  and  $T$ . An upper limit for the root mean square (RMS) displacement  $\langle s^2 \rangle^{1/2}$  of the vortices from their ideal positions in the perfect vortex lattice, due to random pinning, can be obtained from  $\sigma_{\text{dis}}$  as follows [50]

$$\langle s^2 \rangle^{1/2} \approx \frac{\sigma_{\text{dis}}}{B_0} \sqrt{2} \left( \sum_{\mathbf{K}} \frac{K^2}{[1 + K^2 \lambda_{ab}^2 / (1 - b)]^2} \right)^{-1/2}. \quad (6.3)$$

The magnetic field dependence of  $\langle s^2 \rangle^{1/2}$  is shown in Fig. 6.9(a). The magnitude of  $\langle s^2 \rangle^{1/2}$  is essentially independent of  $H$ , except perhaps at low fields where the interaction between vortices is weakest. This suggests that there are no significant changes in the

vortex lattice geometry as a function of magnetic field. The degree of disorder in the vortex lattice does appear somewhat larger for higher  $T$ .

For a perfect triangular vortex lattice the intervortex spacing is given by

$$L = \left( \frac{2\phi_0}{\sqrt{3}B_0} \right)^{\frac{1}{2}}. \quad (6.4)$$

Since the distance between vortices decreases with increasing field, the RMS deviation of the vortices from their ideal positions grows as a percentage of  $L$  [see Fig. 6.9(b)]. At low temperatures  $\langle s^2 \rangle^{1/2}/L$  is less than 2 %, even at  $H = 0.31H_{c2}(T)$ . This small disorder is consistent with the STM and SANS experiments on NbSe<sub>2</sub> discussed earlier.

The radius of a vortex core is not a uniquely defined quantity, since there exists no sharp discontinuity between a normal vortex core and the superconducting material. Nevertheless, a useful definition can be made taking into account the dramatic spatial changes observed in quantities such as the order parameter  $\psi(\mathbf{r})$ , the local density of states  $N(\mathbf{E}, \mathbf{r})$ , the supercurrent density  $J_s(\mathbf{r})$  and the local magnetic field strength  $B(\mathbf{r})$  near the center of a vortex line. Since the supercurrent density  $J_s(\mathbf{r})$  can be easily obtained from the fitted field profile through the Maxwell relation  $\mathbf{J}(\mathbf{r}) = (c/4\pi)\nabla \times \mathbf{B}(\mathbf{r})$ , we define an effective core radius  $r_0$  to be the distance from the vortex center for which  $J_s(r)$  reaches its maximum value. As shown in Fig. 6.10,  $J_s(r)$  rises steeply from zero at the vortex center to its maximum value  $J_{s_{\max}}$  at  $r_0$ .

The magnetic field dependence of  $r_0$  in NbSe<sub>2</sub> is shown in Fig. 6.11, where  $r_0$  is obtained from  $J_s(r)$  profiles created from the fitted field profiles  $B(r)$ . The deduced values of  $r_0$  are less sensitive (than  $\lambda$ ) to the choice of the theoretical model for  $B(r)$ . This is because a good approximation of  $J_s(r)$  can be obtained by taking the *curl* of any function  $B(r)$  which fits the measured field distribution well. This includes an insensitivity to the assumed vortex-lattice geometry, provided a good fit is obtained. Since  $r_0$  is fairly robust to the validity of the theoretical field distribution used to fit the

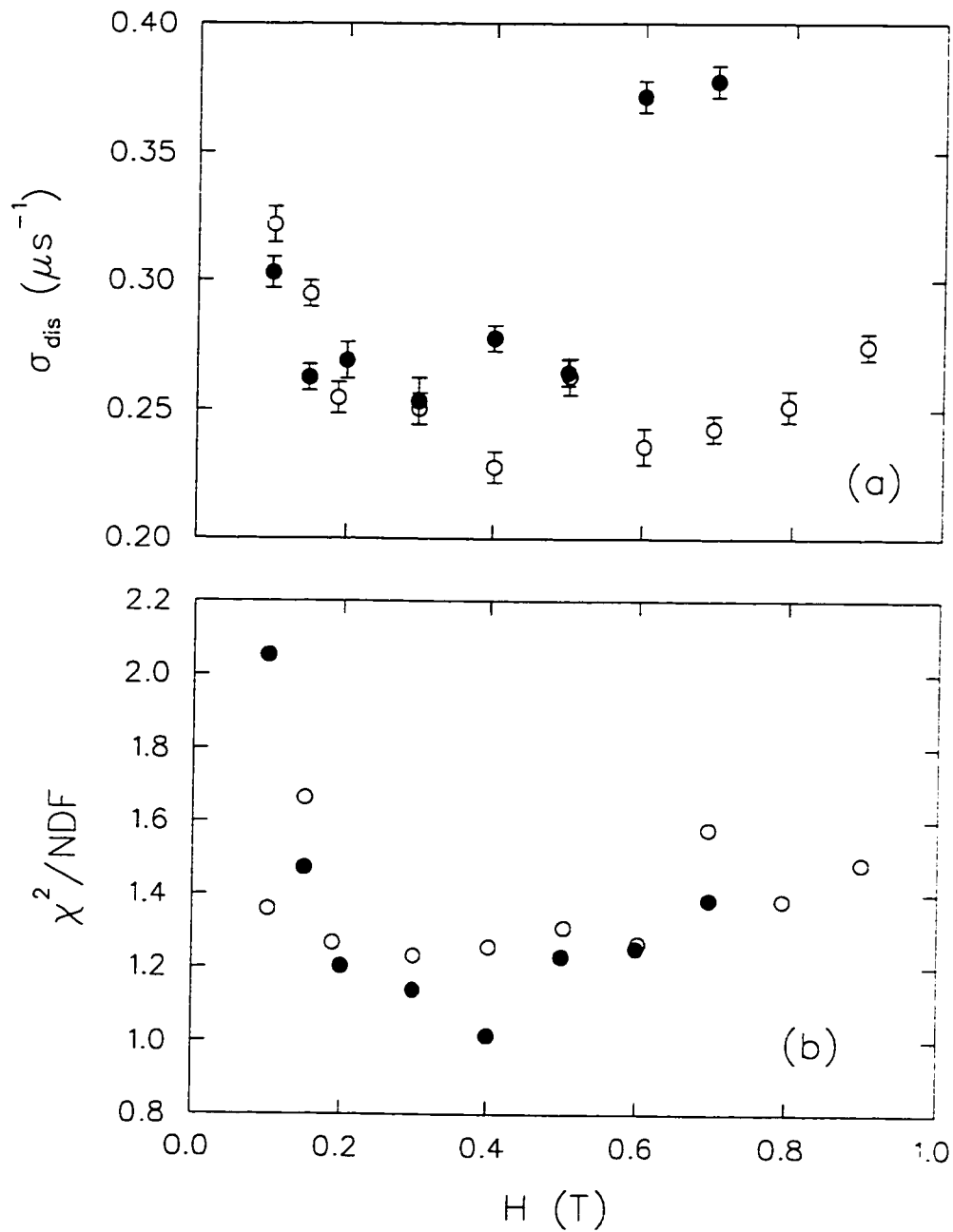


Figure 6.8: The magnetic field dependence of (a) the additional broadening parameter  $\sigma_{\text{dis}}$  and (b) the ratio of  $\chi^2$  to the number of degrees of freedom (NDF) for NbSe<sub>2</sub> at  $T = 0.33 T_c$  (open circles) and  $T = 0.6 T_c$  (solid circles).

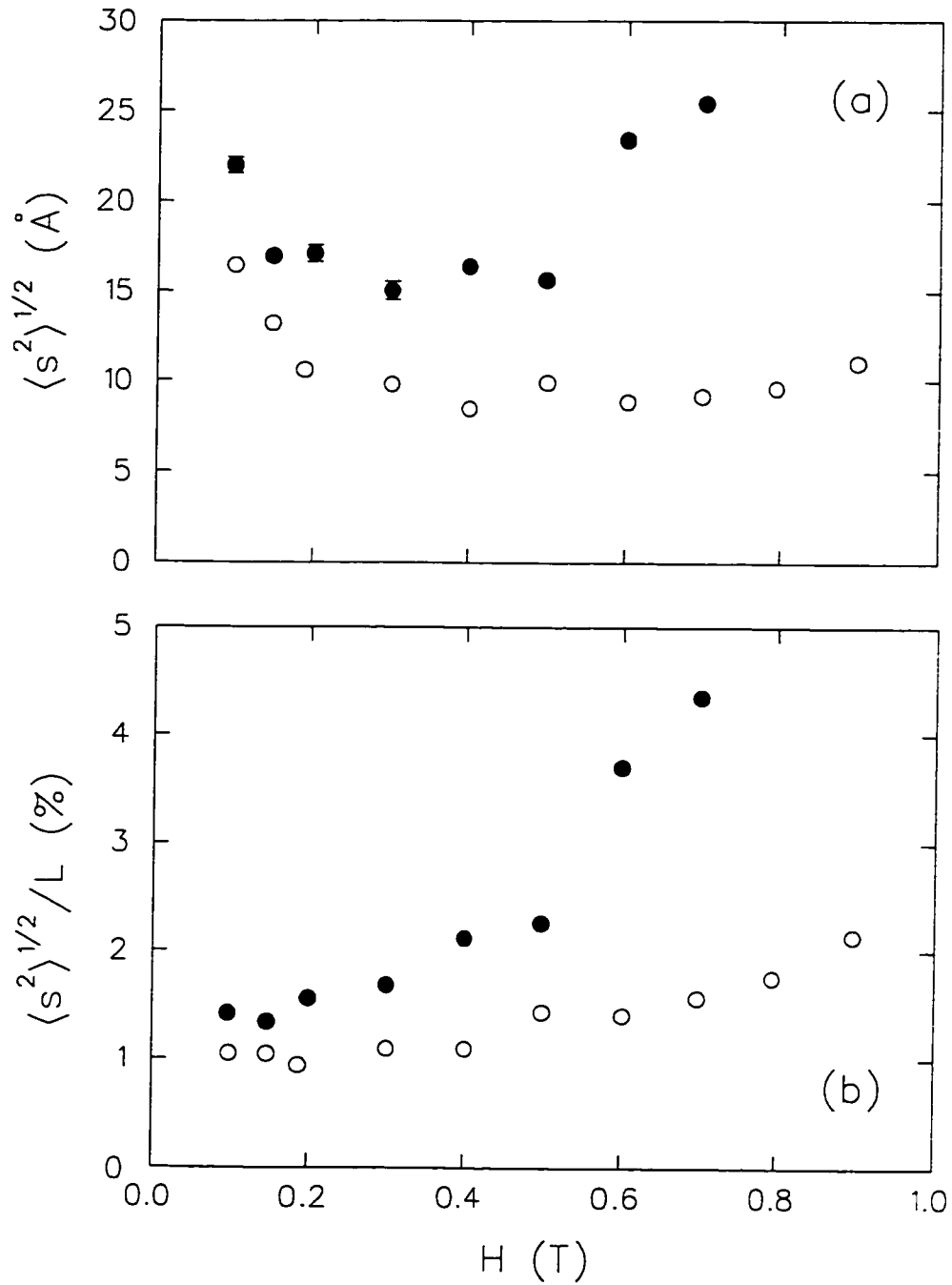


Figure 6.9: The magnetic field dependence of (a) the RMS displacement  $\langle s^2 \rangle^{1/2}$  of the vortices from their ideal positions and (b)  $\langle s^2 \rangle^{1/2}$  expressed as a percentage of the intervortex spacing  $L$ . The data is for NbSe<sub>2</sub> at  $T = 0.33 T_c$  (open circles) and  $T = 0.6 T_c$  (solid circles).



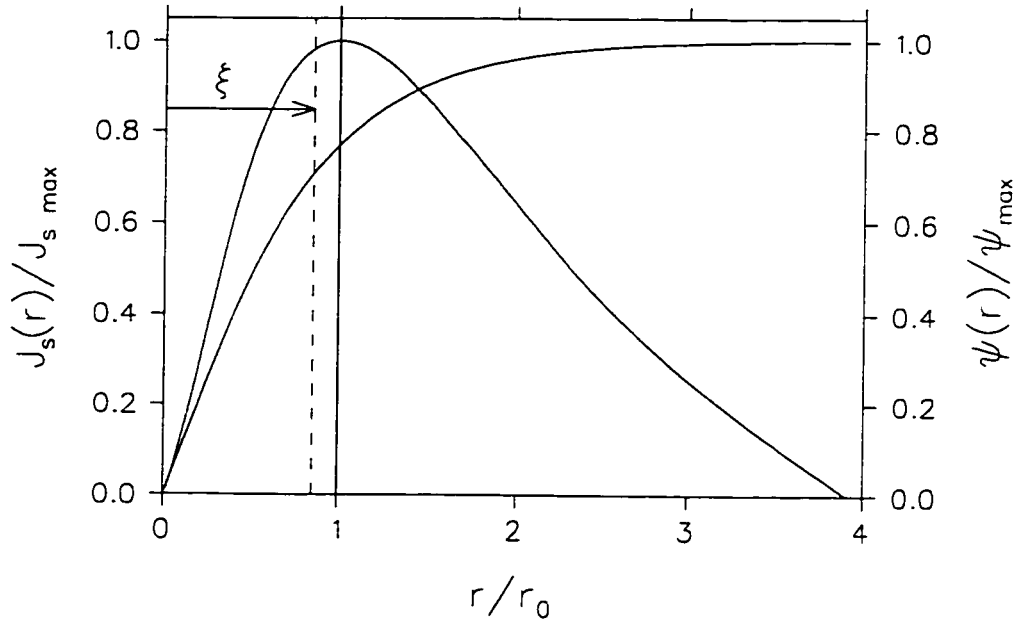


Figure 6.10: The dependence of the supercurrent density  $J_s(r)$  and the order parameter  $\psi(r)$  on the distance  $r$  from the center of a vortex line.  $J_s(r)$  is normalized to its maximum value  $J_{s_{\max}}$  at a distance  $r=r_0$ , whereas  $\psi(r)$  is normalized to its maximum value  $\psi_{\max}$  far from the vortex core.

data, then provided a good fit is obtained, the vortex-core radius can be determined from  $\mu$ SR with few theoretical assumptions. We note that discrepancies between the three models considered here do appear at low fields (see Fig. 6.11) because of the reduced statistics at the high-field tail of the measured internal field distribution. Since there are far fewer vortices in the sample at these low fields, there is a reduction in the number of events originating from muons which stop in the vicinity of the vortex cores. As a result, the high-field tail shows more "statistical wiggles", which in turn allows for a greater variation in the tail of the fitted  $B(r)$ . Increasing the number of recorded muon decay events in the  $\mu$ SR spectra at low  $H$  would rectify this problem and should lead to better agreement between the three models in Fig. 6.11 at all magnetic fields.

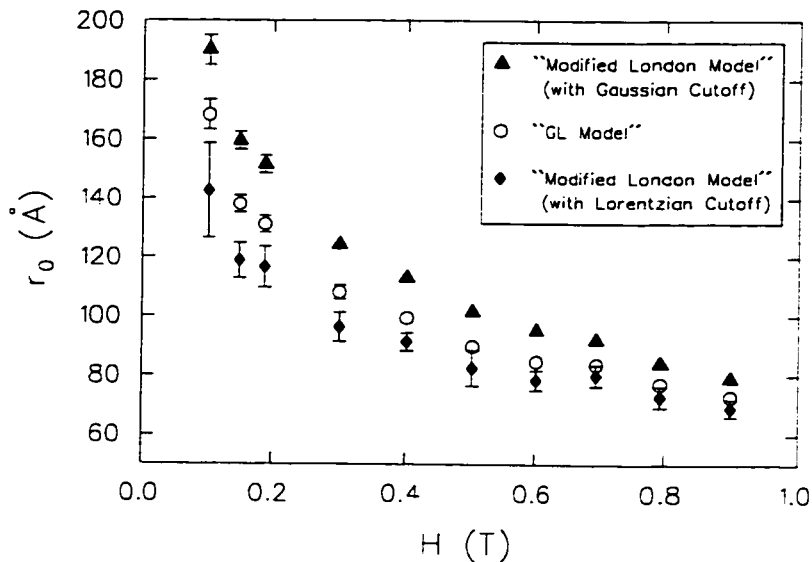


Figure 6.11: The magnetic field dependence of the vortex-core radius  $r_0$  in NbSe<sub>2</sub> at  $T = 0.33 T_c$ , determined from fits to three different models for the field profile  $B(\mathbf{r})$  of the vortex lattice.

Golubov and Hartmann [205] have shown that the shrinking of the vortex core radius with increasing magnetic field can be attributed to increased vortex-vortex interactions. They solved the microscopic equations in the dirty limit (*i.e.* the Usadel equations) self-consistently and showed that the order parameter  $\psi(r)$  and the LDOS reach their maximum values closer to the vortex center when  $H$  is increased. From the LDOS, these authors calculated tunneling current  $I(r)$  profiles from the vortex center as a function of  $H$  in order to model STM measurements of  $r_0(H)$  in NbSe<sub>2</sub> [206]. The magnetic field dependence of  $r_0$  in NbSe<sub>2</sub> determined by STM at  $T = 0.6 T_c$  is shown in Fig. 6.12 along with that determined by  $\mu$ SR at  $T = 0.6 T_c$  and  $0.33 T_c$ . The definition of  $r_0$  in the STM experiment was arbitrarily chosen to be the radius at which the measured  $I(r)$  had diminished to  $1/\sqrt{2}$  of its maximum value at the vortex-core center. It was shown in Ref. [205] that this gives a value of  $r_0$  which is somewhat larger than the

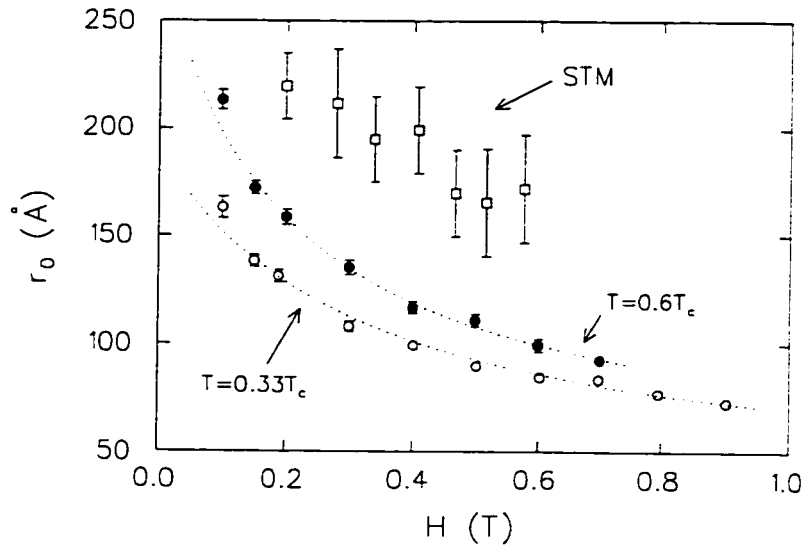


Figure 6.12: The magnetic field dependence of the vortex-core radius  $r_0$  in NbSe<sub>2</sub> determined at the surface by STM [206] at  $T = 0.6 T_c$  (open squares) and in the bulk by  $\mu$ SR [4] at  $T = 0.33 T_c$  (open circles) and  $T = 0.6 T_c$  (solid circles). The dashed curves are given by Eq. (6.5).

commonly used theoretical definition, *i.e.* the radius at which  $\psi(r)$  rises from zero at the core center to  $1/\sqrt{2}$  of its maximum value well away from the core. The different definitions of  $r_0$  are the main reason for the difference in magnitude of  $r_0$  between the STM and  $\mu$ SR experiments at  $T = 0.6 T_c$ . Also, we found from the microscopic theory (see Ref. [4]) that  $J_s(r)$  does not reach its maximum value at exactly the radius where  $\psi(r)$  reaches  $1/\sqrt{2}$  of its maximum value, at all temperatures and magnetic fields. For this reason, our definition of  $r_0$  is robust to changes in  $T$  and  $H$  and should better reflect the actual  $H$ -dependence of the vortex-core radius.

The authors of Ref. [205] reported good agreement between the STM measurements of  $r_0(H)$  and the dirty-limit microscopic theory. Although the magnitude of  $r_0$  is reasonably predicted from their calculations, the error bars in the STM measurements

are too large to conclude whether there is precise agreement with the theory. In a  $\mu$ SR experiment, typically  $2 \times 10^8$  muons sample the local magnetic field of approximately  $10^{11}$  vortices in the bulk of a few  $\text{mm}^2$  sample, as opposed to an STM experiment which averages  $r_0$  from a few vortices at the surface. As a result of this statistical improvement, the  $\mu$ SR data shown in Fig. 6.12 have smaller error bars and less scatter. This improvement allowed us to show in Ref. [4] that  $r_0$  decreases more strongly with magnetic field than predicted by the dirty-limit microscopic theory. This finding was not surprising since NbSe<sub>2</sub> is in the clean limit. To our knowledge, there have yet to be any calculations of the  $H$ -dependence of  $r_0$  from the microscopic theory in the clean limit. However, in Ref. [4] we showed that the  $\mu$ SR results fit well to the simple phenomenological equation

$$r_0(H) = \frac{\lambda_{ab}(H)}{\kappa'(H)} = r_0(0) \frac{[1 + \beta h]}{[1 + \gamma h]}, \quad (6.5)$$

where  $\kappa' = \lambda_{ab}/r_0$  and  $r_0(0)$ ,  $\beta$  and  $\gamma$  are temperature dependent constants. The excellent fits to this equation are shown as dashed curves in Fig. 6.12 where  $r_0(0) = 191 \text{ \AA}$  and  $282 \text{ \AA}$  at  $T = 0.33 T_c$  and  $0.6 T_c$ , respectively. Equation (6.5) was derived from our observation that both  $\lambda_{ab}$  and  $\kappa'$  increased linearly with  $H$ . The latter is shown in Fig. 6.14(b) along with field dependence of  $\kappa = \lambda_{ab}/\xi_{ab}$  in Fig. 6.14(a) [see Table 6.3 for the fitted parameters]. Since  $h = H/H_{c2} = 3\Phi_0/\sqrt{2}L^2B_{c2}$  for a triangular vortex lattice and  $H_{c2}(T)$  can be obtained from measurement, for a given temperature  $r_0$  in Eq. (6.5) is a function of only the distance between vortices,  $L$ . This observation supports the physical interpretation for the reduction in  $r_0$ , namely a shrinking of the vortex cores due to the increased interaction between vortices—which are closer together at high magnetic fields.

The effective coherence length  $\xi_{ab}$  in Eq. (4.13) which best fits the data is plotted in Fig. 6.13 as a function of magnetic field. The variation of  $\xi_{ab}(H, T)$  is similar to that

of  $r_0(H, T)$ , which was shown earlier to be model independent. The curves through the data points were generated from the fitted relations for  $\lambda_{ab}(H)$  and  $\kappa(H)$  given in Table 6.3. It should be kept in mind that  $\xi_{ab}$  must be considered an “effective” coherence length. For instance, according to Eq. (2.73) of the GL theory, the coherence length near  $H_{c2}$  at  $T = 0.33 T_c$  should be  $106.5 \text{ \AA}$ , where  $H_{c2}(0.33 T_c) = 2.9 \text{ T}$ . However, at  $2.9 \text{ T}$  the fitted curve in Fig. 6.13 gives  $\xi_{ab} = 49.1 \text{ \AA}$ . Similarly, at  $T = 0.6 T_c$ , Eq. (2.73) yields  $\xi_{ab} = 131.6 \text{ \AA}$ , whereas the fitted curve in Fig. 6.13 gives  $78.7 \text{ \AA}$ . A reduced value of  $\xi_{ab}$  may be obtained if the fitted theoretical field distribution overestimates the length of the high-field tail in the  $\mu\text{SR}$  line shape. However, according to Fig. 6.5, it is highly unlikely that the fits are substantially overestimating the length of the high-field tail. The discrepancy between the measured  $\xi_{ab}$  and that predicted in Eq. (2.73) is most likely due to the theoretical difference between  $\xi_{ab}$  in Eq. (4.13) and the “true” GL coherence length. Given that GL theory is really only valid near the phase boundary, it is reasonable that deviations occur at low  $T$  and low  $H$ .

Assuming that the shrinking of the cores is associated with the strength of the vortex-vortex interactions, the increase in  $r_0$  and  $\xi_{ab}$  with decreasing magnetic field should saturate when the vortices are sufficiently far apart (*i.e.* when  $\lambda_{ab} < L$ ). From Eq. (6.4) and the fitted expressions for  $\lambda_{ab}(H)$  in Table 6.3, the field at which this saturation occurs can be estimated. In particular, at  $T = 0.33 T_c$  there should be no change in the size of the vortex cores below  $H \approx 0.12 \text{ T}$ , whereas this crossover field is  $H \approx 0.10 \text{ T}$  at  $T = 0.6 T_c$ .

A few remarks are now necessary with regard to the behaviour of  $\kappa(H)$  and  $\kappa'(H)$  in Fig. 6.14. The behaviour of  $\kappa(H)$  implies that NbSe<sub>2</sub> becomes more type-II like with increasing magnetic field. In GL theory,  $\kappa$  is independent of both  $H$  and  $T$ . However, this definition is strictly valid only near the superconducting-to-normal phase

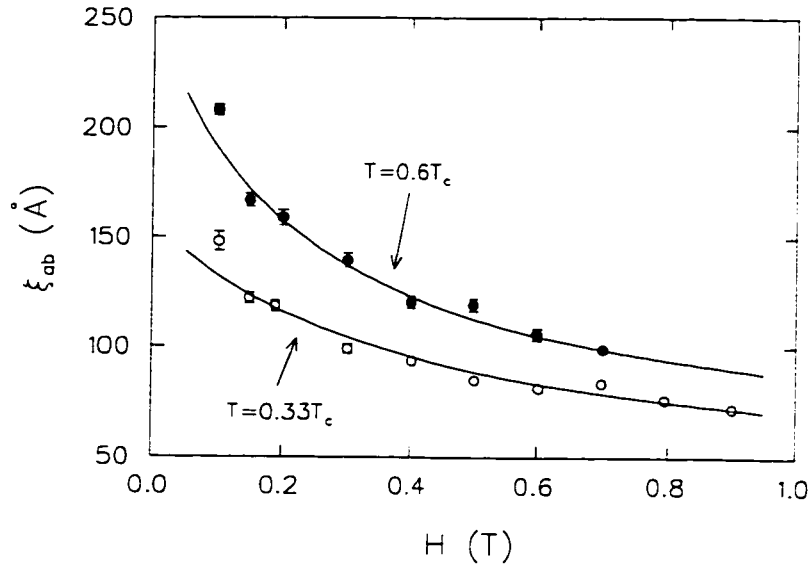


Figure 6.13: The magnetic field dependence of the parameter  $\xi_{ab}$  in Eq. (4.13) at  $T = 0.33 T_c$  (open circles) and  $T = 0.6 T_c$  (solid circles).

transition. Our results imply that the conventional GL equations with field-independent  $\lambda$  and  $\xi$  are not applicable deep in the superconducting state. Even if  $\lambda_{ab}$  were field independent, an increase of  $\kappa$  and  $\kappa'$  with  $H$  would still arise from the decrease of  $\rho_0$  which has been independently observed in  $NbSe_2$  by STM. Furthermore, attempts to fix  $\kappa(H)$  and  $\kappa'(H)$  to constant values in the fitting procedure yield higher values of  $\chi^2$  and unphysical results—such as a residual background signal which is 50 % of the total signal amplitude.

Figure 6.15 shows a typical muon precession signal displayed for convenience in a reference frame rotating at about 1.5 MHz below the Larmor precession frequency of a free muon. The curves through the data points are examples of fits to the theoretical polarization function for fixed values of  $\xi_{ab}$ , where  $\lambda_{ab}$  and all other parameters were free to vary. Only the first 3  $\mu s$  of data are shown in Fig. 6.15 since the signal from the

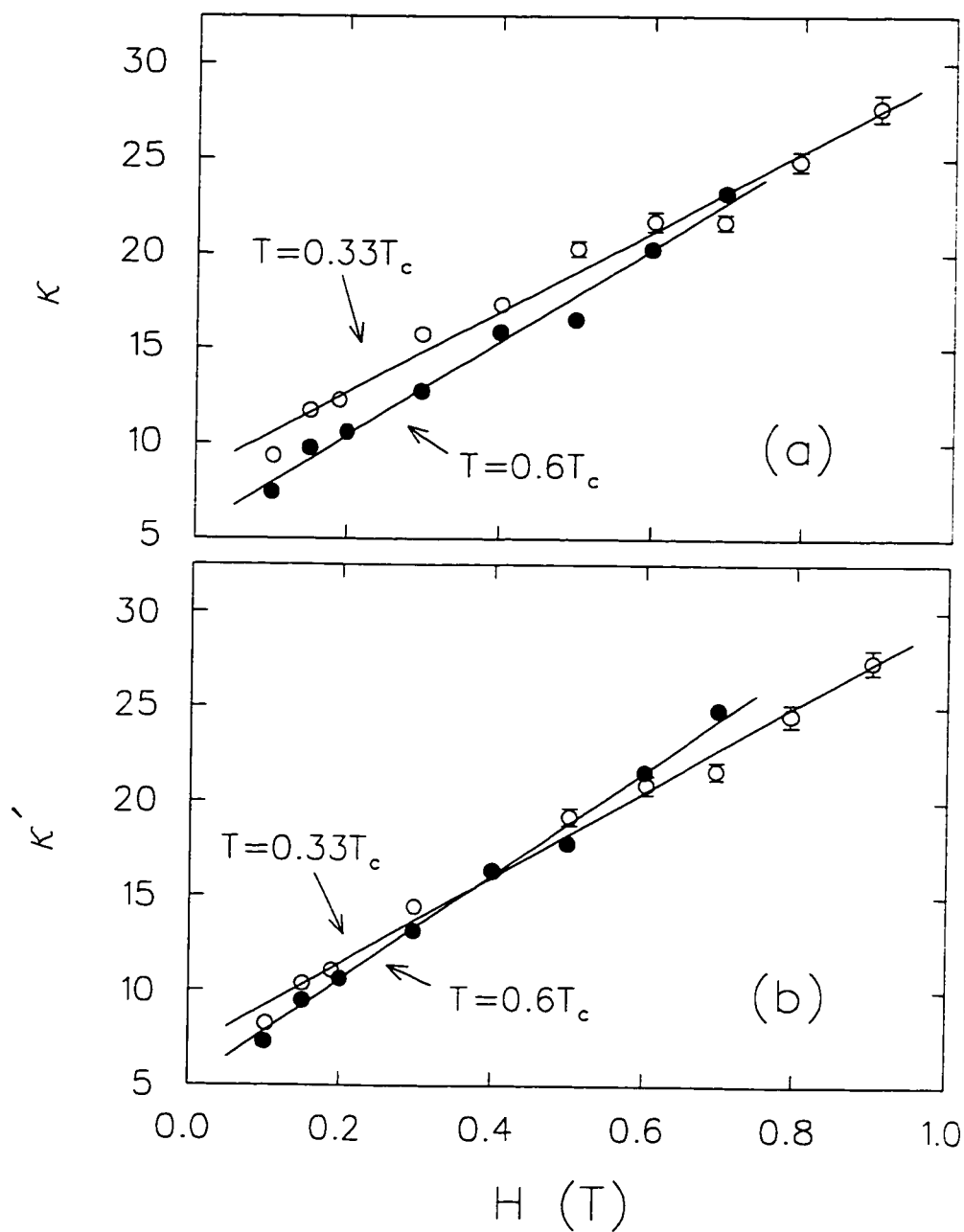


Figure 6.14: The magnetic field dependence of (a)  $\kappa = \lambda_{ab}/\xi_{ab}$  and (b)  $\kappa' = \lambda_{ab}/r_0$  in NbSe<sub>2</sub> at  $T = 0.33 T_c$  (open circles) and  $T = 0.6 T_c$  (solid circles).

vortex lattice essentially decays over this time range—although the fits were actually performed over the first 6  $\mu\text{s}$ . Figure 6.16 shows the difference between the data points and the fitted curve for the fits in Fig. 6.15. There is a clear oscillation for the fits corresponding to  $\xi_{ab} = 80 \text{ \AA}$  and  $\xi_{ab} = 160 \text{ \AA}$ , indicating a missed frequency or frequencies. The ratio of  $\chi^2$  to the number of degrees of freedom (NDF) is shown in Fig. 6.17(a) as a function of  $\xi_{ab}$  for two different applied magnetic fields. Note that the value of  $\xi_{ab}$  for which  $\chi^2/\text{NDF}$  reaches its minimum value is quite different for the two fields. Figure 6.17(b) shows the behaviour of the free parameter  $\kappa$  for these same fits. The best fits indicate that  $\kappa$  is dependent on magnetic field.

The reduction in  $r_0$  and  $\xi_{ab}$  with increasing temperature which is shown in Fig. 6.12 and Fig. 6.13, respectively, is expected from theoretical predictions for a  $s$ -wave vortex [140,148,150]. However, as shown in Fig. 6.18(b), the vortex core radius does not decrease as steeply with temperature as predicted by theory. The dashed line in Fig. 6.18(b) is a fit to the theory of Kramer and Pesch [140] [see Eq. (4.11)] where  $r_0(T) = \alpha T/T_c$ , with  $\alpha = 299 \text{ \AA}$ . Part of the problem is that these theoretical calculations pertain to a single isolated vortex. Given the apparent strong influence of vortex-vortex interactions, the vortex-lattice effect should not be ignored in theoretical calculations for  $r_0(T)$ . For a given magnetic field,  $\lambda_{ab}$  will grow with increasing temperature [see Fig. 6.18(a)], whereas the intervortex spacing  $L$  remains constant. The strength of the vortex-vortex interactions will increase at higher field as the ratio  $\lambda_{ab}/L$  increases, leading to additional changes in the electronic structure of the vortex cores. Since these interactions become stronger with increasing  $T$ , the difference between the measured value of  $r_0$  and that predicted for an isolated vortex core will increase monotonically with temperature.

The solid line through the data in Fig. 6.18(a) is a fit to the empirical relation



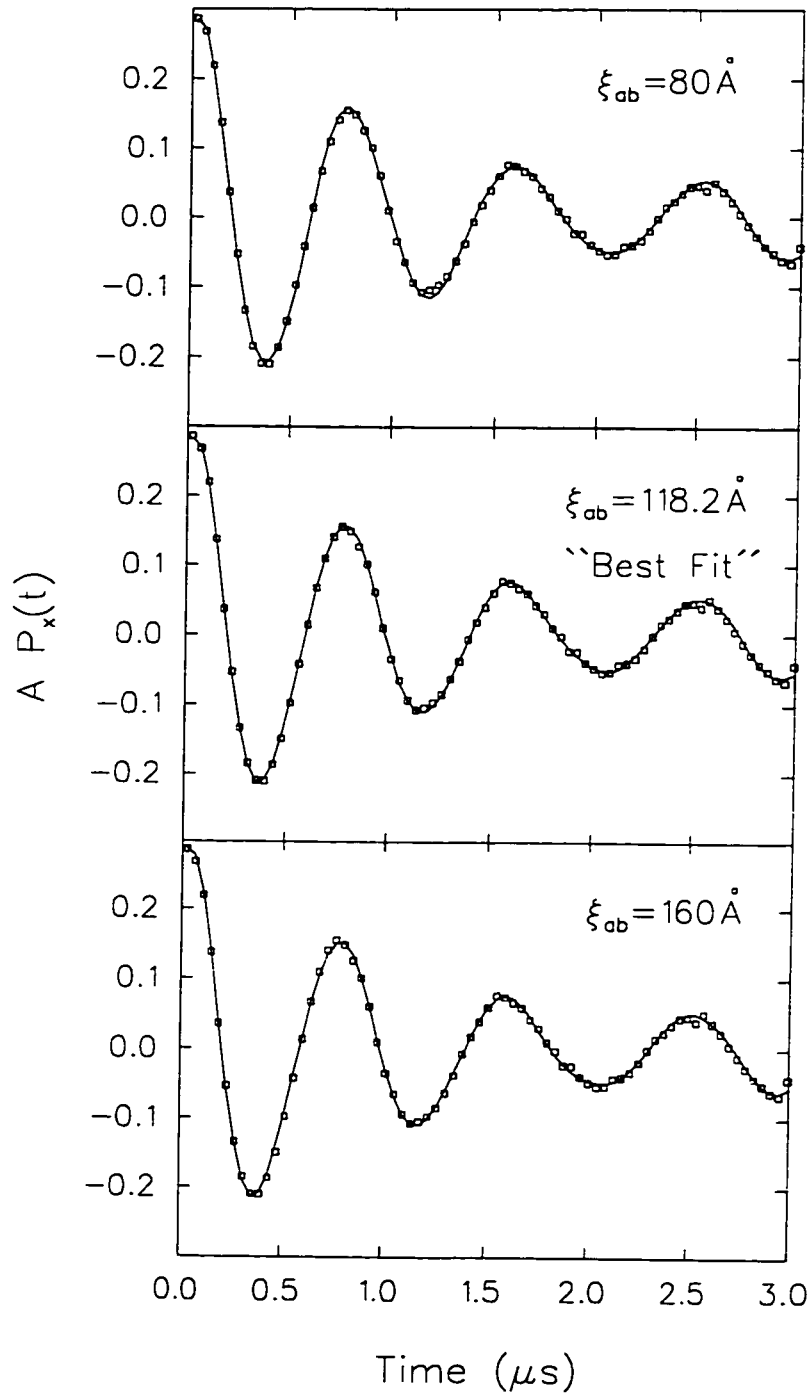


Figure 6.15: The muon spin precession signal in  $\text{NbSe}_2$  after field cooling to  $T = 0.33 T_c$  in a magnetic field  $H = 0.19 \text{ T}$ . The solid curves are fits to the theoretical muon polarization function assuming the field profile from the analytical GL model with fixed values of  $\xi_{ab}$  (i.e. 80, 118.2 and 160  $\text{\AA}$ ).

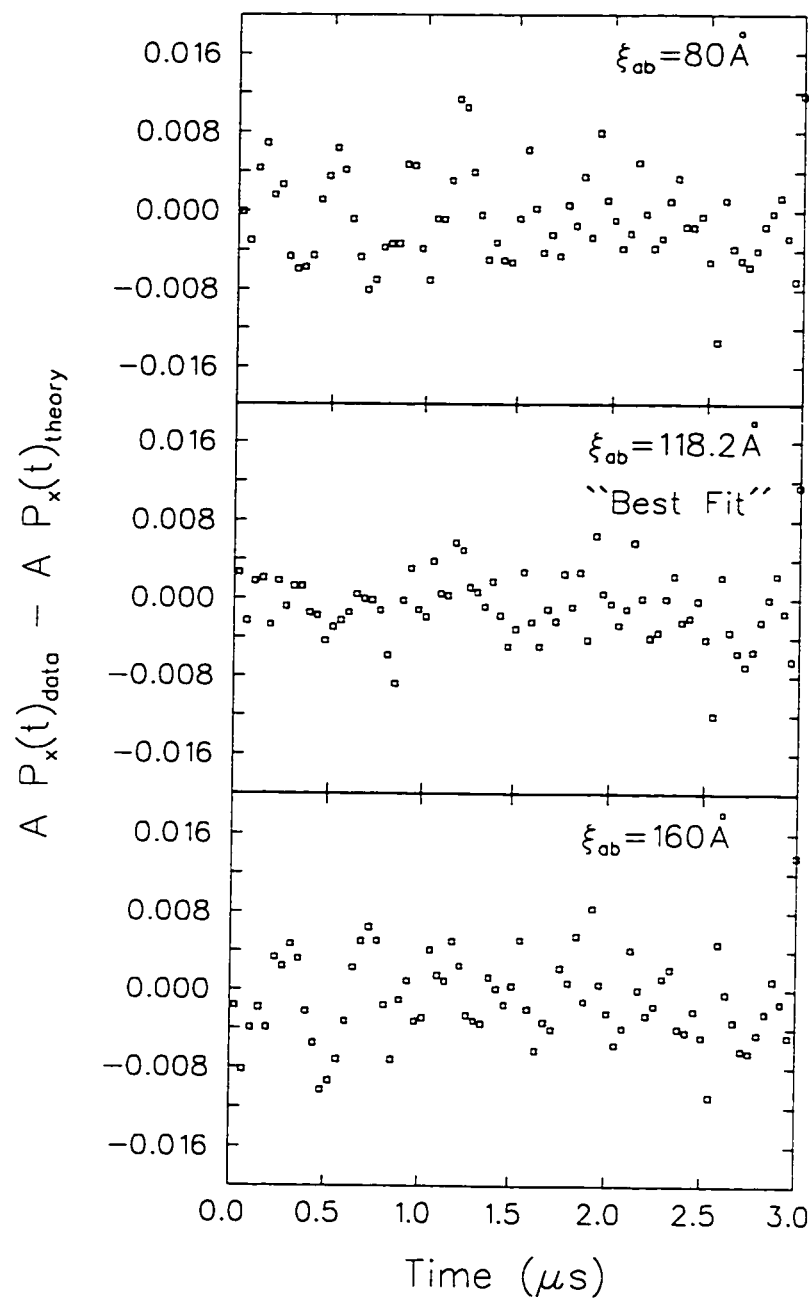


Figure 6.16: The difference between the measured  $\mu\text{SR}$  spectrum and the theoretical muon polarization function for the fits in Fig. 6.15.

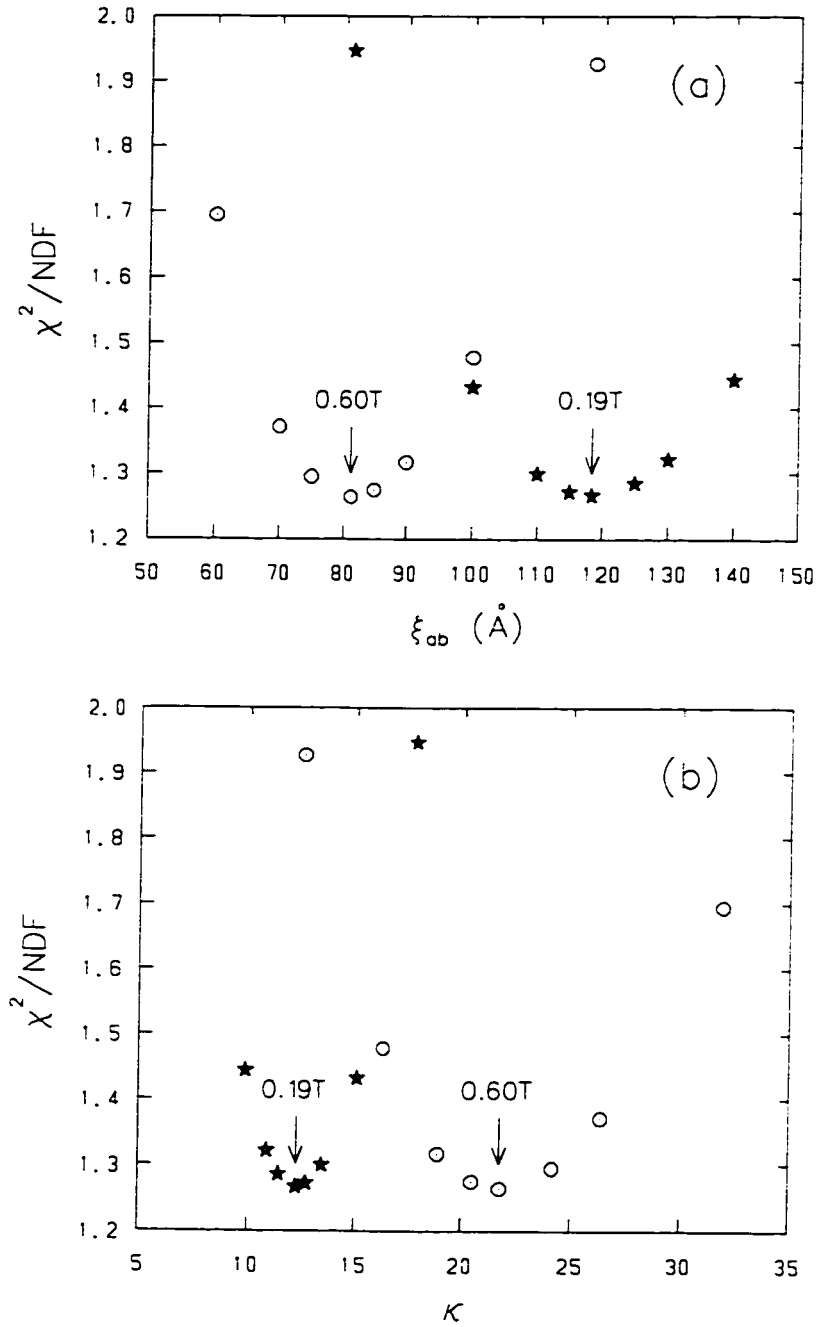


Figure 6.17: The ratio of  $\chi^2$  to the number of degrees of freedom (NDF=872) as a function of (a)  $\xi_{ab}$  and (b)  $\kappa$  (from the same fits) for  $H=0.19$  T (stars) and  $H=0.60$  T (circles) at  $T=0.33 T_c$ .

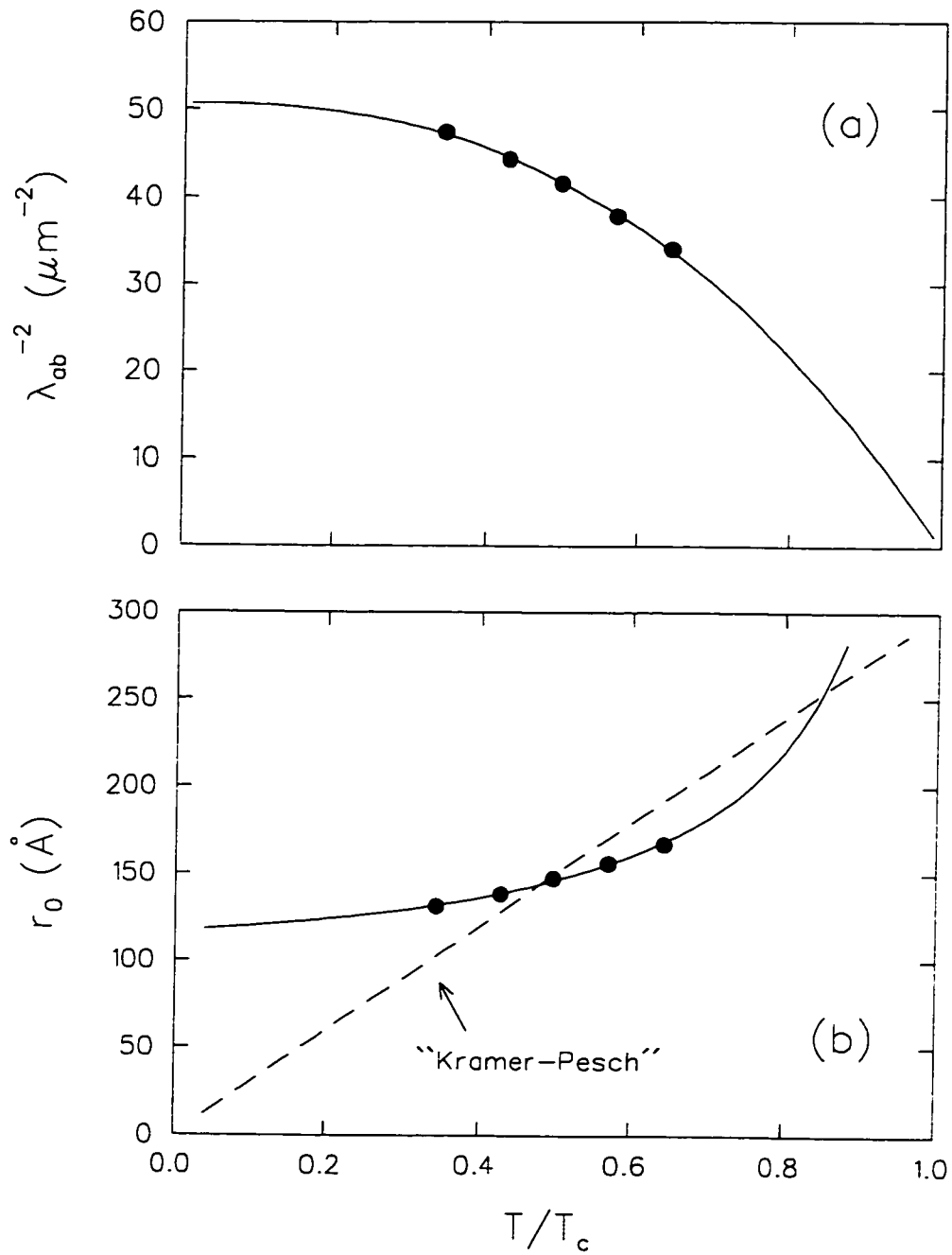


Figure 6.18: The temperature dependence of (a)  $\lambda_{ab}^{-2}$  and (b)  $r_0$  in NbSe<sub>2</sub> in a magnetic field  $H = 0.19$  T. The dashed line in (b) is what is expected from the Kramer-Pesch effect [140].

$\lambda_{ab}^{-2}(T) = \lambda_{ab}^{-2}(0)[1 - t^p]$  with  $\lambda_{ab}^{-2}(0) = 50.7 \mu\text{m}^{-2}$ ,  $p = 2.48$  and  $t = T/T_c$ . Although this is considered to be consistent with a weak-coupling BCS superconductor [1] (which shows a  $T$ -dependence of  $\lambda^{-2}$  which is close to  $(1 - t^2)$ ), there is no real low temperature data to obtain a proper fit to the BCS expression of Eq. (2.27). From the empirical fit and an observed weak linear- $T$  dependence for  $\kappa'$ , the temperature dependence of the vortex-core radius is given by

$$r_0(T) = \frac{\lambda_{ab}(T)}{\kappa'(T)} = r_0(0) [1 - t^p]^{-\frac{1}{2}} [1 - \gamma t]^{-1} . \quad (6.6)$$

where  $r_0(0) = 117 \text{ \AA}$  and  $\gamma = 0.23$ . This equation appears as the solid line fit in Fig. 6.18(b). Note that the change in  $r_0(T)$  is weakest at low temperatures where the strength of the interaction force between vortices is small. The measurements here are well above the quantum limit in NbSe<sub>2</sub> (see Ref. [148]) so a complete saturation of  $r_0$  is not observed. As noted earlier, the weak increase in  $\kappa$  (or  $\kappa'$ ) with decreasing temperature is predicted from the microscopic theory.

## Chapter 7

### Experiment: $\text{YBa}_2\text{Cu}_3\text{O}_{6.95}$

In this chapter, recent  $\mu\text{SR}$  measurements of the  $\hat{a}-\hat{b}$  plane magnetic penetration depth  $\lambda_{ab}$  and the vortex core size ( $\sim \xi_{ab}$ ) in the high- $T_c$  compound  $\text{YBa}_2\text{Cu}_3\text{O}_{6.95}$  are presented. The oxygen concentration in this superconductor is that which gives the maximum value of the transition temperature  $T_c$ .

Figures 7.1 and 7.2 show the Fourier transforms of the muon precession signal in the optimally doped compound  $\text{YBa}_2\text{Cu}_3\text{O}_{6.95}$  as a function of temperature and magnetic field, respectively. In Figure 7.2 it was necessary to renormalize the Fourier amplitudes to the same maximum height, because of a reduction in the signal amplitude with increasing magnetic field. Asymmetry loss is due to the finite timing resolution of the counters, a reduction in the radii of the decay positron orbits and a dephasing of the muon beam before it reaches the sample. The last originates from muons with slightly different momenta and/or beam trajectories, which take different times to traverse the magnetic field and therefore precess different amounts prior to arrival at the sample.

The basic features expected for a rigid 3D vortex lattice are observed in these Fourier transforms, although their signal-to-noise ratio <sup>1</sup> is not as good as those for  $\text{NbSe}_2$ . In addition, the high-field cutoff is not clearly visible at low temperatures, which is partly a result of the much smaller coherence length (and vortex-core radius) in this material. The smaller value of  $r_0$  means that fewer muons stop in the vicinity of the vortex

---

<sup>1</sup>Recall from Chapter 4 that the Fourier transform diminishes the signal-to-noise ratio somewhat by weighting all of the time bins equally.

cores, resulting in less signal-to-noise in the high-field tail. Consequently,  $\xi_{ab}$  and  $r_0$  are difficult to determine in this material so deep in the superconducting state. Since the signal-to-noise ratio scales with  $\sqrt{N}$ , where  $N$  is the number of counts, it takes an impractical amount of time to make significant improvements in the high-field tail of the measured field distribution. To dramatically improve the signal-to-noise ratio in the high-field tail, it is necessary to go to higher magnetic fields where there are more vortices in the sample. According to the spectra presented in Ref. [50], at low temperatures this means magnetic fields in excess of at least 5 T. Unfortunately, as just mentioned, there are problems associated with the signal amplitude at such large  $H$ . Currently, efforts are underway to construct an apparatus which operates effectively in such strong magnetic fields. This “high-field” apparatus will include the use of higher timing resolution counters and a reduction in the distance between the decay positron counters and the sample. A high-field cutoff is clearly visible at high temperatures, as shown in Fig. 7.1. This is because  $r_0$  increases with  $T$  as was just observed in the case of  $\text{NbSe}_2$ .

As noted earlier, oxygen vacancies and twin planes may pin vortices in  $\text{YBa}_2\text{Cu}_3\text{O}_{7-x}$ . The strength of this pinning can be studied by determining the sensitivity of the  $\mu\text{SR}$  spectrum to small changes in magnetic field. Figure 7.3(a) shows the Fourier transform of the muon spin precession signal in “detwinned”  $\text{YBa}_2\text{Cu}_3\text{O}_{6.95}$  (O3) after field cooling to  $T = 5$  K in a magnetic field of  $H = 1.50$  T. When the applied field is decreased by 0.02 T, the residual background signal shifts down to the new applied field  $H = 1.48$  T [see Fig. 7.3(b)]. However, the signal originating from the sample does not shift in response to the small change in applied field. This shows that the vortex lattice is firmly pinned. In addition, the absence of any detectable background peak in the unshifted signal implies that there are no nonsuperconducting inclusions in the sample. As the

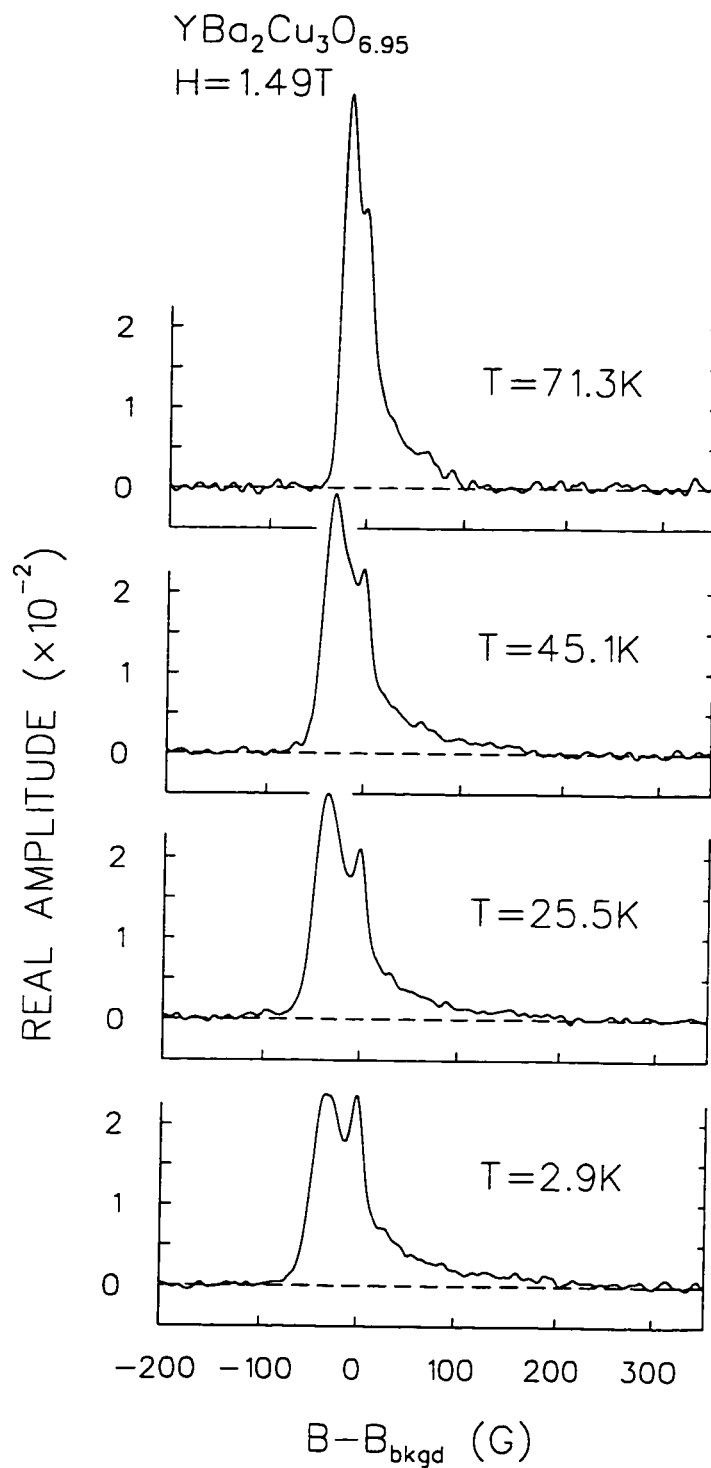


Figure 7.1: The Fourier transforms of the muon spin precession signal in  $\text{YBa}_2\text{Cu}_3\text{O}_{6.95}$  (O1) after field cooling to  $T=2.9, 25.5, 45.1$  and  $71.3$  K in a magnetic field  $H=1.49$  T.



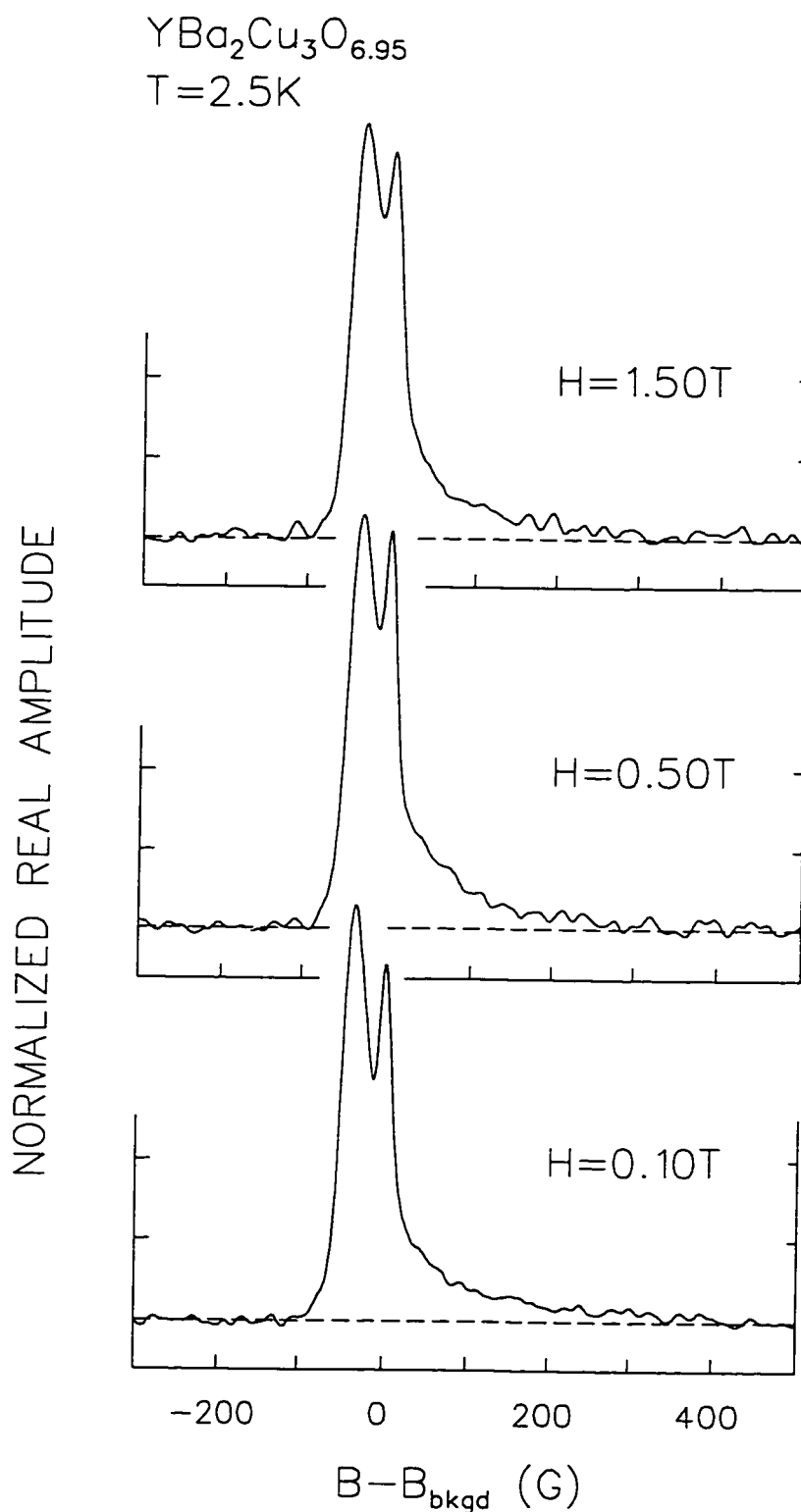


Figure 7.2: The Fourier transforms of the muon spin precession signal in  $\text{YBa}_2\text{Cu}_3\text{O}_{6.95}$  (O2) after field cooling to  $T=2.5\text{K}$  in magnetic fields of  $H=0.10$ ,  $0.50$  and  $1.50\text{T}$ .

temperature is increased, the shape of the Fourier transform changes due to the changes in  $\lambda_{ab}$  and  $\xi_{ab}$ . However, the signal remains unshifted indicating that the vortices are still pinned. Eventually, the temperature is large enough that thermal fluctuations depin some of the 3D vortex lines, as shown in Fig. 7.4. Raising the temperature even further results in thermal depinning of the remaining fixed vortex lines. On the other hand, the vortex lattice is not so strongly pinned in  $\text{NbSe}_2$ . When the applied magnetic field on  $\text{NbSe}_2$  was shifted by a small amount at low temperatures, the sample signal always shifted with the background signal.

The muon precession signals for  $\text{YBa}_2\text{Cu}_3\text{O}_{6.95}$  were fit in a manner similar to that for  $\text{NbSe}_2$ , with the following additional constraints and assumptions:

1. As explained in Ref. [2], because of the interplay between  $\lambda_{ab}$  and  $\sigma_f$ , which arises because of the poor statistics in the high-field tail, it was necessary to fix one of these parameters with respect to the other. In particular, the following linear correlation is assumed, based on the general trend observed in the fits performed without this constraint

$$\frac{1}{\lambda_{ab}^2} = \frac{\sqrt{\sigma_f^2 - \sigma_N^2}}{C} \approx \frac{\sigma_f}{C} \quad (7.1)$$

where  $C$  is a constant and  $\sigma_N$  is the Gaussian muon depolarization rate in the normal state.

2. An equilateral triangular vortex lattice is assumed for the summation over reciprocal lattice vectors  $\mathbf{K}$  in the theoretical field profile  $B(\mathbf{r})$ . As discussed in the previous chapter, this is a reasonable assumption because of the high pinning temperature in  $\text{YBa}_2\text{Cu}_3\text{O}_{6.95}$ . The cutoff in the summation was done in a way which preserves circular symmetry around the vortex cores. The symmetry of the cores themselves is of minor significance in determining  $\lambda_{ab}$ , since their contribution to the measured field distribution is small in the field range

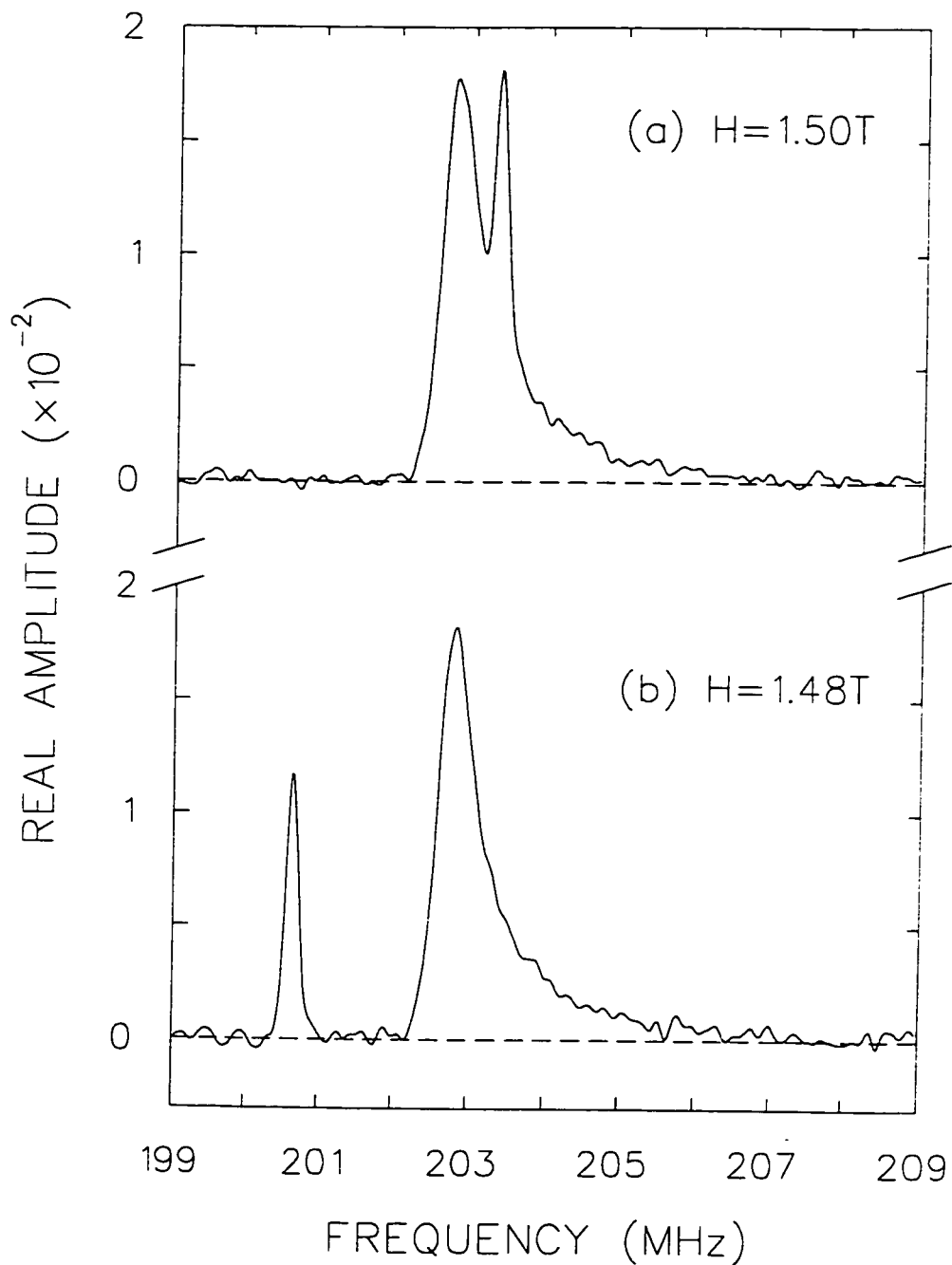


Figure 7.3: (a) The Fourier transform of the muon spin precession signal in “detwinned”  $\text{YBa}_2\text{Cu}_3\text{O}_{6.95}$  (O3) after field cooling to  $T = 5\text{ K}$  in a magnetic field  $H = 1.50\text{ T}$ . (b) Same as (a) except that the field was lowered by  $0.02\text{ T}$  while the sample was at  $T = 5\text{ K}$ .

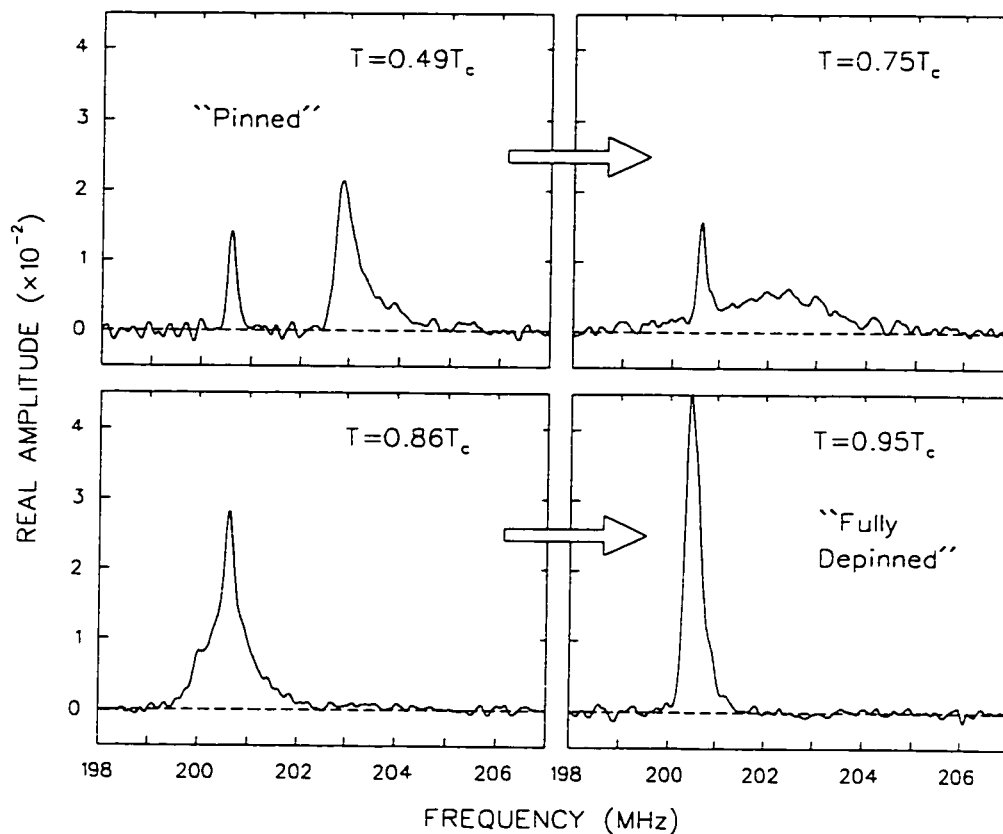


Figure 7.4: The "field-shifted"  $\mu\text{SR}$  frequency spectrum from Fig. 22(b) after warming to  $T = 0.49, 0.75, 0.86$  and  $0.95 T_c$ .

considered here. The theoretical triangular lattice does not include deformations of the vortex-lattice geometry due to mass anisotropy and/or twin planes. The in-plane mass anisotropy ratio  $\gamma = (m_a/m_b)^{1/2}$  has been measured by Basov *et al.* [172] in  $\text{YBa}_2\text{Cu}_3\text{O}_{6.95}$  using far infrared reflectance. They find that in single crystals similar to those used in the present study, the ratio of the zero-field penetration depths along the  $\hat{a}$  and  $\hat{b}$  directions is  $\gamma = \lambda_a/\lambda_b = 1.47(14)$ . A simple scaling argument [196] can be used to show that it is not necessary to incorporate the in-plane anisotropy  $\gamma$  into the field profile. The argument is as follows: The orthorhombic crystal structure for  $\text{YBa}_2\text{Cu}_3\text{O}_{6.95}$  implies that the effective masses along the crystallographic axes are such that  $m_c > m_a > m_b$ . When a magnetic field is applied along the  $\hat{c}$ -axis direction, three adjacent vortex lines form a lattice in the  $\hat{a}$ - $\hat{b}$  plane which is a stretched version of an isotropic triangular lattice [162]. The unit cell is a centered rectangular lattice and the supercurrents flow in an elliptical path around the vortex cores, since  $\gamma = \xi_b/\xi_a = \lambda_a/\lambda_b$ . However, the magnetic field distribution is unaltered from the isotropic case since any change in  $\gamma$  is compensated for by rescaling the coordinates in Eq. (4.10) or Eq. (4.13). Of course, this argument does not take into account pinning effects at twin planes. The Fourier transform of the measured muon precession signal in detwinned  $\text{YBa}_2\text{Cu}_3\text{O}_{6.95}$  (O3) [see Fig. 7.3], does however show the same basic features as that for the twinned crystals. The subtle differences that do exist between the  $\mu\text{SR}$  line shapes of twinned and detwinned crystals, in the field range considered here, can only be determined by fitting the data. Unfortunately, we have yet to carry out a complete study of detwinned  $\text{YBa}_2\text{Cu}_3\text{O}_{6.95}$ . A discussion regarding the effects of twin planes on the outcome of a  $\mu\text{SR}$  experiment in the vortex state will be reserved for the underdoped compound, which is considered later in this report.

3. Due to the absence of a sharp high-field cutoff in the field distribution at low temperatures, in previous attempts to model the measured field distribution in  $\text{YBa}_2\text{Cu}_3\text{O}_{6.95}$  (see Refs. [2.3]) the GL parameter  $\kappa = \lambda_{ab}/\xi_{ab}$  was fixed to a constant value. To obtain a reasonable value for  $\kappa$  some of the high temperature spectra in which the cutoff was clearly visible were fit and the results averaged to give a value of  $\kappa = 68$ . The low temperature data were fit by assuming this value and assuming that  $\kappa$  was independent of both temperature and magnetic field. Given the observed field-dependence of  $\kappa$  in  $\text{NbSe}_2$ , the latter assumption is likely invalid. Nevertheless, the fits in Refs. [2.3] were found to be not very sensitive to the value of  $\kappa$  anyway. For instance, as noted in Ref. [2], increasing  $\kappa$  to 73 changes  $\lambda_{ab}(0)$  by less than 3 Å. The data for the underdoped compound, which will be presented later in this report, confirm that the assumption of a  $T$ -independent  $\kappa$  is reasonable, but that an  $H$ -independent  $\kappa$  is not. The reason is likely related to the shrinking of the vortex cores with increasing magnetic field. In this thesis I have re-analyzed the  $\mu\text{SR}$  data from Ref. [3] in terms of the analytical GL model and in doing so, I allowed  $\kappa$  to vary “freely” in the fitting procedure.

Figure 7.5 shows the temperature dependence of  $\lambda_{ab}^{-2}$  in  $\text{YBa}_2\text{Cu}_3\text{O}_{6.95}$  (O1) at  $H = 0.5$  T, from fits assuming the analytical GL model [see Eq. (4.13)]. The linear temperature dependence at low  $T$  supports an unconventional pairing state in which there are nodes in the superconducting energy gap. The solid curve in Fig. 7.5 represents the zero-field microwave measurements of  $\Delta\lambda_{ab}(T) = \lambda_{ab}(T) - \lambda_{ab}(1.35 \text{ K})$  performed by Hardy *et al.* [14] on similar high quality  $\text{YBa}_2\text{Cu}_3\text{O}_{6.95}$  crystals. To plot  $\lambda_{ab}^{-2}(T)$  for the microwave data, our extrapolated value of  $\lambda_{ab}(1.35 \text{ K})$  was used. The excellent agreement between the measurements in the vortex state and those in the Meissner state

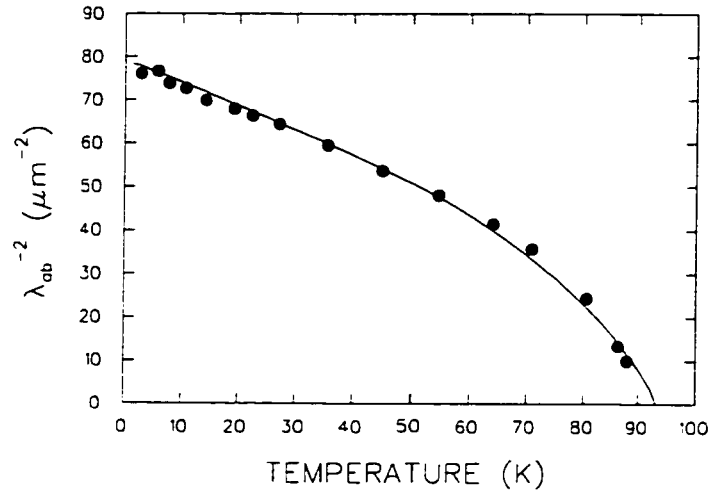


Figure 7.5: The temperature dependence of  $\lambda_{ab}^{-2}$  in  $\text{YBa}_2\text{Cu}_3\text{O}_{6.95}$  (O1) at  $H = 0.498$  T. The solid curve through the points represents the microwave measurements of Ref. [14] which are explained in the text.

indicate that the variation of the superfluid fraction as a function of temperature is identical in both phases. Furthermore, this confirms that the assumption of a triangular vortex lattice in the fitting procedure introduces at most only a small systematic error in the absolute value of  $\lambda_{ab}$ . This is reasonable since it has been shown theoretically that including additional terms in the free energy of the vortex state produces only minor changes in the internal field distribution [178]. This can be confirmed by fitting the data to a theoretical field profile which assumes an inappropriate vortex-lattice configuration. For instance, if a square vortex lattice is assumed in the fitting procedure, the quality of the fits is found to be much worse and the absolute value of  $\lambda_{ab}(T)$  does change dramatically. However, the temperature dependence of  $\lambda_{ab}(T) - \lambda_{ab}(0)/\lambda_{ab}(0)$  from these fits is nearly identical to that obtained assuming a triangular vortex lattice.

Our  $\mu\text{SR}$  measurements of  $\lambda_{ab}(T)$  presented in Ref. [2] suggest that the strength of the term linear in  $T$  depends on magnetic field. However, as noted in Ref. [3], this

effect is artificially created by prematurely cutting off the summation over reciprocal lattice vectors. The problem is easily rectified by increasing the sum until any further increase does not affect the deduced value of  $\lambda_{ab}(T)$ . Although the term linear in  $T$  is found to be  $H$ -independent here,<sup>2</sup> the absolute value of  $\lambda_{ab}$  does depend strongly on magnetic field. In Ref. [3],  $\lambda_{ab}$  was measured in the vortex state of  $\text{YBa}_2\text{Cu}_3\text{O}_{6.95}$  (O1, O2) as a function of magnetic field. The internal field distribution was fit assuming the ML model with a Gaussian cutoff factor. The results of this study are listed in Table 7.4. Yaouanc *et al.* [121] suggest that the observed field dependence is probably explained if a more appropriate cutoff function is used. Using the conventional GL equations, they have shown that the variance of the field distribution  $\Delta_c^2 = (\langle B_c^2 \rangle - \langle B_c \rangle^2)$  depends on magnetic field. Through rough calculations of the variance from our measurements in Ref. [2], they find good agreement with the field dependence predicted by the conventional GL theory. Unfortunately, as noted above, the results in Ref. [2] are flawed. The field dependence for  $\lambda_{ab}$  has since been shown to be much stronger [3]. It is unlikely that this field dependence is related to an improper treatment of the vortex cores, since the small cores in  $\text{YBa}_2\text{Cu}_3\text{O}_{6.95}$  contribute very little to the variance at low fields. Nevertheless, to properly account for the finite size of the vortex cores, the data has been re-analyzed here using the analytical GL model as suggested by the authors of Ref. [121].

Figure 7.6 shows the low temperature behaviour of  $\lambda_{ab}^{-2}$  in  $\text{YBa}_2\text{Cu}_3\text{O}_{6.95}$  (O2) obtained from this new analysis for three of the magnetic fields considered. As in Ref. [3], excellent fits are obtained to a linear relation

$$\lambda_{ab}^{-2}(T) = \lambda_{ab}^{-2}(0)[1 - \alpha t], \quad (7.2)$$

where  $t = T/T_c$  and  $T_c$  is the transition temperature at zero magnetic field. The results

---

<sup>2</sup>This assumes that  $\lambda_{ab}^{-2}(T)$  is normalized as in Eq. (7.2).



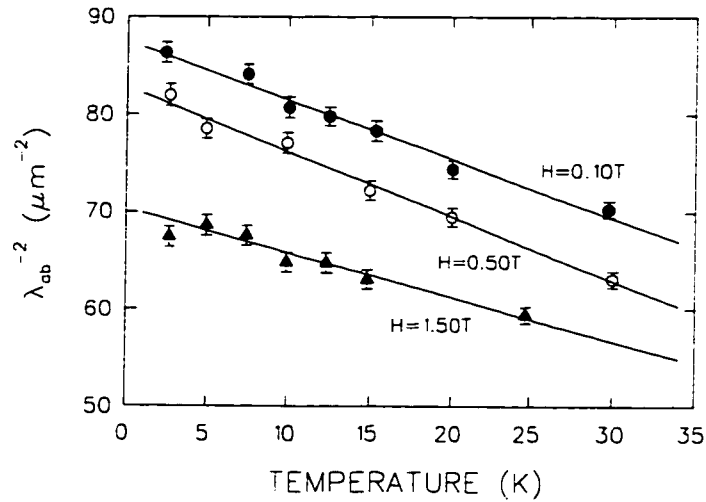


Figure 7.6: The temperature dependence of  $\lambda_{ab}^{-2}$  in  $\text{YBa}_2\text{Cu}_3\text{O}_{6.95}$  (O2) for magnetic fields of  $H = 0.10$  T (solid circles),  $0.50$  T (open circles) and  $1.50$  T (solid triangles).

of these fits appear in Table 7.4. The term linear in  $T$  is essentially independent of magnetic field, so that  $\alpha$  agrees well with the microwave cavity measurements of Ref. [14] at all magnetic fields considered.

Figure 7.7 shows the magnetic field dependence of  $\lambda_{ab}$  extrapolated to  $T = 0$  for sample O1 (open circles) and sample O2 (solid circles). The solid and dashed curves are fits to the power-law relation

$$\lambda_{ab}(H, T=0) = \lambda_{ab}(0, 0) + \beta H^p. \quad (7.3)$$

Table 7.5 shows the parameters from these fits together with those from the analysis in Ref. [3]. Over this narrow field range the data is reasonably described by a relation which depends linearly on  $H$ . Moreover, the strength of this linear term is essentially the same in both types of analysis, as found for  $\text{NbSe}_2$ . This is reasonable here, since the fits are not very sensitive to the field distribution near the vortex cores. The scatter in the data is remarkably small given the variety of conditions under which they were

| Magnetic Field [T] | Beamline/Year | $C$<br>[ $10^6 \text{ \AA}^2/\mu\text{s}$ ] | Modified London Model                   |                           | Analytical GL Model                     |                           |
|--------------------|---------------|---|---|---------------------------|---|---------------------------|
|                    |               |   | $\lambda_{ab}(T=0)$<br>[ $\text{\AA}$ ] | $\alpha$<br>[ $10^{-1}$ ] | $\lambda_{ab}(T=0)$<br>[ $\text{\AA}$ ] | $\alpha$<br>[ $10^{-1}$ ] |
| (i)                |               |   |   |                           |   |                           |
| 0.191              | m20/1993      | 1.955                                       | 1188(8)                                 | 6.0(3)                    | 1115(7)                                 | 4.8(4)                    |
| 0.192              | m15/1993      | 1.943                                       | 1181(7)                                 | 6.5(6)                    | 1114(6)                                 | 6.2(2)                    |
| 0.498              | m15/1992      | 1.835                                       | 1208(13)                                | 6.6(3)                    | 1129(12)                                | 6.3(2)                    |
| 0.731              | m15/1994      | 1.827                                       | 1222(20)                                | 6.3(5)                    | 1165(18)                                | 6.3(4)                    |
| 1.003              | m15/1993      | 1.625                                       | 1228(16)                                | 6.3(4)                    | 1168(12)                                | 6.0(4)                    |
| 1.488              | m15/1992      | 1.784                                       | 1272(7)                                 | 5.8(4)                    | 1195(6)                                 | 5.9(4)                    |
| 1.952              | m15/1993      | 2.275                                       | 1351(37)                                | 7.3(7)                    | 1261(34)                                | 5.5(8)                    |
| (ii)               |               |   |   |                           |   |                           |
| 0.103              | m20/1995      | 1.195                                       | 1149(6)                                 | 6.2(2)                    | 1069(6)                                 | 6.4(4)                    |
| 0.497              | m20/1995      | 1.485                                       | 1171(9)                                 | 7.5(4)                    | 1099(9)                                 | 7.5(3)                    |
| 1.500              | m20/1995      | 1.833                                       | 1277(14)                                | 6.6(6)                    | 1192(12)                                | 6.1(7)                    |

Table 7.4: Parameters from fits of  $\lambda_{ab}^{-2}(T)$  to Eq. (7.2) for (i) sample O1 and (ii) sample O2. The constant  $C$  is defined in Eq. (7.1).

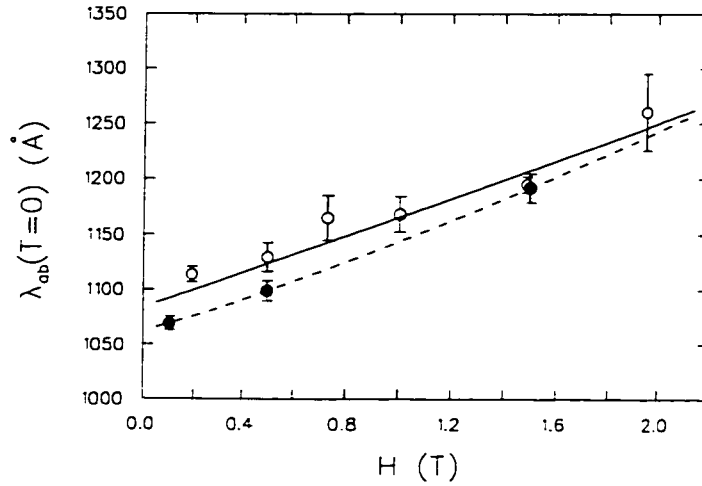


Figure 7.7: The magnetic field dependence of  $\lambda_{ab}$  extrapolated to  $T = 0$  in  $\text{YBa}_2\text{Cu}_3\text{O}_{6.95}$  (O1) (open circles) and  $\text{YBa}_2\text{Cu}_3\text{O}_{6.95}$  (O2) (solid circles).

recorded (see Table 7.4). This demonstrates the reliability of the fitting procedure for extracting a consistent value of  $\lambda_{ab}$ , despite variations in the experimental arrangement which cause changes in the size of the background signal. Although the fits to Eq. (7.3) suggest that  $\lambda_{ab}(T = 0) \propto H$  in the vortex state, the measurements are only for very small values of reduced field,  $0.0009 < h < 0.016$  (assuming<sup>3</sup> that  $H_{c2}(0) = 120$  T), so that it is difficult to draw any firm conclusion about the precise way in which  $\lambda_{ab}$  varies with  $H$ .

The strong field dependence for  $\lambda_{ab}$  in  $\text{YBa}_2\text{Cu}_3\text{O}_{6.95}$  is obtained from both types of analysis, and is considerably stronger than that found in  $\text{NbSe}_2$ . Figure 7.8 shows the field dependence of  $\lambda_{ab}$  at  $T = 0.33 T_c$  for both of these materials. The solid lines are a fit to the equation

$$\frac{\lambda_{ab}(H)}{\lambda_{ab}(0)} = 1 + \varepsilon \left[ \frac{H}{H_{c2}(0.33 T_c)} \right]. \quad (7.4)$$

<sup>3</sup>The lower limit for  $H_{c2}(0)$  in  $\text{YBa}_2\text{Cu}_3\text{O}_7$  is 120 T according to measurements which are summarized in a table on p.338 of Ref. [207].

| Modified London Model      |                  |        | Analytical GL Model        |                  |          |
|----------------------------|------------------|--------|----------------------------|------------------|----------|
| $\lambda_{ab}(0.0)$<br>[Å] | $\beta$<br>[Å/T] | $p$    | $\lambda_{ab}(0.0)$<br>[Å] | $\beta$<br>[Å/T] | $p$      |
| (i)<br>1181(4)             | 52(4)            | 1.5(1) | 1084(3)                    | 81(1)            | 1.0(1)   |
| (ii)<br>1147(5)            | 71(8)            | 1.5(2) | 1063(2)                    | 80(3)            | 1.16(12) |

Table 7.5: Parameters from fits of  $\lambda_{ab}(H, T=0)$  to Eq. (7.3) for (i) sample O1 and (ii) sample O2.

where  $\varepsilon = 1.6$  with  $H_{c2}(0.33 T_c) = 2.9$  T for  $\text{NbSe}_2$  and  $\varepsilon = 5.4$  for  $\text{YBa}_2\text{Cu}_3\text{O}_{6.95}$ , assuming  $H_{c2}(0.33 T_c) = 95$  T. Undoubtedly some of the field dependence is due to the effects of a nonlinear supercurrent response, similar to that observed in the Meissner state. However, as noted earlier, nonlocal effects associated with nodes at the Fermi surface should be more important in  $\text{YBa}_2\text{Cu}_3\text{O}_{6.95}$ .

Figure 7.9 shows the temperature dependence of the linear coefficient  $\beta_2(T)$  determined from Eq. (2.50) for  $\text{YBa}_2\text{Cu}_3\text{O}_{6.95}$  (O1). The large error bars are due to the scatter and to temperature variations between the different data sets. The scatter in the data at each temperature was too large to deduce the precise field dependence, so a linear dependence on  $H$  was assumed. The finite value of  $\beta_2(T)$  at  $T=0$  is consistent with the field-induced pair breaking effects expected in a superconductor with nodes in the energy gap. We note that  $\beta_2(T)$  is approximately 30 times smaller at low  $T$  and about 10 times smaller at  $T \approx 0.5 T_c$  than the values reported by Maeda *et al.* [38] for microwave cavity perturbation measurements in the Meissner state of  $\text{YBa}_2\text{Cu}_3\text{O}_{7-\delta}$ . However, very recently Bidinosti *et al.* [208] have determined the field dependence

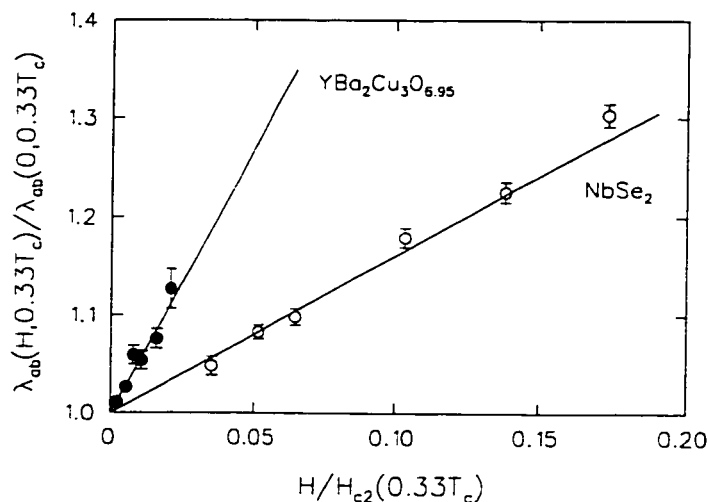


Figure 7.8: The magnetic field dependence of  $\lambda_{ab}(H)/\lambda_{ab}(0)$  in  $\text{YBa}_2\text{Cu}_3\text{O}_{6.95}$  (O1) (solid circles) and  $\text{NbSe}_2$  (open circles) at  $T = 0.33 T_c$ .

of  $\Delta\lambda_{ab}$  in  $\text{YBa}_2\text{Cu}_3\text{O}_{6.95}$  in the Meissner state from AC susceptibility measurements. They find that the coefficient of the term linear in  $H$  is approximately an order of magnitude smaller than that reported by Maeda *et al.* Nevertheless, the different definition of the penetration depth in the  $\mu\text{SR}$  experiment (which was discussed earlier) makes a comparison to these Meissner state experiments very difficult.

It is possible that some of the measured field dependence for  $\lambda_{ab}$  is due to changes in the vortex-lattice geometry with increasing magnetic field—which is predicted in a number of theoretical studies [178,179,180]. It is currently unknown if such geometry changes actually occur. However, if they do, the question is whether these changes are subtle over the narrow field range considered here. We now show that the fits to the data suggest that there are no significant changes in the vortex-lattice geometry. This does not necessarily imply that the theories are wrong, since the strong pinning of the vortex lines in the  $\text{YBa}_2\text{Cu}_3\text{O}_{6.95}$  samples studied here likely prevents such geometrical

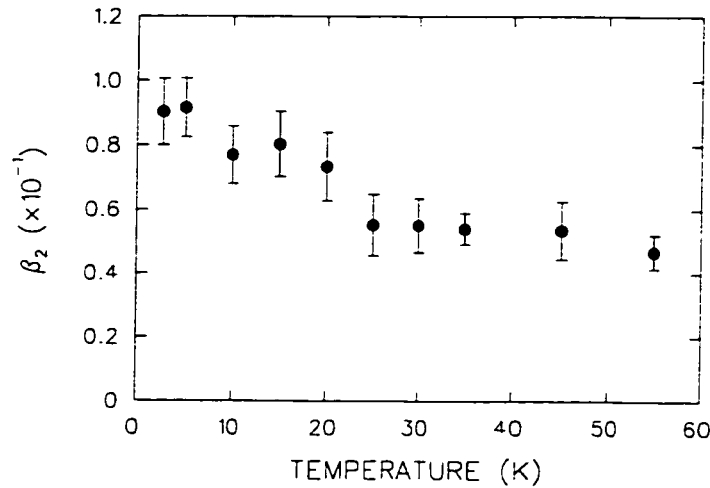


Figure 7.9: The temperature dependence of the coefficient  $\beta_2(T)$  of the term linear in  $H$  [see Eq. (2.50)] in  $\text{YBa}_2\text{Cu}_3\text{O}_{6.95}$  (O1).

changes from occurring.

Figure 7.10(a) shows the temperature dependence of the additional broadening parameter  $\sigma_f$  in  $\text{YBa}_2\text{Cu}_3\text{O}_{6.95}$  (O1) at  $H = 0.19$  T (open circles) and  $H = 1.48$  T (solid circles). Due to the imposed constraint of Eq. (7.1),  $\sigma_f(T)$  exhibits the same linear dependence on  $T$  as  $\lambda_{ab}^{-2}(T)$ . Despite this constraint, we find that  $\sigma_f(0.19 \text{ T}) > \sigma_f(1.48 \text{ T})$ , while  $\lambda_{ab}^{-2}(0.19 \text{ T}) > \lambda_{ab}^{-2}(1.48 \text{ T})$ —which implies that the line width of the measured internal field distribution is definitely larger at smaller fields.

The RMS displacement  $\langle s^2 \rangle^{1/2}$  of the vortex lines from their ideal positions in a perfect triangular lattice [determined from Eq. (6.3)], is plotted as a function of temperature in Fig. 7.11(a)<sup>4</sup>. The value of  $\langle s^2 \rangle^{1/2}$  is much larger at  $H = 0.19$  T than at  $H = 1.48$  T. This is most likely due to an enhancement in the random pinning of vortex

<sup>4</sup>In  $\text{YBa}_2\text{Cu}_3\text{O}_{7-\delta}$ , the muon depolarization rate in the normal state  $\sigma_N$  is extremely small, so that  $\sigma_{\text{dis}} \approx \sigma_f$ .

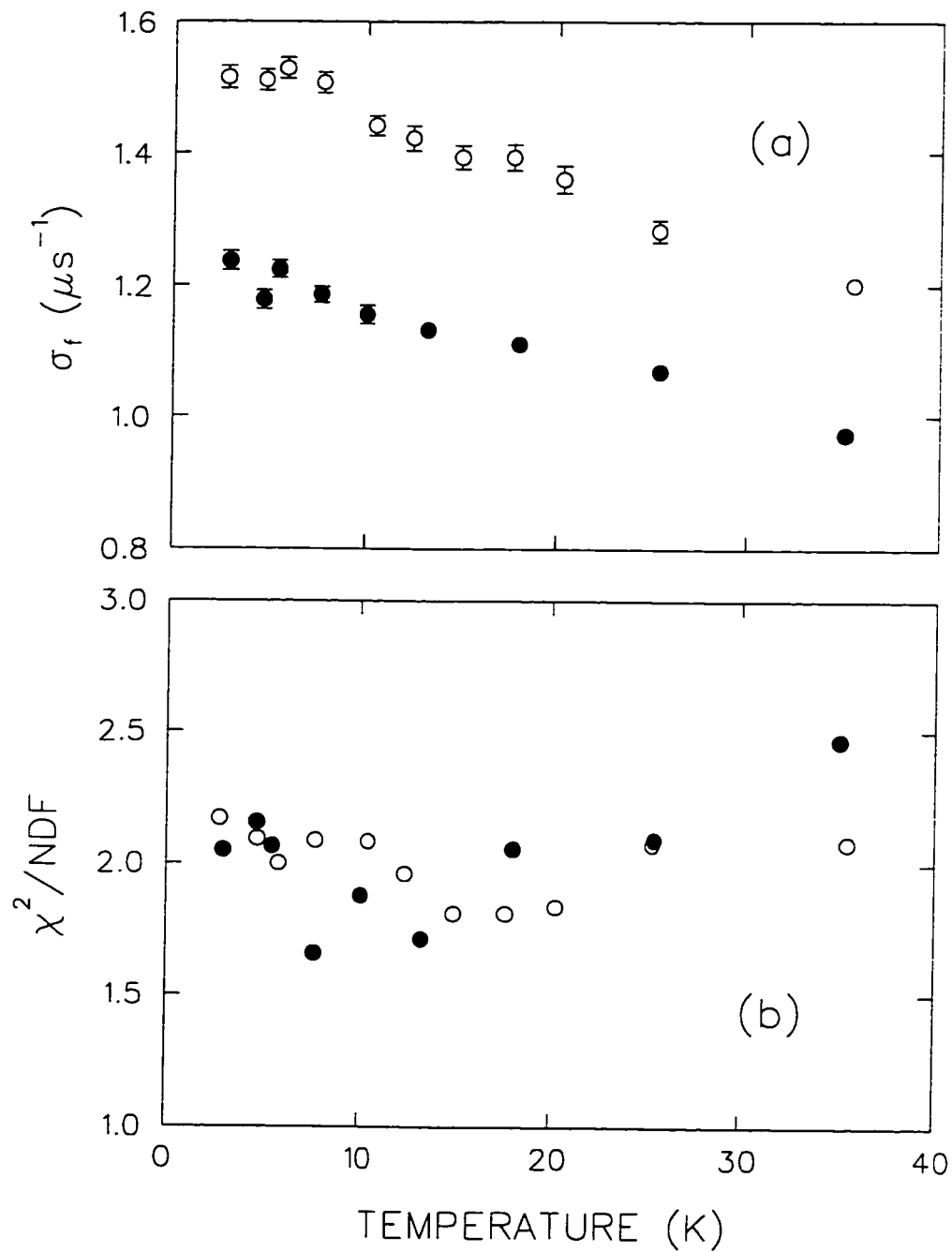


Figure 7.10: The temperature dependence of (a) the additional broadening parameter  $\sigma_f$  and (b) the ratio of  $\chi^2$  to the number of degrees of freedom (NDF) for  $\text{YBa}_2\text{Cu}_3\text{O}_{6.95}$  (O1) at  $H = 0.192$  T (open circles) and  $H = 1.488$  T (solid circles).

lines by point defects at the smaller magnetic field. Figure 7.11(b) shows  $\langle s^2 \rangle^{1/2}$  as a percentage of  $L$  in  $\text{YBa}_2\text{Cu}_3\text{O}_{6.95}$  (O1). The close agreement at the two different magnetic fields suggests that at low temperatures, where thermal fluctuations are small, the disorder in the vortex lattice scales with the nearest-neighbor distance between vortex lines, as was found in  $\text{NbSe}_2$ . This result is inconsistent with a dramatic change in the vortex-lattice geometry in going from  $H = 0.19$  T to  $H = 1.48$  T at low  $T$ . Further evidence that there are no significant distortions in the vortex lattice over this narrow field range is given by the consistency in the quality of the fits assuming a triangular vortex lattice. Figure 7.10(b) shows that  $\chi^2$  normalized to the number of degrees of freedom is essentially independent of magnetic field and temperature in the region of the phase diagram considered in this experiment. Certainly this would not be the case if there were a sharp transition *e.g.* from a triangular to a fourfold-symmetric vortex lattice.

Figure 7.12 shows the temperature dependence of  $\kappa$  in  $\text{YBa}_2\text{Cu}_3\text{O}_{6.95}$  (O1) at the different magnetic fields considered. The scatter in the data reflects the uncertainty which arises in fitting a field distribution which has a small signal-to-noise ratio in the high-field tail. Surprisingly, there is less scatter in the data at the lower fields where there are fewer vortices in the sample. This suggests that the vortex-core radius must be significantly larger at smaller  $H$ , as was the case in  $\text{NbSe}_2$ . The data in Fig. 7.12 suggests that  $\kappa$  is either independent of temperature or increases very weakly with increasing  $T$ . However,  $\kappa$  depends strongly on magnetic field in  $\text{YBa}_2\text{Cu}_3\text{O}_{6.95}$ . Figure 7.13 shows the best fits to the data sets at the different magnetic fields in Fig. 7.12, assuming a  $T$ -independent value of  $\kappa$ . The solid line in Fig. 7.13 is a fit to the linear relation

$$\kappa(H) = \kappa(0)[1 + \eta h]. \quad (7.5)$$



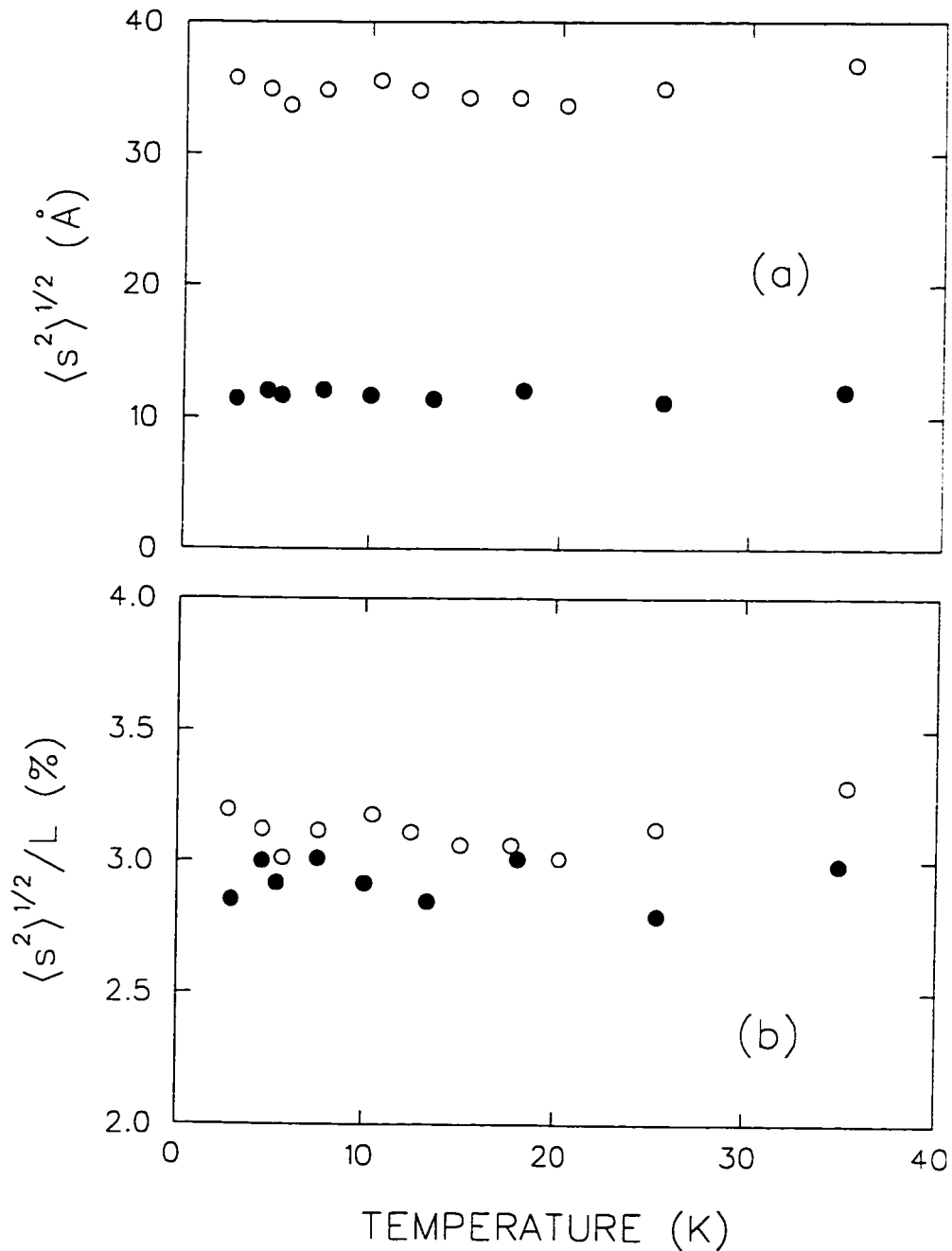


Figure 7.11: The temperature dependence of (a) the RMS displacement  $\langle s^2 \rangle^{1/2}$  of the vortices from their ideal positions and (b)  $\langle s^2 \rangle^{1/2}$  expressed as a percentage of the intervortex spacing  $L$ . The data is for  $\text{YBa}_2\text{Cu}_3\text{O}_{6.95}$  (O1) at  $H = 0.192$  T (open circles) and  $H = 1.488$  T (solid circles).

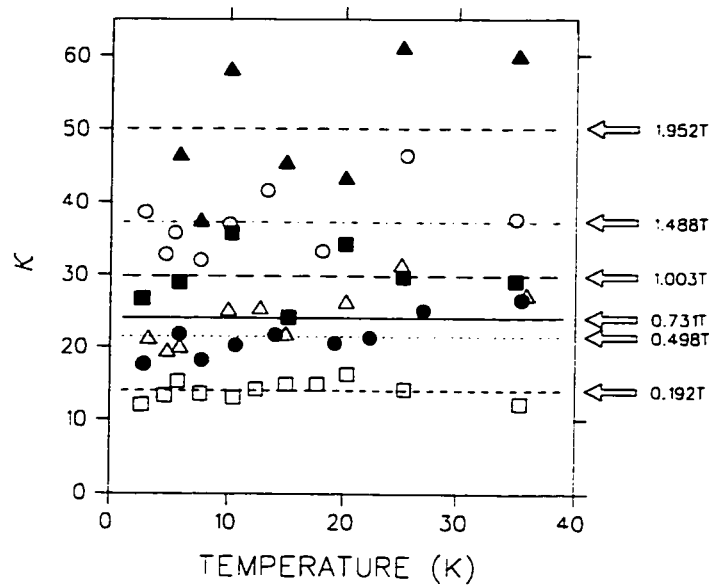


Figure 7.12: The temperature dependence of  $\kappa = \lambda_{ab}/\xi_{ab}$  in  $\text{YBa}_2\text{Cu}_3\text{O}_{6.95}$  (O1) at  $H = 0.192$  T (open squares),  $0.498$  T (solid circles),  $0.731$  T (open triangles),  $1.003$  T (solid squares),  $1.488$  T (open circles) and  $1.952$  T (solid triangles).

where  $h = H/H_{c2}(0)$  and  $H_{c2}(0) = 120$  T. The best fit is obtained for  $\kappa(0) = 10.6(3)$  and  $\eta = 212(10)$ .

Figure 7.14 shows the first  $1.5 \mu\text{s}$  of a typical muon precession signal in  $\text{YBa}_2\text{Cu}_3\text{O}_{6.95}$  displayed in a reference frame rotating at about  $3.3$  MHz below the Larmor precession frequency of a free muon. The curves through the data points are examples of fits (actually performed over the first  $6 \mu\text{s}$ ) to the theoretical polarization function for fixed values of  $\xi_{ab}$ . The only additional constraint in these fits was that  $\sigma_f \propto \lambda_{ab}^{-2}$ . Differences in the quality of the fits for the various values of  $\xi_{ab}$  are most noticeable at early times. This is seen more clearly in Fig. 7.15 which shows the difference between the data points and the fitted curve for fits similar to those in Fig. 7.14. The ratio of  $\chi^2$  to the number of degrees of freedom (NDF) is shown in Fig. 7.16(a) as a function of

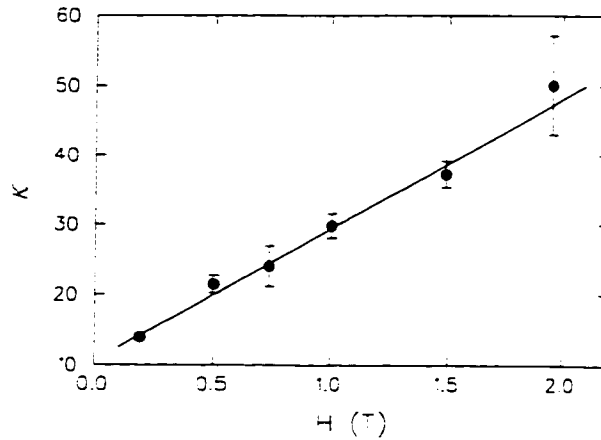


Figure 7.13: The magnetic field dependence of  $\kappa = \lambda_{ab}/\xi_{ab}$  in  $\text{YBa}_2\text{Cu}_3\text{O}_{6.95}$  (O1) extrapolated to  $T=0$ .

$\xi_{ab}$  for two of the magnetic fields considered. Figure 7.16(b) shows the values of the free parameter  $\kappa$  obtained from the same fits as in Fig. 7.16(a). Note that the distribution of data points around the minimum value of  $\chi^2/\text{NDF}$  is asymmetric. Since  $\lambda_{ab}$  is essentially unchanged in the fits for different values of  $\xi_{ab}$ , this asymmetry reflects the lack of statistics from the vortex cores in the measured internal field distribution. In particular, the fits can tolerate a smaller value of  $\xi_{ab}$  and a longer high-field tail. At the lower field in Fig. 7.16, the minimum is much sharper because of the increased size of the vortex cores.

Despite the scatter in the data for  $\kappa(T)$ , a smooth plot for the temperature dependence of  $\xi_{ab}$  can be generated from Eq. (7.2) for  $\lambda_{ab}(T)$  and the fitted constant values of  $\kappa(T)$ . Such plots are shown in Fig. 7.17 at different magnetic fields where  $\xi_{ab}(T)$  is given by the following relation

$$\xi_{ab}(T) = \frac{\lambda_{ab}(T)}{\kappa(T)} = \frac{\lambda_{ab}(0)}{\kappa(0)\sqrt{1-\alpha t}}. \quad (7.6)$$

The values of  $\alpha$  are given in Table 7.4. The strength of the  $T$ -dependence of  $\xi_{ab}$  is

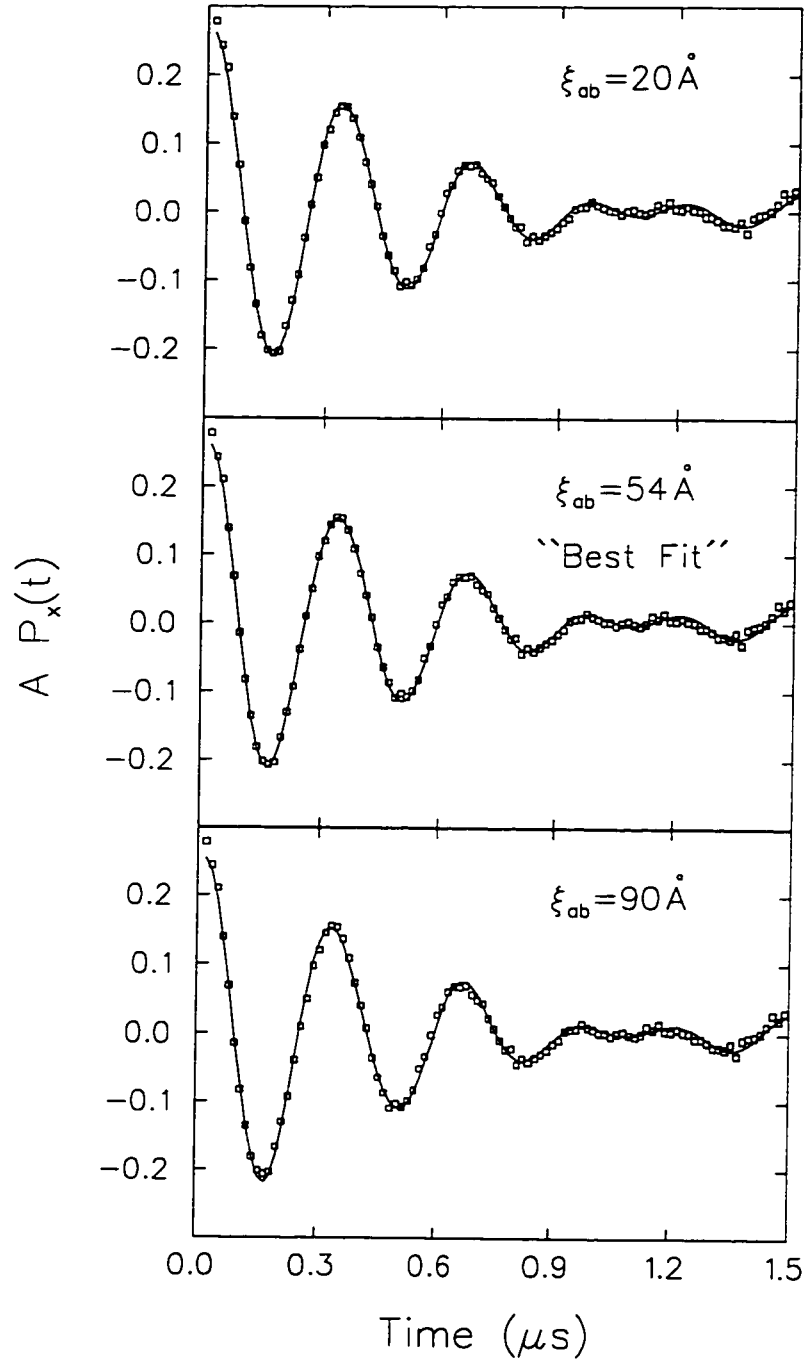


Figure 7.14: The muon spin precession signal in  $\text{YBa}_2\text{Cu}_3\text{O}_{6.95}$  after field cooling to  $T = 5.8 \text{ K}$  in a magnetic field  $H = 0.498 \text{ T}$ . The solid curves are fits to the theoretical muon polarization function assuming the field profile from the analytical GL model with fixed values of  $\xi_{ab}$  (i.e. 20, 54 and 90  $\text{ \AA}$ ).

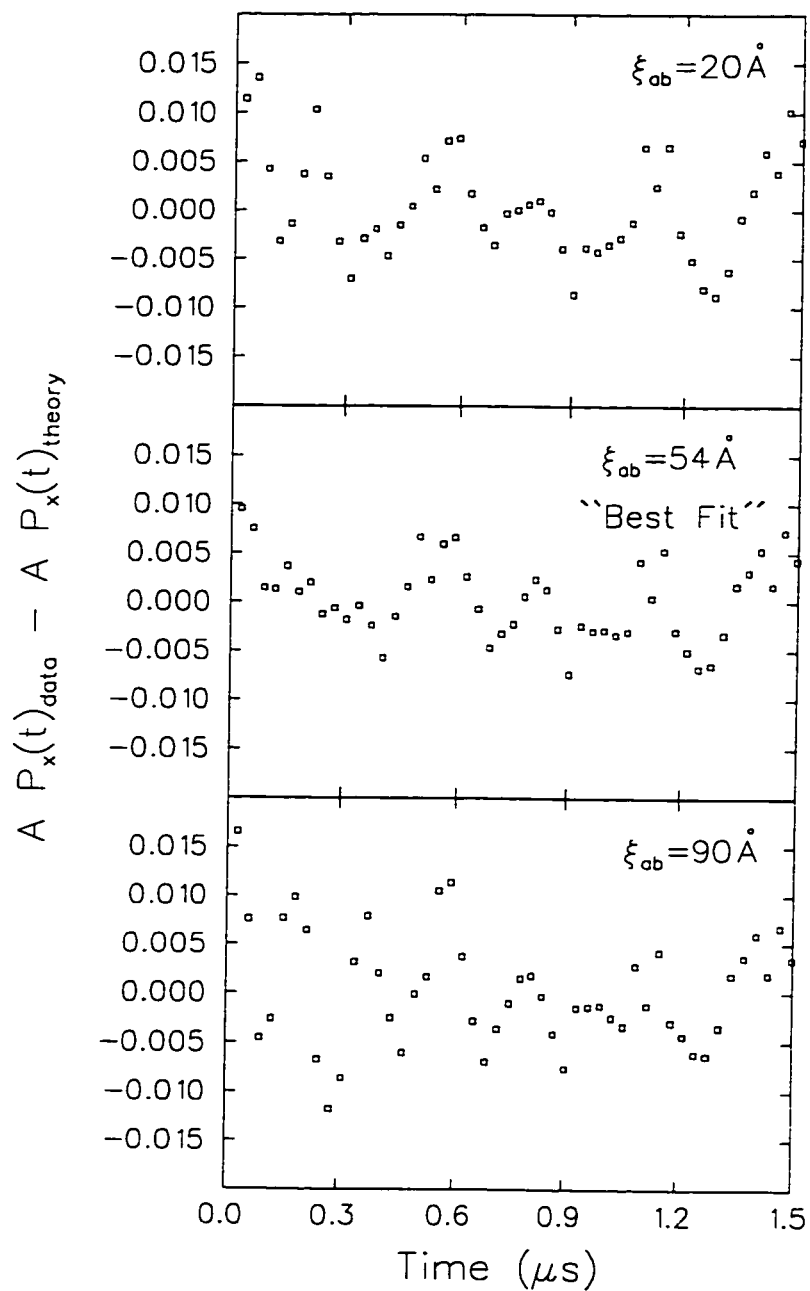


Figure 7.15: The difference between the measured  $\mu\text{SR}$  spectrum and the theoretical muon polarization function for fits similar to those in Fig. 7.14 but with the bin size doubled.

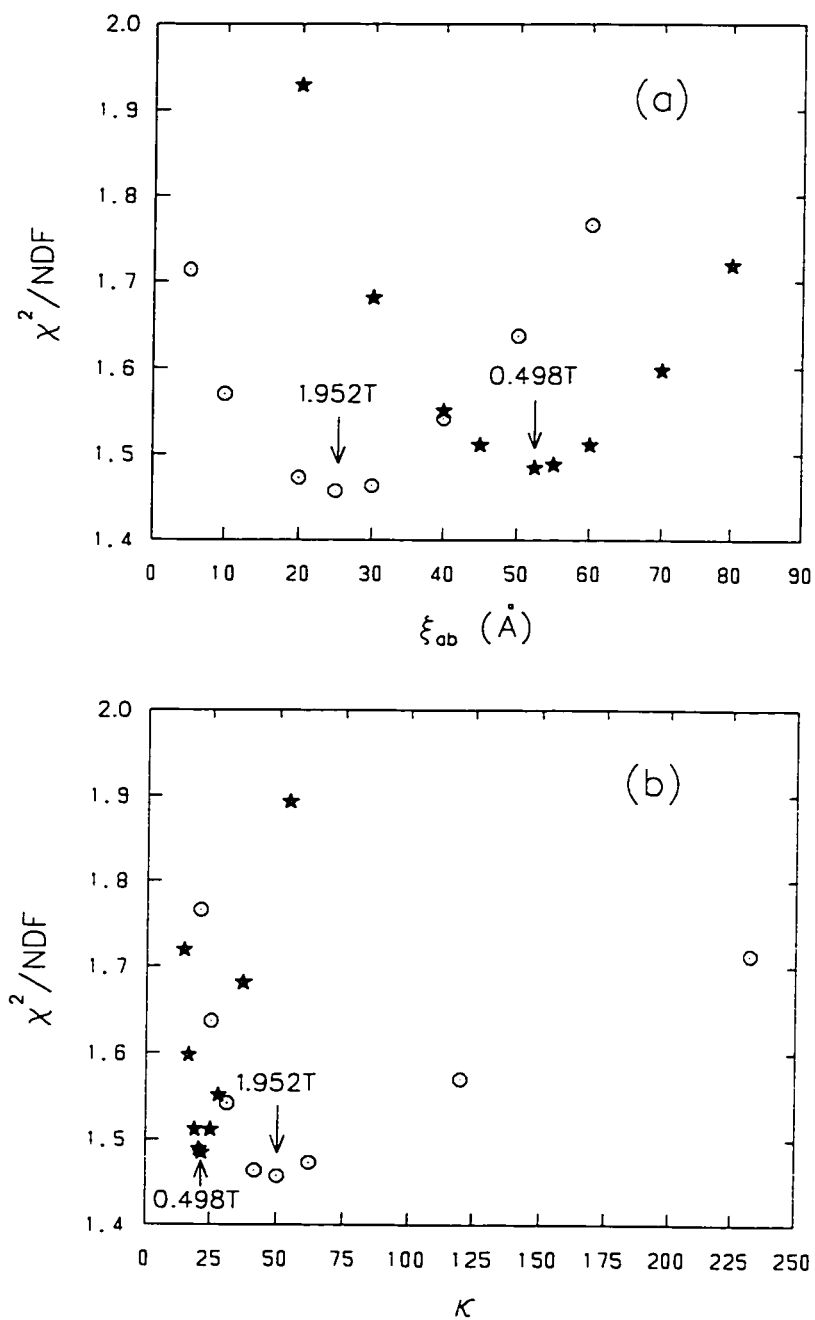


Figure 7.16: The ratio of  $\chi^2$  to the number of degrees of freedom (NDF) as a function of (a)  $\xi_{ab}$  and (b)  $\kappa$  (from the same fits) for  $H = 0.498$  T (stars, NDF=1148) and  $H = 1.952$  T (circles, NDF=1196) at  $T = 5.8$  K.

considerably weaker than in  $\text{NbSe}_2$ . It should be noted that thermal fluctuations of the vortex lines will lead to an increase in the measured size of the vortex cores, as explained in section 4.2. As in  $\text{NbSe}_2$ , there is a clear reduction in the magnitude of  $\xi_{ab}$  with increasing magnetic field, which is consistent with a shrinking of the vortex cores due to the increased strength of the vortex-vortex interactions.

The magnetic field dependence of  $\xi_{ab}$  extrapolated to  $T = 0$  is shown in Fig 7.18. The solid curve represents the combination of the fitted relations for  $\lambda_{ab}(H)$  and  $\kappa(H)$ , namely, Eq. (7.3) and Eq. (7.5). Recall that in the data analysis assuming the analytical GL model it was found that  $p \approx 1$  in Eq. (7.3), so that the relation for  $\xi_{ab}(H)$  at  $T = 0$  is

$$\xi_{ab}(H, 0) = \frac{\lambda_{ab}(H, 0)}{\kappa(H, 0)} = \xi_{ab}(0, 0) \frac{[1 + \beta' h]}{[1 + \eta h]}. \quad (7.7)$$

where  $\xi_{ab}(0, 0) = \lambda_{ab}(0, 0)/\kappa(0, 0) = 102 \text{ \AA}$ ,  $\beta' = \beta H_{c2}(0)/\lambda_{ab}(0) = 8.97$  and  $\eta = 212$  using the values in Table 7.5.

Our findings are most easily interpreted in terms of vortex cores which contain discrete quasiparticle bound states. At  $H = 6 \text{ T}$ , which is the field at which the STM experiment [197] on  $\text{YBa}_2\text{Cu}_3\text{O}_{7-\delta}$  was performed, Eq. (7.7) gives  $\xi_{ab}(T = 0) = 12.8 \text{ \AA}$  and with the help of Eq. (7.6) gives  $\xi_{ab}(T = 4.2 \text{ K}) = 13.0 \text{ \AA}$ . Using the formula  $E_\mu = 2\mu\Delta_0^2/E_F$  [124] and taking  $\xi_{ab}(T = 0)$  to be the BCS coherence length  $\xi_0 = \hbar v_f/\pi\Delta_0$ , the lowest bound energy level is estimated to be  $E_{1/2} = 2\hbar^2/m_e\pi^2\xi_{ab}^2 \approx 9.1 \text{ meV}$ . This estimate agrees well with the STM result of  $E_{1/2} = 5.5 \text{ meV}$  and the value of  $9.5 \text{ meV}$  obtained from an infrared absorption experiment [198] on  $\text{YBa}_2\text{Cu}_3\text{O}_{7-\delta}$  thin films. The STM measurement implies that  $\xi_{ab} \approx 17 \text{ \AA}$  at  $6 \text{ T}$ . The moderate agreement found here strongly supports our assertion that the coherence length rises appreciably with decreasing magnetic field. This is one of the most important findings of this study, because theoretical predictions and the interpretation of experiments on the high- $T_c$

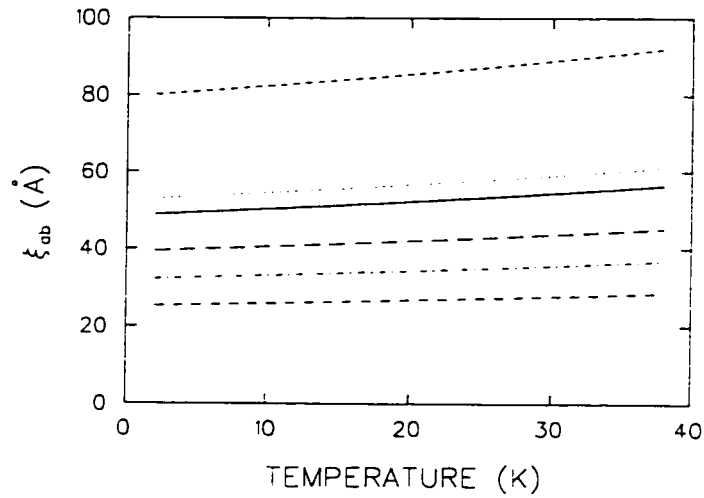


Figure 7.17: The temperature dependence of  $\xi_{ab}$  in  $\text{YBa}_2\text{Cu}_3\text{O}_{6.95}$  (O1) at the same magnetic fields as in Fig. 7.12. The magnetic field increases from the top curve ( $H = 0.192$  T) to the bottom curve ( $H = 1.952$  T).

materials are often based on the assumption that  $\xi_{ab}$  is extremely small. The results herein imply that the spacing between energy levels becomes larger with increasing magnetic field because of the reduction in  $\xi_{ab}$ —which is analogous to a reduction in the radius of a cylindrical potential well. In this picture numerous bound states should exist in the vortex cores of  $\text{YBa}_2\text{Cu}_3\text{O}_{6.95}$  at low fields (*i.e.*  $< 1$  T).



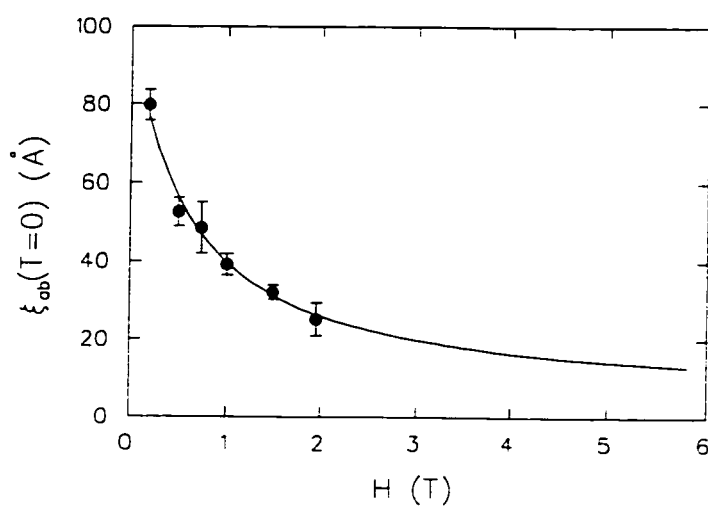


Figure 7.18: The magnetic field dependence of  $\xi_{ab}$  in  $\text{YBa}_2\text{Cu}_3\text{O}_{6.95}$  (O1) extrapolated to  $T=0$ . The solid curve is given by Eq. (7.7).

## Chapter 8

### Experiment: $\text{YBa}_2\text{Cu}_3\text{O}_{6.60}$

In this chapter, recent  $\mu\text{SR}$  measurements of the  $\hat{a}-\hat{b}$  plane magnetic penetration depth  $\lambda_{ab}$  and the vortex core size ( $\sim \xi_{ab}$ ) in the high- $T_c$  superconductor  $\text{YBa}_2\text{Cu}_3\text{O}_{6.60}$  are presented.

Figure 8.1 shows the  $\mu\text{SR}$  line shapes for the underdoped compound  $\text{YBa}_2\text{Cu}_3\text{O}_{6.60}$  (U1) and the optimally doped compound  $\text{YBa}_2\text{Cu}_3\text{O}_{6.95}$  (O1), at similar temperature and magnetic field. The width of the field distribution in the underdoped compound is considerably smaller due to a larger  $\lambda_{ab}$ . Furthermore, the high-field cutoff is much more pronounced due to both a larger vortex-core radius and the longer  $\lambda_{ab}$ . In the analysis that follows, it is found that at  $H = 1.49$  T the fractional volume of the sample occupied by the vortex cores in  $\text{YBa}_2\text{Cu}_3\text{O}_{6.60}$  is nearly two times greater than in  $\text{YBa}_2\text{Cu}_3\text{O}_{6.95}$ .

Figure 8.2 shows what happens to the internal field distribution in  $\text{YBa}_2\text{Cu}_3\text{O}_{6.60}$  upon warming the sample in an applied field of 1.49 T. In going from  $T = 0.04 T_c$  (see Fig. 8.1) to  $T = 0.42 T_c$  (*i.e.* 24.8 K), the asymmetry of the line shape suggests that the vortex lattice is comprised of 3D-flux lines arranged in a regular pattern. However, at  $T = 0.59 T_c$  the line shape becomes more symmetric, and is completely symmetric at  $T = 0.76 T_c$ . The loss of asymmetry in the  $\mu\text{SR}$  line shape is a strong indication that the vortex lattice has melted and/or it has undergone a 3D-to-2D transition. In order for  $\lambda_{ab}(H, T)$  and  $\xi_{ab}(H, T)$  to be determined in  $\text{YBa}_2\text{Cu}_3\text{O}_{6.60}$  using  $\mu\text{SR}$  spectroscopy.

a rigid 3D-vortex lattice must exist. We will therefore begin by restricting ourselves to the low-temperature region of the  $H$ - $T$  phase diagram, and reserve the discussion of the vortex lattice in  $\text{YBa}_2\text{Cu}_3\text{O}_{6.60}$  at higher temperatures till the end of this section.

Due to the larger contribution of the vortex cores to the measured internal field distribution, it is unnecessary to relate or fix any of the parameters in the fitting procedure. In this way the data is analyzed exactly as it was for  $\text{NbSe}_2$ . We note that the theoretical field distribution is generated assuming a triangular vortex lattice. This is reasonable, since we know of no experiments which have imaged the vortex lattice in  $\text{YBa}_2\text{Cu}_3\text{O}_{6.60}$ . As was explained for  $\text{YBa}_2\text{Cu}_3\text{O}_{6.95}$ , in the absence of twin boundary pinning the  $\hat{a}$ - $\hat{b}$  plane anisotropy will stretch the triangular lattice in a way which does not change the shape of the internal field distribution. Figure 8.3 shows the temperature dependence of the fitted  $\lambda_{ab}^{-2}$  in  $\text{YBa}_2\text{Cu}_3\text{O}_{6.60}$  (U1) using the analytical GL model for the field profile of the vortex lattice. The curves through the data points are merely guides for the eye. At higher temperatures where the vortex lattice is no longer a rigid 3D structure, the fitted value of  $\lambda_{ab}^{-2}$  merely characterizes the width of the field distribution and is not the penetration depth as defined at lower temperatures. Note that the transition in the vortex-lattice structure occurs at a lower temperature in the larger magnetic field. Figure 8.3 suggests that measurements of  $\lambda_{ab}$  should be restricted to temperatures below 25 K for applied magnetic fields greater than 1.5 T.

Figure 8.4 shows the temperature dependence of  $\lambda_{ab}^{-2}$  in  $\text{YBa}_2\text{Cu}_3\text{O}_{6.60}$  (U2) at low  $T$ , for three of the magnetic fields considered. As in  $\text{YBa}_2\text{Cu}_3\text{O}_{6.95}$ , there is a strong linear decrease in the superfluid fraction with increasing temperature. The solid lines are a fit to Eq. (7.2). The fitted parameters appear in Table 8.6 along with those for an analysis assuming the ML model with a Gaussian cutoff factor. Note that the coefficient  $\alpha$  of the term linear in  $t$  is weaker than in the optimally doped compound and is at most

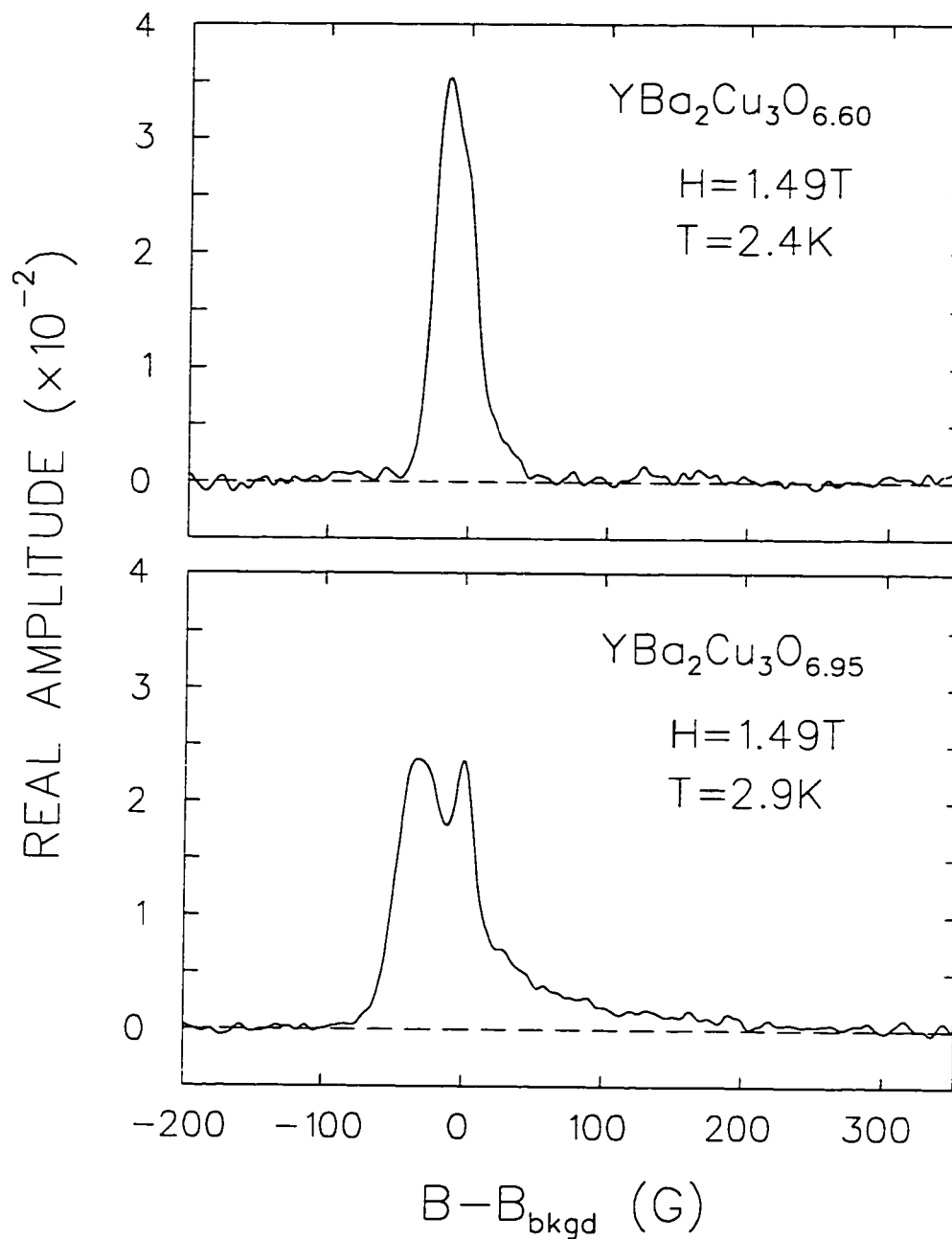


Figure 8.1: The Fourier transforms of the muon spin precession signal in (top panel)  $\text{YBa}_2\text{Cu}_3\text{O}_{6.60}$  (U1) at  $T = 2.4$  K and (bottom panel)  $\text{YBa}_2\text{Cu}_3\text{O}_{6.95}$  (O1) at  $T = 2.9$  K after field cooling in a magnetic field of  $H = 1.49$  T.

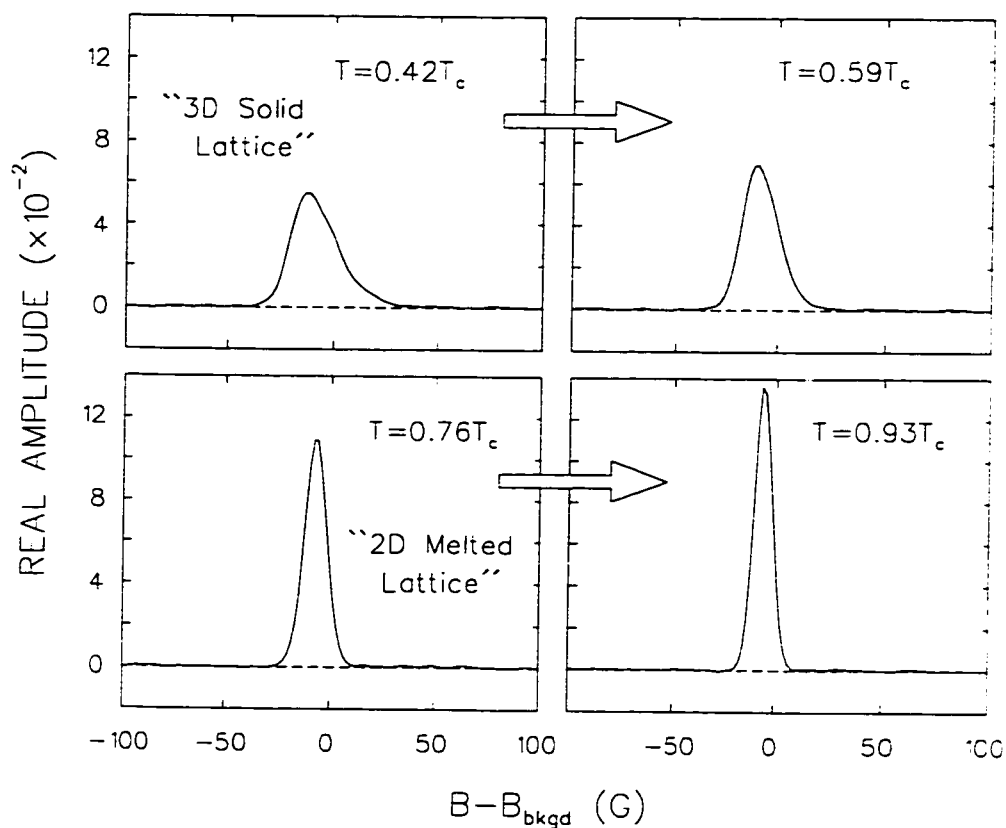


Figure 8.2: The evolution of the  $\mu\text{SR}$  line shape measured in  $\text{YBa}_2\text{Cu}_3\text{O}_{6.60}$  upon warming the sample, subsequent to field cooling to  $T = 2.4$  K in a magnetic field  $H = 1.49$  T.

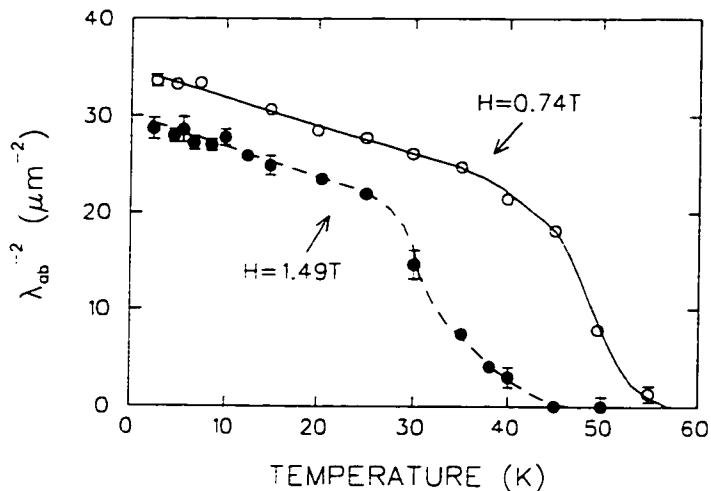


Figure 8.3: The temperature dependence of the fitted  $\lambda_{ab}^{-2}$  in  $\text{YBa}_2\text{Cu}_3\text{O}_{6.60}$  (U1) at magnetic fields of  $H = 0.74\text{ T}$  (open circles) and  $1.49\text{ T}$  (solid circles). The curves through the data points are merely guides for the eye. Beyond  $T = 35\text{ K}$  at  $H = 0.74\text{ T}$  and  $T = 25\text{ K}$  at  $H = 1.49\text{ T}$ , the fitted  $\lambda_{ab}$  no longer represents the length scale over which the field decays from the vortex cores.

only weakly dependent on magnetic field. This is consistent with conclusions drawn from earlier  $\mu\text{SR}$  measurements of the muon depolarization rate  $\sigma$  for various oxygen dopings in  $\text{YBa}_2\text{Cu}_3\text{O}_{7-\delta}$  [209]. As shown in the inset of Fig. 8.4, there is also excellent agreement with microwave cavity measurements of  $\Delta\lambda_{ab}(T) = \lambda_{ab}(T) - \lambda_{ab}(1.25\text{ K})$  in zero magnetic field [210]. According to the Meissner-phase measurements in Ref. [210], the strength of the term linear in  $t$  changes substantially as a function of oxygen doping only in the  $\hat{b}$ -direction (*i.e.* the direction of the  $\text{CuO}$  chains). In particular, the value of the coefficient linear in  $t$  for the temperature dependence of  $\lambda_b$  is reduced in the underdoped compound. One interpretation is that the oxygen vacancies in the  $\text{CuO}$  chains act as pair-breaking defects.

The magnetic-field dependence of  $\lambda_{ab}$  extrapolated to  $T = 0$  is shown in Fig. 8.5.

| Magnetic Field [T] | Beamline/Year | <i>Modified London Model</i> |                        | <i>Analytical GL Model</i> |                        |
|--------------------|---------------|------------------------------|------------------------|----------------------------|------------------------|
|                    |               | $\lambda_{ab}(T=0)$ [Å]      | $\alpha$ [ $10^{-1}$ ] | $\lambda_{ab}(T=0)$ [Å]    | $\alpha$ [ $10^{-1}$ ] |
| (i)                |               |                              |                        |                            |                        |
| 0.742              | m15/1994      | 2212(18)                     | 4.1(2)                 | 1698(15)                   | 4.9(2)                 |
| 1.013              | m15/1994      | 2248(17)                     | 4.0(3)                 | 1739(23)                   | 4.7(2)                 |
| 1.490              | m15/1994      | 2393(40)                     | 4.5(6)                 | 1810(32)                   | 5.7(8)                 |
| (ii)               |               |                              |                        |                            |                        |
| 0.500              | m15/1996      | 2286(11)                     | 4.1(2)                 | 1754(13)                   | 4.6(2)                 |
| 0.850              | m15/1996      | 2396(18)                     | 4.1(2)                 | 1815(16)                   | 5.7(3)                 |
| 1.250              | m15/1996      | 2450(19)                     | 3.9(4)                 | 1846(17)                   | 4.8(4)                 |

Table S.6: Parameters from fits of  $\lambda_{ab}^{-2}(T)$  to Eq. (7.2) for (i) sample U1 and (ii) sample U2.

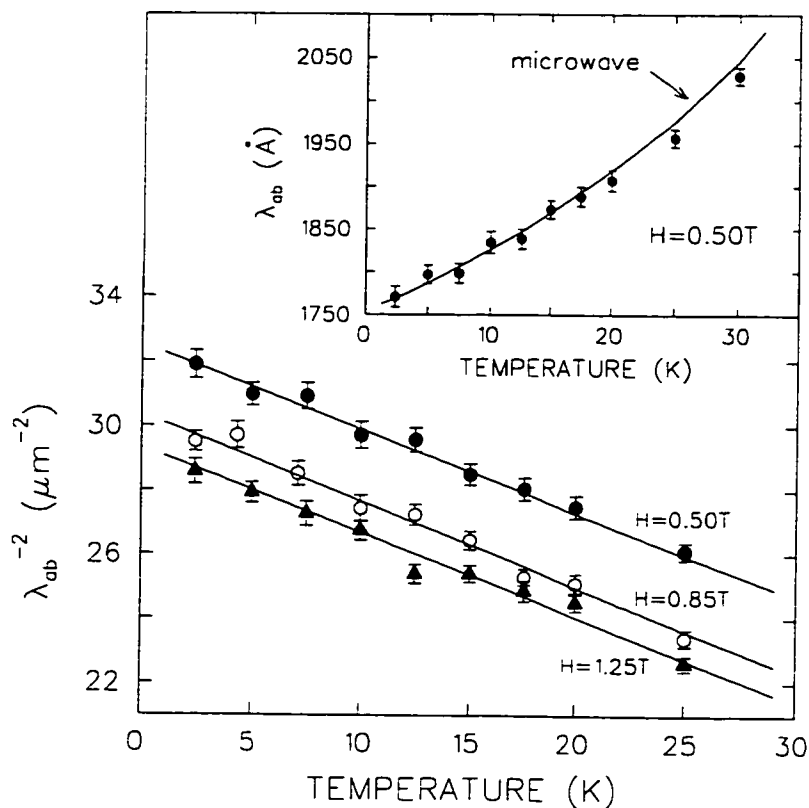


Figure 8.4: The temperature dependence of  $\lambda_{ab}^{-2}(T, H)$  in  $\text{YBa}_2\text{Cu}_3\text{O}_{6.60}$  (U2) for applied fields of 0.5 (solid circles), 0.85 (open circles) and 1.25 T (solid triangles). Inset: The  $T$ -dependence of  $\lambda_{ab}$  at 0.5 T. The solid line shows the microwave measurements of  $\Delta\lambda_{ab}(T) = \lambda_{ab}(T) - \lambda_{ab}(1.25 \text{ K})$  in zero field [210] assuming our value  $\lambda_{ab}(1.25 \text{ K}) = 1762 \text{ \AA}$ .



There is a clear difference in the magnitude of  $\lambda_{ab}(H)$  determined from measurements in the twinned (U1) and detwinned samples (U2). This difference is likely due to vortex-lattice distortions in U1 caused by twin boundary pinning of the vortex lines. Such distortions introduce a systematic uncertainty in the determination of  $\lambda_{ab}$ . As noted earlier, fitting to a theoretical field distribution which assumes the wrong vortex-lattice geometry seriously affects the magnitude of the extracted  $\lambda_{ab}$ , but has little effect on the  $T$  or  $H$ -dependence.

The lines in Fig. 8.5 are fits to Eq. (7.3) assuming  $p = 1$ . The fitted parameters are:  $\lambda_{ab}(0,0) = 1586 \text{ \AA}$  and  $J = 149 \text{ \AA/T}$  in the twinned sample (U1) and  $\lambda_{ab}(0,0) = 1699 \text{ \AA}$  and  $J = 121 \text{ \AA/T}$  in the detwinned sample (U2). To roughly estimate  $H_{c2}(0)$  in  $\text{YBa}_2\text{Cu}_3\text{O}_{6.60}$ , we can use the ratio of the coherence length between this compound and  $\text{YBa}_2\text{Cu}_3\text{O}_{6.95}$ . It was noted earlier, that at  $H = 1.49 \text{ T}$  the fractional volume of the sample occupied by the vortex cores is nearly two times greater in the underdoped compound. This implies that  $\xi_{ab}$  in  $\text{YBa}_2\text{Cu}_3\text{O}_{6.60}$  is  $\approx \sqrt{2}$  times the coherence length in  $\text{YBa}_2\text{Cu}_3\text{O}_{6.95}$ . Taking  $H_{c2}(0) = 120 \text{ T}$  for  $\text{YBa}_2\text{Cu}_3\text{O}_{6.95}$  and assuming  $H_{c2} \propto \xi_{ab}^{-2}$ , we may estimate  $H_{c2}(0) \approx 60 \text{ T}$  in  $\text{YBa}_2\text{Cu}_3\text{O}_{6.60}$ . Using  $H_{c2}(0)$  in place of  $H_{c2}(0.33 T_c)$  in Eq. (7.4), the coefficient linear in  $h$  (*i.e.*  $\varepsilon$ ) at  $T = 0$  is 5.6 and 4.2 in U1 and U2, respectively. On the other hand, for the  $\text{YBa}_2\text{Cu}_3\text{O}_{6.95}$  compound treated earlier,  $\varepsilon = 9.0$  in both the O1 and O2 samples. The linear dependence of  $\lambda_{ab}(H)$  on  $H$  when plotted as a function of reduced field is therefore smaller in  $\text{YBa}_2\text{Cu}_3\text{O}_{6.60}$  than in  $\text{YBa}_2\text{Cu}_3\text{O}_{6.95}$ . It is predicted that the presence of impurities should reduce the field dependence of the penetration depth in the nonlinear supercurrent response of a  $d_{x^2-y^2}$ -wave superconductor [36]. It appears as though oxygen vacancies in the chains of the underdoped compound have a similar effect.

In the analysis of the  $\mu\text{SR}$  spectra for the optimally doped compound it was assumed

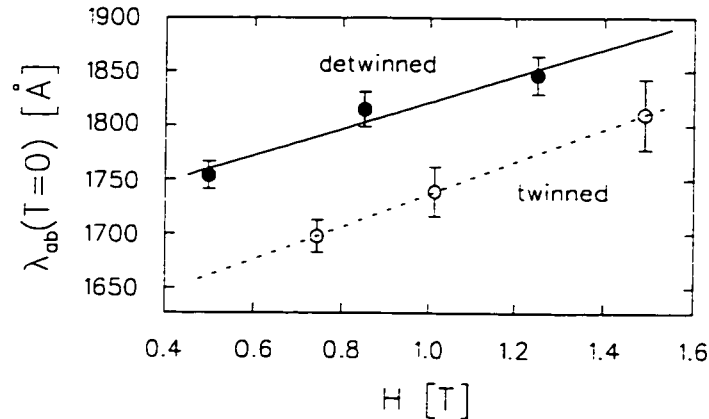


Figure 8.5: The magnetic field dependence of  $\lambda_{ab}$  extrapolated to  $T = 0$  in  $\text{YBa}_2\text{Cu}_3\text{O}_{6.60}$ . The data for the twinned (U1) sample are shown as open circles, whereas the solid circles designate the detwinned (U2) sample.

that  $\sigma_f \propto \lambda_{ab}^{-2}$ . As shown in Fig. 8.6, fits to the underdoped compound without this constraint reveal that this is a reasonable approximation. Moreover, the range of values of  $\sigma_f$  is small, so that the uncertainty introduced by this assumption into the analysis of the  $\text{YBa}_2\text{Cu}_3\text{O}_{6.95}$  data is also small.

The variation of the additional broadening parameter  $\sigma_f$  with temperature in  $\text{YBa}_2\text{Cu}_3\text{O}_{6.60}$  (U2) is shown in Fig. 8.7(a) for  $H = 0.50$  T (open circles) and  $H = 1.25$  T (solid circles). The magnitude of  $\sigma_f$  is nearly the same at the two magnetic fields shown. As in the optimally doped compound, there is a reduction in the value of  $\sigma_f$  with increasing temperature and the quality of the fits are independent of temperature and magnetic field [see Fig. 8.7(b)]. Figure 8.8(a) shows the temperature dependence of  $\langle s^2 \rangle^{1/2}$  calculated from  $\sigma_f$  at these fields. The field dependence of  $\langle s^2 \rangle^{1/2}$  is weaker in  $\text{YBa}_2\text{Cu}_3\text{O}_{6.60}$  than in the optimally doped compound. When the RMS displacement of the vortex lines from their ideal positions is expressed as a percentage of the intervortex spacing  $L$  [see Fig 8.8(b)], the percent disorder at  $H = 0.50$  T agrees well with that for  $\text{YBa}_2\text{Cu}_3\text{O}_{6.95}$

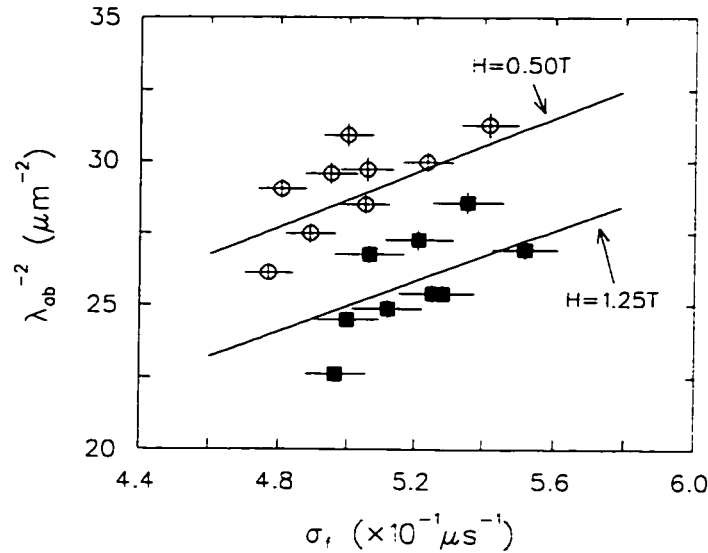


Figure 8.6: The magnetic penetration depth  $\lambda_{ab}$  as a function of the additional broadening parameter  $\sigma_f$  in  $\text{YBa}_2\text{Cu}_3\text{O}_{6.60}$  (U2) at  $H = 0.50$  T (open circles) and 1.25 T (solid squares). The solid lines are fits to Eq. (7.1).

[see Fig 7.11(b)]. However, the percent disorder is actually slightly larger at  $H = 1.25$  T in the underdoped compound. This may reflect the quasi-2D nature of the vortex lines in  $\text{YBa}_2\text{Cu}_3\text{O}_{6.60}$ . In particular, there is likely some degree of pinning-induced misalignment between the 2D vortex lattices in adjacent layers at the stronger field, so that the vortex lines are no longer straight. Similar values of  $\sigma_f$  and  $\langle s^2 \rangle^{1/2}$  were found in the twinned sample U1.

Figure 8.9 shows the temperature dependence of the GL parameter  $\kappa$  in  $\text{YBa}_2\text{Cu}_3\text{O}_{6.60}$  (U2) at three magnetic fields. There is far less scatter in the data at the higher fields compared to the optimally doped samples (note that the vertical scale is larger than in Fig. 7.12). This is due to the increased size of the vortex cores in the underdoped compound over the full field range considered. The horizontal lines in Fig. 8.9 are fits to a  $T$ -independent  $\kappa$ . The field dependence of  $\kappa$  obtained from these fits and those

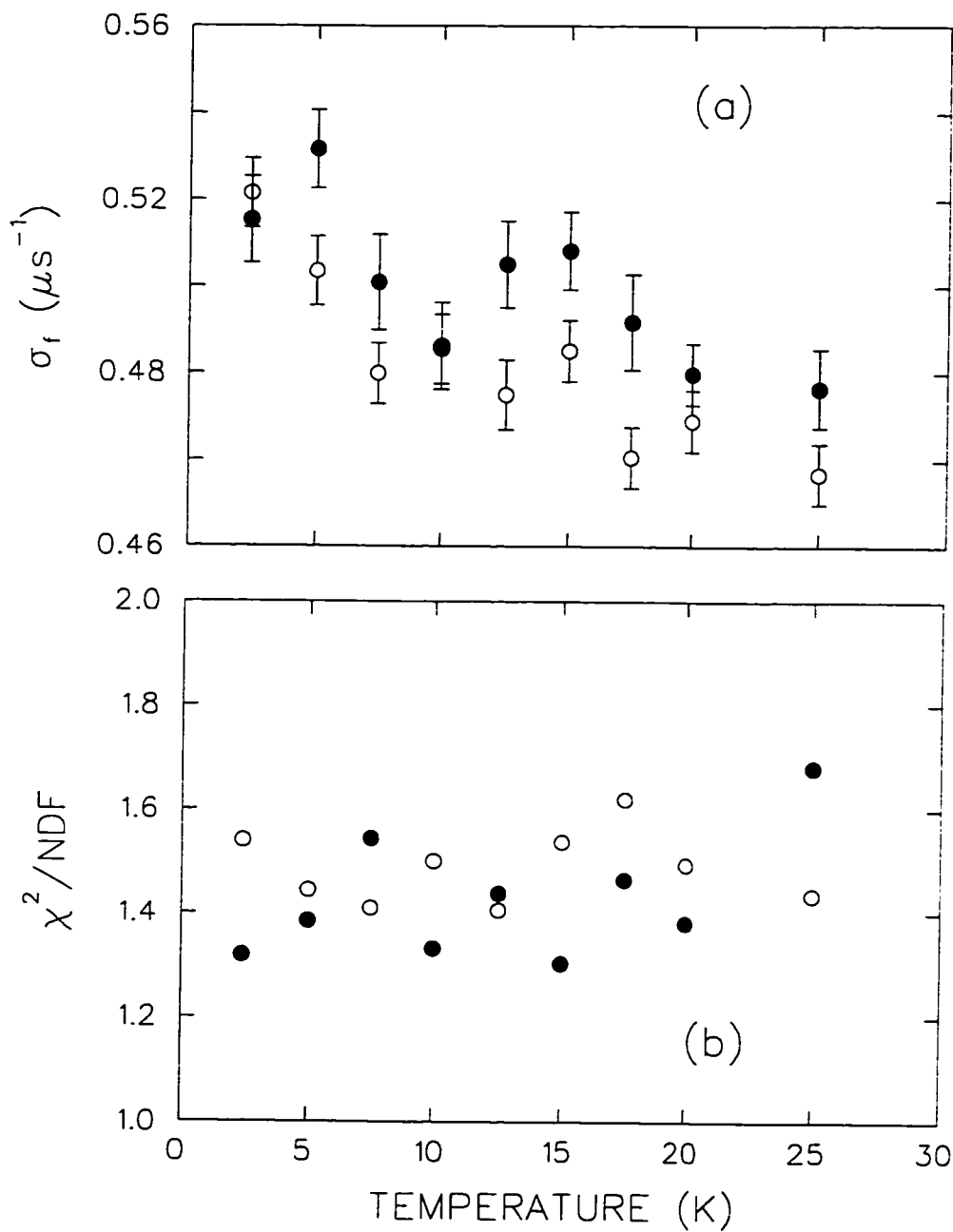


Figure 8.7: The temperature dependence of (a) the additional broadening parameter  $\sigma_f$  and (b) the ratio of  $\chi^2$  to the number of degrees of freedom (NDF) for  $\text{YBa}_2\text{Cu}_3\text{O}_{6.60}$  (U2) at  $H = 0.50$  T (open circles) and  $H = 1.25$  T (solid circles).

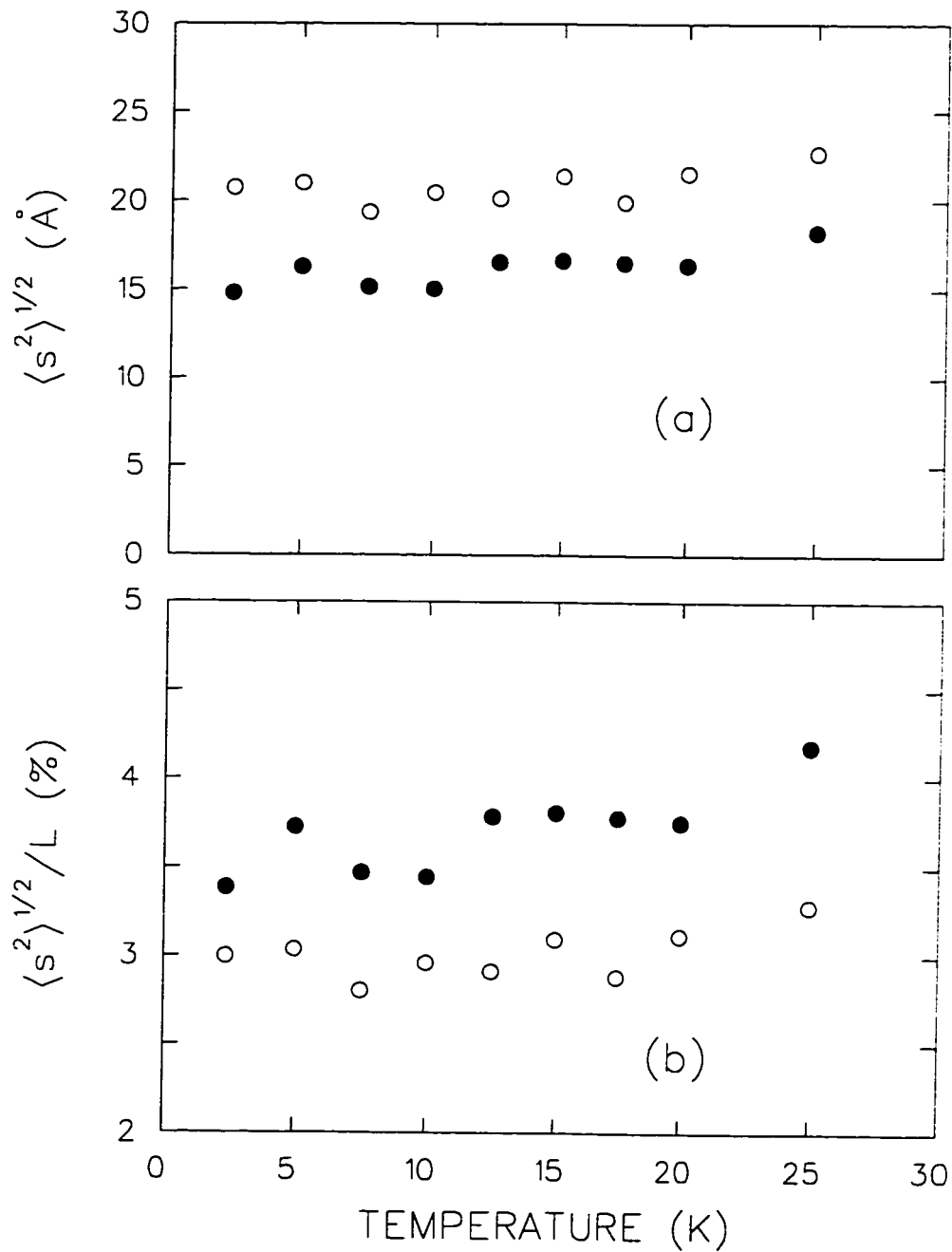


Figure 8.8: The temperature dependence of (a) the RMS displacement  $\langle s^2 \rangle^{1/2}$  of the vortices from their ideal positions and (b)  $\langle s^2 \rangle^{1/2}$  expressed as a percentage of the intervortex spacing  $L$ . The data is for  $\text{YBa}_2\text{Cu}_3\text{O}_{6.60}$  ( $U_2$ )  $H = 0.50$  T (open circles) and  $H = 1.25$  T (solid circles).

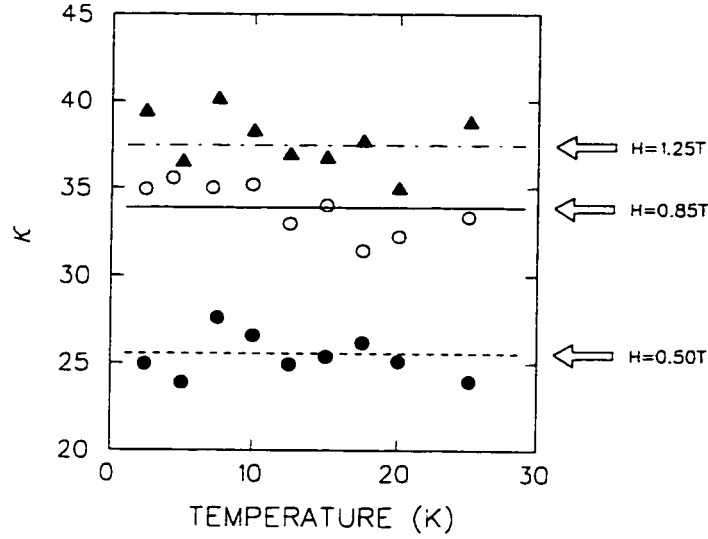


Figure 8.9: The temperature dependence of  $\kappa = \lambda_{ab}/\xi_{ab}$  in  $\text{YBa}_2\text{Cu}_3\text{O}_{6.60}$  (U2) at  $H = 0.50$  T (solid circles),  $0.85$  T (open circles) and  $1.25$  T (solid triangles).

for the twinned sample (U1) is shown in Fig. 8.10. The values of  $\kappa$  in the twinned and detwinned samples agree well enough that a single fit to Eq. (7.5) was performed. The fit gives  $\kappa(0) = 17(2)$  which is larger than in  $\text{YBa}_2\text{Cu}_3\text{O}_{6.95}$ , and  $\eta = 53(9)$  [assuming  $H_{c2}(0) = 60$  T], which is smaller than in  $\text{YBa}_2\text{Cu}_3\text{O}_{6.95}$  but still considerably greater than in  $\text{NbSe}_2$ . The larger value of  $\kappa$  results from the substantial increase in the penetration depth in the CuO chain direction, whereas the reduced value of the coefficient linear in  $h$  stems from the weaker field dependence of  $\lambda_{ab}$ .

Figure 8.11(a) shows  $\xi_{ab}$  as a function of temperature in  $\text{YBa}_2\text{Cu}_3\text{O}_{6.60}$  (U2), whereas Fig. 8.11(b) shows the temperature dependence of  $r_0$  obtained from the  $J_s(r)$  profiles. The net change in  $\xi_{ab}$  over the temperature range  $T = 0$  to  $T = 30$  K is greater than in  $\text{YBa}_2\text{Cu}_3\text{O}_{6.95}$ , although when  $\xi_{ab}$  is plotted as a function of reduced temperature, the

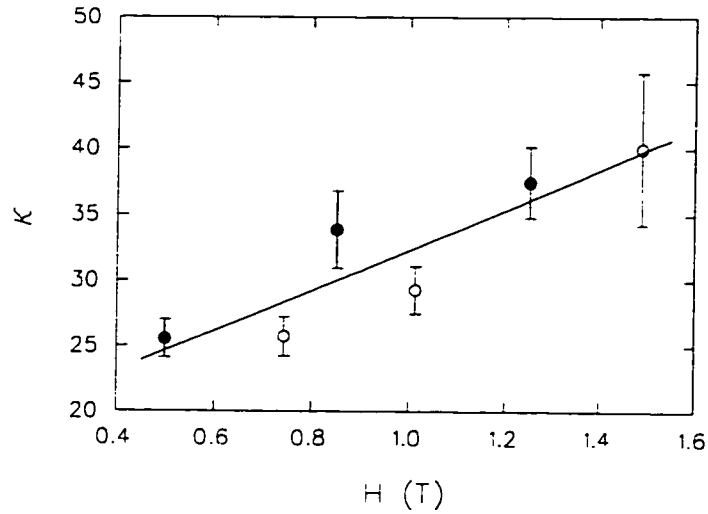


Figure 8.10: The magnetic field dependence of  $\kappa = \lambda_{ab}/\xi_{ab}$  in  $\text{YBa}_2\text{Cu}_3\text{O}_{6.60}$  extrapolated to  $T=0$ . The data for the twinned (U1) sample are shown as open circles, whereas the solid circles designate the detwinned (U2) sample.

term linear in  $t$  is weaker. For instance, fitting to the linear relation

$$\xi_{ab}(T) = \xi_{ab}(0)[1 + \epsilon t]. \quad (\text{S.1})$$

at  $H \approx 0.5$  T gives  $\xi_{ab}(0) = 68.7 \text{ \AA}$  and  $\epsilon = 0.27$  in  $\text{YBa}_2\text{Cu}_3\text{O}_{6.60}$ , whereas  $\xi_{ab}(0) = 56.7 \text{ \AA}$  and  $\epsilon = 0.37$  in  $\text{YBa}_2\text{Cu}_3\text{O}_{6.95}$ . The larger value of  $\xi_{ab}$  in the underdoped material implies that the energy scale of the quasiparticle bound states in the core is reduced. However, in this conventional picture of a vortex core, the smaller value of  $\epsilon$  in  $\text{YBa}_2\text{Cu}_3\text{O}_{6.60}$  contradicts what is expected from the Kramer-Pesch effect alone. If the quantum limit is realized in both of these materials below  $T = 30$  K, the major source of the  $T$ -dependence for  $\xi_{ab}$  may not be the Kramer-Pesch effect at all. In both compounds,  $\epsilon$  is essentially independent of magnetic field.

The values of  $\xi_{ab}(H)$  and  $r_0(H)$  extrapolated to  $T = 0$  are shown in Fig. 8.12 for both the twinned (U1) and detwinned (U2) samples. Note that there is good

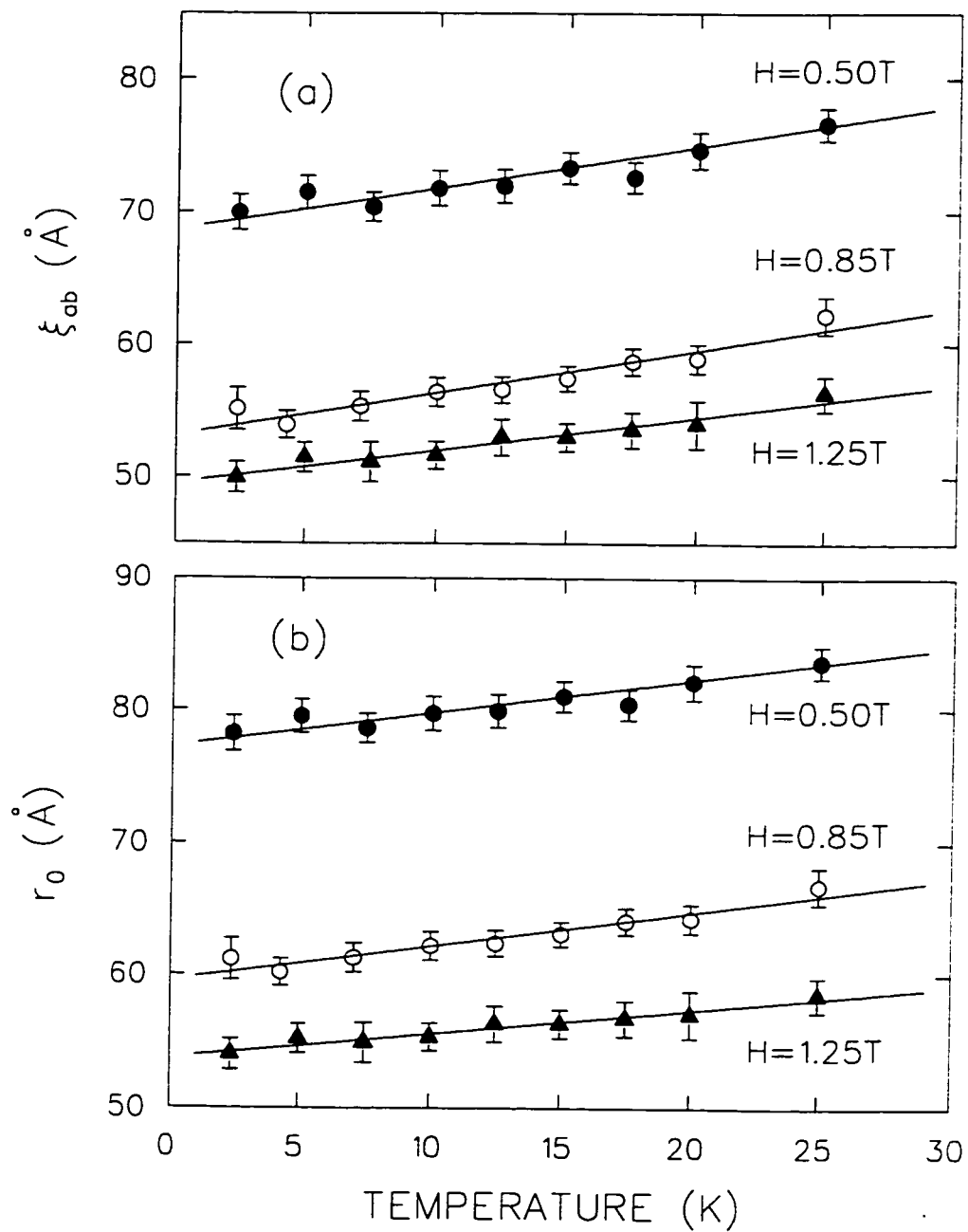


Figure 8.11: The temperature dependence of (a)  $\xi_{ab}$  and (b)  $r_0$  in  $\text{YBa}_2\text{Cu}_3\text{O}_{6.60}$  (U2) at  $H=0.50\text{ T}$  (solid circles),  $0.85\text{ T}$  (open circles) and  $1.25\text{ T}$  (solid triangles).



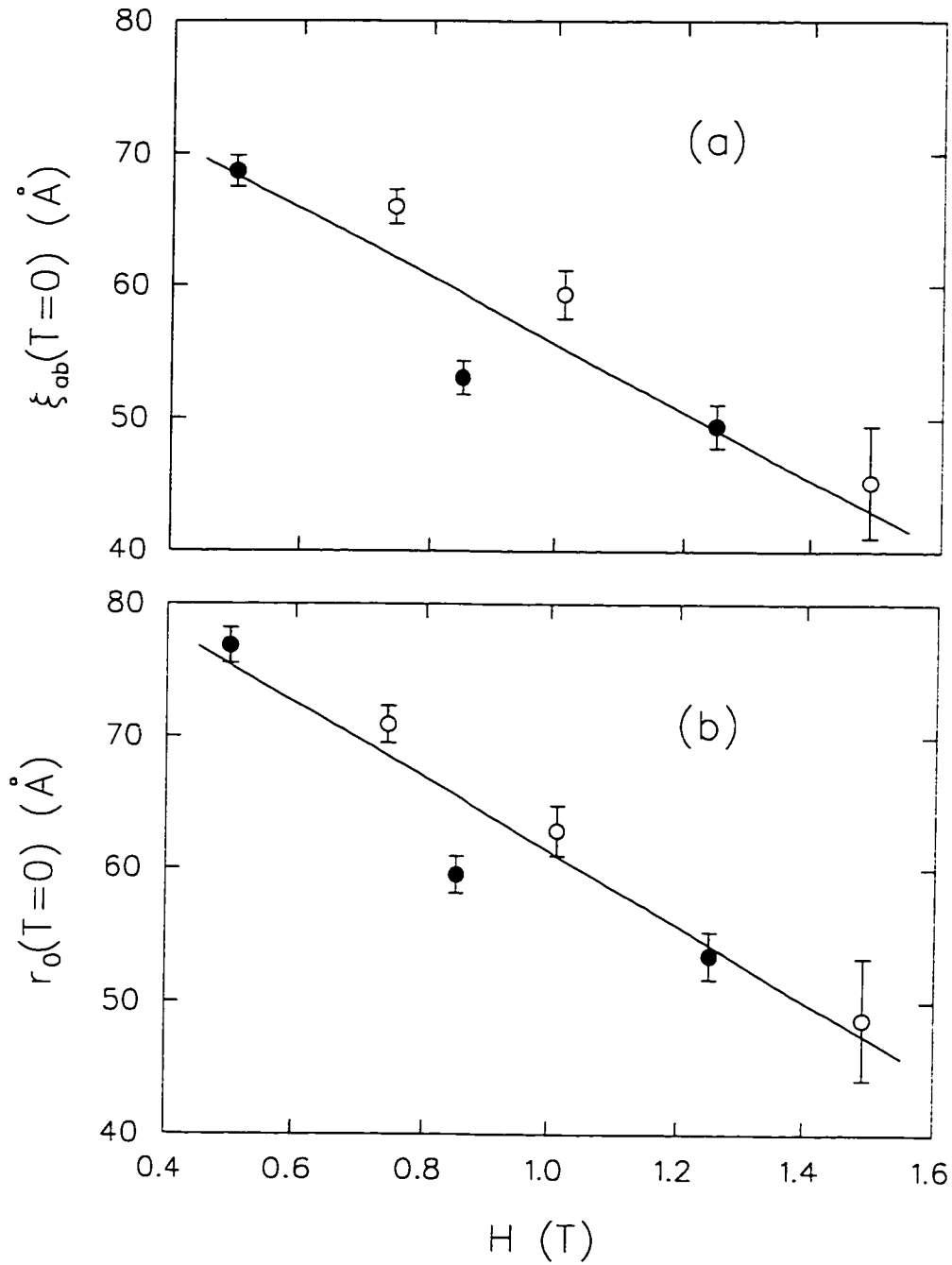


Figure 8.12: The magnetic field dependence of (a)  $\xi_{ab}$  and (b)  $r_0$  in  $\text{YBa}_2\text{Cu}_3\text{O}_{6.60}$  extrapolated to  $T = 0$ . The data for the twinned (U1) sample are shown as open circles, whereas the solid circles designate the detwinned (U2) sample.

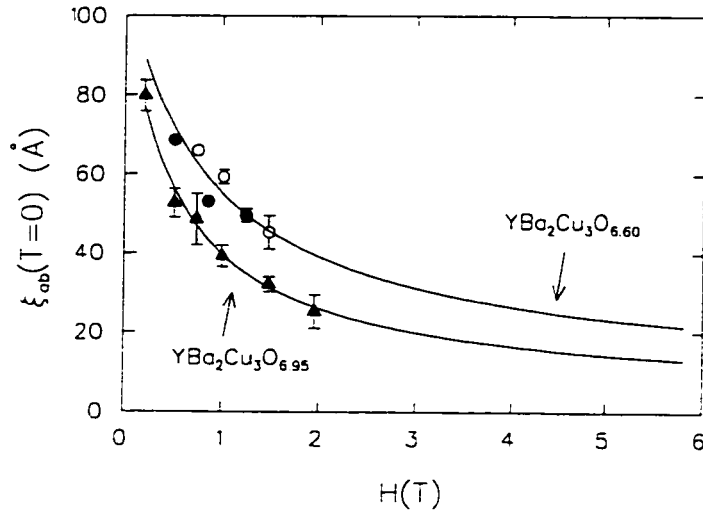


Figure 8.13: The magnetic field dependence of  $\xi_{ab}$  in  $\text{YBa}_2\text{Cu}_3\text{O}_{6.60}$  (U1:open circles, U2:solid circles) and  $\text{YBa}_2\text{Cu}_3\text{O}_{6.95}$  (O1:triangles) extrapolated to  $T = 0$ . The solid curves are described in the text.

agreement between both samples, which implies that the twin planes have little effect on the vortex-core size. The magnetic field dependence of  $\xi_{ab}(T=0)$  in  $\text{YBa}_2\text{Cu}_3\text{O}_{6.60}$  is shown compared to that in  $\text{YBa}_2\text{Cu}_3\text{O}_{6.95}$  in Fig. 8.13. The coherence length in the vortex state is larger in the underdoped material at all fields considered. The solid curve through the data points of the optimally doped sample was described in the previous section. The solid curve through the data points for  $\text{YBa}_2\text{Cu}_3\text{O}_{6.60}$  was obtained by averaging the linear best-fit lines for  $\lambda_{ab}(H)$  and  $\kappa(H)$  of samples U1 and U2, so that  $\xi_{ab}(H) = 107[1 + 0.082H]/[1 + 1.095H]$ . As was explained in the discussion for  $\text{NbSe}_2$ , the curves in Fig. 8.13 should flatten out at low fields, when  $\lambda_{ab} < L$  (*i.e.* there should be no change in the vortex core radius when the vortices are isolated from each other). From our  $\mu\text{SR}$  results, the coherence length should stop rising below  $H \approx 0.19 T$  in  $\text{YBa}_2\text{Cu}_3\text{O}_{6.95}$  and below  $H \approx 0.09 T$  in  $\text{YBa}_2\text{Cu}_3\text{O}_{6.60}$ .

Let us now return to the discussion of vortex-lattice melting in  $\text{YBa}_2\text{Cu}_3\text{O}_{6.60}$ , which occurs well below the superconducting-to-normal phase transition. As noted earlier, the sudden loss of asymmetry in the  $\mu\text{SR}$  line shape as the temperature is raised may be interpreted as a melting transition for the vortex lattice (see Fig. 8.2). In the melted phase the vortices are mobile, giving rise to a vortex structure with no long range spatial order. As indicated in Fig. 8.3, the melting temperature  $T_m$  depends strongly on magnetic field. By monitoring the changes in shape of the measured field distribution with increasing temperature, at several different magnetic fields, we find that the melting transition can be described by

$$H_m(T_m) \approx \nu(T_c - T_m)^n, \quad (8.2)$$

where  $\nu = 0.059(4)$  T/K,  $n \approx 1$  and  $T_c$  is the zero-field critical temperature. Although this gives a power-law exponent of 1, the temperature increments for these measurements were too large to determine  $T_m$  any better than  $\pm 5$  K. Furthermore,  $n$  is usually greater than 1.0 as discussed in section 4.2.

The dimensionality of the “melted” vortex lattice is of equal interest here. The question is whether the “melted” lattice consists of straight 3D-vortex lines, highly flexible 3D-vortex lines or pancake vortices in which the phase coherence is destroyed across neighboring  $\text{CuO}_2$  planes. The strong magnetic field dependence of  $T_m$  favours the latter scenario. Within the LD model, the pancake vortices are aligned and weakly coupled between neighboring  $\text{CuO}_2$  layers at low temperatures in the absence of disorder. As the temperature is increased, thermal fluctuations of the strings of pancake vortices becomes significant. The displacement of the 2D-pancake vortices within a layer by thermal fluctuations is opposed by the strength of the Josephson-coupling between pancakes in neighboring  $\text{CuO}_2$  layers. At low magnetic fields, the vortex-vortex interactions within a layer are weak, so that the displacement of an individual vortex does not

necessarily affect the other vortices in the layer. Thus, for small thermal fluctuations a 3D structure is maintained in the majority of the sample. It has been suggested that at low fields, the vortex lattice first melts into a state consisting of mobile 3D vortex lines, which are destroyed upon further increase in the temperature as the pancakes which makeup the vortex lines breakup [110].

On the other hand, at high magnetic fields, the interaction between pancake vortices within a  $\text{CuO}_2$  layer is stronger than the interaction between pancake vortices between neighboring layers. In this case, the vortex lattice behaves in a quasi-2D manner, consisting of weakly interacting 2D-vortex lattices in different  $\text{CuO}_2$  layers. Thermal fluctuations cause the 2D lattices to move back and forth over top of each other. For larger fluctuations the pancakes within the layers become mobile. The effect of temperature and magnetic field on the  $\mu\text{SR}$  line shape in  $\text{YBa}_2\text{Cu}_3\text{O}_{6.60}$  is similar to that previously observed in  $\mu\text{SR}$  experiments on  $\text{Bi}_2\text{Sr}_2\text{CaCu}_2\text{O}_{8+\delta}$  [107,111] and arises here due to a reduction in the  $\hat{c}$ -axis coherence length relative to that in the optimally doped compound  $\text{YBa}_2\text{Cu}_3\text{O}_{6.95}$ .

Pinning will of course also lead to vortex displacements. As discussed earlier, the effects of pinning on the vortex structure in the low and high-field regimes will be considerably different in the pancake-vortex model. Figure 8.14 shows the  $\mu\text{SR}$  line shape in "twinned"  $\text{YBa}_2\text{Cu}_3\text{O}_{6.60}$  (U1), obtained by cooling the sample through the transition to low temperature in different magnetic fields. The field distributions at  $H = 0.74$  T and  $H = 1.49$  T exhibit the characteristic features of a 3D-ordered vortex lattice. However, the field distribution which arises from field cooling in a magnetic field of 2.91 T does not exhibit the expected high-field tail for a 3D-ordered vortex lattice, but rather shows a low-field tail. From the melting-line expression obtained above, the lattice should melt at  $T_m \approx 9.5$  K at  $H = 2.91$  T, which is higher than

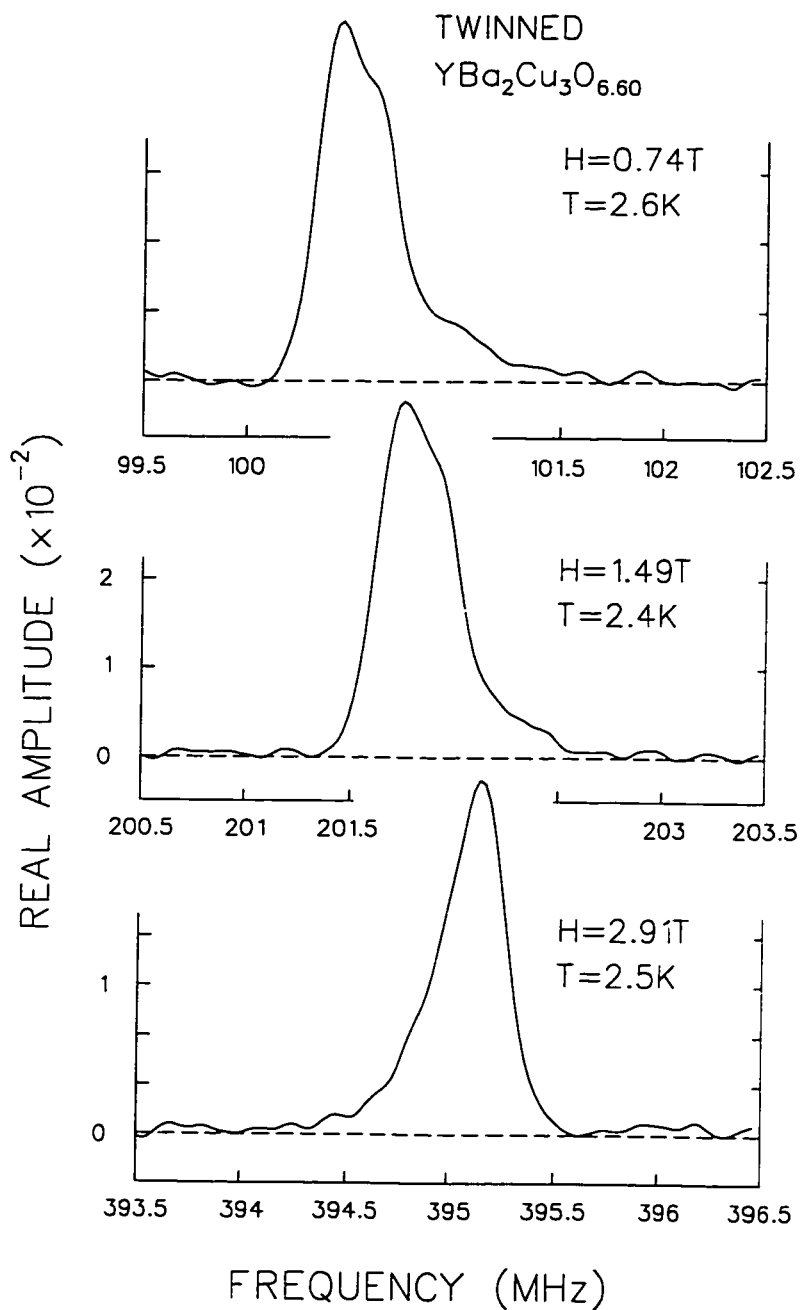


Figure 8.14: The Fourier transforms of the muon spin precession signal in twinned  $\text{YBa}_2\text{Cu}_3\text{O}_{6.60}$  (U1) at  $T \approx 0.04 T_c$  after field cooling in magnetic fields of  $H = 0.74$ ,  $1.49$  and  $2.91$  T.

$T = 2.5$  K in Fig. 8.14. The most natural interpretation is that the 2D-vortex lattices become misaligned with respect to each other due to pinning brought about by pointlike defects within the layers. The origin of the low-field tail in  $\text{Bi}_2\text{Sr}_2\text{CaCu}_2\text{O}_{8+\delta}$  has been previously attributed to the geometry of the sample [112.211.212]. In a flat rectangular sample, the average magnetic field penetrating near the crystal edges is smaller than that in the center of the sample, due to non-uniform demagnetization. As a result, the density of vortices is smaller near the sample edges. The sample-geometry effect of course also exists when the vortex lattice is 3D and ordered. However, the variations of the internal field distribution due to the vortex lattice “swamp” out the effect. Also, in the case of  $\text{YBa}_2\text{Cu}_3\text{O}_{6.95}$  and at low fields in  $\text{YBa}_2\text{Cu}_3\text{O}_{6.60}$ , the high pinning temperature likely freezes in a nearly uniform density of vortices in the sample, which remains uniform upon cooling. A tiny low-field tail is visible in all of the line shapes shown earlier.

The effect of the sample geometry on the measured internal field distribution can occur without vortex pinning—as evidenced by the existence of a large low-field tail in the  $\mu\text{SR}$  line shape for  $\text{Bi}_2\text{Sr}_2\text{CaCu}_2\text{O}_{8+\delta}$  in the melted phase [107]. The top panel of Figure 8.15 shows the  $\mu\text{SR}$  line shape measured in the twinned sample of  $\text{YBa}_2\text{Cu}_3\text{O}_{6.60}$  (U1) obtained by field cooling in a magnetic field  $H \approx 2.89$  T to  $T = 2.5$  K, followed by an increase of approximately 0.01 T in the applied field. Note that the small background signal shifts to the new applied field at  $H \approx 2.90$  T, but the signal from the sample does not. This verifies that the vortex lattice is not melted and strongly supports the picture of a dimensional transition which is induced at high magnetic fields in the presence of pinning. When the temperature is raised, the 2D-vortex lattices depin within the layers and the lattice melts (see middle and bottom panels in Fig. 8.15). Although not shown, at  $T \approx 15$  K the lattice is still pinned. Since this temperature is greater than the estimated  $T_m$  at this field (*i.e.* 9.5 K), it is likely that  $n > 1$  in the

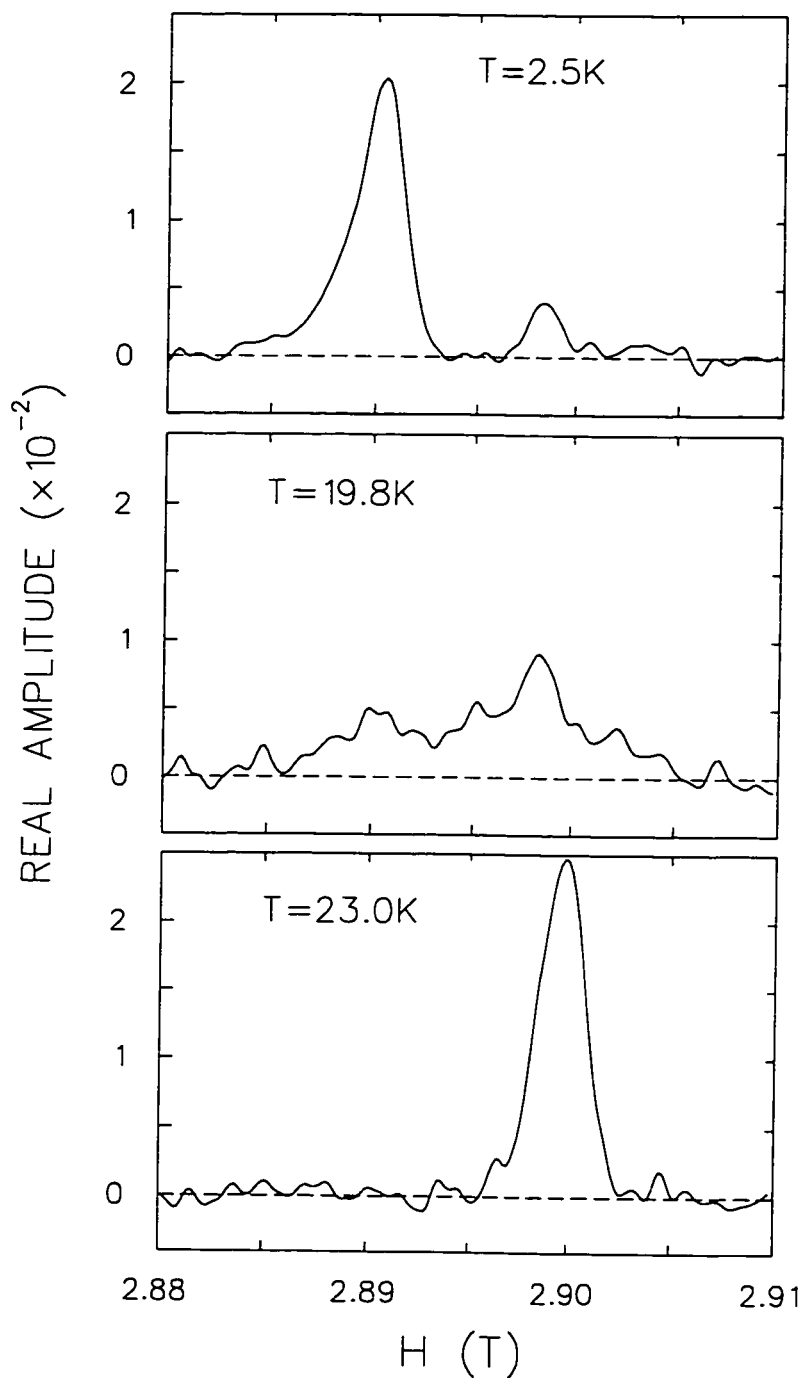


Figure 8.15: Top panel: The Fourier transform of the muon spin precession signal in twinned  $\text{YBa}_2\text{Cu}_3\text{O}_{6.60}$  (U1) after field cooling at  $H \approx 2.89\text{ T}$  to  $T = 2.5\text{ K}$  followed by an increase in the field to  $2.90\text{ T}$ . The middle and bottom panels are the  $\mu\text{SR}$  line shapes upon warming the sample to  $T = 19.8\text{ K}$  and  $23.0\text{ K}$ , respectively.

expression for the melting line transition.

Figure 8.16 shows the measured field distributions in “detwinned”  $\text{YBa}_2\text{Cu}_3\text{O}_{6.60}$  (U2) as a function of magnetic field at low temperatures. The asymmetries in the line shapes in the top two panels are similar to those for the twinned sample, showing the features characteristic of a 3D vortex lattice. However, at  $H = 2.99$  T where the line shape should exhibit the features associated with the misaligned 2D-vortex lattices, the line shape still shows a high-field tail. Note that the temperature in the bottom panel is  $T = 10$  K, compared to  $T = 2.5$  K in the bottom panel of Figure 8.14—which makes it even more surprising that the line shape is still asymmetric. Also, when the detwinned sample is field cooled in a magnetic field of 3.4 T to  $T = 10$  K, the measured field distribution still shows a small high-field tail and the background signal can be field shifted. The dimensional crossover observed in the twinned sample should not arise from pinning by the twin boundaries, since they extend the full depth of the sample and displace the 2D-vortex lattices equivalently in all layers. Since the two samples were not from the same batch, the absence of the dimensional crossover in the detwinned sample (U2) at fields comparable to those in the twinned sample (U1), is likely related to differences in the pointlike defects in the samples. In particular, these results suggest that defects in the  $\text{CuO}_2$  layers are greater in the twinned sample.



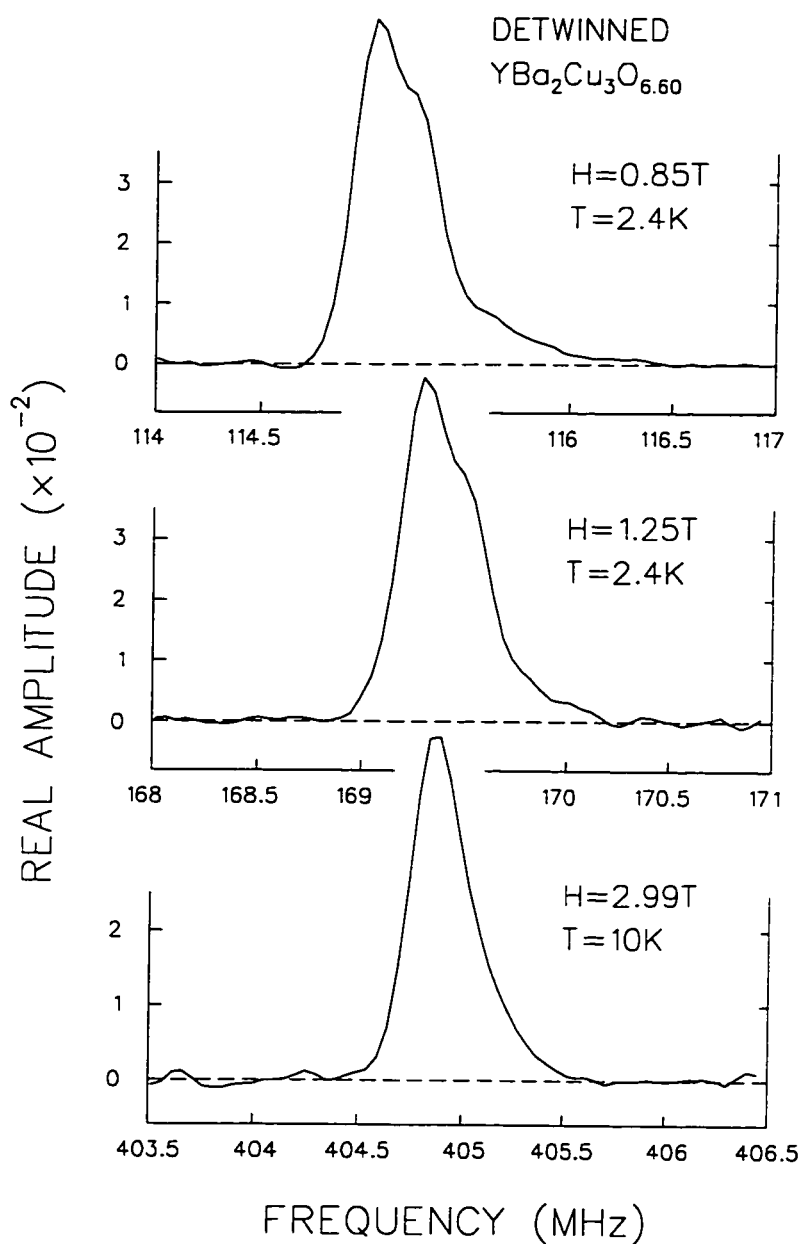


Figure 8.16: The Fourier transform of the muon spin precession signal in twinned  $\text{YBa}_2\text{Cu}_3\text{O}_{6.60}$  (U2) after field cooling to  $T=2.5\text{K}$  in magnetic fields of  $H=0.85\text{T}$  and  $1.25\text{T}$  and field cooling to  $T=10\text{K}$  in a magnetic field of  $2.99\text{T}$  (bottom panel).

## Chapter 9

### Conclusions

The linear temperature dependence of  $\lambda_{ab}^{-2}$  at low  $T$  found in the vortex state of both  $\text{YBa}_2\text{Cu}_3\text{O}_{6.95}$  and  $\text{YBa}_2\text{Cu}_3\text{O}_{6.60}$  provides strong support for a superconducting energy gap with lines nodes. The strength of the coefficient linear in  $T$  was shown to agree extremely well with other measurements of  $\lambda_{ab}$  in the Meissner state. This agreement implies that the change in the superfluid fraction as a function of temperature is identical in both phases.

The absolute value of  $\lambda_{ab}(T=0)$  extrapolated to zero magnetic field from the  $\mu\text{SR}$  measurements is approximately 10-15% smaller than that obtained from far infrared measurements of  $\lambda_{ab}(T=0)$  in zero field. The difference is perhaps reasonable given the very different nature of the  $\mu\text{SR}$  and far infrared methods. Although the absolute magnitude of  $\lambda_{ab}$  is sensitive to the assumed theoretical model for the field distribution of the vortex lattice, the temperature dependence is relatively independent of the choice of model. It is possible that the presence of vortices also influences the absolute value of  $\lambda_{ab}$  in the vortex state. The ratio of the penetration depths for the underdoped and optimally doped samples determined by  $\mu\text{SR}$  is comparable to that found from far infrared measurements on similar crystals.

The magnetic field dependence of  $\lambda_{ab}$  measured here in the vortex state of both  $\text{NbSe}_2$  and  $\text{YBa}_2\text{Cu}_3\text{O}_{7-\delta}$  is not completely understood. The field dependence of  $\lambda_{ab}$  in  $\text{NbSe}_2$  may be due to nonlinear effects, since it is found that  $\langle J_s \rangle \propto \sqrt{\lambda_{ab}}$ —which is the same relation for nonlinear effects in the Meissner state. However, according to

the calculations in Ref. [40], the nonlinear effects are only a small correction to the supercurrent response and therefore cannot account for the size of the field dependence (measured here) in the vortex state of NbSe<sub>2</sub>. It is possible that the assumption of a small vortex-core radius by the authors in Ref. [40] affected their calculations of the effective penetration depth measured by  $\mu$ SR. The field dependence of  $\lambda_{ab}$  in YBa<sub>2</sub>Cu<sub>3</sub>O<sub>7- $\delta$</sub>  is likely predominantly due to the nonlocal effects associated with nodes on the Fermi surface, as outlined in Ref. [40]. However, more detailed measurements of the field dependence on untwinned samples of YBa<sub>2</sub>Cu<sub>3</sub>O<sub>7- $\delta$</sub>  may be required to confirm this. The stronger field dependence measured in YBa<sub>2</sub>Cu<sub>3</sub>O<sub>7- $\delta$</sub>  (relative to that in NbSe<sub>2</sub>) could be explained by this additional effect alone—although, the effects of a nonlinear supercurrent response are also expected to be stronger in a superconductor with nodes on the Fermi surface than in a conventional superconductor.

In NbSe<sub>2</sub>,  $\lambda_{ab}$  was found to increase linearly with increasing field. The precise form of the field dependence of  $\lambda_{ab}(H)$  in the vortex state of YBa<sub>2</sub>Cu<sub>3</sub>O<sub>7- $\delta$</sub>  could not be determined, due to the narrow range of reduced field which the measurements cover. The strength of the field dependence in the vortex state is found to be weaker than that reported from microwave cavity perturbation measurements in the Meissner state, which find  $\Delta\lambda_{ab} \propto H$  in YBa<sub>2</sub>Cu<sub>3</sub>O<sub>6.95</sub> [38]. However, very recent AC susceptibility measurements [208] suggest that the field dependence is much weaker in the Meissner state than that reported in Ref. [38]. In the vortex state, nonlocal effects associated with nodes on the Fermi surface likely dominate the behaviour of  $\lambda_{ab}(H)$ , whereas nonlinear effects are believed to be the primary source of the  $H$ -dependence in the Meissner state. One must be careful in making comparisons between measurements of the penetration depth in the Meissner and vortex states. Differences may be solely due to the way in which the penetration depth is defined in the techniques used.

The measurements of  $r_0$  as a function of temperature and magnetic field are an

important contribution to the general understanding of the characteristic length scale  $\xi_{ab}$ . It has been shown here that in the conventional theory of the vortex state,  $\xi_{ab}$  behaves essentially in the same manner as the vortex-core size. The sharp decrease in the vortex-core radius  $r_0$  (and hence  $\xi_{ab}$ ) with increasing magnetic field is attributed to increased vortex-vortex interactions. In  $\text{YBa}_2\text{Cu}_3\text{O}_{7-\delta}$ ,  $\xi_{ab}$  is generally assumed to be a small quantity (*e.g.* typical values being 12-14 Å). However, the results herein indicate that at least in the vortex state, this is really only the case in moderate magnetic fields. The extrapolated zero-field value of  $\xi_{ab}$  in  $\text{YBa}_2\text{Cu}_3\text{O}_{6.95}$  is  $\approx 80$  Å, which “may” imply that  $\xi_{ab}$  is larger in the Meissner state than what is generally assumed. Deoxygenation is found to increase the magnitude of  $\xi_{ab}$ , which in the vortex state implies that the cores will overlap at a reduced value of  $H_{c2}$ . It is important to note that while  $r_0$  is rather insensitive to the choice of the fitted model, the precise relationship between  $r_0$  and  $\xi_{ab}$  does depend on the model.

The shrinking of the vortex-core radius with decreasing temperature in  $\text{NbSe}_2$  is consistent with the traditional picture of discrete bound quasiparticle states in the core. As  $r_0$  shrinks, the energy level spacing increases. The change in the size of the vortex core should saturate when the thermal energy is less than the energy level spacing. The substantially weaker temperature dependence of  $r_0$  found in  $\text{YBa}_2\text{Cu}_3\text{O}_{7-\delta}$  suggests that this occurs at much higher temperatures in this compound. The smaller core size and the reduction of the  $T$ -dependence in  $\text{YBa}_2\text{Cu}_3\text{O}_{7-\delta}$  both imply that there are fewer bound quasiparticle states in the vortex cores than in  $\text{NbSe}_2$ .

It should be noted that since the temperature and field dependence of  $\xi_{ab}$  found here originates from changes in the electronic structure of the vortex cores, there is no reason to expect that  $\xi_{ab}$  should exhibit similar behaviour in the Meissner state. Furthermore, it is really the vortex core size which has been measured in this thesis. Although this is generally considered to be an indirect measurement of the coherence

length, it is not entirely clear whether this coherence length is fundamentally the same as the coherence length in the Meissner state.

Finally, the results of these measurements indicate that the London and GL models with field independent  $\lambda$  and  $\xi$  are not applicable deep in the superconducting state. The fact that the data were analyzed with models in which  $\lambda$  and  $\xi$  were not defined as functions of magnetic field does not invalidate this conclusion. The field dependence of both  $\lambda$  and  $\xi$  appears to be associated with the unique properties of the vortex lattice.

## Bibliography

- [1] M. Tinkham. *Introduction to Superconductivity: Second Edition* (McGraw-Hill, New York, pp. 167-168, 1996).
- [2] J.E. Sonier, R.F. Kiefl, J.H. Brewer, D.A. Bonn, J.F. Carolan, K.H. Chow, P. Dosanjh, W.N. Hardy, Ruixing Liang, W.A. MacFarlane, P. Mendels, G.D. Morris, T.M. Riseman and J.W. Schneider. *Phys. Rev. Lett.* **72**, 744 (1994).
- [3] J.E. Sonier, R.F. Kiefl, J.H. Brewer, D.A. Bonn, S.R. Dunsiger, W.N. Hardy, Ruixing Liang, W.A. MacFarlane, T.M. Riseman, D.R. Noakes and C.E. Stronach. *Phys. Rev. B* **55**, 11789 (1997).
- [4] J.E. Sonier, R.F. Kiefl, J.H. Brewer, J. Chakhalian, S.R. Dunsiger, W.A. MacFarlane, R.I. Miller, A. Wong, G.M. Luke and J.W. Brill. *Phys. Rev. Lett.* **79**, 1742 (1997).
- [5] J.E. Sonier, R.F. Kiefl, J.H. Brewer, D.A. Bonn, S.R. Dunsiger, W.N. Hardy, Ruixing Liang, W.A. MacFarlane, R.I. Miller, T.M. Riseman, D.R. Noakes, C.E. Stronach and M.F. White Jr., *Phys. Rev. Lett.* **79**, 2875 (1997).
- [6] R.D. Parks. *Superconductivity* (Marcel Dekker, Inc., New York, p.88, 1969).
- [7] F. London and H. London. *Proc. Roy. Soc.* **A149**, 71 (1935).
- [8] C.J. Gorter and H. Casimir. *Physica* **1**, 306 (1934).
- [9] J. Bardeen, L.N. Cooper and J.R. Schrieffer. *Phys. Rev.* **108**, 1175 (1957).
- [10] B. Muhlschlegel. *Z. Phys.* **155**, 313 (1959).
- [11] F. Gross *et al.*, *Z. Phys.* **64**, 175 (1964).
- [12] J. Annett, N. Goldenfeld and S.R. Renn. *Phys. Rev. B* **43**, 2778 (1991).
- [13] P.J. Hirshfeld and N. Goldenfeld. *Phys. Rev. B* **48**, 4219 (1993).
- [14] W.N. Hardy, D.A. Bonn, D.C. Morgan, R. Liang and Kuan Zhang. *Phys. Rev. Lett.* **70**, 3999 (1993).
- [15] Jian Mao, D.H. Wu, J.L. Peng, R.L. Greene and Steven M. Anlage. *Phys. Rev. B* **51**, R3316 (1995).

- [16] H. Srikanth, B.A. Willemsen, T. Jacobs, S. Sridhar, A. Erb, E. Walker and R. Flükiger, *Phys. Rev. B* **55**, R14733 (1997).
- [17] T. Jacobs, S. Sridhar, Qiang Li, G.D. Gu and N. Koshizuka, *Phys. Rev. Lett.* **75**, 4516 (1995).
- [18] O. Waldmann, F. Steinmeyer, P. Müller, J.J. Neumeier, F.X. Régi, H. Savary and J. Schneck, *Phys. Rev. B* **53**, 11825 (1996).
- [19] T. Shibauchi, N. Katase, T. Tamegai and K. Uchinokura, *Physica C* **264**, 227 (1996).
- [20] Shih-Fu Lee, D.C. Morgan, R.J. Ormeno, D.M. Broun, R.A. Doyle, J.R. Waldram and K. Kadowaki, *Phys. Rev. Lett.* **77**, 735 (1996).
- [21] C. Panagopoulos, J.R. Cooper, G.B. Peacock, I. Gameson, P.P. Edwards, W. Schmidbauer and J.W. Hodby, *Phys. Rev. B* **53**, R2999 (1996).
- [22] G.M. Luke, Y. Fudamoto, K. Kojima, M. Larkin, J. Merrin, B. Nachumi, Y.J. Uemura, J.E. Sonier, T. Ito, K. Oka, M. de Andrade, M.B. Maple and S. Uchida, (Beijing Conference).
- [23] M. Prohammer and J.P. Carbotte, *Phys. Rev. B* **43**, 5370 (1991); P.J. Hirshfeld and N. Goldenfeld, *Phys. Rev. B* **48**, 4219 (1993).
- [24] D. Achkir, M. Poirier, D.A. Bonn, Ruixing Liang, W.N. Hardy, *Phys. Rev. B* **48**, 13184 (1993).
- [25] D.A. Bonn, S. Kamal, K. Zhang, R. Liang, D.J. Barr, E. Klein and W.N. Hardy, *Phys. Rev. B* **50**, 4051 (1994).
- [26] Dong Ho Wu, Jian Mao, S.N. Mao, J.L. Peng, X.X. Xi, T. Venkatesan, R.L. Greene and Steven M. Anlage, *Phys. Rev. Lett.* **70**, 85 (1993).
- [27] Steven M. Anlage, Dong Ho Wu, Jian Mao, S.N. Mao, X.X. Xi, T. Venkatesan, J.L. Peng and R.L. Greene, *Phys. Rev. B* **50**, 523 (1994).
- [28] A.B. Pippard, *Proc. Roy. Soc.* **A216**, 547 (1953).
- [29] I. Kosztin and A.J. Legget, *Phys. Rev. Lett.* **79**, 135 (1997).
- [30] S.K. Yip and J.A. Sauls, *Phys. Rev. Lett.* **69**, 2264 (1992).
- [31] A.B. Pippard, *Proc. Roy. Soc.* **A203**, 210 (1950).
- [32] Yu. V. Sharvin and F. Gantmakher, *Soviet Phys. JETP* **12**, 866 (1961).

- [33] S. Sridhar and J.E. Mercereau, Phys. Rev. B **34**, 203 (1986).
- [34] T. Hanaguri, Y. Iino, A. Maeda and T. Fukase, Physica C **246**, 223 (1995).
- [35] D. Xu, S.K. Yip and J.A. Sauls, Phys. Rev. B **51**, 16233 (1995).
- [36] B.P. Stojković and O.T. Valls, Phys. Rev. B **51**, 6049 (1995).
- [37] A. Maeda, Y. Iino, T. Hanaguri, N. Motohira, K. Kishio and T. Fukase, Phys. Rev. Lett. **74**, 1202 (1995).
- [38] A. Maeda, T. Hanaguri, Y. Iino, S. Masuoka, Y. Kokata, Jun-ichi Shimoyama, K. Kishio, H. Asaoka, Y. Matsushita, M. Hasegawa and H. Takei, J. Phys. Soc. Jpn. **65**, 3638 (1996).
- [39] S. Sridhar, Dong-Ho Wu and W. Kennedy, Phys. Rev. Lett. **63**, 1873 (1989).
- [40] M.H. Amin, I. Affleck and M. Franz, (to be published).
- [41] V.L. Ginzburg and L.D. Landau, Zh. Eksp. Teor. Fiz. **20**, 1064 (1950).
- [42] R.D. Parks, *Superconductivity* (Marcel Dekker, Inc., New York, p.357, 1969).
- [43] V.L. Ginzburg, Sov. Phys. Solid State **2**, 1824 (1960).
- [44] G. Schatz and A. Weidinger, *Nuclear Condensed Matter Physics* (John Wiley and Sons Ltd., 1992).
- [45] J.H. Brewer, R.F. Kiefl, J.F. Carolan, P. Dosanjh, W.N. Hardy, S.R. Kreitzman, Q. Li, T.M. Riseman, P. Schleger, H. Zhou, E.J. Ansaldo, D.R. Noakes, L.P. Le, G.M. Luke, Y.J. Uemura, K. Hepburn-Wiley and C.E. Stronach, Hyperfine Interactions **63**, 177 (1990).
- [46] S.F.J. Cox, J. Phys. C **20**, (1987).
- [47] A. Schenck, *Muon Spin Rotation Spectroscopy: Principles and Applications in Solid State Physics* (Adam Hilger Ltd., 1985).
- [48] T.M. Riseman, Ph.D. thesis, University of British Columbia (1993).
- [49] J.H. Brewer, *Encyclopedia of Applied Physics, Vol. 11* pp.23-53 (VCH Publishers, Inc., 1994).
- [50] T.M. Riseman, J.H. Brewer, K.H. Chow, W.N. Hardy, R.F. Kiefl, S.R. Kreitzman, R. Liang, W.A. MacFarlane, P. Mendels, G.D. Morris, J. Rammer, J.W. Schneider, D. Niedermayer and S.L. Lee, Phys. Rev. B **52**, 10569 (1995).



- [51] Y.Q. Song, W.P. Halperin, L. Tonge, T.J. Marks, M. Ledvij, V.G. Kogan and L.N. Bulaevskii, *Phys. Rev. Lett.* **70**, 3127 (1993).
- [52] G. Blatter, M.V. Feigel'man, V.B. Geshkenbein, A.I. Larkin and V.M. Vinokur, *Rev. Mod. Phys.* **66**, 1125 (1994).
- [53] M. Murakami, *Studies of High Temperature Superconductors: Critical Current, Flux Pinning and Optical Studies of High Temperature Superconductors*, **22**, 1 (Nova Science Publishers Inc., 1997).
- [54] E.H. Brandt, *J. Low Temp. Phys.* **26**, 709 (1977).
- [55] E.H. Brandt, *J. Low Temp. Phys.* **26**, 735 (1977).
- [56] E.H. Brandt, *J. Low Temp. Phys.* **28**, 263 (1977).
- [57] E.H. Brandt, *J. Low Temp. Phys.* **28**, 291 (1977).
- [58] E.H. Brandt and U. Essmann, *Phys. Status Solidi (b)* **144**, 13 (1987).
- [59] A.I. Larkin and Yu.V. Ovchinnikov, *J. Low Temp. Phys.* **34**, 409 (1979).
- [60] A. Sudbo and E.H. Brandt, *Phys. Rev. Lett.* **67**, 3176 (1991); *Phys. Rev. B* **43**, 10482 (1991).
- [61] E.H. Brandt, *Phys. Rev. Lett.* **66**, 3213 (1991).
- [62] M.V. Feigel'man and V.M. Vinokur, *Phys. Rev. B* **41**, 8986 (1990); V.M. Vinokur, M.V. Feigel'man, V.B. Geshkenbein and A.I. Larkin, *Phys. Rev. Lett.* **65**, 259 (1990).
- [63] D.E. Farrell, J.P. Rice and D.M. Ginsberg, *Phys. Rev. Lett.* **67**, 1165 (1991).
- [64] R.G. Beck, D.E. Farrell, J.P. Rice, D.M. Ginsberg and V.G. Kogan, *Phys. Rev. Lett.* **68**, 1594 (1992).
- [65] H. Safar, P.L. Gammel, D.A. Huse, D.J. Bishop, J.P. Rice and D.M. Ginsberg, *Phys. Rev. Lett.* **69**, 824 (1992).
- [66] W.K. Kwok, S. Fleshler, U. Welp, V.M. Vinokur, J. Downey, G.W. Crabtree and M.M. Miller, *Phys. Rev. Lett.* **69**, 3370 (1992).
- [67] M. Charalambous, J. Chaussy and P. Lejay, *Phys. Rev. B* **45**, 5091 (1992).
- [68] H. Safar, P.L. Gammel, D.A. Huse, D.J. Bishop, W.C. Lee, J. Giapintzakis and D.M. Ginsberg, *Phys. Rev. Lett.* **70**, 3800 (1993).

- [69] M. Charalambous, J. Chaussy, P. Lejay and V. Vinokur, *Phys. Rev. Lett.* **71**, 436 (1993).
- [70] W.K. Kwok, J. Fendrich, U. Welp, S. Fleshler, J. Downey and G.W. Crabtree, *Phys. Rev. Lett.* **72**, 1108 (1994).
- [71] W.K. Kwok, J. Fendrich, S. Fleshler, U. Welp, J. Downey and G.W. Crabtree, *Phys. Rev. Lett.* **72**, 1092 (1994).
- [72] J.A. Fendrich, W.K. Kwok, J. Giapintzakis and C.J. van der Beek, *Phys. Rev. Lett.* **74**, 1210 (1995).
- [73] A. Schilling, H.R. Ott and Th. Wolf, *Phys. Rev. B* **46**, 14253 (1992).
- [74] T. Nishizaki, Y. Onodera, N. Kobayashi, H. Asaoka and H. Takei, *Phys. Rev. B* **53**, 82 (1996).
- [75] R. Liang, D.A. Bonn and W.N. Hardy, *Phys. Rev. Lett.* **76**, 835 (1996).
- [76] U. Welp, J.A. Fendrich, W.K. Kwok, G.W. Crabtree and B.W. Veal, *Phys. Rev. Lett.* **76**, 4809 (1996).
- [77] B. Billon, M. Charalambous, J. Chaussy, R. Koch and R. Liang, *Phys. Rev. B* **55**, R14753 (1997).
- [78] M. Roulin, A. Junod and E. Walker, *Science* **273**, 1210 (1996).
- [79] A. Schilling, R.A. Fisher, N.E. Phillips, U. Welp, D. Dasgupta, W.K. Kwok and G.W. Crab, *Nature (London)* **382**, 791 (1996).
- [80] A. Junod, M. Roulin, J.Y. Genoud, B. Revaz, A. Erb and E. Walker, *Physica C* **275**, 245 (1997).
- [81] A. Schilling, R.A. Fisher, N.E. Phillips, U. Welp, W.K. Kwok and G.W. Crabtree, *Phys. Rev. Lett.* **78**, 4833 (1997).
- [82] M. Suenaga, A.K. Ghosh, Y. Xu and D.O. Welch, *Phys. Rev. Lett.* **66**, 1777 (1991).
- [83] H. Drulis, Z.G. Xu, J.W. Brill, L.E. De Long and J.C. Hou, *Phys. Rev. B* **44**, 4731 (1991).
- [84] M.F. Schmidt, N.E. Israeloff and A.M. Goldman, *Phys. Rev. Lett.* **70**, 2162 (1993); *Phys. Rev. B* **48**, 3404 (1993).
- [85] J.W. Lynn, N. Rosov, T.E. Grigereit, H. Zhang and T. W. Clinton, *Phys. Rev. Lett.* **72**, 3413 (1994).

- [86] E.M. Forgan, R. Cubitt, M. Yethiraj, D.K. Christen, D.M. Paul, S.L. Lee and P.L. Gammel, *Phys. Rev. Lett.* **74**, 1697 (1995).
- [87] P.L. Gammel, U. Yaron, A.P. Ramirez, D.J. Bishop, A.M. Chang, R. Ruel, L.N. Pfeiffer, E. Bucher, G.D. Anna, D.A. Huse, K. Mortensen, M.R. Eskildsen and P.H. Kes, *Phys. Rev. Lett.* **80**, 833 (1998).
- [88] K. Ghosh, S. Ramakrishnan, A. K. Grover, Gautam I. Menon, Girish Chandra, T.V. Chandrasekhar Rao, G. Ravikuma, P. K. Mishra, V. C. Sahni, C. V. Tomy, G. Balakrishnan, D. Mck Paul, and S. Bhattacharya, *Phys. Rev. Lett.* **76**, 4600 (1996).
- [89] D.R. Nelson, *Phys. Rev. Lett.* **60**, 1973 (1988).
- [90] D.R. Nelson and H.S. Seung, *Phys. Rev. B* **39**, 9153 (1989).
- [91] E.H. Brandt, *Phys. Rev. Lett.* **63**, 1106 (1989).
- [92] A. Houghton, R.A. Pelcovits and A.A. Sudbø, *Phys. Rev. B* **40**, 6763 (1989).
- [93] F. Lindemann, *Phys. Z. (Leipzig)* **11**, 69 (1910).
- [94] M.P.A. Fisher, *Phys. Rev. Lett.* **62**, 1415 (1989).
- [95] D. Ertas and D.R. Nelson, *Physica C* **272**, 79 (1996).
- [96] T. Giamarchi and P.Le. Doussal, *Phys. Rev. B* **55**, 6577 (1997).
- [97] G. Blatter and B.I. Ivlev, *Phys. Rev. Lett.* **70**, 2621 (1993).
- [98] G. Blatter and B.I. Ivlev, *Phys. Rev. B* **50**, 10272 (1994).
- [99] L. Krusin-Elbaum, L. Civale, F. Holtzberg, A.P. Malozemoff and C. Field, *Phys. Rev. Lett.* **67**, 3156 (1991).
- [100] D.S. Fisher, M.P.A. Fisher and D.A. Huse, *Phys. Rev. B* **43**, 130 (1991).
- [101] J.R. Clem, *Phys. Rev. B* **43**, 7837 (1991).
- [102] W.E. Lawrence and S. Doniach, in *Proceedings of the Twelfth International Conference on Low Temperature Physics*, edited by E. Kanda (Academic Press of Japan, Kyoto, 1971), p. 361.
- [103] Ji-Min Duan, *Phys. Rev. B* **49**, 6252 (1994).
- [104] A.E. Koshelev, L.I. Glazman and A.I. Larkin, *Phys. Rev. B* **53**, 2786 (1996).

- [105] D.R. Harshman, R.N. Kleiman, M. Inui, G.P. Espinosa, D.B. Mitzi, A. Kapitulnik, T. Pfiz, D. Ll. Williams, *Phys. Rev. Lett.* **67**, 3152 (1991).
- [106] D.R. Harshman, E.H. Brandt, A.T. Fiory, M. Inui, D.B. Mitzi, L.F. Schneemeyer and J.V. Waszczak, *Phys. Rev. B* **47**, 2905 (1993).
- [107] S.L. Lee, P. Zimmermann, H. Keller, M. Warden, I.M. Savic, R. Schauwecker, D. Zech, R. Cubitt, E.M. Forgan, P.H. Kes, T.W. Li, A.A. Menovsky and Z. Tarnawski, *Phys. Rev. Lett.* **71**, 3862 (1993).
- [108] C. Bernhard, Ch. Niedermayer, U. Binniger, A. Hofer, Ch. Wenger, J.L. Tallon, G.V.M. Williams, E.J. Ansaldo, J.I. Budnick, C.E. Stronach, D.R. Noakes and M.A. Blankson-Mills, *Phys. Rev. B* **52**, R7050 (1995); *Phys. Rev. B* **53**, 8790 (1996).
- [109] W.J. Kossler, A.D. Goonewardene, A.J. Greer, D. Li, Williams, E. Koster, D.R. Harshman, J.Z. Liu and R.N. Shelton, *Phys. Rev. B* **56**, 2376 (1997).
- [110] L.I. Glazman and A.E. Koshelev, *Phys. Rev. B* **43**, 2835 (1991).
- [111] S.L. Lee, M. Warden, H. Keller, J.W. Schneider, D. Zech, P. Zimmermann, R. Cubitt, E.M. Forgan, M.T. Wylie, P.H. Kes, T.W. Li, A.A. Menovsky and Z. Tarnawski, *Phys. Rev. Lett.* **75**, 922 (1995).
- [112] J.W. Schneider, S. Schafroth and P.F. Meier, *Phys. Rev. B* **52**, 3790 (1995).
- [113] V. Gomis, I. Catalan, B. Martinez, A. Gou, X. Obradors and J. Fontcuberta, *Physica C* **235-240**, 2623, (1994).
- [114] B. Pümpin, H. Keller, W. Kündig, W. Odermatt, I.M. Savic, J.W. Schneider, H. Simmler, P. Zimmerman, E. Kaldis, S. Rusiecki, Y. Maeno and C. Rossel, *Phys. Rev. B* **42**, 8019 (1990).
- [115] D.R. Harshman, G. Aeppli, E.J. Ansaldo, B. Batlogg, J.H. Brewer, J.F. Carolan, R.J. Cava, M. Celio, A.C.D. Chaklader, W.N. Hardy, S.R. Kretzmann, G.M. Luke, D.R. Noakes and M. Senba, *Phys. Rev. B* **36**, 2386 (1987).
- [116] R.F. Kiefl, T.M. Riseman, G. Aeppli, E.J. Ansaldo, J.F. Carolan, R.J. Cava, W.N. Hardy, D.R. Harshman, N. Kaplan, J.R. Kempton, S.R. Kretzmann, G.M. Luke, B.X. Yang and D.Ll. Williams, *Physica C* **153-155**, 757 (1988).
- [117] Y.J. Uemura, V.J. Emery, A.R. Moodenbaugh, M. Suenga, D.C. Johnston, A.J. Jacobson, J.T. Lewandowski, J.H. Brewer, R.F. Kiefl, S.R. Kretzmann, G.M. Luke, T. Riseman, C.E. Stronach, W.J. Kossler, J.R. Kempton, X.H. Yu, D. Opie and H.E. Schone, *Phys. Rev. B* **38**, 909 (1988).

- [118] D.R. Harshmann, L.F. Schneemeyer, J.V. Waszczak, G. Aeppli, R.J. Cava, B. Batlogg, L.W. Rupp, E.J. Ansaldo and D.Ll. Williams, A.C.D. Chaklader, W.N. Hardy, S.R. Kreitzman, G.M. Luke, D.R. Noakes and M. Senba, *Phys. Rev. B* **39**, 851 (1989).
- [119] E.M. Forgan and S.L. Lee, *Phys. Rev. Lett.* **75**, 1422 (1995).
- [120] E.H. Brandt, *Phys. Status Solidi* **51**, 345 (1972).
- [121] A. Yaouanc, P. Dalmas de Réotier and E.H. Brandt, *Phys. Rev. B* **55**, 11107 (1997).
- [122] E.H. Brandt, *J. Low Temp. Phys.* **73**, 355 (1988).
- [123] E.H. Brandt, *Phys. Rev. B* **37**, 2349 (1988).
- [124] C. Caroli, P.G. de Gennes and J. Matricon, *Phys. Lett.* **9**, 307 (1964).
- [125] P.G. de Gennes, *Superconductivity of Metals and Alloys* (Benjamin, New York, pp. 152-154, 1966).
- [126] J. Bardeen, R. Kümmel, A.E. Jacobs and L. Tewordt, *Phys. Rev.* **187**, 556 (1969).
- [127] L. Neumann and L. Tewordt, *Z. Physik* **189**, 55 (1966).
- [128] L.P. Gor'kov, *Sov. Phys. JETP* **7**, 505 (1958).
- [129] L.P. Gor'kov, *Sov. Phys. JETP* **9**, 1364 (1959).
- [130] U. Brandt, W. Pesch and L. Tewordt, *Z. Physik* **224**, 335 (1969).
- [131] J.M. Delrieu, *J. Low Temp. Phys.* **6**, 197 (1972).
- [132] E.H. Brandt, *Phys. Status Solidi* **64**, 467 (1974).
- [133] E.H. Brandt, *Phys. Status Solidi* **65**, 469 (1974).
- [134] Yu. N. Ovchinnikov and E.H. Brandt, *Phys. Status Solidi* **67**, 301 (1975).
- [135] G. Eilenberger, *Z. Phys.* **214**, 195 (1968).
- [136] K.D. Usadel, *Phys. Rev. Lett.* **25**, 507 (1970).
- [137] K.D. Usadel, *Phys. Rev. B* **4**, 99 (1971).
- [138] L. Kramer, W. Pesch and R.J. Watts-Tobin, *J. Low Temp. Phys.* **14**, 29 (1974).
- [139] W. Pesch and L. Kramer, *J. Low Temp. Phys.* **15**, 367 (1974).

- [140] L. Kramer and W. Pesch. *Z. Phys.* **269**, 59 (1974).
- [141] S.G. Döettinger, R.P. Huebener and S. Kittelberger. *Phys. Rev. B* **55**, 6044 (1997).
- [142] J. Rammer, W. Pesch and L. Kramer. *Z. Phys. B* **68**, 49 (1987).
- [143] U. Klein. *J. Low Temp. Phys.* **69**, 1 (1987).
- [144] H.F. Hess, R.B. Robinson, R.C. Dynes, J.M. Valles Jr. and J.V. Waszczak. *Phys. Rev. Lett.* **62**, 214 (1989).
- [145] J.D. Shore, M. Huang, A.T. Dorsey and J.P. Sethna. *Phys. Rev. Lett.* **62**, 3089 (1989).
- [146] F. Gygi and M. Schlüter. *Phys. Rev. B* **41**, 822 (1990).
- [147] U. Klein. *Phys. Rev. B* **41**, 4819 (1990).
- [148] N. Hayashi, T. Isoshima, M. Ichioka and K. Machida. (submitted to *Phys. Rev. B*).
- [149] S. Ullah, A.T. Dorsey and L.J. Buchholtz. *Phys. Rev. B* **42**, 9950 (1990).
- [150] F. Gygi and M. Schlüter. *Phys. Rev. B* **43**, 7609 (1991).
- [151] H.F. Hess, R.B. Robinson and J.V. Waszczak. *Phys. Rev. Lett.* **64**, 2711 (1990).
- [152] H.F. Hess. *Physica C* **185-189**, 259 (1991).
- [153] H.F. Hess, C.A. Murray and J.V. Waszczak. *Phys. Rev. Lett.* **69**, 2138 (1992).
- [154] M. Ichioka, N. Hayashi and K. Machida. *Phys. Rev. B* **55**, 6565 (1997).
- [155] N. Hayashi, M. Ichioka and K. Machida. *Phys. Rev. B* **56**, 9052 (1997).
- [156] N. Hayashi *et al.*, (to be published).
- [157] A.A. Abrikosov. *Soviet Phys. JETP* **5**, 1174 (1957).
- [158] V. Fesenko, V. Gorbunov, A. Sidorenko and V. Smilga. *Physica C* **211**, 343 (1993).
- [159] J.R. Clem. *J. Low Temp. Phys.* **18**, 427 (1975).
- [160] Z. Hao, J.R. Clem, M.W. McElfresh, L. Civale, A.P. Malozemoff and F. Holtzberg. *Phys. Rev. B* **43**, 2844 (1991).

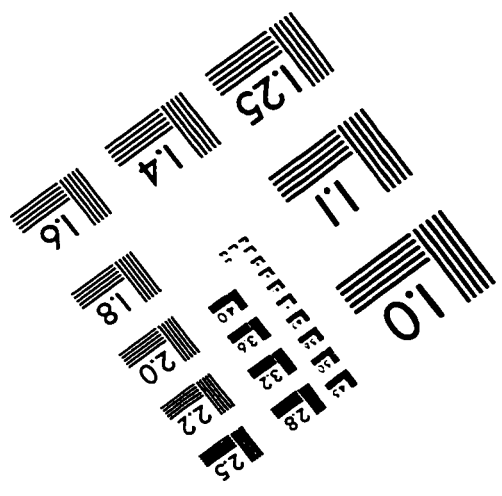
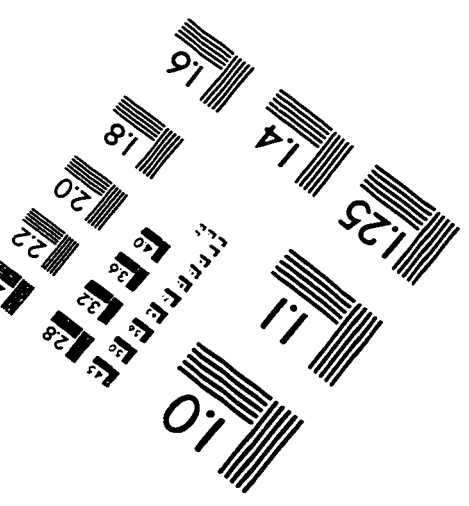
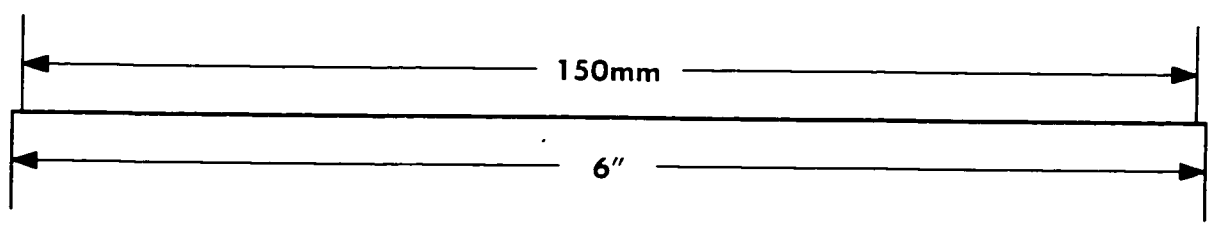
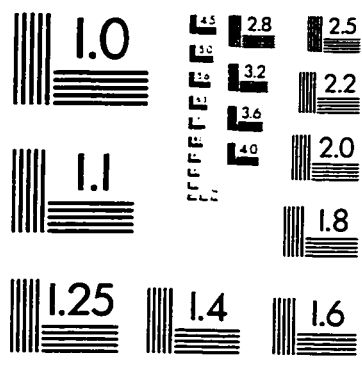
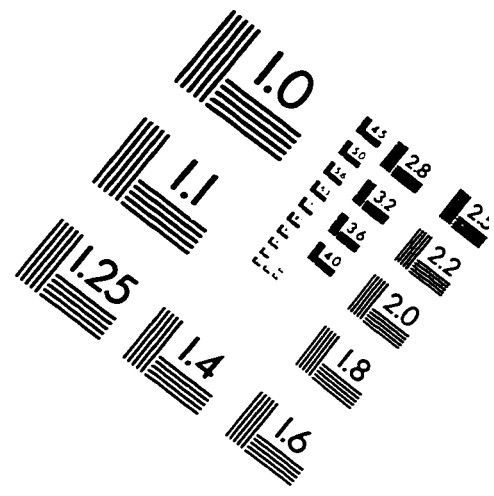
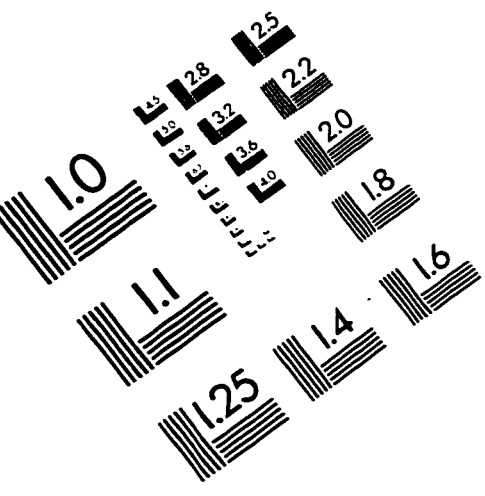
- [161] E.H. Brandt. *Phys. Rev. Lett.* **78**, 2208 (1997).
- [162] L.J. Campbell, M.M. Doria and V.G. Kogan. *Phys. Rev. B* **38**, 2439 (1988).
- [163] S.L. Thiemann, Z. Radović and V.G. Kogan. *Phys. Rev. B* **39**, 11406 (1989).
- [164] L.L. Daemen, L.J. Campbell and V.G. Kogan. *Phys. Rev. B* **46**, 3631 (1992).
- [165] P.L. Gammel, D.A. Huse, R.N. Kleiman, B. Batlogg, C.S. Oglesby, E. Bucher, D.J. Bishop, T.E. Mason and K. Mortensen. *Phys. Rev. Lett.* **72**, 278 (1994).
- [166] P.I. Soininen, C. Kallin, A.J. Berlinsky. *Phys. Rev. B* **50**, 13883 (1994).
- [167] Y. Ren, J.H. Xu and C.S. Ting. *Phys. Rev. Lett.* **74**, 3680 (1995).
- [168] A.J. Berlinsky, A.L. Fetter, M. Franz, C. Kallin and P.I. Soininen. *Phys. Rev. Lett.* **75**, 2200 (1995).
- [169] J.H. Xu, Y. Ren and C.S. Ting. *Phys. Rev. B* **52**, 7663 (1995).
- [170] J.H. Xu, Y. Ren and C.S. Ting. *Int. J. Mod. Phys. B* **10**, 2699 (1996).
- [171] M. Franz, C. Kallin, P.I. Soininen, A.J. Berlinsky and A.L. Fetter. *Phys. Rev. B* **53**, 5795 (1996).
- [172] D.N. Basov, R. Liang, D.A. Bonn, W.N. Hardy, B. Dabrowski, M. Quijada, D.B. Tanner, J.P. Rice, D.M. Ginsberg, T. Timusk. *Phys. Rev. Lett.* **74**, 598 (1995).
- [173] D.N. Basov. (private communication, 1997).
- [174] R. Heeb, A. van Otterlo, M. Sigrist and G. Blatter. *Phys. Rev. B* **54**, 9385 (1996).
- [175] M. Ichioka, N. Enomoto and K. Machida. (to be published).
- [176] M.R. Eskildsen, P.L. Gammel, B.P. Barber, U. Yaron, A.P. Ramirez, D.A. Huse, D.J. Bishop, C. Bolle, C.M. Lieber, S. Oxx, S. Sridhar, N.H. Andersen, K. Mortensen and P.C. Canfield. *Phys. Rev. Lett.* **78**, 1968 (1997).
- [177] Y. De Wilde, M. Iavarone, U. Welp, V. Metlushko, A.E. Koshelev, I. Aranson, G.W. Crabtree and P.C. Canfield. *Phys. Rev. Lett.* **78**, 4273 (1997).
- [178] I. Affleck, M. Franz and M.H. Amin. *Phys. Rev. B* **55**, R704 (1996).
- [179] M. Franz, I. Affleck and M.H.S. Amin. *Phys. Rev. Lett.* **79**, 1555 (1997).
- [180] J. Shiraishi, M. Kohmoto and K. Maki. (to be published).

- [181] N. Schopohl and K. Maki. *Phys. Rev. B* **52**, 490 (1995).
- [182] M. Ichioka, N. Hayashi, N. Enomoto and K. Machida. *Phys. Rev. B* **53**, 15316 (1996).
- [183] Y. Morita, M. Kohmoto and K. Maki. *Phys. Rev. Lett.* **78**, 4841 (1997).
- [184] M. Franz and M. Ichioka. *Phys. Rev. Lett.* (in press).
- [185] Yong Wang and A.H. MacDonald. *Phys. Rev. B* **52**, R3876 (1995).
- [186] M. Franz and Z. Tešanović. (in press).
- [187] P.L. Gammel, D.J. Bishop, G.J. Dolan, J.R. Kwo, C.A. Murray, L.F. Schneemeyer and J.V. Waszczak. *Phys. Rev. Lett.* **59**, 2592 (1987).
- [188] G.J. Dolan, F. Holtzberg, C. Feild and T.R. Dinger. *Phys. Rev. Lett.* **62**, 218 (1989).
- [189] L.Ya. Vinnikov, L.A. Gurevich, G.A. Emelchenko, G.A. Kazaryan, N.N. Kolesnikov, M.P. Kulakov, D.Ya. Lenchinenko and Yu.A. Ossipyan. *Solid State Commun.* **70**, 1145 (1989).
- [190] P. Kim, Z. Yao and C.M. Lieber. *Phys. Rev. Lett.* **77**, 5118 (1996).
- [191] E.M. Forgan, D. Paul McK., H.A. Mook, P.A. Timmins, H. Keller, S. Sutton and J.S. Abell. *Nature* **343**, 735 (1990).
- [192] N. Rosov, J.W. Lynn and T.E. Grigereit. *J. Appl. Phys.* **76**, 6772 (1994).
- [193] R. Cubitt, E.M. Forgan, G. Yang, S.L. Lee, D.McK. Paul, H.A. Mook, M. Yethiraj, P.H. Kes, T.W. Li, A.A. Menovsky, Z. Tarnawski and K. Mortensen. *Nature* **365**, 407 (1993).
- [194] M. Yethiraj, H.A. Mook, G.D. Wignall, R. Cubitt, E.M. Forgan, D.M. Paul and T. Armstrong. *Phys. Rev. Lett.* **70**, 857 (1993).
- [195] B. Keimer, W.Y. Shih, R.W. Erwin, J.W. Lynn, F. Dogan and I.A. Aksay. *Phys. Rev. Lett.* **73**, 3459 (1994).
- [196] M.B. Walker and T. Timusk. *Phys. Rev. B* **52**, 97 (1995).
- [197] I. Maggio-Aprile, Ch. Renner, A. Erb, E. Walker and Ø. Fischer. *Phys. Rev. Lett.* **75**, 2754 (1995).
- [198] K. Karrai, E.J. Choi, F. Dunmore, S. Liu, H.D. Drew, Qi Li, D.B. Fenner, Y.D. Zhu and Fu-Chun Zhang. *Phys. Rev. Lett.* **69**, 152 (1992).



- [199] X. Jiang, Wu Jiang, S.N. Mao, R.L. Greene, T. Venkatesan and C.J. Lobb, *Physica C* **254**, 175 (1995).
- [200] S.C. Zhang, *Science* **275**, 1089 (1997).
- [201] D.P. Arovas, A.J. Berlinsky, C. Kallin and Shou-Cheng Zhang, *Phys. Rev. Lett.* **79**, 2867 (1997).
- [202] J.E. Sonier, J.H. Brewer, R.F. Kiefl, J. Chakhalian, D.A. Bonn, S.R. Dunsiger, W.N. Hardy, Ruixing Liang, R.I. Miller, D. Arseneau, S.D. Kretzman, B. Hitti, D.R. Noakes and C.E. Stronach, (to be published).
- [203] Ruixing X. Liang, P. Dosanjh, D.A. Bonn, D.J. Barr, J.F. Carolan and W.N. Hardy, *Physica C* **195**, 51 (1992).
- [204] J.W. Schneider, R.F. Kiefl, K.H. Chow, S. Johnston, J.E. Sonier, T.L. Estle, B. Hitti, R.L. Lichti, S.H. Connell, J.P.F. Sellschop, C.G. Smallman, T.R. Anthony and W.F. Banholzer, *Phys. Rev. Lett.* **71**, 557 (1993).
- [205] A.A. Golubov and U. Hartmann, *Phys. Rev. Lett.* **72**, 3602 (1994).
- [206] U. Hartmann, T. Drechsler and C. Heiden, *SPIE Conf. Proc.* **1855**, 140 (1993).
- [207] C.P. Poole Jr., H.A. Farach and R.J. Creswick, *Superconductivity* (Academic Press, Inc., San Diego, p.338, 1995).
- [208] C. Bidinosti, (private communication, 1997).
- [209] J.L. Tallon, C. Bernhard, U. Binniger, A. Hofer, G.V.M. Williams, E.J. Ansaldo, J.I. Budnick and Ch. Niedermayer, *Phys. Rev. Lett.* **74**, 1008 (1995).
- [210] D.A. Bonn, S. Kamal, A. Bonakdarpour, Ruixing Liang, W.N. Hardy, C.C. Homes, D.N. Basov and T. Timusk, *Czech. J. Phys.* **46**, 3195 (1996).
- [211] M.V. Indenbom, H. Kronmüller, T.W. Li, P.H. Kes and A.A. Menovsky, *Physica C* **222**, 203 (1994).
- [212] E.M. Forgan, M.T. Wylie, S. Lloyd, M.P. Nutley, S.L. Lee, R. Cubitt, C. Aegerter, H. Keller and T.W. Li, *Hyperfine Interactions* **105**, 61 (1997).

# IMAGE EVALUATION TEST TARGET (QA-3)



**APPLIED IMAGE, Inc**  
 1653 East Main Street  
 Rochester, NY 14609 USA  
 Phone: 716/482-0300  
 Fax: 716/288-5989

© 1993, Applied Image, Inc., All Rights Reserved